Mihaela Irina Ploscaru

SELF-ASSEMBLY PROPERTIES OF $Mo_6S_{9-x}I_x$ NANOWIRES WITH DIFFERENT (BIO)MATERIALS

Doctoral Dissertation

SAMO-UREJANJE $Mo_6S_{9-x}I_x$ NANOŽIC Z RAZLIČNIMI (BIO)MATERIALI

Doktorska disertacija

Supervisor: Prof.Dr., Dragan Mihailovic

MAY 2008

MEDNARODNA PODIPLOMSKA ŠOLA JOŽEFA STEFANA
JOŽEF STEFAN INTERNATIONAL POSTGRADUATE SCHOOL
Ljubljana, Slovenia

Index

Abstract

This thesis presents a study of different nanoscale functional properties of $Mo_6S_{9-X}I_x$ nanowires and demonstrates a straight-forward functionalization route based on self-assembly. In order to ascertain their basic functional properties, studies of dispersion and electromobility under different conditions were performed. It was found that the nanowire bundles, due to their large diameters and long lengths, cannot travel through electrophoresis gel like DNA, CNTs and other familiar entities. The gel pores are too small, thus the individual thicker $Mo_6S_{9-X}I_x$ bundles and especially the agglomerated networks and meshes become trapped in the wall of the gel pockets, blocking the pores completely. Despite the fact that the nanowires exhibited no travel through the gel, their definite movement towards the positive wall of the gel pocket revealed their negative charge in aqueous solution. Dielectrophoresis was used to manipulate $Mo_6S_{9-X}I_x$ nanowires and to construct point-field emitters. $Mo_6S_{9-X}I_x$ emitters proved to be comparable in performance, durability and current stability to SWCNTs emitters.

Dispersability of $Mo_6S_{9-X}I_x$ nanowires in different pH has been tested by performing sedimentation studies and microscopic characterization. It was found that decreasing the solution pH also resulted in significant diameter reduction of the nanowires. However, the quantity of the sediments seemed to increase as well, implying disintegration of structures. The most stable dispersion showed a neutral pH.

Armed with the results from dispersion studies, a functionalization of $Mo_6S_{9-X}I_x$ nanowires in aqueous solution with different (bio) molecules was obtained, and nanowires with gold colloids in two, three and even in multi-terminal connectors were functionalized. The bond between the nanowires and the gold colloids appears to be a covalent bond facilitated by the compatible distances between Au-Au and the Mo-Mo atoms in the nanowire. In the next step, the attachment of thyroglobulin and green fluorescent protein to two different types of nanowires, as-grown nanowires and sulfonated nanowires was successfully performed. The sulfonated nanowires were seen to be decorated over their entire surface with protein, whereas in the case of as-grown material the proteins connected to the ends of the nanowires. Topographic and force-curve AFM measurements enabled the determination of the fingerprints of $Mo_6S_{9-X}I_x$ nanowires, proteins and substrates, and made it possible to distinguish between different types of nanostructures which self-assemble in solution.

Abbreviations

ac	=	alternative current
AFM	=	atomic force microscopy
AuNPs	=	gold nanoparticles
BF	=	bright field
BSA	=	bovine serum albumin
CNTs	=	carbon nanotubes
CNTFETs	=	carbon nanotube field effect transistors
CRT	=	cathode ray tube
dc	=	direct current
DEP	=	dielectrophoresis
DF	=	dark field
DFT	=	density functional theory
DMF	=	dimethyl formamide
DMSO	=	dimethyl sulfoxide
DMT	=	Dejaguin-Muller-Toporov
DNA	=	deoxyribonucleic acid
DTT	=	dithiothreitol
DWCNTs	=	double-walled carbon nanotubes
EC	=	electrochemical
e.g.	=	for example
EM	=	electron microscopy
FETs	=	field-effect transistors
GA	=	gum arabic
GFP	=	green fluorescent protein
HAS	=	human serum albumin
hcp	=	hexagonal close-packed
HOPG	=	highly oriented pyrolytic graphite
HRTEM	=	high resolution transmissive electron microscope
i.e.	=	that is
IEF	=	isoelectric focusing
IPA	=	isopropanol
ITP	=	isotachophoresis
JKR	=	Johnson-Kendall-Roberts
LDI-MS	=	laser desorption-ionization mass spectroscopy
LUMO	=	lowest unoccupied molecular orbital
MBE	=	moving boundary electrophoresis
MoDTC	=	molybdenum dithiocarbamate
MWs	=	molecular wires
MWCNTs	=	multi-wall carbon nanotubes
NC-AFM	=	atomic force microscope in non-contact mode
NMP	=	1-methyl-2-pyrrolidone
NTs	=	nanotubes
PAGE	=	polyacrylamide gel electrophoresis
PAO	=	polyalphaolefine
PEG	=	poly(ethylene glycol)
PEO	=	poly(ethylene oxide)
PET	=	poly(ethylene terephthalate)
pH	=	potential of hydrogen
pI	=	isoelectric point
PNA	=	peptide nucleic acids

Ppy	=	polypyrrole
PSS	=	polystyrene sulfonate
PVP	=	poly(vinyl pyrrolidone)
PZT	=	lead zirconate titanates
Re	=	real
RNA	=	ribonucleic acid
SAXS	=	small-angle X-ray scattering
SDS	=	sodium dodecyl sulfate
SEM	=	scanning electron microscopy
SET	=	single electron transport
SFM	=	scanning force microscope
SiNW	=	silicon nanowire
SPB	=	surface plasmon band
SPM	=	scanning probe microscope
SPR	=	surface plasmon resonance
STM	=	scanning tunneling microscopy
SWCNTs	=	sindle-wall carbon nanotubes
TBE	=	trisbase-boric acid-EDTA
TEM	=	transmission electron microscopy
Tg	=	thyroglobulin
UHV	=	ultra high vacuum
UV	=	ultra violet light
VLS	=	vapor-liquid-solid
VRH	=	variable range hopping
ZE	=	zone electrophoresis

1 Introduction

1.1 Inorganic nanotubes: background and theoretical considerations

The ability of carbon to bond with itself and with other atoms in various combinations of chains and rings forms the basis for the widespread scientific discipline of modern organic chemistry. Until recently we knew for certain of just two types of carbon crystalline structure, diamond and graphite. Despite the best efforts of some synthetic chemists like Roald Hoffmann, Orville Chapman and others, attempts to prepare novel forms of molecular or polymeric carbon were fruitless. Soon there after, in August 1985, Harold Kroto and Richard Smalley, collaborating at Rice University, launched a series of experiments on the vaporization of graphite. The first to be discovered were the hollow, cage-like buckminsterfullerene molecules (Kroto et al., 1985), also known as buckyballs, or C_{60} fullerenes (Figure 1). In accordance with the Euler rule, the C_{60} molecule was found to be composed of 20 hexagons and 12 symmetrically disposed pentagons.

In fact, what had been discovered was not just a single molecule but an infinite class of new molecules: C_{60}, C_{70}, C_{84}, etc. Following this discovery, in 1991 Sumio Iijima observed multiwall nanotubes (MWCNTs) (Figure 1) formed in a carbon arc discharge (Iijima, 1991) and two years later, he and Donald Bethune independently observed single-wall nanotubes (SWCNTs) (Iijima et al., 1993; Bethune et al., 1993). Now, more than ten years after their discovery, we know a great deal about nanotubes. We know that carbon nanotubes are made of rolled graphene sheets capped at each end with half of a fullerene molecule of the same diameter. These structures can be viewed therefore as an elongated form of a fullerene. Both fullerenes and nanotubes are seamless structures that contain carbon atoms that only form bonds with three other atoms. The absence of dangling bonds makes these structures energetically very stable. Nonetheless, the deviation from planarity induces a non-negligible amount of stress into the fullerenes; this explains many of their chemical and physical properties.

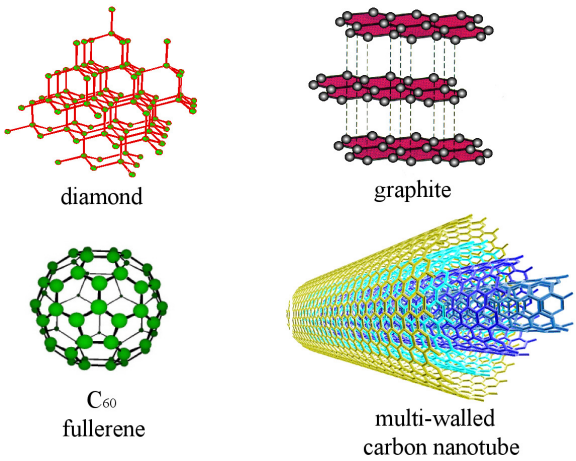

Figure 1: *Carbon*. A gallery of known carbon forms.

Despite the important properties that carbon nanotubes (CNTs) have shown since their discovery, scientists have had to face a series of obstacles. One is that carbon nanotubes are normally produced as random mixtures of metallic and semiconducting tubes (Mintmire et al., 1992; Hamada et al., 1992; Saito et al., 1992; Issi et al., 1995). While it is possible to measure the electronic properties of single tubes and to choose the right one for a given experimental set-up, any large scale application would depend on selective synthesis or efficient separation. Another important issue is that carbon nanotubes are generally insoluble in any solvents, resulting in their poor processability for many proposed potential applications. Over time, several strategies have been developed for the dispersability of the nanotubes: one is to functionalize them (Duesberg et al., 2004; Chen et al., 1998), but this process strongly changes their physical and chemical

properties (Garg and Sinnott, 1998); another is to add a surfactant (Moor et al., 2003) or a polymer (Wise et al., 2004). Unfortunately, both approaches tend to change their physical and chemical properties thus affecting their proper basic characterization.

Mainly due to the disadvantages mentioned above as well as other difficulties, scientists' attention turned towards the synthesis of other inorganic, one-dimensional structures. It is quite natural to assume that the formation of fullerene and nanotubes is not limited to carbon but can occur also in other two-dimensional layered compounds, such as WS_2 (Tenne et al., 1992) or its structural analog MoS_2 (Margulis et al., 1993; Feldman et al., 1995). In contrast to the graphite, which is made of mono-atomic carbon sheets arranged in a hexagonal honeycomb and held together by van der Waals forces, these inorganic tubes are made of stacked molecular sheets (Figure 2). For example, in the case of MoS_2 each molecular sheet consists of a six fold-bonded molybdenum layer sandwiched between two threefold-bonded sulfur layers. In analogy to graphite, weak van der Waals forces are responsible for the stacking of the S-Mo-S layers together. Unlike carbon fullerenes and nanotubes, which can be readily synthesized in single-wall form, here concentric multilayer structures are usually obtained.

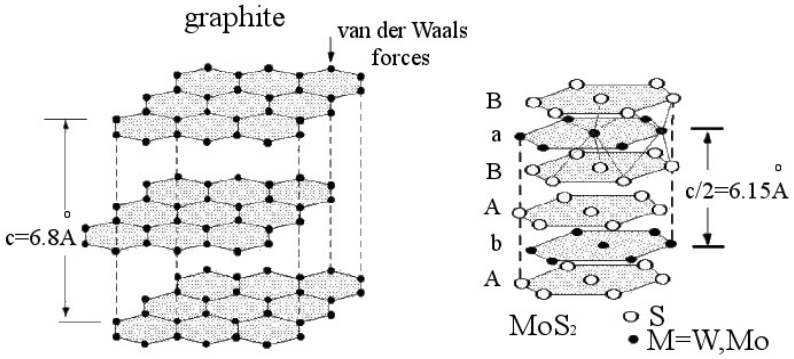

Figure 2: *Comparison of different sturctures*. Schematic drawing of graphite and MoS_2 structure.

However, these nanotubes are far from being the only inorganic nanotubes made. In recent years, a variety of inorganic materials nanotubes has been theoretically studied, synthesized and characterized:

- transition metal chalcogenide NTs: MoS_2 (Margulis et al., 1993; Feldman et al., 1995), $MoSe_2$ (Nath and Rao, 2001), WS_2 (Tenne et al., 1992), WSe_2 (Nath and Rao, 2001), NbS_2 (Nath and Rao, 2001), $NbSe_2$ (Galvan et al., 2001), TaS_2 (Nath and Rao, 2001), ZrS_2 (Nath and Rao, 2002), HfS_2 (Nath and Rao, 2002), TiS_2 (Chen et al., 2003), ZnS (Dloczik et al., 2001), NiS (Jiang et al., 2001), CdSe (Rao et al., 2001), CdS (Rao et al., 2001);
- oxide NTs

a) transition metal oxides: TiO_2 (Hoyer, 1996), ZnO (Wu et al., 2002; Zhang et al., 2002), GaO/ZnO (Hu et al., 2003), VO_x (Niederberger et al., 2003), $W_{18}O_{49}$ (Hu et al., 200), V_2O_5 (Satishkumar et al., 1997; Spahr et al., 1998), Al_2O_3 (Pu et al., 2001), In_2O_3 (Cheng and Samulski, 2001), Ga_2O_3 (Cheng and Samulski, 2001), $BaTiO_3$ (Hernandez et al., 2002), $PbTiO_3$ (Hernandez et al., 2002);

b) silicon oxides: SiO_2 (Lin et al., 2000), MoO_3 (Satishkumar et al., 2000), RuO_2 (Satishkumar et al., 2000);

c) rare earth oxides: Er, Tm, Yb, Lu oxide (Yada et al., 2002);

- transition metal halogen NTs: $NiCl_2$ (Hacohen et al., 1998);
- mixed phase and metal doped NTs: $PbNb_nS_{2n+1}$ (Bernaerts et al., 1997), $Mo_{1-x}WS_2$ (Nath et al., 2002), $W_xMo_yC_zS_z$ (Hsu et al., 2000), Nb-WS_2 (Zhu et al., 2001), WS_2-carbon nanotubes (Whitby et al., 2002), NbS_2-carbon nanotubes (Zhu et al., 2002), Au-MoS_2 (Remskar et al., 2000), Ag-WS_2 (Remskar et al., 2000), Ag-MoS_2 (Remskar et al., 2000), $Cu_{5.5}FeS_{6.5}$ (Peng et al., 2001);
- boron- and silicon-based NTs: BN (Chopra et al., 1995; Loiseau et al., 1996), BCN (Stephan et al., 1994), Si (Sha et al., 2002);
- metal nanotubes: Au (Busbee et al., 2003), Co (Tourillon et al., 2000), Fe (Tourillon et al., 2000), Cu (Han et al., 2001), Ni (Han et al., 2001), Te (Mayers and Xia, 2002), Bi (Li et al., 2001).

All these nanotubes have been synthesized by various methods. These methods can be categorized into six major approaches based on the reaction media that were used during the preparation: sulfurization,

decomposition of the precursor crystals, template growth, precursor-assisted pyrolysis, misfit rolling and direct synthesis from the vapor phase.

Overview of the synthesis of inorganic nanotubes

The synthesis of inorganic nanotubes has witnessed substantial growth in recent years. A short overview of the most commonly used methods will be presented.

Nanotubes of disulfides and diselenides of Mo and W have been prepared using various methods. The most commonly used method is the synthesis from stable oxides such as MoO_3 and WO_3 (Tenne et al., 1992; Margulis et al., 1993; Feldman et al., 1995). The oxides are first heated at high temperatures in a reducing atmosphere and then reacted with H_2S or H_2Se. Later recognizing that the trisulfides MoS_3 and WS_3 are likely to be the intermediates in the formation of disulfide nanotubes, disulfide nanotubes were obtained just by decomposing the trisulfides. Likewise, the same procedure was used for obtaining diselenides. The trisulfide route was indeed found to provide a general route for the synthesis of the nanotubes of many metal disulfides such as NbS_2 (Nath and Rao, 2001), TaS_2 (Nath and Rao, 2001), ZrS_2 (Nath and Rao, 2002), HfS_2 (Nath and Rao, 2002), etc. Another route for obtaining Mo and W dichalcogenides is to use the decomposition of the precursor ammonium salt, such as $(NH_4)_2MX_4$ (X=S, Se and M=Mo, W). The hydrothermal method can also be employed for the synthesis of dichalcogenide nanotubes, where the organic amine is taken as one of the components in the reaction mixture.

Similarly, the hydrothermal route has shown to be productive for the synthesis of other inorganic materials such as SiO_2 (Lin et al., 2000), V_2O_5 (Spahr et al., 1998), and ZnO (Zhang et al., 2002). Synthesis from surfactants of CdSe and CdS (Rao et al., 2001) has also been reported. Here the metal oxide reacts with the sulfidizing/selenidizing agent in the presence of a surfactant such as TritonX. Oxide gels in the presence of surfactants or suitable templates form nanotubes as well. For example, by coating carbon nanotubes with oxide gels and then burning off the carbon, one obtains nanotubes and nanowires of a variety of metal oxides including SiO_2 (Satishkumar et al., 1997). Boron nitride nanotubes have been obtained by striking an electric arc between HfB_2 electrodes in a N_2 atmosphere (Loiseau et al., 1996).

Gold nanorods with high aspect ratios have been synthesized in high yields by a seed-mediated growth process (Busbee et al., 2003). Gold seeds are prepared by reduction of the metal salt $HAuCl_4$ with a strong reducing agent. The growth steps involve the addition of more metal salt to the seed solution, with a weak reduction agent, in the presence of a surfactant. Ni and Cu microtubules several centimeters in length can be easily prepared using the method of pyrolysis of composite fibers consisting of a polyethylene terephthalate (PET) core fiber and an electroless-plated metal skin layer. With this approach, the diameter, wall thickness and length of metal microtubules can be controlled (Han et al., 2001).

Under appropriate growth conditions the mixed layer compounds $(PbS)_{1+x}(NbS_2)_n$ have been shown to crystallize from a vapor phase as hollow cylindrical scrolls (Bernaerts et al., 1997). Another interesting set of structures of inorganic nanowires are coated carbon nanotubes. These were obtained by Whitby (Whitby et al., 2002) by pyrolizing H_2S/N_2 over MWCNTs thinly coated with WO_3. The high resolution transmission electron microscope (HRTEM) images revealed the presence of WS_2 arrays on the tube surface.

Theoretical considerations

The basis of the growth mechanism of inorganic nanotubes is the lack of bending resistance of thin quasi two-dimensional crystal sheets (Remskar et al., 1996). This bending can be spontaneous, as in the case of transitional metals dichalcogenides and in mixed layer compounds grown from vapor phase (Bernaerts et al., 1997), or geometrically influenced by template growth in the channels of a membrane (Sha et al., 2002) or as the coating of a nanofiber (Whitby et al., 2002). Theoretical considerations suggest that due to the strain energy, narrow tubular structures are less stable than the corresponding layer stripes (Seifert et al., 2002). Thus, when the diameter passes a critical radius, the strain in the tubes becomes smaller than the energy associated with the edges (dangling bonds) in the layered stripes. Therefore, the cylindrical geometries with self-closed layers become clearly the most stable structures.

The simple rolling of crystal sheets does not usually lead to the growth of nanotubes longitudinally if the stacking order and orientation relationship between two adjacent turns is not satisfied. It is to be noticed that the geometry of the folded sheets is cylindrical, but such a formation can only grow in the radial direction until the strain energy no longer exceeds the energy gained by the van der Waals interactions

between layers. The interaction between the layers is weak and interlayer distances are arbitrary.

On the other hand, if the conditions for stacking order and orientation relationship are satisfied, the interaction between the adjacent turns is stronger. However, two limiting cases still exist from the macroscopic point of view. In the case where van der Waals interaction energies between the planes are much smaller then those associated with covalent bonds, dislocations will be generated on bending. Yet it is possible that dislocations will not form on bending and the system will remain defect less (Mendelev et al., 2002). Microscopically, the matching of adjacent layers at the atomic level, with the respective extension and/or contraction effects, contributes to the elastic energy caused by the enlarged circumference and by the bending of the molecular layers. The total elastic energy per primitive cell is larger in nanotubes than in microtubes, where the elastic energy is distributed over a large number of atoms.

The symmetry of inorganic NTs is explained in terms of line groups (Milosevic et al., 2000), which describe the quasi-one-dimensional systems holding the translational periodicity of elementary structural units along one axis. These structural units have their own point group symmetry and are arranged by operations of the generalized translation group. The theory is formulated for nanotubes with walls one, two or three molecular layers thick.

Properties and applications of inorganic nanotubes

Superior physical and chemical properties of inorganic nanotubes have been predicted and some of them have already been confirmed by experiments. Whereas quantum dots exhibit a blue shift with decreasing size of the nanoparticles, both experiment and theory has shown that the band-gap of semiconducting nanotubes, such as GaSe and MoS_2, shrinks with decreasing nanotube diameter. This effect can be ascribed to two factors: the small quantum size effect of the closed nanostructure and the deformation of the chemical bonds in the curved sheet leading to a perfect hybridization of the atomic orbitals. Furthermore, whereas armchair nanotubes were often found to have an indirect (Δ-Γ) electronic transition, zig-zag nanotubes possess a direct (Γ-Γ) transition suggesting that they could emit strong luminescence on optical or electrical excitation (Greenaway and Nitsche, 1965). Numerous publications have been dedicated to the calculations of the band structures of nanotubes. For example, BN nanotubes were found to have a high band-gap regardless their chiralities. Both experiment and theory show that the band-gap of such nanotubes shrinks to the point where they become metallic (giant Stark effect) with the application of a large transversal electric field (Khoo et al., 2004; Ishigami et al., 2005). Furthermore, BN can be used as nano-insulating devices for encapsulating conducting materials like metallic wires. Filled BN nanotubes are expected to be useful in nanoscale electronic devices and for the preparation of nano-structured ceramics.

The thermal stability of 1D nanostructures is of critical importance for their implementation as building blocks in nanoscale electronic and photonic devices. It is well known that the melting point of a solid material will be greatly reduced when it is processed in the form of nanostructures (Buffat and Borel, 1976). In a series of studies, Link and co-workers used spectroscopic methods to investigate the photothermal melting and shape transformation of gold nanorods dispersed in micellar solution (Link et al., 2000). They found that the nanorods were melted and transformed into spherical particles when exposed to femtosecond laser pulses at moderate energies. At higher energies or when exposed to nanosecond laser pulses, these nanorods were fragmented and then transformed into spherical particles with smaller dimensions. Wu and co-workers used in-situ high-temperature TEM to investigate the melting and crystallization of Ge nanowires encapsulated by carbon sheaths (Wu and Yang, 2000 and 2001). The germanium nanowires (10-100 nm in diameter) were prepared using the vapor-liquid-solid (VLS) method and subsequently coated with carbon sheaths 1-5 nm thick to confine the molten Ge and prevent the formation of liquid droplets at high temperature. Two distinct features were observed in the melting-recrystallization cycle: one was the significant lowering of the melting point, which was found to be inversely proportional to the diameter of the nanowire. The other was the large hysteresis loop associated with the melting-recrystallization cycle. By taking advantage of the relatively low melting points of the nanowires encapsulated in carbon sheaths, Wu and co-workers demonstrated the capability to manipulate individual nanowires using techniques such as cutting, interconnecting and welding.

Understanding the mechanical properties of nanostructures is essential for the atomic-scale manipulation and modification of these materials, which have been known to behave quantitatively different when the dimensions are reduced from micro- to nanoscale. Several years ago, Lieber's group pioneered the use of atomic force microscopy (AFM) in determining the mechanical properties (elasticity, strength and toughness) of individual SiC nanorods (Wong et al., 1997). Based on their measurements, the Young's modulus of 610-660 GPa was estimated for these nanorods in concordance with the theoretical predictions (Song et al., 2001) for oriented SiC. The high Young's modulus implies that these materials are

a class of promising candidates for use as reinforcing elements in generating strong composites (with ceramics, metal or polymers serving as the matrix).

Miniaturization in electronics through the "bottom-up" technique has improved considerably in recent years. The prototype devices that have been demonstrated include field-effect transistors (FETs), p-n junctions, bipolar junction transistors, resonant tunneling diodes, etc. As the critical dimension of an individual device becomes smaller and smaller, the electron transport properties of their components become an important issue. Studies from a number of groups indicated that some metal nanowires might undergo a transition to become semiconducting as their diameters are reduced (Zhang et al., 2000). Another issue related to the electronic applications of chemically synthesized nanowires is the assembly of these building blocks into various device architectures. Kovtyukhova and co-workers have synthesized nanorods containing diode-junctions and then assembled them into arrayed systems (Kovtyukhova et al., 2001). A number of interesting experiments were recently conducted with titanate nanotubes $H_2Ti_3O_7$. By adding these nanotubes to organic light-emitting diodes, the luminosity was improved and turn-on voltage decreased. These effects were attributed to the lower barrier for hole injection from the electrode to the organic semiconductor and to the improved hole transport in the organic film (Qian et al., 2004; Tokudome et al., 2005).

Another important property of inorganic nanostructures is the capacity to sense different molecules, either for medical, environmental or security-checking applications. The extremely high surface-to-volume ratios associated with these nanostructures make their electrical properties extremely sensitive to species adsorbed on surfaces. Thus Penner and co-workers fabricated a hydrogen sensor using Pd nanowires (Walter et al., 2002; Favier et al., 2001) supported on the surface of a polymeric thin film. Each nanowire contained many break junctions along their longitudinal axis that could be reduced as hydrogen gas was adsorbed into the crystal lattice. The resistance of these nanowires exhibited a strong dependence on the concentration of the hydrogen gas. In other experiments, Cui and co-workers have modified the surfaces of semiconductor nanowires and implemented them as highly sensitive, real-time sensors for pH and biological species (Cui et al., 2001). The mechanism can be understood in terms of the change in surface charge as caused by protonation and deprotonation. More recently, Law and co-workers fabricated the first room-temperature photochemical NO_2 sensors based on individual single crystalline oxide nanowires and nanoribbons (Law et al., 2002). For n-type SnO_2 single crystals, the intrinsic carrier concentration is determined by deviations from the stoichiometry in the form of equilibrium oxygen vacancies, which are predominantly atomic defects. The electrical conductivity of nanocrystalline SnO_2 depends strongly on surface states produced by molecular adsorption that often lead to space-charge-layer changes and band modulation. Nitrogen dioxide acts as an electron-trapping adsorbate on SnO_2 surfaces, and can be monitored by measuring the electrical conductance of the material.

Finally, we must not forget that nanotubes and nanowires with sharp tips are promising candidates for applications related to cold cathode or field emission of electrons. Lee et al. have investigated the field-emission characteristics of Si and SiC nanorods using current-voltage measurements (Zhou et al., 2000). Both nanorods exhibited good field-emission characteristics. The turn-on field for both types of nanorods was 15 and 20 $V\mu m^{-1}$, respectively and the current density of 0.01 $mAcm^{-2}$ was comparable with those observed for other field emitters made of CNTs and diamond.

1.2 Nanowires: overview

Beside nanotubes and rolled-up structures, in the last decade the interest was directed towards the studying of nanowire systems. Typical nanowires are often referred to as 1 dimensional (1D) materials which have interesting properties that are not seen in bulk counterparts. It is generally accepted that quantum confinement of electrons by the potential wells of nanometer sized structures may provide one of the most powerful means to control the electrical, optical, magnetic and thermoelectrical properties of a solid-state functional material. In a comparison with quantum dots and wells, the advancement of 1D nanostructures has been slow until very recently, as hindered by the difficulties associated with the synthesis and fabrication of these nanostructures with well controlled dimensions, morphology, phase purity and chemical composition. Nowadays, 1D structures can be fabricated using a number of advanced nanolithographic techniques (Cerrina et al., 1996), such as electron beam or focused ion beam writing (Gibson, 1997 and Matsui et al., 1996), proximal-probe patterning (Hong et al., 1999 and Dagata, 1995), and x-ray or extreme UV lithography. In addition, also methods based on chemical synthesis may be used for generating 1D nanostructures.

Many materials were found to naturally grow into 1D nanostructures due to the highly anisotropic bonding in the crystallographic structure. One of the most known example is the polysulphur nitride, $(SN)_x$, an inorganic polymer studied extensively due to its metallic and superconducting properties (Stejny et al.,

1981 and Stejny et al., 1979). Uniform nanowires ~20 nm in diameter and hundreds of μm in length could be easily grown from vapor phase and some of them might also aggregate into bundles.

Molybdenum Chalcogenide molecular wires

Another interesting group of nanostructures are the molybdenum chalcogenides. With the general formula $M_2Mo_6X_6$ (M= Li, Na ...etc; X= S, Se, Te), this family of compounds consists of higly anisotropic quasi-one-dimensional conductors (Tessema et al., 1991). Their structure can be understood as chains of Mo_6X_6 separated by the M element. Some of these compounds exhibit a metal-semiconducting phase transition. There are speculations that these transitions arise due to a fluctuating Peierls gap that is believed to be uncorrelated from one Mo chain to another (Tarascon et al., 1984). Further studies showed that these molecular wires can be dissolved in polar solvents, such as dimethylsulphoxide or N-methylformamide, yielding subnanometer wide molecular wires as well as larger bundles of ~1 μm in diameter with lengths up to 20 μm (Tarascon et al., 1985, Golden et al., 1995 and 1996). Using STM, Venkataraman and Lieber (1999), investigated the structural and electronic properties of the Mo_6Se_6 molecular wires. Their tunneling spectroscopic measurements indicated the existence of sharp peaks in the local density states. This observation was consistent with the Van Hove singularities characteristic of 1D conductors. No evidence for the opening of an energy gap (the metal-to-insulator transition) was found in their conductance measurements with temperatures down to 5K. Messer et al. (2000) studied the self-organization properties of these molecular wires into mesoscopic bundles. Their TEM and low-angle XRD studies indicated that the crystallinity along each individual molecular wire could be well maintained while the spacing between these inorganic wires could be varied in the range of 2-4 nm by changing the length of surfactant molecules. Moreover, it was found that the counter cations within the $Li_2Mo_6Se_6$ nanowires can be readily exchanged to form $[Mo_3Se_3^-]$ nanowires with different counter cations and hence electrical properties tunable from semiconducting to superconducting.

Selenium and tellurium wires

Se and Te chalcogens represent another ideal system for generating nanostructures with 1D morphologies. It was seen that Se and Te atoms tend to form polymeric, helical chains through covalent bonding, which can be readily packed into a hexagonal lattice through van der Waals interactions. These two materials are also interesting for their photoconductivity, piezoelectricity and high reactivity to generate important functional materials.

Gates et al. (2000) have found a solution-phase route to large scale synthesis of uniform nanowires of trigonal selenium (t-Se) with lateral dimensions controllable in the range of 10 to 100 nm and length up to several hundred microns. Formation of t-Se seeds could also be induced using other means such as sonication (Gates et al., 2002). Nearly complete transformation of a-Se colloids to t-Se wires was often observed after 5 hours of growth. By varying the concentration of amorphous selenium (a-Se) in the initial suspension, it was possible to control the diameters of the resultant nanowires. Recently, Sun et al. (2006), reported the synthesis of one-dimensional indium selenide nanowires, a III-IV group compound semiconductor nanostructure with potential applications in data storage, solar cells and optoelectronics. By the nondestructive removal of Se from one-dimensional $NbSe_3$ nanostructure, Hor et al. (2005) obtained superconducting $NbSe_2$ nanowires. The conversion takes place in the narrow reaction temperature range of 600 ºC – 700 ºC. Transport measurements on individual nanowires confirm their superconductivity with T_c ~ 7.2 K. Confinement induced enhancement of the critical fields and resistance steps in the R-I characteristics were observed also.

Theoretical calculations, performed by Kahaly et al. (2008) showed a smooth evolution of properties as one approaches the bulk, through progressively thicker nanowires. The undercoordination of atoms at the surface of the nanowires results in the reduction of cohesive energy, rearrangement of atoms at the surface, consequent changes in the interhelical distances d by approximately 1%, stronger interhelical Se-Se bonds, the decrease in the pitch of the helices and of the values of the Young's modulus with the decreasing diameter of the nanowires. Also the optical conductivity and dielectric properties of the nanowires are more strongly dependent on the plane of polarization of light than in the bulk.

The synthesis for Te nanowires is very similar to the one used for Se nanowires. Using the vapor-phase method, Furuta et al. (1975), obtained on a solid substrate Te whiskers of various morphologies by controlling the temperature. Recently Chen et al. (2007) reported the fabrication of Te nanowires parallel and perpendicular to the c-axis of Te by vapor deposition method on a substrate of $NaNO_2$ particles. A facile visible-light-assisted solution-phase approach has been developed to synthesize trigonal Te 1D nanostructures (Zhang et al., 2007). The diameter of the Te nanowires can be varied by controlling the

nucleation and growth process through modulation of the pH value of the reaction mixture.

As in the case of Se nanowires, also for Te nanowires theoretical calculations have been performed (Ghosh et al., 2007). Similarly as for the Se nanowires it has been observed that reduction of the atom coordination number at the surface of the nanowires results in the rearrangement of the atoms at the surface, stronger intrahelical Te-Te bonds, in the reduction of the lattice parameter c with decreasing size, in changes of the intrahelical distances d by ~ 1%, and in the reduction of the Young's modulus. These structural changes correlated with the decreasing overlap of the electronic wave functions of different helices and the electronic structure of the nanowires, exhibit a blue shift in the band gap with decreasing diameter of the nanowires.

Due to the structural similarities of the pure trigonal Se and Te phases and due to their similar growth conditions, 1D alloy nanostructures were synthesized. Xia et al. (2006) found that it was possible to generate monodispersed nanowires of Se/Te alloys with lateral dimensions in the range of 50 nm via the homogeneous nucleation and solution growth process (14). Using an even more simple method, Qin et al. (2006) obtained nanowires with diameter as small as 8 nm. They showed that using sodium dodecylbenzene sulfonate (SDBS) as a surfactant, the lateral dimension of Se/Te nanowires can be controlled.

Metal and oxide nanowires

Metal nanowires have been the focus of many recent studies because of their potential use as the active components or interconnectors in the fabrication of electronic, photonic and sensing devices. They also provide an ideal system to experimentally probe transport properties under various physical confinements. Metal nanowires that are a few microns in length can be prepared using a variety of methods including template synthesis (Foss et al., 1992 and Sun et al., 2000), solution phase reduction (Jana et al., 2001) and physical vapor deposition (PVD) onto carbon nanotubes (Zhang et al., 2000).

Baik et al. (2008) fabricated Fe nanowires on nanoporous templates using a pulse electro deposition in sulfuric and oxalic acid. Other reports demonstrate also the preparation of Ag nanobbelts by refluxing an aqueous silver colloidal dispersion (Bai et al., 2007) or by reducing $AgNO_3$ with ascorbic acid in the presence of poly acrylic acid (PAA) (Sun et al., 2003); the growth of Cu nanobelts on the surface of an Al TEM grid by galvanic reduction (Huang et al., 2007) and the growth of Ni nanobelts through a hydrothermal method (Liu et al., 2003) have also been shown. Recently, Zhang et al. (2006) reported on the synthesis of gold nanowires by the reduction of $HAuCl_4$ with α-D-glucose under sonication. Alternatively Sander et al. (2003) produced gold nanowires by electrochemical deposition on prefabricated gold nanorod arrays. AFM measurements made by Marszalek et al. (2000) showed that Au nanowires elongate under stretching in quantized steps up to three integer multiples of 0.176 nm and that they spontaneously shorten in steps of 0.152 nm when relaxed.

One of the most commonly used techniques used for the growth of nanowires is vapor-liquid-solid VLS process. Si and Ge nanowires have been grown using this method, where a metal catalyst (generally Au) is used to decompose the source gas and form an eutectic (Givargizov, 1975 and Greytak et al., 2004). Excess decomposition of the source gas leads to the precipitation of nanowires from an eutectic. Qi et al. (2007) used this method to produce SiGe nanowires using disilane as the Si source, which provides a higher degree of flexibility in tuning the stoichiometry. Other approaches include pulse laser ablation transforming SiGe thin films, in the presence of Au particles, through a three-step annealing process (He et al., 2005 and Deng et al., 1996). SiGe, in the form of single-crystal nanowires, offers the potential of enhancing the above optical, thermal and electrical properties compared to bulk. .

1D ZnO nanostructures have attracted recent interest due to their unique properties such as wide band gap (3.37 eV), large excitation binding energy (60 meV), excellent chemical stability and practical applications including field emission (Lee et al., 2002 and Zhao et al., 2006), dye-sensitized solar cells (Law et al., 2005), photodetectors (Lu et al., 2006) and light emitting diodes (Saito et al., 2002). The synthesis of this nanostructures includes methods like solid-vapor deposition (Pan et al., 2001 and Wang et al., 2004), thermal evaporation (Wang et al., 2004), metal-organic chemical vapor deposition (Lee et al., 2005), template assisted method (Jie et al., 2004) and aqueous solution method (Tak and Yong, 2005). Jo et al. (2003) recently prepared ZnO nanowires on a Si substrate via thermal evaporation of ZnO and graphite powder at 950 ºC, using Au as a catalyst. Lee et al. (2002) studied thermal evaporation process for synthesizing well-aligned ZnO nanowires at 550 ºC using cobalt as a catalyst.

Another interesting materials are the silicon oxide nanowires. These nanowires are good candidates to assist in miniaturization of optical fibers and to construct nanosized waveguides (Yu et al., 1998 and Tong et al., 2005). Various techniques have been employed by now to synthesize SiO_x nanowires, including chemical vapor deposition (Yan et al., 2005 and Xiao et al., 2006), laser ablation (Aharonovich et al., 2008

and Yu et al., 1998), thermal growth (Wang et al., 2006) and carbon reduction methods (Li et al., 2004). Theoretical studies addressed the formation of SiO_x nanowires through anisotropic incorporation of $(SiO_2)_n$ clusters (Zhang et al., 2006), but their results haven't been experimentally tested yet.

Recently, Law et al. (2002) fabricated the first room-temperature photochemical NO_2 sensors based on individual single-crystalline oxide nanowires and nanoribons. They demonstrated the concept with SnO_2 nanowires as a typical example. The electrical conductivity of nanocrystalline SnO_2 depends strongly on surface states produced by molecular adsorption that often lead to space-charge-layer changes and band modulation. NO_2, acts as an electron-trapping absorbate on SnO_2 crystal surfaces and can be detected by monitoring the electrical conductance of the material.

Conclusions

The research on nanostructured systems, particularly on 1D structures, allowed an increasing study of the physical and chemical principles in nanoscale structures. 1D nanostructures, in spite of the difficulties to obtain an accurate control of fabrication parameters, are ideal to study transport phenomena at nanometric scale, often preferred when compared to 0D and 2D systems In time, different and various methods were and will be further developed for the preparation of nanotubes, nanowires, nanobbelts, and other similar materials.

It is noticeable that high interest for 1D nanostructures lays in electronics, where smaller dimensions have historically allowed the production of denser, faster circuits. However, one-dimensional nanostructures and most of the applications derived from these materials are still in an early stage of technical development.

In this thesis we will focus on the type of 1D cluster chains similar to the well known "Chevrel phase" materials. These materials fall under the family of $Mo_6S_{9-x}I_x$ nanowires containing cluster including blocks. Further in this thesis the Chapter 3 will focus on their synthesis method and reveal various properties. As the title of the thesis suggests, the functionalization properties of $Mo_6S_{9-x}I_x$ nanowires will widely exposed and discussed. (Di)electrophoresis method will be mentioned as an straight forward route for trapping the nanowires on Ni electrodes for use in field-emission measurements (Chapter 4). Since in their structure the nanowires contain sulfur, our attention was directed towards the functionalization of $Mo_6S_{9-x}I_x$ nanowires with gold and different (bio)molecules; Chapter 6 is reserved for the functionalization of the nanowires with gold colloids, followed by Chapter 7, that speaks of the protein attachment on the nanowires.

2 Characterization methods

For the measurement and characterization of our sample we used different techniques. Transmission Electron Microscopy (TEM) and Scanning Electron Microscopy (SEM) measurements were carried out to characterize the $Mo_6S_{9-x}I_x$ nanowires as a raw material. For imaging and for force measurements of bare nanowires and nanowires attached with different (bio)materials when deposited on HOPG substrate, Atomic Force Microscopy (AFM) techniques were employed. This chapter will introduce the basics of the abovementioned techniques.

2.1 Scanning Electron Microscopy (SEM) and Transmission Electron Microscopy (TEM)

The history of electron microscopy (EM) began about fifty years ago. The main idea behind the development of these microscopes was to overcome some of the limitations of light microscopes. It was shown that by using electrons with wavelengths of much less than 0.1 nm, the resolution of the microscopes would improve considerably.

Two types of EM have since been developed: scanning electron microscopes (SEMs) (Figure 3a), which are mainly used for morphology studies (Goldstein et al., 2003; Chescoe and Goodhew, 1990) and transmission electron microscopes (TEMs) (Figure 3b), which are used for studying the internal structure of the specimen (Reimer, 1997).

a.  b. 

Figure 3: *Electron Microscopes.* Full image of a (a) Scanning Electron Microscope and of a (b) Transmission Electron Microscope.

2.1.1 Scanning Electron Microscopy (SEM)

Obtaining a low-magnification (<1000x) image of a three-dimensional object is remarkably easy with an SEM. Its basic components are the electron gun, the lens system, the electron collector, the visual and photorecording cathode ray tube and the microscope electronics (Figure 4). The first scanning electron microscope was developed and described in 1942 by Zworykin et al. (Zworykin et al., 1942).

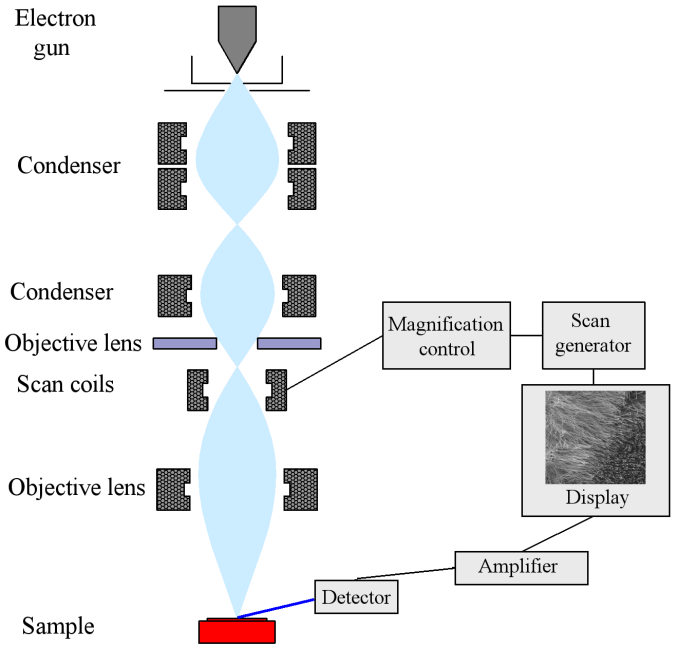

Figure 4: *Scanning Electron Microscope*. A schematic representation of the inside of a Scanning Electron Microscope.

The basic principle of SEM is very simple. As a fine beam of electrons hits the specimen, it liberates electrons from the surface layers of the sample, which are then collected by a detector. The electron beam is generated in the electron gun. Several types of electron guns are used depending on the intensity of the current that can be produced in a small spot, on the stability of the emitted current, and on the lifetime of the source. As can be seen from Figure 5, an electron gun consists of three parts: a wire filament serving as the cathode (negative electrode), the grid cap or the Wehnelt cylinder (control electrode) and the anode (positive electrode). Most of the electron microscopes use a thermionic gun (Figure 5 left). It is robust, relatively cheap and does not require an ultra high vacuum. The electrons are emitted from a heated filament, mostly made from tungsten or lanthanum hexaboride (LaB_6). The amount of electron emission and the focusing of the electrons are controlled by the Wehnelt cylinder. The emitted electrons in the gun are accelerated from the negative potential of the filament to the ground potential at the anode. A hole in the anode allows a fraction of these electrons to proceed down through the microscope column.

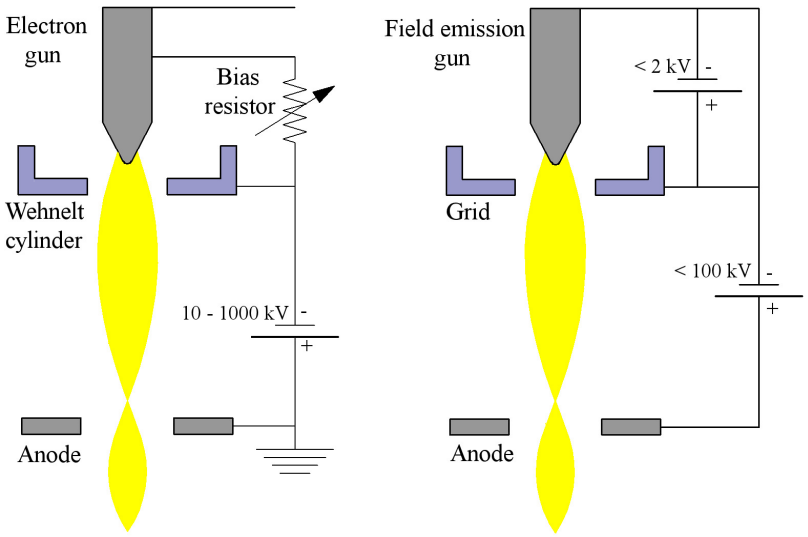

Figure 5: *Electron guns*. A schematic drawing of the thermionic (left) and field emission electron gun (right).

In addition to thermionic emission, modern microscopes can be equipped with field emission sources (Figure 5, right), where a very strong electric field (10^9 Vm^{-1}) is used to extract electrons from a metal filament. Lower temperatures give much higher source brightness than in thermionic guns.

Brightness is a very important parameter as image quality at high magnification is almost entirely dependent on it. In electron microscopy, brightness is defined as the beam current per unit area per solid angle:

$$B = I / S\Omega \tag{1}$$

Passing from the anode of the electron gun, the beam, which typically has an energy ranging from few hundred eV to 50 keV, is focused by one or two condenser lenses into a beam with a very fine focal spot sized between 1 nm and 5 nm. The beam then passes through a pair of scanning coils, which deflects the beam in a raster fashion over a rectangular area of the sample surface, before entering an objective lens, which focuses the beam on the sample surface. Complex interactions of the electrons with the atoms of the specimen produce a variety of signals which are collected by a detector. The resulting signal is then amplified and displayed on a cathode ray tube (CRT) or computer screen.

Electron beam-sample interaction in SEM

When the electron beam hits the sample, the electrons will scatter through the sample within a defined area called the interaction volume. This volume depends on the atomic number of the material being examined, on the acceleration voltage being used, and on the incident angle for the electron beam. During the electron-sample interaction secondary electrons, backscattered electrons, X-rays, heat, light, etc. will be formed (Figure 6). The image formation in the SEM mainly depends on inelastically scattered electrons that form secondary electrons. Due to their low energy, these electrons originate from within a few nanometers from below the surface. The brightness of the signal depends on the number of secondary electrons reaching the detector. If the beam hits the sample perpendicular to the surface, then a certain number of electrons "escape" from within the sample. As the angle of incidence increases, more secondary electrons will be emitted. Thus steep surfaces tend to be brighter than flat surfaces, which results in images with well-defined, three-dimensional features.

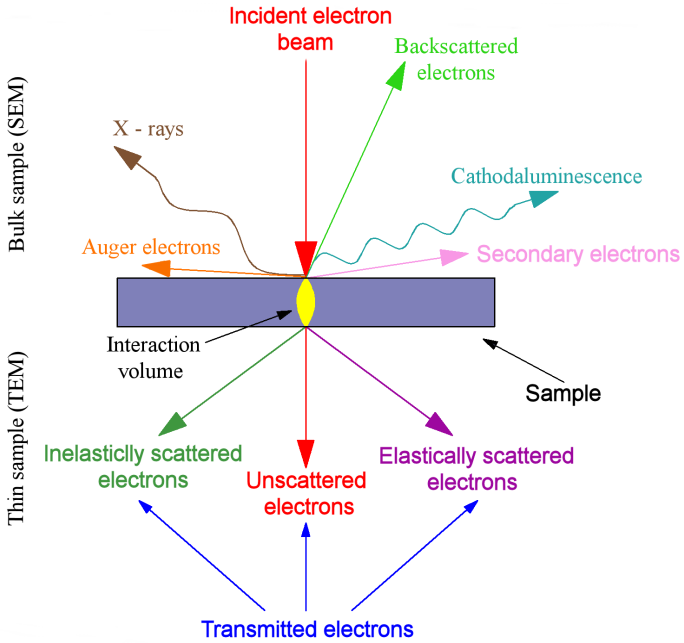

Figure 6: *Schematic of the electron-sample interaction.*

In addition to the secondary electrons, backscattered electrons can be detected as well. These are elastically scattered incident electrons that escape from the sample backwards. The intensity of these electrons varies directly with the specimen atomic number: elements with a high atomic number appear to be brighter than elements with a low atomic number. This interaction is used to detect contrast between areas with different chemical compositions. There are fewer backscattered electrons emitted from a sample than secondary electrons.

Resolution of the Scanning Electron Microscope

The spatial resolution of the SEM (Joy, 1984) depends on the size of the electron spot (0.4 - 5 nm), which in turn depends on the magnetic electron-optical system which produces the scanning beam. Likewise, the resolution is limited by the size of the interaction volume. Both parameters are very large compared to the distance between atoms, so the resolution of the SEM is not high enough to image down to atomic scale. The advantages of SEM are that it can image a large area of a specimen, can image bulk materials not just thin foils, and has the possibility to measure the composition and the nature of the specimen. Depending on the instrument, the resolution can be between 1 nm to 20 nm.

For our experiments a JOEL JXA-840A Scanning Electron Microscope was used with a thermionic tungsten emitter. The minimum optical resolution that can be reached is around 10 nm, strongly dependent on the conductivity of the sample, since charging severely affects scattering processes.

2.1.2 Transmission Electron Microscopy (TEM)

Competing with the Scanning Electron Microscope is the Transmission Electron Microscope (TEM). This microscope operates on the same basic principle as the light microscope but uses electrons instead of light. The first practical TEM was built by Albert Prebus and James Hillier in 1938. Many measurements with the TEM are performed in both the material and biological sciences.

The elements of a TEM are very similar to the ones in a SEM – a schematic representation is shown in Figure 7. The electron beam is formed by a thermionic or field emission electron gun, similar to that in a SEM. The condenser lenses then focus the electron beam to a spot on the order of 1 mm on the thin sample to be investigated. The first image formed by the objective lens is magnified typically 20-50 times. The diffraction patterns are focused in the back focal plane of the lens. Inserting an objective aperture in the back focal plane of the lens allows the selection of particular group of electrons to contribute to the final image. Afterwards, the image is passed down through the projector lenses, enlarged and then projected on a phosphorescent screen.

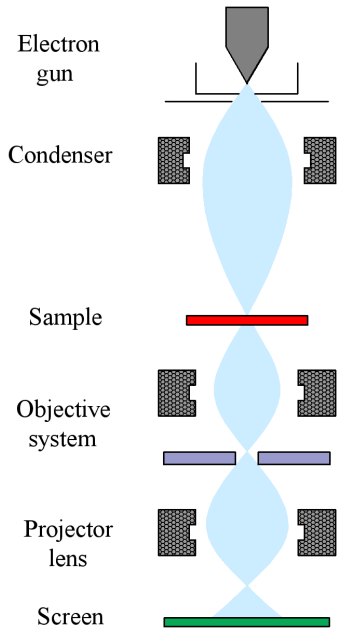

Figure 7: *Transmission Electron Microscope.* A schematic diagram of a Transmission Electron Microscope.

Electron beam-sample interaction in TEM

Specimen interaction is what makes electron microscopy possible. When the energetic electrons strike the sample, two types of interaction appear: inelastic interaction, where the energy is transferred from the incident electrons to the sample (secondary electrons, which are used for SEM images, are also produced among others), or elastic interaction, where no energy is transferred and the electrons are either passing through the sample unhindered or are scattered. As shown in Figure 6, for thin samples all unscattered and inelastically and elastically scattered electrons contribute to the image formation in the TEM. The

transmission of unscattered electrons is inversely proportional to the specimen thickness. Areas of the specimen that are thicker will have fewer transmitted unscattered electrons and will appear darker but thinner areas will have more transmitted electrons and will thus appear lighter. The elastically scattered electrons also contribute to image formation in TEM.

TEM operation modes

TEM has two basic modes of operation, namely the bright field mode and the dark field mode. In the bright field (BF) mode of the TEM (Figure 8b), an aperture is placed in the back focal plane of the objective lens which allows only the electrons in the transmitted beam (direct beam) to pass. In this case, specimen thickness and diffraction contrast contribute to image formation.

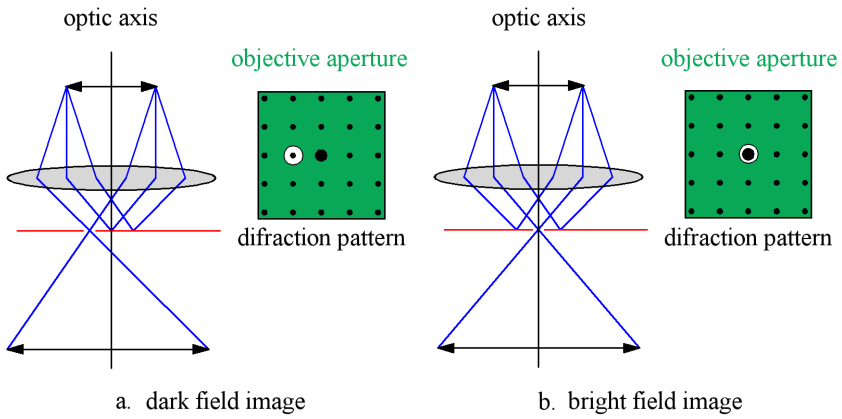

Figure 8: *TEM operational modes.* Schematic configurations of (a) dark field image and (b) bright field image. The white circle in both images represents the aperture through which the scattered electrons are allowed to pass, as in the case of DF image mode, or the direct beam is allowed to pass, as in the case of BF image mode.

Similar in purpose to the BF technique is the dark field (DF) (Figure 8a) imaging mode, where one or more diffracted beams are allowed to pass the objective aperture, while the direct beam is blocked. Dark field images present very useful information such as planar defects, stacking faults or particle size.

Despite all the interesting applications of the transmission electron microscope, there are a number of drawbacks to this technique. The preparation of a thin enough sample to be electron transparent makes the TEM microscopy time-consuming. Destruction of the crystalline structure of the sample during the preparation process can also occur. The small field of view is also an inconvenience raising the possibility that the region analyzed may not be characteristic to the whole sample. Furthermore, it is possible that the sample may be damaged by the electron beam, as in the case of biological materials.

2.2 Atomic Force Microscopy

The Atomic Force Microscope (AFM) is perhaps the most versatile member of the scanning probe microscope family (SPMs). In contrast to the electron microscope family, these microscopes generate images by “feeling” the specimen with the help of a probe.

Scanning probe microscopy began in the early 1980s when Binning and Rohrer (Binning et al., 1982) revolutionized microscopy with the invention of the Scanning Tunneling Microscope (STM). The importance of this discovery was recognized with the award of the Nobel Prize in Physics. A few years later Binning and colleagues (Binning et al., 1986) announced the construction of the second member of the SPM family – the Atomic Force Microscope (AFM), also known as the Scanning Force Microscope (SFM). Commercial AFMs began to appear in the early 1990s and have evolved through several generations. In Figure 9 an SPM Dimension 3100 (www.veeco.com) model from Veeco can be seen, which was used for our experiments as well.

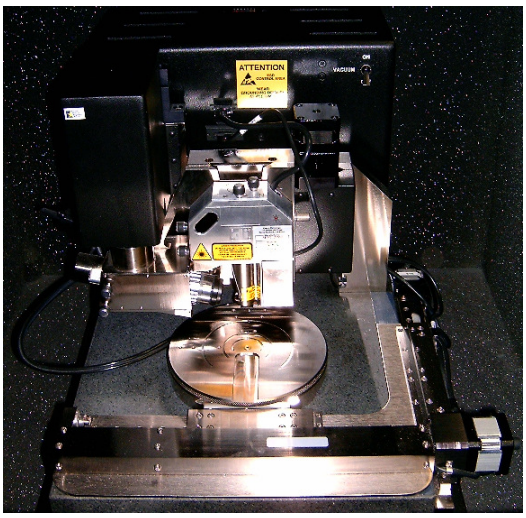

Figure 9: *Scanning Probe Microscope.* AFM Dimension 3100 model from Veeco.

The principle on which the AFM works, the different types of probes that can be used, the sample preparation as well as the tip-sample interactions will be discussed further in the next chapters.

2.2.1 Main components of the AFM

In contrast to the other microscopes that have been presented till now, the atomic force microscope is probably the easiest to be understood, even at high school level. It works on the principle of "feeling" the sample as a sharp probe scans the surface. A good analogy is of a blind person feeling objects with their fingers and then building up a mental image of what they touch. Like the blind person's fingers, this method of imaging can produce a good detailed picture. Besides taking the topography of the surface, the AFM can also give information about its softness or hardness, about the material characteristics and even about forces between the tip-sample.

The schematic in Figure 10 illustrates the main features of an atomic force microscope. The most important part is the probe which does the "feeling." The probe or the AFM cantilever is usually a hard material on which the tip is mounted and is made of silicon or silicon nitride.

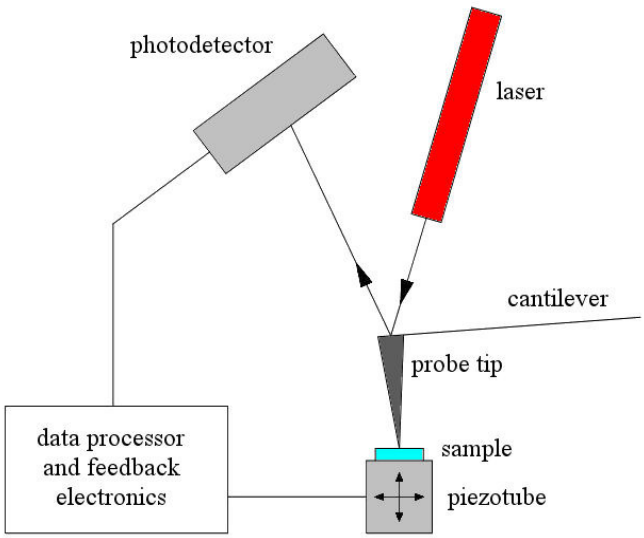

Figure 10: *Atomic Force Microscope.* Schematic representation of the Atomic Force Microscope.

Another crucial part of the AFM is the scanning mechanism. This is done by means of a piezo-ceramic actuator, which changes its position under applied voltage. The most frequently used driver is a hollow-tube scanner, which can move the sample or the cantilever in all three perpendicular directions.

The final feature of the instrument is the detection system. Here, a laser beam is focused onto the end of the cantilever, preferably directly over the tip, and then reflected onto a photodiode detector. In the majority

of the instruments, the photodiode is split into two segments (see Figure 15). As the tip moves in response to the sample topography during scanning, the angle of the reflected beam changes and so the laser spot on the photodiode moves.

When the sample is scanned the topography of the sample surface causes the cantilever to deflect as the forces between the tip and sample changes (Figure 11). The level of deflection is controlled by a feedback loop mechanism which moves the sample in the appropriate direction at each imaging point. The x, y and z displacements of the piezoelectric scanner are recorded and displayed to produce an image of the sample surface.

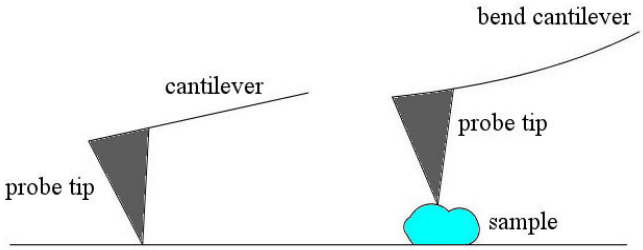

Figure 11: *Scanning process of the AFM.*

Types of cantilevers

As mentioned previously, the most important part of the AFM is the probe since this is the part that interacts with the sample. The probe consists of a cantilever with a sharp tip at the end. The tip may either be glued onto the cantilever or may be integrated, i.e. the cantilever is directly fabricated with a sharp tip at the end. Modern AFM tips and cantilevers are made by micro-fabrication, using techniques like lithographic photo-masking, etching or vapor deposition. The typical materials used are silicon, silicon nitride or diamond. They can also be coated with different materials if specific measurements want to be performed.

Two shapes of cantilevers are most commonly available commercially. One is of a triangular geometry as seen in Figure 12a, also called the "V" shape. It is designed to minimize the twisting of the cantilever during scanning and is used typically for contact mode topography. The other form in which the cantilever can be manufactured is the rectangular form (Figure 12b). This type is usually used for measuring frictional properties of the sample.

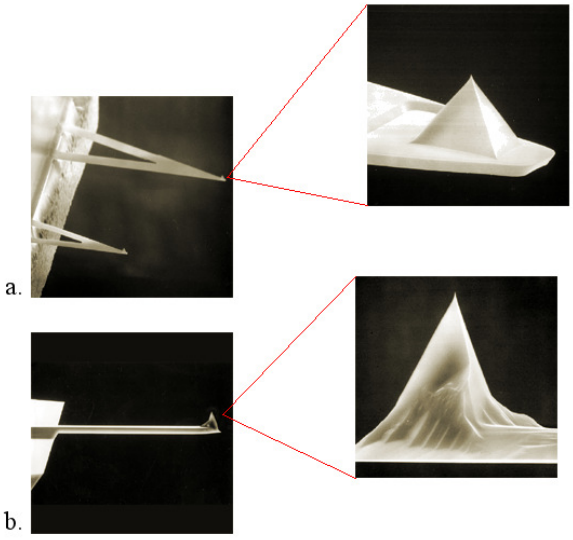

Figure 12: *AFM cantilever types.* SEM image of AFM cantilever: (a) a "V" shape cantilever and a higher resolution in the inset, and (b) a rectangular cantilever with its higher magnification in the inset.

Regardless of its shape the cantilever should fulfill several requirements:

- it should have a small spring constant to allow detection of small forces;

- its resonant frequency should be high to minimize sensitivity to mechanical vibrations;
- the tip should have a small opening angle if rough surfaces are to be studied, and large if the sample is flat (Figure 13 a and b); and,
- for atomic resolution measurements the tip should be sharp (Figure 13c).

What should be taken into consideration when choosing the tip for the measurements is that sharp tips with small opening angles are very sensitive to mechanical contact. In contrast, relatively large opening angle tips are preferable due to their resilience.

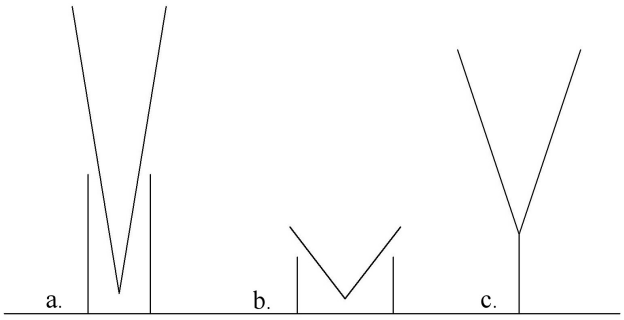

Figure 13: *AFM tip shapes.* Schematic representation of different shapes of the tip: (a) tip with small opening angle suitable for rough surfaces, (b) tip with large opening angle suitable for flat surfaces, and (c) sharp tip for atomic resolution measurements.

The piezoelectric scanner

Having some knowledge about the probes used, we shall now examine how a sample is scanned in an AFM. There are two ways of moving a sample under the AFM tip: the sample can be moved and the tip is kept in place, or the sample can be stationary and the tip is moveable. The DI 3100 model used for our experiments employed the latter scanning method.

The piezoelectric scanner is actually a tube with thin walls made from hard piezoelectric ceramic, usually lead zirconate titanate (PZT). These materials have the property to compress, twist or distort proportionally upon the applied field. The AFM scanner is constructed by combining independently operated piezo electrodes for x, y and z directions into a single tube (Figure 14). Whether the piezo elongates or contracts depends on the polarity of the applied voltage. AC voltage applied to the different electrodes of the piezoelectric scanner produce its movement along the three major axes.

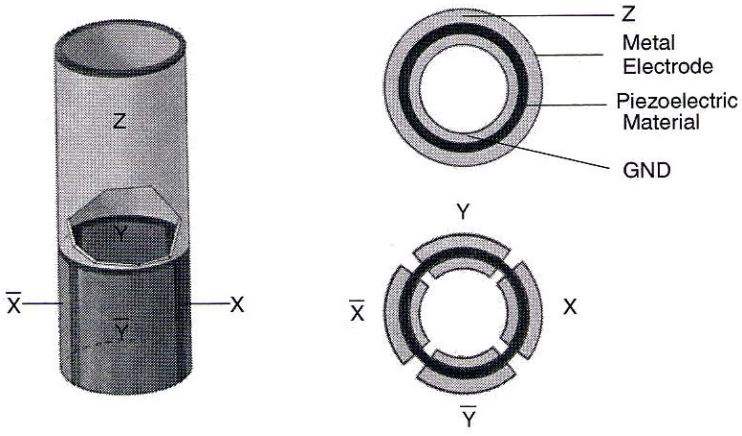

Figure 14: *AFM scanner.* Schematic representation of a piezoelectric tube scanner.

The optical detection system

With the tip making contact with the sample one can ask how the height change of the tip can be monitored as it passes across the sample. These movements can be very small when imaging atomic resolution.

The majority of the AFM designs are based on the optical detection system. Here a laser beam is reflected by the cantilever and collected by a photodiode (Meyer et al., 1989) (Figure 15). As the tip scans the surface it encounters different changes in the relief, the laser beam reflected by the deflected cantilever falling on different parts of the photodiode. Further on the signal is collected and translated into a topographic image.

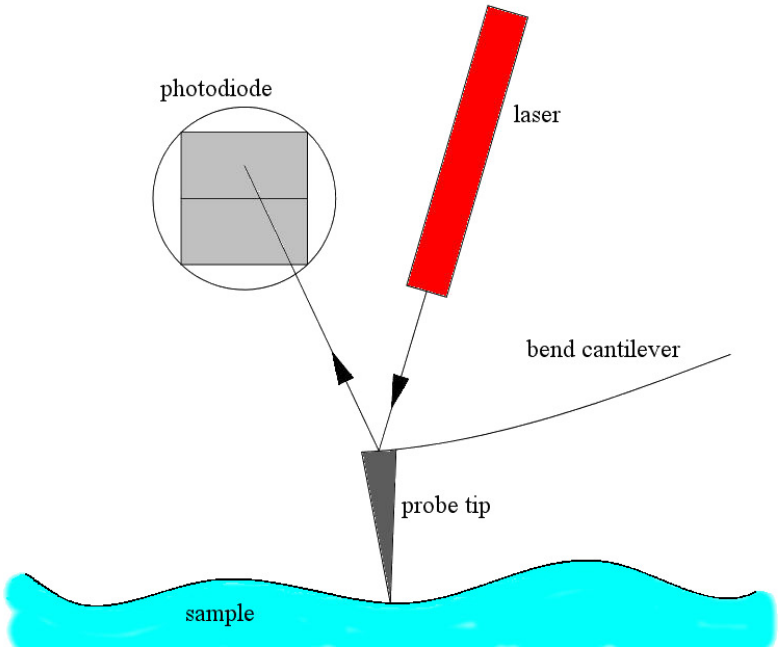

Figure 15: *Optical detection scheme.*

2.2.2 Tip sample interaction

As briefly mentioned at the beginning, the AFM relies on "feeling" the sample with the help of the cantilever. As the surface is scanned forces between tip and sample are sensed (Cappella and Dietler, 1999). In the simplest case, by measuring the cantilever's deflection δ_c and knowing its stiffness k, the forces can be calculated from Hook's law:

$$F = -k\delta_c \tag{2}$$

But the distance controlled during the measurements is actually the z-piezo position (Figure 16). Thus, the relation that connects these two parameters is given by the following relation:

$$D = Z - (\delta_c + \delta_s) \tag{3}$$

where D is the tip-sample separation and δ_s is the sample deformation.

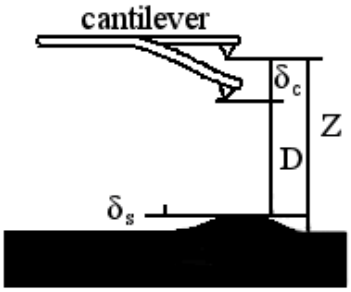

Figure 16: *The measured distances.* The tip-sample distances where the actual measured distance is the z-piezo position.

The forces are measured at the AFM by collecting a force curve (Figure 17) which is a plot of the cantilever deflection as a function of the z-piezo position. At the beginning, the tip is far from the surface and no interaction can be detected. As the tip approaches the surface, at one point it "jumps" to contact due to the attractive forces between the tip and the sample. Once the tip comes into contact, the forces increase linearly as the tip is moved further. In the retraction process the sample and the tip might remain together crossing the original contact point. When the spring force of the cantilever is great enough, the tip "jumps" out of the sample contact.

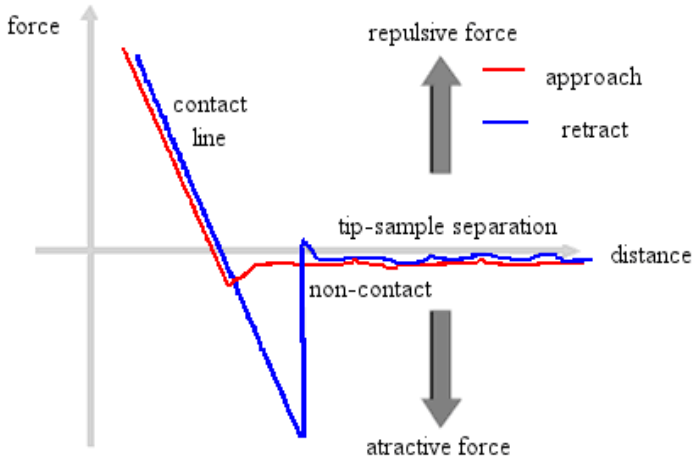

Figure 17: *Force-distance curves.* Schematic of the force-distance curve for a tip approaching the sample and then retracted.

However, the forces on the tip as it moves towards or away from the sample are different (Heinz and Hoh, 1999). In the approaching portion Van der Waals forces are dominant. These forces appear as a small negative deflection just prior to contact. Other forces that can be detected are electrostatic and polymer brush forces or elastic forces. The withdrawing curves can sometimes follow the same path as in the approaching process. Usually, though, some hysteresis can appear due to the adhesion forces. In ambient conditions the sample is covered with a layer of water forming a capillary bridge between the tip and the sample. A different form of adhesion occurs when a polymer is "cached" between the AFM tip and the surface. Usually the force curves exhibit a negative deflection as the polymer is stretched until it breaks or detaches from the tip or substrate. In the case of multiple polymer attachments saw-tooth patterns can be observed. Unbinding forces between specific biological receptor-ligand systems can also be noticed in the withdrawing curves. In the simplest case the magnitude of the adhesion is a direct measure of the binding force.

Table 1: *Force-distance curves and force laws for their interpretation (Heinz et al,. 1999).*

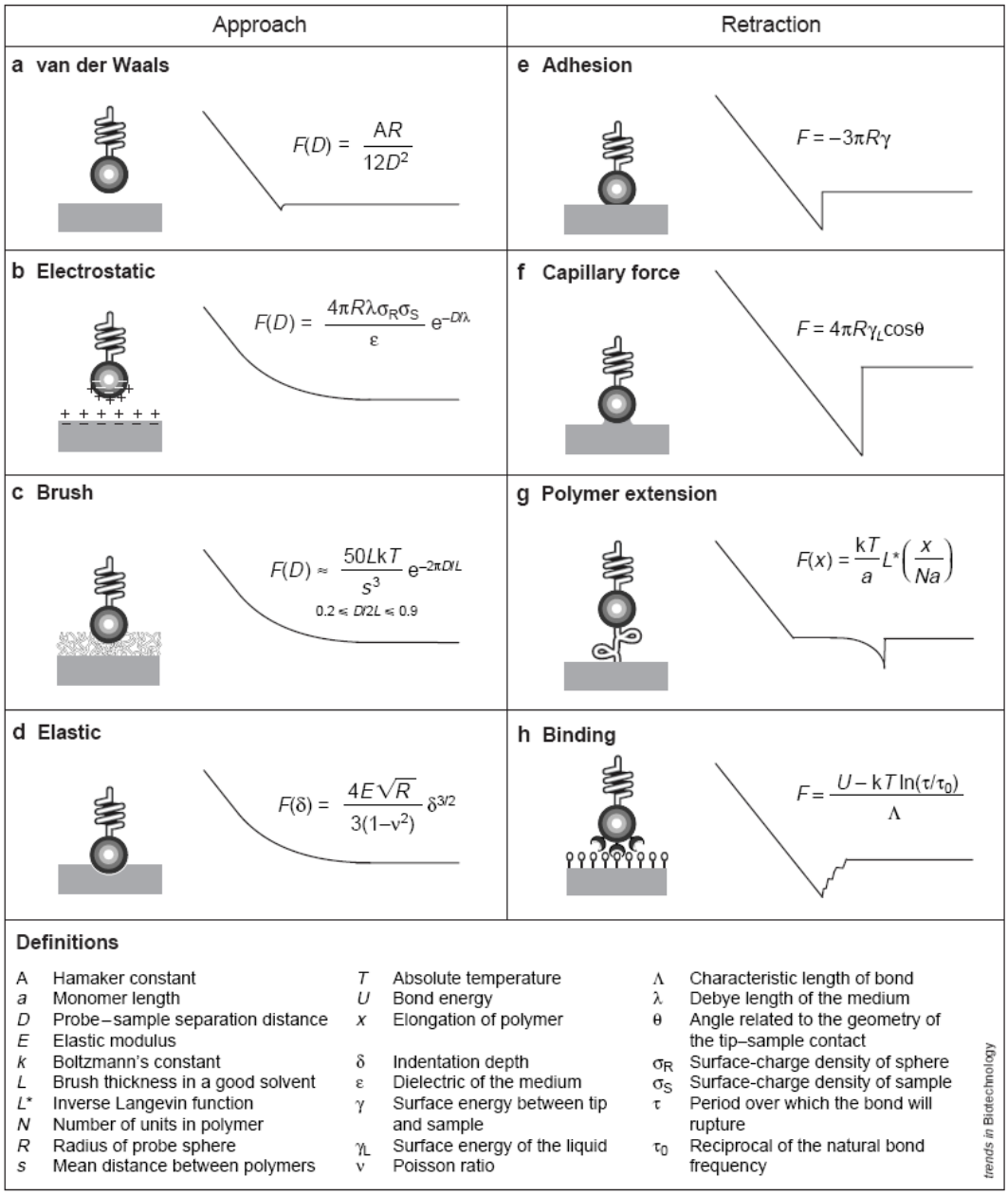

We can conclude that the interpretation of AFM force curves relies almost entirely on establishing the force laws. These force laws describe force as a function of the probe-sample separation distance (D) rather than a function of the z-piezo position. The transformation to D is obtained by subtracting the lever deflection from the z-piezo movement (Butt, 1992). Table 1 is a review of the possible forces present in the approaching and withdrawing process together with the corresponding force laws.

Basic operational modes

With the schematic force curves from Figure 10 in mind, we can conclude that two regimes are characteristic for AFM operation. One is the ***AFM contact mode*** where the tip makes a soft "physical contact" with the sample and it works in the repulsive regime of the intermolecular force curve as can be seen in Figure 18a. The permanent contact with the surface makes it unsuitable for soft samples. To overcome this problem ***AFM tapping mode*** was developed. In this mode, the tip is oscillating at its resonant frequency (in the order of hundreds of kHz) and barely "tapping" the surface. It works also in the repulsive regime and the operating region is indicated on the force-curve from Figure 18b. The tapping mode overcomes problems associated with friction, adhesion, electrostatic and other difficulties, but the scanning speed is much lower than in contact mode.

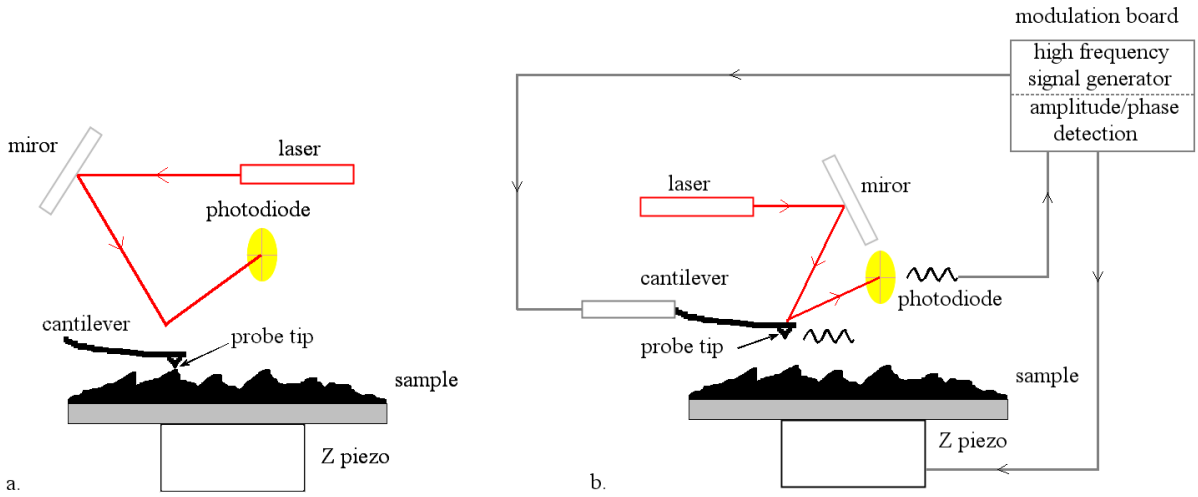

Figure 18: *AFM operational modes.* Basic operational modes of the atomic force microscope: (a) AFM contact mode and (b) AFM tapping mode and non-contact mode.

The last operational mode is the ***AFM non-contact mode (NC-AFM)***. Here the tip oscillates at its resonant frequency but the spacing between it and the surface is from 5 to 15 nm. The repulsive forces are replaced in this case by the attractive ones (see Figure 18b). In NC-AFM the tip suffers no degradation effect, which can happen in the other modes.

The AFM measurements presented in this thesis were made with the DI 3100 Scanning Probe Microscope, Nanoscope IV controller.

3 $Mo_6S_{9-x}I_x$ nanowires

Although graphite, with its anisotropic two-dimensional lattice, is the stable form of carbon under ambient conditions, on nanometer scales it forms zero- and one-dimensional structures, namely fullerenes (Kroto et al., 1985) and nanotubes (Iijima, 1991; Iijima and Ichihashi, 1993; Bethune et al., 1993), respectively. This is, however, not limited to carbon, and in recent years fullerene-like structures and nanotubes have been synthesized from numerous compounds with layered two-dimensional structures. The nanowires with the proposed formula $Mo_6S_{9-x}I_x$ (Vrbanic et al., 2004) are such a material. In structure, this material is similar to the transitional metal chalcogenides clusters, known also as Chevrel phase (Chevrel et al., 1971; Chevrel et al., 1979; Fischer, 1978).

3.1 Overview of Chevrel phases

In 1971 Chevrel et al. reported the existence of a new series of ternary molybdenum sulfides. These materials may be written with the general formula $M_xMo_6X_8$, where M stands for a metal and X stands for a chalcogen, and have superconducting properties (Fischer, 1978). The chalcogens are: oxygen (O), sulfur (S), selenium (Se), tellurium (Te), polonium (Po) and ununhexium (Uh). Compounds have also been made in which the Mo atoms from the formula $M_xMo_6X_8$ were replaced by rhenium (Re), ruthenium (Ru) and rhodium (Rh) (Perrin et al., 1978; Perrin et al., 1980).

Most of these materials can be prepared simply by mixing the appropriate amount of the elements and leaving them to react in sealed quartz tubes for about 24 hours at temperatures varying from 1000^o C to 1250^o C (Chevrel et al., 1971; Sergent and Chevrel, 1973). The resulting material is a grey powder. In cases when the M element itself is volatile in the synthesis the binaries M_xX_y (X= S, Se, Te) are used. Another method used for obtaining the Chevrel materials is the chemical-vapor deposition technique.

As simple as it is to obtain the Chevrel materials, it is difficult to characterize them. Thus, understanding their crystalline structure is of great importance. It has been found that the fundamental structural unit in the Chevrel phases is the cluster Mo_6X_8 (Figure 19). Furthermore, it was discovered that if the M element from the general formula $M_xMo_6X_8$ is a small cation, integer x can vary continuously between the values 1 and 46 but if M is a large cation, x has a defined value or is limited to a narrow interval (examples: $PbMo_{6.35}S_8$, $LaMo_6S_8$, $BaMo_{6.35}S_8$).

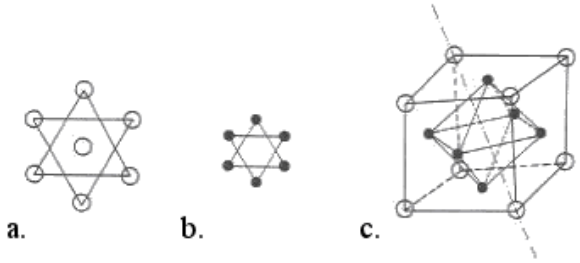

Figure 19: *Schematic of the Mo_6X_8 unit.* (a) A view of the X positions along the ternary axis; (b) A view of the Mo positions along the ternary axis; and, (c) A view of the complete unit (the ternary axis is represented by the dashed line) (Fischer et al., 1978).

In the case of the X element being sulfur, the Mo_6S_8 cluster becomes unstable at 470 ^oC and starts to decompose. Consequently, the stabilization of the structure can be obtained either by introducing the M element or by substituting sulfur by a halogen (Sergent et al., 1977).

Interesting from a structural point of view is the packing of the Mo_6X_8 clusters. Crystallographic studies have shown that nearly all ternary molybdenum chalcogenides crystallize in a hexagonal-rhombohedral structure with the rhomboheral angle α close to 90^o (Chevrel et al., 1971; Sergent and Chevrel, 1973). Bars and co-workers were the first who started the chain of structural investigations of this class of materials (Bars et al., 1973). We now know that the $M_xMo_6X_8$ (X= S, Se, Te) compounds can be thought of as building blocks of Mo_6S_8 units. In such a cubic unit the X atoms are situated at the corners and the Mo

atoms at the face centers (see Figure 19c). The Mo_6S_8 units are arranged in a simple rhombohedral lattice, each of them rotated 25° degrees around the ternary axis inside the $M_xMo_6X_8$ structure.

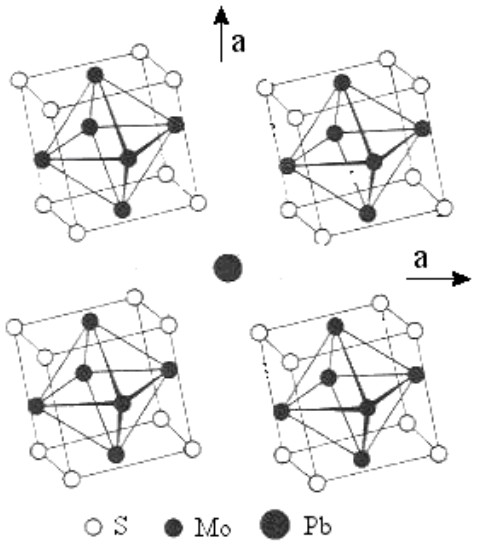

Figure 20: *$PbMo_6S_8$ compound.* Structure of the $PbMo_6S_8$ compound along the rhombohedral axis (Marezio et al., 1973).

This arrangement of the units leaves some empty channels where additional metal atoms can be inserted forming the $M_xMo_6X_8$ compound. Figure 20 shows as example the $PbMo_6S_8$ compound as described by Marezio et al. (1973). Over the years Chevrel and co-workers synthesized more other compounds containing clusters with formulas Mo_9X_{11} and $Mo_{12}X_{14}$ (Chevrel, 1981; Chevrel et al., 1980; Zheng et al., 1995) (Figure 21). These units consist of stacks of three and four staggered Mo_3X_3 units which are capped with chalcogens. The metal-metal and metal-chalcogen distances in these large clusters are in the same range as in the Mo_6X_6 cluster, between 2.6 Å and 2.8 Å.

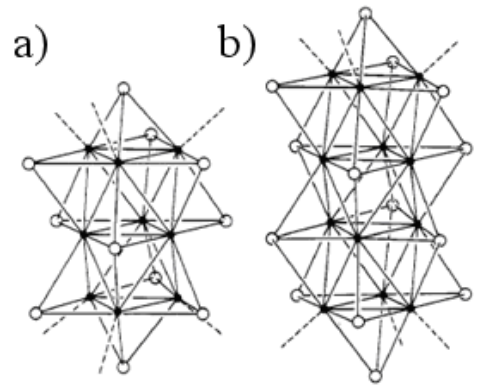

Figure 21: *Structure of (a) Mo_9X_{11} and (b) $Mo_{12}X_{14}$ units (Chevrel et al., 1980).*

Along with the determination of structural characteristics of these varieties of compounds, further interest was raised by their properties. Since their discovery, the unusual superconducting properties of these compounds have generated a large number of different investigations. Experiments have revealed a critical temperature ranging up to about 15K (see Table 2).

Table 2: *Table of the critical temperature for different compounds.*

compound	*critical temperature T_c [K]*	*references*
$Mo_6S_6Br_2$	13.8	Sergent et al., 1977
Mo_6Se_7Br	7.1	Sergent et al., 1977
Mo_6Se_7I	7.6	Sergent et al., 1977

$Mo_6Te_6I_2$	2.6	Sergent et al., 1977
$Mo_4Re_2Te_8$	3.5	Brown et al., 1986
$Li_2Mo_6S_8$	4.2	Chevrel et al., 1971
$Mg_{1.14}Mo_{6.6}S_8$	3.5	Perin et al., 1978
$PbMo_{6.4}S_8$	15.2	Perin et al., 1978, Matthias et al., 1972
$LaMo_6Se_8$	11.4	Marezio et al., 1973
$Er_{1.2}Mo_6Se_8$	6.2	Marezio et al., 1973
$Cu_2Mo_6Se_8$	5.9	Shelton et al., 1976
$Pb_{1.2}Mo_6Se_8$	6.7	Shelton et al., 1976

A striking feature of these materials is that most of them are superconducting regardless of the superconducting properties of the M element. The explanation can be found in the fact that the conductive electrons in these compounds are the 4d-electrons of Mo. Thus, the superconductivity is determined by the electronic structure of the Mo_6X_8 clusters. It was indicated by Bergmann and Rainer (1973) that the external modes of the Mo_6X_8 lattice are situated in the frequency range of $\omega \sim 2\pi T_c$ ($\omega \sim 12$ meV) favorable for superconductivity properties. In addition, it was found that the trend in T_c variation might be connected with the changes in the density of states. As a result, we expect compounds of the type $M_2^I Mo_6S_8$ (M^I= monovalent atom) and $M_1^{II} Mo_6S_8$ (M^{II}= divalent atom) to have a relatively high density of states and thus a high T_c. On the other hand, it is expected that compounds of this type $M_3^I Mo_6S_8$ and $M_1^{III} Mo_6S_8$ (M^{III}= trivalent atom) to have a low density of states and low T_c (Sergent et al., 1977). Moreover, Marezio and coworkers (1973) pointed out that the variation of T_c can be correlated to the volume of the unit cell: an increase in volume results in an increase in transition temperatures. This correlation can also be found in the case of rare earth compounds $(RE_x)Mo_6S_8$ (Sergent et al., 1978).

Another property accompanying superconductivity that raises great interest in Chevrel phase materials is the extraordinarily high critical field H_{c2} of many of these compounds. Theoretical calculations and experimental work found that the critical field in Chevrel phases was actually the orbital critical field (Odermatt et al., 1974; Foner et al., 1974; Fisher et al., 1974). The reason for this high field is to be found in the particular molecular structure of these materials, which leads to a short coherent length ζ_0 and to a short mean free path l. The reason for the weak paramagnetic pair-breaking, which allows the orbital effect to determine the H_{c2}, is probably the relatively high value of spin-orbit parameter λ_{so} (~ 10). Also, the magnetic (Zheng et al., 1995) and electronic (Tobola et al., 2003) properties of Chevrel phases with different metals at the M position were extensively studied both experimentally and theoretically.

The above overview of Chevrel phase materials is an introductory field for $Mo_6S_{9-x}I_x$ nanowires, the experimental object of this thesis. $Mo_6S_{9-x}I_x$ nanowires are very similar to the well-known Chevrel compounds with the difference that there are no cross-links between individual columns. The synthesis method and some properties of these materials will be presented further on.

3.2 The synthesis and the structure of $Mo_6S_{9-x}I_x$ compounds

$Mo_6S_{9-x}I_x$ nanowires can be synthesized in a single step reaction direct from the pure elements. Accordingly, molybdenum, sulfur and iodine powders are weighed and sealed in a quartz ampoule with an inside pressure of 10^{-2} Pa (Figure 22). The quantities chosen for the elements depend on the desired stoichiometry and the quantity of the final product to be obtained (see Equation 4):

$$x : y : z = \frac{m_{Mo}}{M_{Mo}} : \frac{m_S}{M_S} : \frac{m_I}{M_I} \tag{4}$$

In the above equation x, y and z are the number of moles; m_{Mo}, m_S, m_I are the masses of the elements placed in the ampoule; and, M_{Mo}, M_S, and M_I are the molecular masses of each element.

Figure 22: *Powder of $Mo_6S_{9-x}I_x$ nanowires.* Nanowires colected directly from the ampoule after the synthesis is finished.

The field ampoules are then introduced into a furnace (Figure 22) and heated to the temperature of 1050^{o}C. The synthesis program is the following: in the first step the temperature in the furnace is set to grow for 1h till reaching 200ºC; in the second step, the temperature is set to grow 8ºC per hour till reaching the value of 1050ºC; the last step is the cooling process till the room temperature. The resulting material is a mixture of $Mo_6S_{9-x}I_x$ nanowires and impurities of MoS_2, Mo_2S_3 or $Mo_6S_6I_2$ crystals. In order to get rid of the impurities the raw material is submitted to a purification process. Thus, the material is dispersed in acetone with the help of an ultrasonic tip for 2 minutes followed by a mild dispersion in ultrasonic bath for 1 hour. The resulted solution is then let to sediment. After 1 hour of sedimentation the solution from the top is filtrated. The pure nanowires collected from the filter paper have a fur-like appearance and are stuck in bundles with diameters of 100 nm up to 1 μm and lengths reaching mm (Figure 23). Upon examination with a transmission electron microscope (TEM), these nanobundles are seen to be composed of very fine nanowires, approximately 1nm in diameter (see Figure 23 inset).

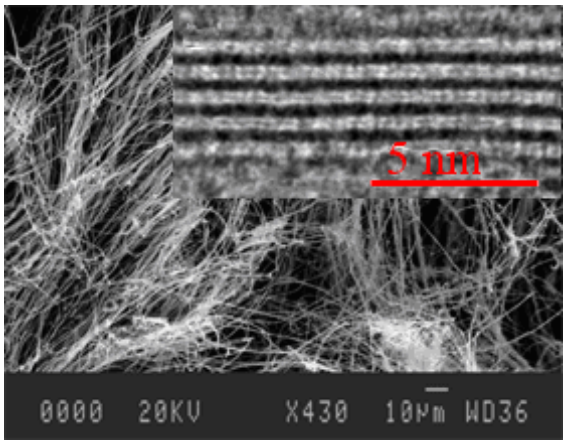

Figure 23: *SEM image of $Mo_6S_{9-x}I_x$ nanowires as grown.* The inset shows a high resolution TEM image of a bundle of nanowires.

For our measurements nanowires with the formula $Mo_6S_3I_6$ were used. The structure of these nanowires is fitted to the space groups of hexagonal-lattice $P6_3$ and trigonal-lattice R3 with the unit cell presented in Figure 24A. Furthermore, the XRD and EXAFS measurements (Meden et al., 2005; Kodre et al., 2006) shows that the individual nanowires are composed of Mo_6 octahedral clusters, separated by bridging anions (I or S) and dressed with six additional anions on the surface of each wire. The nearest-neighbor Mo-S and Mo-Mo distances were determined to be at 2.43 Å and 2.68 Å respectively. The distance at which I atoms were placed from Mo atoms in the starting models ranged from 3.15 to 2.78 Å: the last distance was confirmed in the EXAFS measurements (Meden et al., 2005; Kodre et al., 2006).

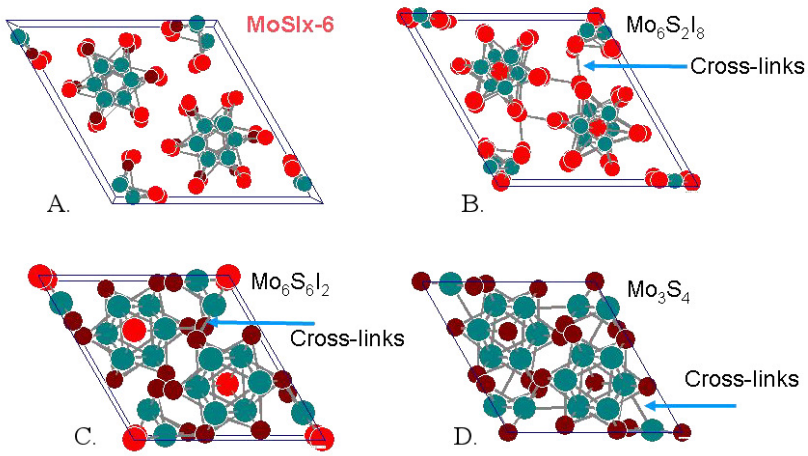

Figure 24: *Structure of $Mo_6S_{9-x}I_x$ nanowires (A) in the comparison with typical impurities (B, C, D) which shows Chevrel Phase properties.*

Meden et al. (2005) proposed that the structure of $Mo_6S_{9-x}I_x$ nanowires is similar to that of Chevrel phases with an octahedral of six Mo ions (Mo_6) forming the building blocks of the wire which is bridged by partially occupied S sites and with its terminal positions occupied by both S and I atoms. They found the structure to be independent of the synthesized stoichiometry. However, the unique feature of $Mo_6S_{9-x}I_x$ nanowires, as also seen in Figure 24, is the absence of cross-links among the wires, which makes them readily dispersible. This property and the fact that they are not superconductive make them slightly different than the Chevrel phase materials.

3.3 Physical properties

In analogy to carbon nanotubes, made by rolling up graphite sheets, we saw that layered transitional metal dichalcogenides can form nanotubes as well. The discovery of molybdenum-based nanowire materials with the general formula $Mo_6S_{9-x}I_x$ in past years has raised considerable interest. Although these materials have only recently been synthesized, some of their properties have already been experimentally and theoretically studied.

3.3.1 Dispersability of $Mo_6S_{9-x}I_x$ nanowires

A prime advantage of these nanowires over the well-known carbon nanotubes is that they can be easily dispersed in various solvents (Nicolosi et al., 2005). Nicolosi et al. (2005) studied the dispersability of $Mo_6S_{9-x}I_x$ nanowires in a range of common solvents. They monitored the optical transmission of the dispersion as a function of time. The transmission was transformed into turbidity using the Lambert-Beer law

$$I/I_0 = e^{-Tl} \tag{5}$$

where I/I_0 is the transmittance, T is the turbidity and l is the sample length. The turbidity can be thought of as the product of the sample concentration C and the effective extinction coefficient α, which represents all absorption and scattering processes. Thus, when dispersing the $Mo_6S_{9-x}I_x$ nanowires in different solvents using the above mentioned method, the turbidity was observed to go to a constant value which represented the turbidity associated with the stable dispersed material in each solvent (Figure 25). From the graph obtained it is clear that the best solvent is isopropanol (IPA), followed by dimethylformamide (DMF) and dimethylsulfoxide (DMSO).

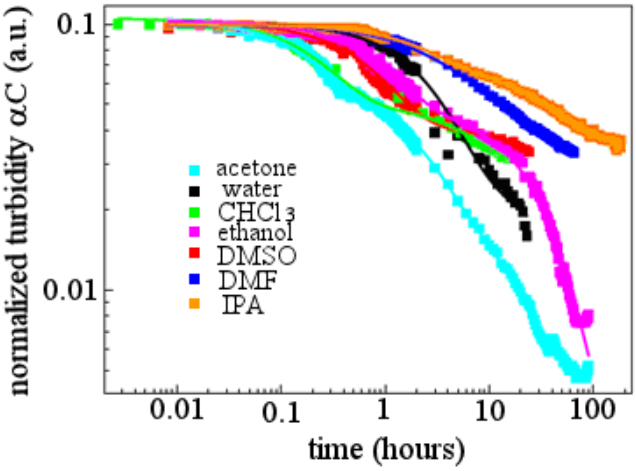

Figure 25: *Sedimentation curves of $Mo_6S_{9-x}I_x$ nanowires dispersed in different solvents (Nicolosi et al., 2005).*

Moreover, it was found that the $Mo_6S_{9-x}I_x$ material consists of three phases: two phases which are insoluble and one which is soluble. Microscopy measurements showed that the insoluble material consists of impurities and thick bundles of nanowires, whereas the soluble phase shows nanowires with diameters ranging 1 to 10 nm (Figure 26).

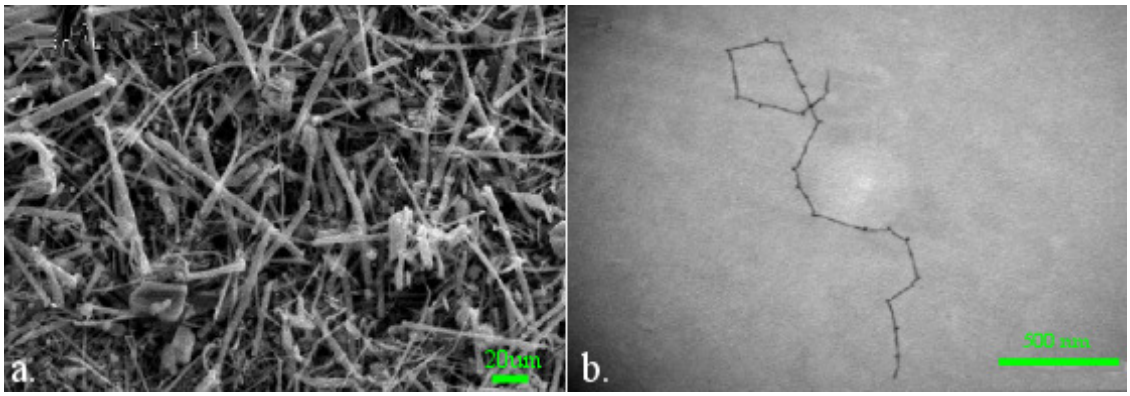

Figure 26: *Dispersed $Mo_6S_{9-x}I_x$ nanowires.* SEM picture of the insoluble phase of $Mo_6S_{9-x}I_x$ material after dispersion (a) and a TEM picture of individual nanowires present in the soluble phase (Nicolosi et al., 2005).

Quantitative measurements were performed also for different concentrations from 0.1 mg/ml down to 0.003 mg/ml. For each concentration the bundle size distribution was calculated by measuring the diameter of the nanowires with a transmission electron microscope (TEM). At high concentrations the diameter of the bundles did not vary much (Figure 27). However, when the concentration dropped down to 0.025 mg/ml, the average diameter fell to approximately 1 nm.

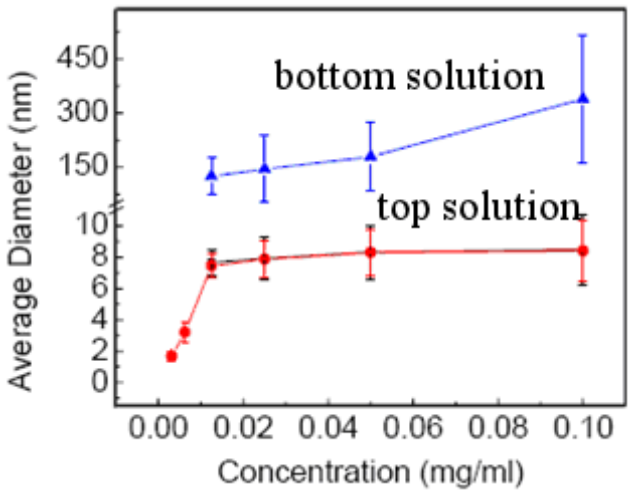

Figure 27: *Average diameters of $Mo_6S_{9-x}I_x$ bundles as a function of concentration.* The blue line represents the average diameter for the insoluble phase (bottom solution), the red line represent the average diameter for the soluble phase (top solution). The solvent used for dispersion is IPA (Nicolosi et al., 2005).

It is worth mentioning that the material that Nicosoli et al. worked with was $Mo_6S_{4.5}I_{4.5}$ nanowires. Using the same technique, McCarthy et al. (2007) dispersed $Mo_6S_3I_6$ nanowires. They found the same diameter decrease when lowering the concentration of the solution. However, the best solvents for these nanowires seem to be dimethylformamide (DMF) and acetone. Thus, it can be concluded that the dispersible solvents differ in changing the stoichiometry of the nanowires.

3.3.2 Tribological properties

Apart from easy dispersability compared with carbon nanotubes, the $Mo_6S_{9-x}I_x$ nanowires have a high Young's modulus (430 GPa for $Mo_6S_3I_6$ and 420 GPa for $Mo_6S_{4.5}I_{4.5}$ nanowires) and a low shear modulus (0.32 GPa for $Mo_6S_3I_6$ and 0.8 GPa for $Mo_6S_{4.5}I_{4.5}$ nanowires) (www.mo6.com). Moreover, the tribological performance of these nanowires in polyalphaolefin (PAO) has shown good friction reducing properties (Joly-Pottuz et al., 2005). A comparison with materials such as MoS_2 and molybdenum dithiocarbamate (MoDTC) is shown in Figure 28. The addition of only 1 wt% of material to PAO base oil results in a sharp decrease of the friction coefficient.

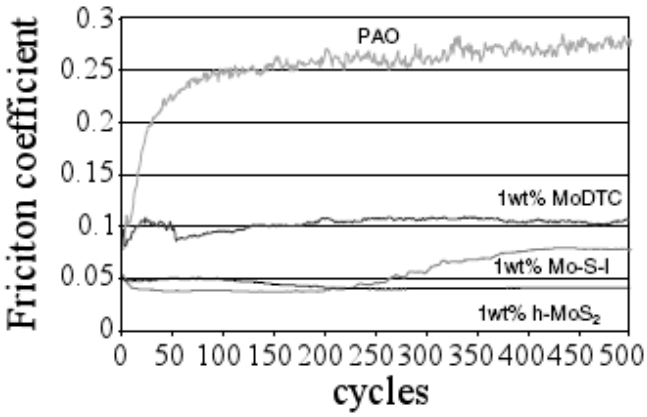

Figure 28: *Comparison of friction coefficient of $Mo_6S_{9-x}I_x$ nanowires with MoS_2 and MoDTC materials, all added 1 wt% in PAO (Joly-Pottuz et al., 2005).*

Moreover, the nanowires were more efficient at ambient temperature than the used anti-friction additives (MoDTC). This has raised special interest in automotive lubrication.

3.3.3 Basic electronic properties

Recently, electronic band structure calculations on $Mo_6S_{9-x}I_x$ nanowires were performed showing these

materials to be semi-metallic (Meden et al., 2005). The electronic band structure for $Mo_6S_{9-x}I_x$ calculated with the density functional theory (DFT) is shown in Figure 29. The common feature of all the studied stoichiometries is the large density of states, high anisotropy and small dispersion (large effective mass) of the electron bands in the plane normal to the nanowires c-axis. The base for these properties was found to be the low electronic coupling between adjacent nanowires. Moreover, the Fermi energy is close to the top of the valence band and crosses the hybridized bands belonging to Mo, S and I.

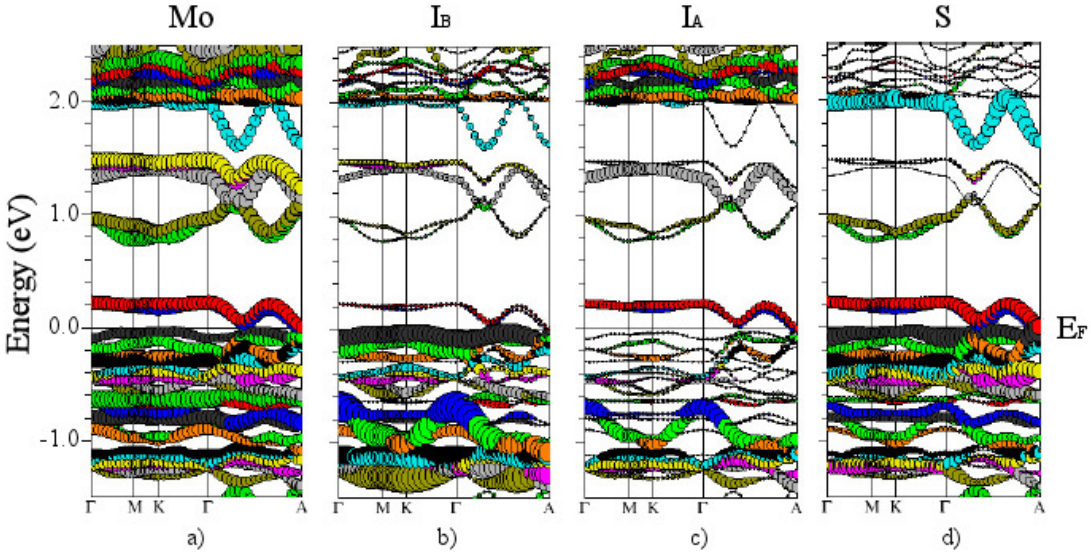

Figure 29: *Electronic band structure.* Electronic band structure of $Mo_6S_{9-x}I_x$ nanowires along the symmetry lines of the Brillouin zone: (a) Mo d band, (b) bridging I atoms, (c) I on Mo_6 octahedral cluster, and (d) S. (Meden et al., 2005).

The two lowest unoccupied molecular orbitals (LUMOs), as seen in Figure 29, are very close to E_F (0.2eV) and are predominantly of Mo(d) and S(p) character. Meden et al. 2005 found a band gap E_g at approximately 0.6 eV. Similar results were obtained also by Zimina et al. (2004) with a band gap at 0.4-0.2 eV.

The semi-metallic character of $Mo_6S_{9-x}I_x$ nanowires was confirmed also by recent experiments on the current-voltage (IV) characteristics. Bercic et al. (2006) measured the resistivity of $Mo_6S_{9-x}I_x$ nanowires networks under different conditions. The annealing was performed at 500, 700 and 900 ^oC. Figure 30a represents the current-voltage characteristics of as-grown and annealed material. The I-V characteristic appears to show linear behavior, whereas the conductivity σ_{300K} changes upon annealing. If at room temperature the nanowires network conductivity σ_{300K} is in the order of σ_{300K}= 0.04 S/m, the values increase as the annealing temperature increases reaching a value of σ_{900K}= 0.2 S/m at a temperature of 900^oC.

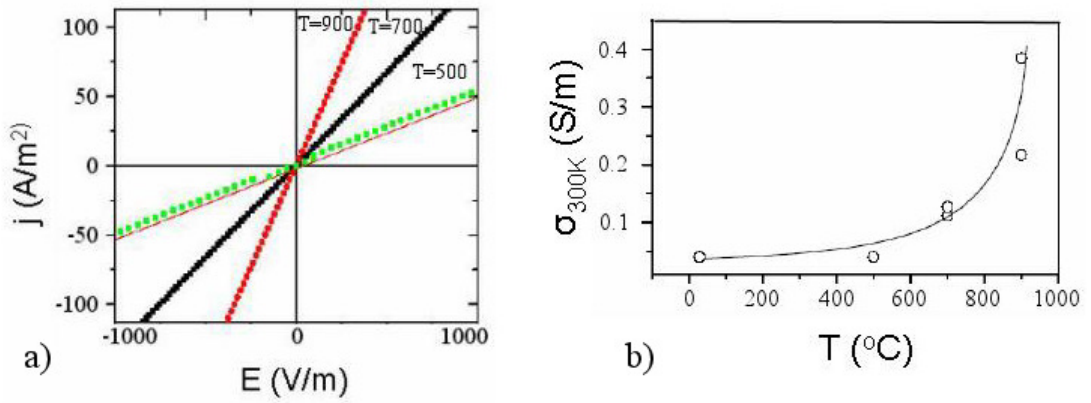

Figure 30: *Semi-metallic character of $Mo_6S_{9-x}I_x$ nanowires.* (a) Current-voltage characteristic of the as-grown $Mo_6S_{9-x}I_x$ network (line) and annealed at 500, 700 and 900 ^oC; (b) the room temperature conductivity σ_{300K} dependency on annealing temperature T (Bercic et al., 2006).

The temperature dependence of resistivity of as-grown material as well as of annealed appears to follow Mott's variable range hopping law (VRH):

$$\sigma = \sigma_0 \exp -(T_0 / T)^{\beta} \tag{6}$$

where σ_0 denotes room temperature conductivity, T_0 some characteristic temperature and β the dimensionality of the system (1/4 for three dimensions and ½ for one dimension). Plots for both samples are shown in Figure 31.

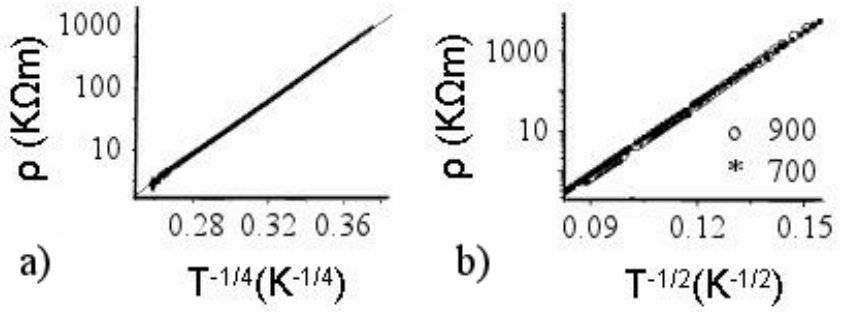

Figure 31: *Resistivity vs. Temperature.* Measurements of a nanowires network (a) and an annealed one at 900 and 700 °C (b) (data fit with an exponential law characteristic of variable range hopping VRH), (Bercic et al., 2006).

Interestingly, β=1/4 fits the data for the raw nanowires network, whereas β=1/2 seems to be better for the annealed samples. This changing of dimensionality can be explained with the effects of inter-bundle and inter-wire hopping. High temperatures change the structure, so that the overall conductance depends mainly on interbundle hopping, whereas in the as-grown case the electrons scatter considerably also between the wires inside of the bundle, thus raising the dimensionality. The observed VRH temperature dependence has been observed previously also in CNT networks. Uplaznik et al. (2006) went further and measured the conductivity of single MoSIx nanowire bundles (~ 7.2 nm) using different contacting methods. The I/V characteristic also showed linear behavior, with conductivity up to σ_{300K}= 10 S/m. Likewise, VRH fits the temperature dependence of resistance well. However, new results of in situ measurements of conductivity of individual nanowire bundles of lengths between 1μm and 50 μm and of diameters between 40 nm and 310nm, showed a conductivity in the range of 10 S/m as measured by Uplaznik et al. (2006). When increasing the bias-voltage from 10 V to 40 V, the conductivity rose to 10^5 S/m (Hummelgard et al., in press 2007).

4 (Di)electrophoresis for the manipulation of $Mo_6S_{9-x}I_x$ nanowires

(Di)electrophoresis was used for our experiments to manipulate $Mo_6S_{9-x}I_x$ nanowires. Using electrophoresis we found out that the nanowires are negatively charged. We were therefore able to separate the nanowires from the impurities present in the solution. Furthermore, dielectrophoresis was shown to be a good method for positioning MoSIx nanowires onto contacts. The resulting electrodes found application in field emission experiments, obtaining promising results.

4.1 Introduction to (di)electrophoresis

4.1.1 Electrophoresis overview

The electrophoresis method was first employed by Arne Tiselius in 1937. The experiments were based on the detection of electrophoretic motion by the moving-boundary method. As the particles migrate in an electric field, the movement of the boundary between the solution of particles and a sample of pure solvent can be observed. Tiselius was awarded the Nobel Prize in chemistry in 1948 for the moving-boundary method (Tiselius, 1948) and since then it has been successfully used to separate complex mixtures of charged macromolecules in solution and to study their physical characteristics.

The term “electrophoresis” originally referred to the migration of large molecular weight charged particles in an electrical field while the term “inophoresis” had been used for the migration of lower molecular weight substances in stabilized media such as gels and powders. Nowadays the general term electrophoresis covers all applications regardless of the studied material or the used medium.

In the early studies electrophoresis measurements were carried out in liquid phase, but as time passed the development of this method progressed from “paper electrophoresis,” cellulose acetate membranes and gel electrophoresis to molecular disc, SDS (sodium dodecyl sulfate), immunoelectrophoresis and finally to isoelectric focusing and high resolution two dimensional electrophoresis. If we summarize, we can distinguish between four basic electrophoretic methods:

- “free” solution electrophoresis or moving boundary electrophoresis (MBE) (Tiselius, 1948; Hannig, 1982);
- zone electrophoresis (ZE) (Mikkers et al., 1979; Jorgenson and Lukacs, 1981; Smithies, 1955; Kohn, 1957);
- isotachophoresis (ITP) (Everaerts et al., 1976; Baumann and Chrambach, 1976);
- isoelectric focusing (IEF) (Awdeh et al., 1968; Stiles and Davies, 1976; Arnaud et al., 2005).

Free solution electrophoresis or moving boundary electrophoresis (MBE)

MBE was the earliest form of electrophoresis. In this method, a boundary is formed at one end of the separation compartment, between the sample to be studied and the solution. By applying the electrical field the boundaries for samples of different electrophoretic mobilities migrate at different rates. Although the substance cannot actually be separated by this method, the position of a boundary after a given time provides the electrophoretic mobility of that sample.

Zone electrophoresis (ZE)

This is one of the most common forms of electrophoresis. In this method a homogeneous buffer of constant

pH is used. The buffer acts as an additional selection mechanism since small molecules will migrate through the pore structure faster than larger ones.

Isotachophoresis (ITP)

The term literally means "same speed transport." Here the ionized samples migrate with identical velocities between the leading electrolyte and the terminating electrolyte. The selectivity is based on their electrophoretic mobilities, e.g. the sample with the highest mobility goes directly towards the leading electrode while the one with lower mobility migrates to the second electrode.

Isoelectric focusing (IEF)

IEF, also known as electrofocusing, takes place in a pH gradient and takes advantage of the fact that the molecule's charge changes with the pH of the surrounding substance. Under an applied current, molecules move towards the anode or the cathode until an isoelectric point is reached (i.e. the pH at which the molecule's charge is zero). An important feature is that the sample must be amphoteric, meaning it must have both acidic and basic functional groups. At this point the migration stops, but diffusion will occur and the sample will enter a region of pH above its isoelectric point (pI). The applied electric field will cause the molecules to migrate back to its pI. Therefore the sample becomes focused to a stationary band. The resolution of this technique is high enough to fraction proteins with only one charge difference into separate bands.

The advantages of the solid support electrophoresis over electrophoresis in "free" solution are in:

- ✓ the possibility of obtaining complete separation regarding mobility, not only limited boundary separation;
- ✓ the ability to study substances with low molecular weight like amino acids, peptides, and nucleotides; and,
- ✓ the reduction of testing sample quantities for the experiments.

Most common types of electrophoretic gels

There are many types of materials used to make gels. A gel is chosen depending on the type of the sample for characterization. In general, the gel matrix should satisfy some demands:

- ✓ adjustable and regular pore size;
- ✓ chemically inert;
- ✓ no electro-osmosis property (i.e. no movement through a membrane or other porous structures upon the applied field).

Two of the most common gels for electrophoresis will be presented. *Agarose* is a natural colloid extracted from sea weed. This gel has very large sized "pores" and is used primarily to separate very large molecules (over 10 nm in diameter) (Meyers et al., 1976). The pore size depends on the concentration of agarose aqueous solution w/v (weight of agarose/volume of water), e.g. pore sizes of 150 nm for 1% or 500 nm for 0.16% (Serwer, 1980). Agarose is a linear polysaccharide (with an average molecular mass of about 120,000 dalton) (Figure 32).

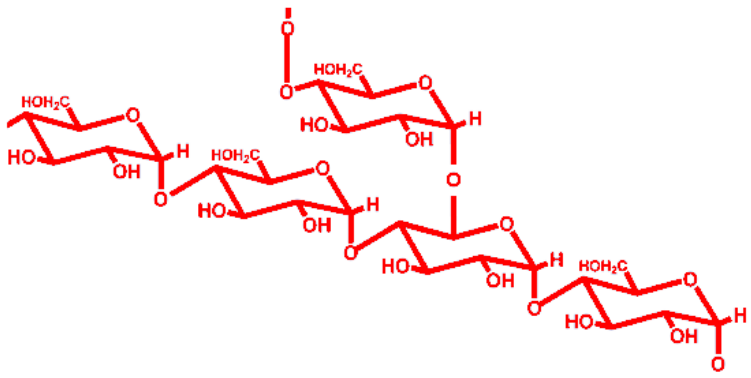

Figure 32: *The chemical structure of agarose.*

The agarose gels are formed by suspending dry agarose in aqueous buffer, then boiling the mixture until a clear solution forms. The liquid is then allowed to cool to room temperature forming a rigid gel.

On the other hand *polyacrylamide* gel, used in polyacrylamide gel electrophoresis (PAGE), which was first described by Raymond and Weintraub in 1959, is a material that is used for skin electrodes and soft contact lenses. It is obtained by chemical co-polymerization of acrylamide monomers with a cross linking reagent usually N,N'-methylenebisacrylamide (Figure 33).

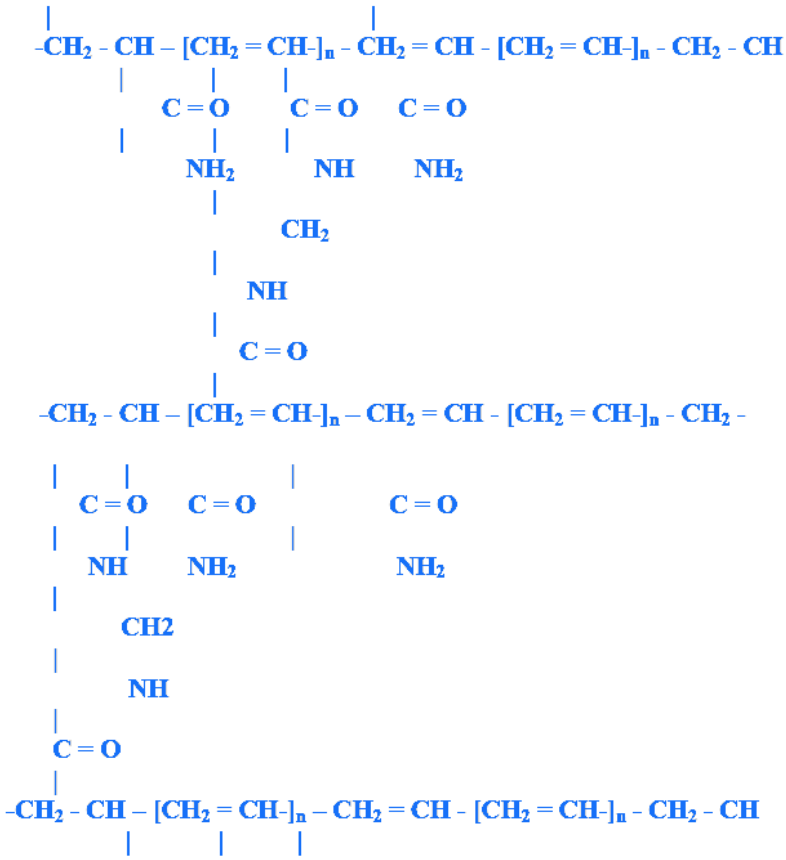

Figure 33: *The chemical structure of PAGE gel.*

The PAGE gel may differ in preparation to provide for different electrophoretic conditions, i.e. homogenous concentration or with varying gradient. The polymerization of PAGE gel should take place in oxygen atmosphere since the oxygen acts as a free radical trap. Gradient gels provide continuous decrease in pore size from the top to the bottom of the gel. PAGE offers greater flexibility and more sharply defined banding than agarose gels.

Theoretical considerations

As mentioned earlier, electrophoresis is the movement of electrically charged particles under the influence of an electric field (Chrambach, 1985; Mosher et al., 1992). The movement is governed by the Lorentz force, which takes in consideration the electrical properties of studied particles (q) and the ambient electrical conditions ($\boldsymbol{E}$) (Equation 7):

$$\vec{F}_e = q * \vec{E} \tag{7}$$

On the other hand, the translational movement of the charged particles is slowed by the frictional forces. These forces depend on the hydrodynamic size of the molecules, their shape, the pore size of the medium in which the electrophoresis takes place, and the viscosity of the buffer. The frictional force is given by the expression:

$$\vec{F}_f = \vec{v} f \tag{8}$$

where v is the velocity of the molecules and f is the frictional coefficient.

In stationary state conditions, the electric force on each molecule will be balanced by the friction force encountered upon moving. Thus the velocity v of molecules moved by electrophoresis is given by the following equation:

$$q * \vec{E} = \vec{v} f \tag{9}$$

$$\frac{q}{f} = \frac{\vec{v}}{\vec{E}} = \mu \tag{10}$$

where, μ is the electrophoretic mobility ($m^2V^{-1}s^{-1}$). Taking into consideration Stoke's law, the electrophoretic mobility can also be expressed as:

$$\mu = \frac{q}{f} = \frac{q}{6\pi\eta r} \tag{11}$$

where η is the viscosity of the medium and r the radius of the particles.

However, for the development of a more detailed theory of electrophoretic phenomena, it is important to take into consideration the physical nature of charged particles in a liquid medium as well. It is well known that colloidal particles dispersed in a solution are electrically charged due to their ionic characteristics and dipolar attributes, and that each particle is surrounded by an electrical double layer. This layer consists of two parts. The inner region, called the *Stern or Helmoltz layer* (Figure 34), is where each particle is surrounded by oppositely charged ions (counter-ions). The ions inside this layer are strongly bound. Surrounding the Stern layer is a cloud-like area composed of a variety of ions of opposite polarities called the *diffuse Gouy-Chapman layer*. In this area the ions are less firmly attached and a boundary exists within which the ions and particles form a stable entity.

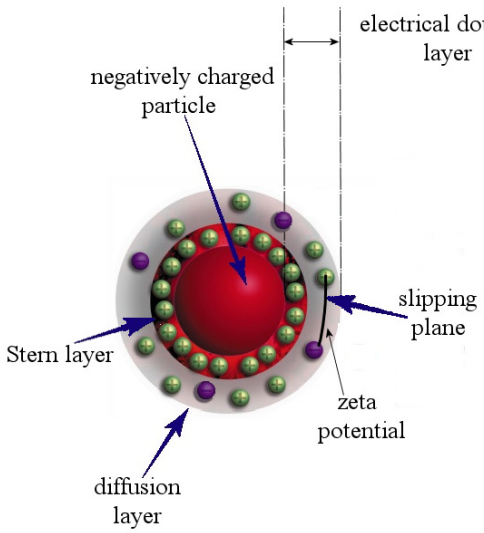

Figure 34: *Representation of electrical double layer that surrounds particles moving in a solution.*

Under applied electric field, the particles move accompanied by the Stern layer and part of the diffuse layer, i.e. the ions in the internal side of the diffuse layer travel with the particle while the ions beyond the boundary do not. This boundary is called the surface of hydrodynamic shear or *slipping plane*. The difference in electrical charge between the Stern layer and the diffuse layer is the *zeta potential* ζ.

The magnitude of the zeta potential gives information about the potential stability of the colloidal system. If all the particles have a large negative or positive zeta potential, they will repel each other resulting in a stable dispersion. If the particles have low zeta potential values (-30mV< ζ < 30mV), then there is no force to prevent the particles to aggregate and the dispersion becomes unstable.

Moreover, the zeta potential is related to the electrophoretic mobility by the Henry equation:

$$\mu = \frac{2\varsigma\varepsilon f(\kappa r)}{3\eta} \tag{12}$$

where, $\varepsilon=\varepsilon_0\varepsilon_r$ is the dielectric constant of the fluid, composed of the vacuum and relative dielectric constants ε_0 and ε_r, η is the viscosity, $f(\kappa r)$ is Henry's function (Michov, 1988), and κ is the Debye-Huckel parameter (Debye and Huckel, 1923) given by the following expression:

$$\kappa = \left(\frac{z^2 e^2 n_0}{\varepsilon k T} \right)^{1/2} \tag{13}$$

where z is the valence of counter-ions, e is the elementary electric charge, n_0 is the average number density of the ions in the solution, k is the Boltzman constant and T is the absolute temperature.

The inverse of the Debye-Huckel parameter, κ^{-1}, gives the thickness of the double layer. Typical values of κ^{-1} range from 1 nm to 1 μm indicating that the double layer phenomenon is confined to a very narrow region adjacent to the surface. Thus, taking into consideration the product κr or the function $f(\kappa r)$, the electrophoretic mobility can be expressed as:

- $\kappa r < 1$ or $f(\kappa r)=1$, (Huckel – Onsager approximation (Huckel, 1924))

$$\mu = \frac{2\varsigma\varepsilon}{3\eta} \tag{14}$$

- $\kappa r > 100$ or $f(\kappa r)=1.5$, (Smoluchowski approximation (Smoluchowski, 1917))

$$\mu = \frac{\varsigma\varepsilon}{\eta} \tag{15}$$

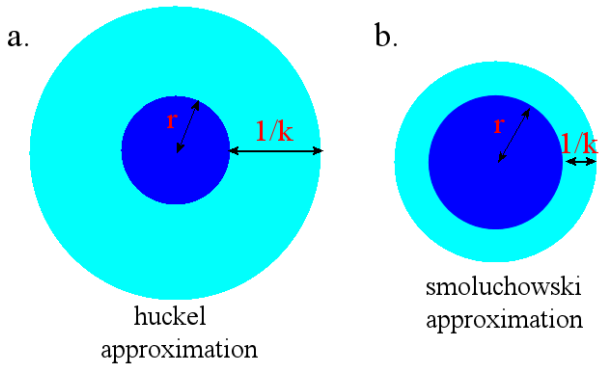

Figure 35: *An illustration of two extreme cases of particles smaller (a) and bigger (b) than the thickness of the double layer.*

The Smoluchowski theory is applicable to very large particles compared with the double layer thickness $1/\kappa$ and for high ionic strength (Figure 35). On the other hand, the Huckel-Onsager equation is expected to be valid for low potentials, low electrolyte concentrations and small enough particles to be considered a point charge (particles are small compared to the thickness of the double layer $1/\kappa$). For intermediate values of κr the values of $f(\kappa r)$ depend on the applied theory (O'Brien and White, 1978; Wiersema et al., 1978; Cassou and Tovar, 2001).

The large number of theoretical approaches and computer models in the literature provides insight into many aspects of electrophoresis. The dynamic computer models, which consider mass transport due to both electromigration and diffusion, are the most advanced as are most general mathematical descriptions of electrophoresis processes.

Applications of electrophoresis

Electrophoresis methods are used for the quantitative characterization of substances or mixture of substances, for purity control, quantitative determinations and preparative purposes. It is an important technique in molecular biology, genetics, microbiology, biochemistry and even in forensics. The application domains range from cells (Bauer, 1987 and 1994; Smolka et al., 2005) and particles (Eychmuller et al., 1990; Petersen and Ballou, 1999) to nanotubes (Wang et al., 2003; Doorn et al., 2002; Umek, 2001) and nucleic acids (Bishop et al., 1967; Fangman, 1978), proteins (Michalski and Shiell, 1999), peptides (Michalski and Shiell, 1999; Cleveland et al., 1977; Collet and Baguna, 1993), amino acids (Mourzina et al., 2005; Warren and Adams, 2000; Poinsot et al., 2006), organic acids (Chiari et al., 1996), drugs (Nishi, 1999; Martinez-Gomez et al., 2006; Liu et al., 1998) – everything that can carry charge.

After the electrophoresis is completed, the gel must be analyzed quantitatively and qualitatively to answer analytical or experimental questions. Since most of the (bio)molecules are not directly visible, the gel must be processed to determine the location and amount of the separated molecules. The method used is the staining of the gel with organic dye, silver stains, fluorescent dye or radioactive labels depending on the analyzed sample.

For example, scientists have performed numerous experiments on DNA molecules. In electrophoretic measurements DNA molecules were observed moving towards the positive electrode due to the net negative charge of the phosphate backbone. After the complete separation the fractions of DNA molecules of different lengths are often visualized using fluorescent dye specific for DNA, such as ethidium bromide. The gel shows bands corresponding to different DNA molecule populations with different molecular weights. The DNA length determination is typically done by a comparison to commercially available DNA ladders containing DNA fragments of known length (Bush and Holmes, 1982; Maniatis et al., 1975; Raymer and Smith, 2007).

In contrast, proteins are usually stained with organic dyes (Raymer and Smith, 2007; Diezel et al., 1972; Bennett and Scott, 1971). Proteins are amphoteric compounds, i.e. their net charge is determined by the pH of the medium in which they are suspended. Most of the organic dyes are believed to be electrostatically attracted to the charged groups on the proteins, forming strong complexes. Proteins can also be detected by fluorescent labeling (Greenspan and Gutman, 1993; Kumar et al., 1995; Shcherbakov and Piendl, 2007) either before or after electrophoresis and then visualized under UV light. This technique involves the covalent binding of a fluorescent dye to terminal amino groups of the proteins. Another possibility for the

(bio)molecule detection separated by electrophoresis is radioactive labeling (Symington et al., 1981). ^{3}H, ^{14}C, ^{32}P, ^{35}S and ^{125}I are the most commonly used isotopes for radioactive labeling.

Staining of the molecules has shown to be very important for the visualization of the molecules. Having standard ladders of known length molecules, the length of unknown molecules can be roughly estimated. For a more accurate estimation theoretical models (Ogston, 1958; Deutsh and Madden, 1989; Slater and Guo, 2001) in parallel with experimental data have been employed (Sol et al., 1975; Maniatis et al., 1975; Johnson and Grossman, 1977). As a result, determination of mobility, length and charge of the molecules as a function of gel concentration or electric field strength has been thoroughly investigated throughout the years.

4.1.2 Dielectrophoresis overview

Work in the field of AC electrokinetics has shown that submicrometer particles can be characterized and manipulated in microelectrode arrays using dielectrophoresis. Thus, the dielectrophoretical manipulation of particles has rapidly become a major area of research, with particular applications in biotechnology and nanotechnology. This method has been applied to characterize and separate latex spheres (Green and Morgan, 1997), viruses (Morgan and Green, 1997; Green et al., 1997; Muller et al., 1996), DNA (Asbury and van den Engh, 1998; Ying et al., 2004) and proteins (Morgan et al., 1999), as well as carbon nanotubes (Krupke et al., 2003 and 2006).

Short description of the phenomenon

Dielectrophoresis (DEP) is the motion of polarizable particles in non-uniform alternating electric fields and arises from the interaction of the field and the induced dipole. The basic theory and early applications of this phenomenon were largely developed by Pohl (Pohl, 1915 and 1978). The essential feature that distinguishes dielectrophoretic effect from electrophoretic is that in the first case ac electric fields are involved, in the latter dc electric fields.

In a uniform electric field the charged particles are moving along the field lines towards the electrode of opposite particle charge (Figure 36a). If the charge is neutral, it will be barely polarized and no movement toward either electrode will be detected.

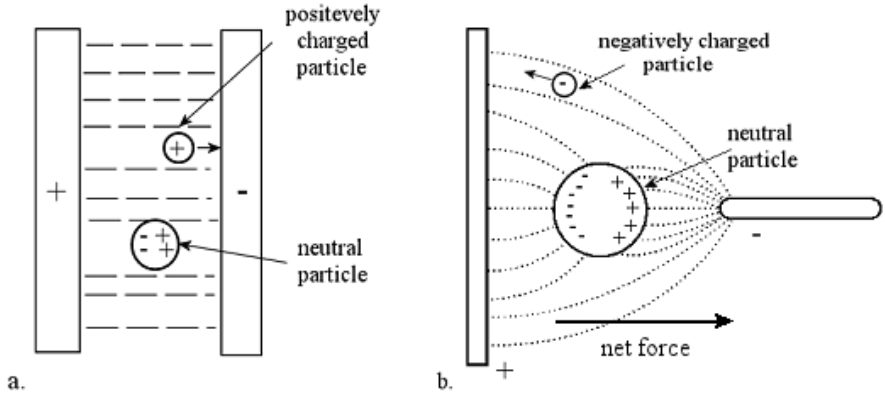

Figure 36: *Behavior in (a) uniform and (b) non-uniform electric fields of charged and neutral particles.*

In a non-uniform field, the situation is different. For the charged particles the behavior is the same as in the case of uniform field, i.e. being pulled along the field lines towards the electrode of opposite polarity. For the neutral particles, the applied field induces a dipole in the particle. The interaction of the induced dipole with the electric field generates a force. Due to the presence of a field gradient, these forces are not equal and there is a net translational movement (Figure 36). If the particle is more conductive than the medium around it, the dipole aligns with the field and the force upon the particle acts towards the region of highest electric field. If the particle is less polarizable than the medium, the dipole aligns against the field and the particles are repelled from regions of high electrical field.

However, it should be mentioned that the sign of the electrodes does not matter since the net force upon the neutral particles is the same. Thus, a polarizable particle is attracted towards the point were the field is

higher regardless of the sign of the electrode (see Figure 37). For that matter, the applied field can be non-alternating as well as alternating.

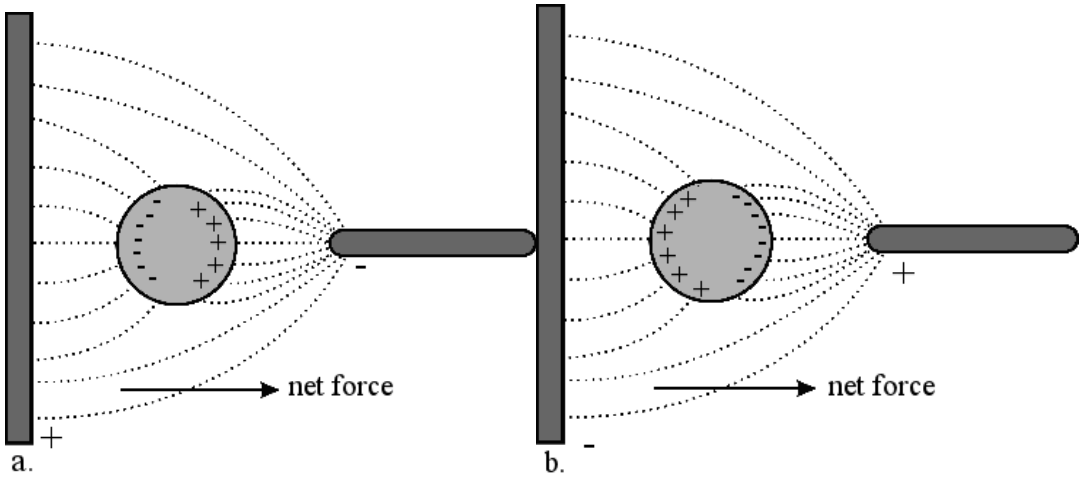

Figure 37: *Behavior of neutral particles in an alternating non-uniform field.* (a) The neutral particle is more conductive than the medium and is attracted towards the electrode where the field is stronger; and (b) the neutral particle is again more conductive than the medium and is moving towards the highest field intensity although the field is reversed.

Theoretical considerations

The instantaneous dielectrophoretic force $\vec{F}(\omega)$ on a particle (Pohl, 1915 and 1978) is given by

$$\vec{F}(\omega) = (\vec{p}(\omega) \cdot \nabla)\vec{E}(\omega) \tag{16}$$

where $\vec{p}(\omega)$ is the induced dipole moment, ∇ is the del vector operator and $\vec{E}(\omega)$ is the electric field. Taking into consideration that the dipole moment can be written also as:

$$\vec{p}(\omega) = \alpha(\omega) v \vec{E}(\omega) \tag{17}$$

where $\alpha(\omega)$ is the polarizability or the dipole moment per unit volume, v is the volume of the particle, the dielectrophoretic force can be rewritten as:

$$\vec{F}(\omega) = v\alpha(\omega)(\vec{E}(\omega) \cdot \nabla)\vec{E}(\omega) \tag{18}$$

$$\vec{F}(\omega) = \frac{1}{2} v\alpha(\omega)\nabla\left|\vec{E}(\omega)\right|^2 \tag{19}$$

If the polarizability is expressed as follows,

$$\alpha = \varepsilon_m \left\{ f(\varepsilon_p^*, \varepsilon_m^*) \right\} \tag{20}$$

where ε_p^* and ε_m^* are the complex permittivities of the particle and medium (the complex permittivity is given by $\varepsilon^* = \varepsilon - j\left(\frac{\sigma}{\omega}\right)$, where ε is the real permittivity, σ the conductivity, $j = \sqrt{-1}$ and ω the angular frequency), the dielectrophoretic force equation is transformed to:

$$\vec{F}(\omega) = \frac{1}{2} v \varepsilon_m \,\mathrm{Re}\left\{ f(\varepsilon_p^*, \varepsilon_m^*) \nabla \vec{E}(\omega)^2 \right\} \tag{21}$$

where Re{} is the real part of the expression in brackets. The force can be described by different expressions depending on the shape of the particles:

- for a *spherical particle,* where the factor $f(\varepsilon_p^*, \varepsilon_m^*)$ is given by the well-known equation of Clausius-Mossotti (Clausius, 1879; Mossoti, 1850; von Hippel):

$$f(\varepsilon_p^*, \varepsilon_m^*) = \left(\frac{\varepsilon_p^* - \varepsilon_m^*}{\varepsilon_p^* + 2\varepsilon_m^*} \right) \tag{22}$$

and the volume of the sphere is $v = \frac{4}{3}\pi r^3$, with *r* being the radius of the particle, the induced dielectrophoretic force is:

$$\vec{F}(\omega) = \frac{1}{2} \pi r^3 \varepsilon_m \,\mathrm{Re}\left\{ \left(\frac{\varepsilon_p^* - \varepsilon_m^*}{\varepsilon_p^* + 2\varepsilon_m^*} \right) \nabla \vec{E}(\omega)^2 \right\} \tag{23}$$

- for an *ellipsoidal particle* (Stratton, 1941; Kakutani et al., 1993), where the factor $f(\varepsilon_p^*, \varepsilon_m^*)$ is given by the equation

$$f(\varepsilon_p^*, \varepsilon_m^*) = \frac{\varepsilon_p^* - \varepsilon_m^*}{(\varepsilon_p^* - \varepsilon_m^*) A_\beta + \varepsilon_m^*} \qquad \beta = x, y, z \tag{24}$$

and the volume $v = \frac{1}{3} 4\pi abc$, with a, b the equatorial radii (along the x and y axes) and c the polar radius (along the z axis), the equation of the force is:

$$\vec{F}(\omega) = \frac{2}{3} \pi abc \varepsilon_m \,\mathrm{Re}\left\{ \frac{\varepsilon_p^* - \varepsilon_m^*}{(\varepsilon_p^* - \varepsilon_m^*) A_\beta + \varepsilon_m^*} \nabla \vec{E}(\omega)^2 \right\} \tag{25}$$

- for an *elongated particle* (like nanowires) (Morgan and Green, 1997), where the factor $f(\varepsilon_p^*, \varepsilon_m^*)$ has the expression

$$f(\omega) = \frac{\varepsilon_p^* - \varepsilon_m^*}{\varepsilon_m^*} \tag{26}$$

and the volume $v = \pi r^2 l$, where *r* is the radius and *l* the length of the cylinder, the dielectrophoretic force is given by:

$$\vec{F}(\omega) = \frac{\pi}{6} r^2 l \varepsilon_m \,\mathrm{Re}\left\{ \frac{\varepsilon_p^* - \varepsilon_m^*}{\varepsilon_m^*} \nabla \vec{E}(\omega) \right\} \tag{27}$$

The direction of the dielectrophoretic (DEP) force, positive or negative, depends on the sign of the Re{ $f(\varepsilon_p^*, \varepsilon_m^*)$ }. Positive DEP occurs when Re{ $f(\varepsilon_p^*, \varepsilon_m^*)$ }>0 and the force is pointing towards the high

field strength. The negative DEP is the reverse of the positive one, i.e. the force is in the direction of decreasing field strength. The frequency dependence of $f(\varepsilon_p^*, \varepsilon_m^*)$ makes DEP a powerful technique of manipulating particles in solution. Since dielectrophoresis is a non-invasive, non-destructive technique, it has potential uses in a wide range of biotechnological and nanotechnological applications.

Applications of dielectrophoresis

A controlled handling of single (bio)molecules is essential for the fabrication and the investigation of devices based on (bio)molecules. An important step in the development of the lab-on-a-chip is the ability to move around liquid samples to different parts of the chip or to separate parts of the sample such as particles, biological cells, or DNA. Dielectrophoresis is a well-defined positioning tool that is ideal for biotechnological and nanotechnological applications (Markx et al., 1994; Muys et al., 2005).

Applications of dielectrophoretic experiments are countless. Further in this chapter we will mention only the most interesting ones and those corresponding to our research interest.

Ever since the discovery of carbon nanotubes (CNTs) their separation has been a challenge. CNTs typically are grown in bundles having both metallic and semiconducting properties. Unfortunately, the separation of the two types has been impossible until Krupke et al. (2003) adopted the dielectrophoretic method. Using microelectrodes prepared by the standard electron-beam lithography Krupke found that semiconducting single-walled carbon nanotubes (SWCNTs) can be separated using negative dielectrophoresis, whereas for metallic nanotubes positive dielectrophoresis should be used. Moreover, the selectivity of the process depends on the field strength and frequency, on the surfactant concentration or solution conductivity, and on the purity of the SWNTs (if they are individual or aggregated in bundles) (Krupke, 2004).

Dielectrophoresis was demonstrated to be a very good technique also for the integration of molecular structures into microscopic electrode arrays. Assembly of gold nanoparticles from suspension connected by molecular bridges (Kretschemer and Fritzsche, 2004; Bhatt and Velev, 2004), immobilization of gold nanoparticles along carbon nanotubes (Zheng et al., 2004), DNA trapping between CNT electrodes (Tuukkanen, 2006), trapping of cells (Wang et al., 1997), single proteins (Holzel et al., 2005) and bioparticles (Hughes and Morgan, 1998), spatial manipulation of single DNA molecules for genetic investigations as well as for the building blocks (Hozel and Bier, 2003; Oana et al., 1999) have been successfully performed using AC fields.

The use of nanocrystals and nanowires in nanodevices as field-effect transistors, photodetectors, x-ray source, high-resolution electron beam instruments and light-emitting diodes raised the interest of researchers. For all these nanodevices the key component might be planar field emission electron source or point emitters. Dielectrophoresis once again proved to be a very elegant technique for the assembly of these components. Successful reports on SWCNTs and double-walled carbon nanotubes (DWCNTs) point emitters (Jung et al., 2006; Zhang et al., 2004), microfabricated electrodes of CdSe nanowires (Zhou et al., 2007), diamond-based films as future cold-cathode materials (Chen et al., 2003), diamond coated silicon and molybdenum emitters (Zhirnov et al., 1996) etc. have been registered.

4.2 Electrophoretical separation of $Mo_6S_{9-x}I_x$ nanowires

$Mo_6S_{9-x}I_x$ nanowires are synthesized in weakly bound bundles of up to 100 nm in diameter and 1 μm in length (see Figure 10a). The big advantage of $Mo_6S_{9-x}I_x$ nanowires over CNTs is that they are easily dispersed in organic solvents like isopropanol, dimethyl-formamide or chloroform (Nicolosi et al., 2005). Since the raw material is not very pure, but contains also crystals of Mo_2S_3, $Mo_6S_6I_2$ and MoS_2, we used (di)electrophoresis for the separation of $Mo_6S_{9-x}I_x$ nanowires from these impurities and also for the separation regarding their diameter.

Experimental approach

The first experiments were carried out in an electrophoretic cell (BIO-rad, power-pac 300 model) and then, in order to use lower quantities of material, a smaller electrophoretic cell was used (B1A model). A gel solution was prepared by weighting out the desired amount of agarose and mix it with a measured amount of electrophoresis buffer, e.g. for an 0.8% gel concentration, 0.8 g of agarose was add to 100ml of TBE (1X) buffer. After that boiling the solution till all the grains of agarose will be dissolved, the gel solution

was poured into a mold and allowed to solidify at room temperature for several hours before use. The pockets were formed by introducing a "comb" mold into the liquid gel and removing it after the cooling. The gel was then put in the electrophoretic cell and covered with the standard TBE buffer.

For the solution we dispersed the nanowires in two different organic solvents: IPA and DMF. The choice of the solvent was made based on the best solubility, in our case IPA. For the third solution, the nanowires were dispersed in water containing SDS surfactant.

The dispersion of $Mo_6S_{9-x}I_x$ nanowires (5 mg) in IPA, DMF and water-SDS solution (10 ml) was made using a 750 W sonication tip for 5 minutes and subsequently a low power ultrasound bath for 1h. The obtained solutions were further mixed with 0.5 ml glycerol and 0.5 ml of deionized water. Glycerol is commonly used in electrophoretic experiments for raising the density of the solution compared to water. The solution is then poured with a transfer pipette into the preformed gel pockets (Figure 38) and carefully submerged in water. The higher density of the solution confines the sample inside of the pockets, preventing random diffusion.

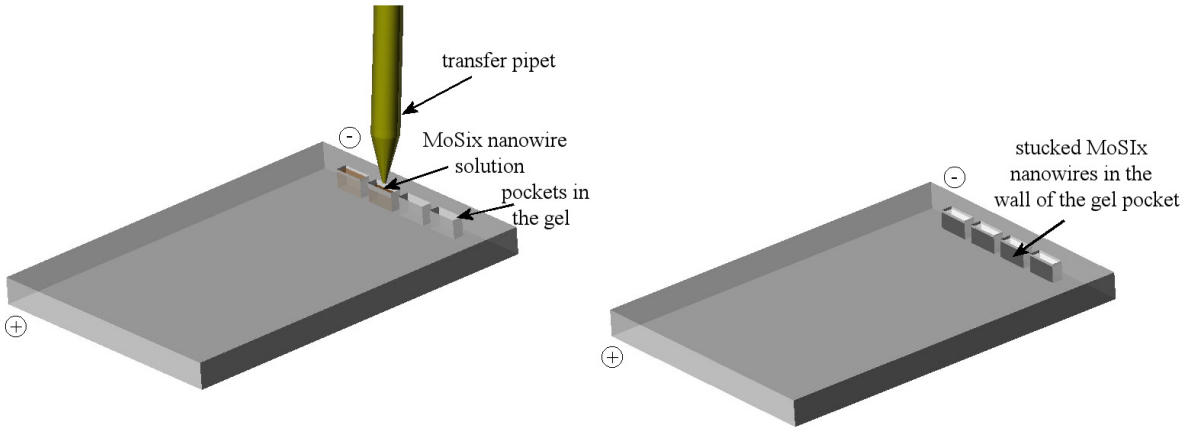

Figure 38: *Schematic of the electrophoretic experiments.* (a) Pockets were formed with the "comb" mold after the cooling of the gel: (b) injection of the sample into the pockets; and (c) the electrophoretic experiment running under a 300V bias for 25 minutes.

When the pockets in the agarose gel were filled with the solutions, an electric field of 300V was applied for 25 minutes in the case when the BioRad electrophoretic cell was used. In the case of the smaller cell, the applied field was of 80V in a time of 90 minutes.

Experimental results

As mentioned above, electrophoresis experiments were performed for separating $Mo_6S_{9-x}I_x$ nanowires from impurities and possibly according to their diameter. We expected to obtain a diffusion of the $Mo_6S_{9-x}I_x$ nanowires into separate fractions as Umek et al. (2001) obtained in their experiments on CNTs (see Figure 39).

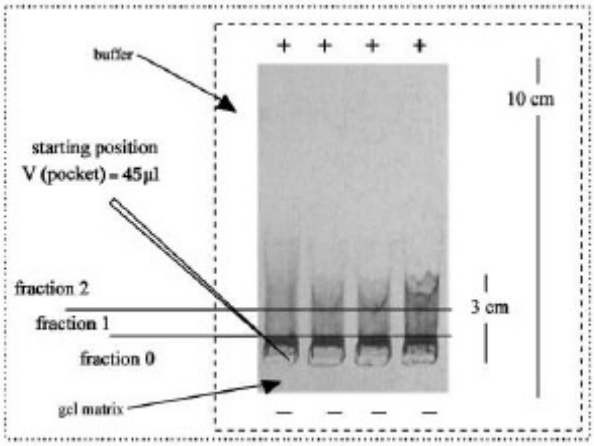

Figure 39: *Electrophoretic experiment results on CNTs obtained by Umek et al. (2001).*

Unfortunately, unlike in the CNTs, no diffusion of the $Mo_6S_{9-x}I_x$ nanowires could be seen. However, by the end of the experiment we observed a pronounced deposition on the pocket wall corresponding to the positive electrode as well as some sedimentation on the bottom of the pocket. For a better understanding of what happened during the electrophoretic experiment microscopy measurements were performed. SEM images were taken of the raw material, of the nanowires dispersed in DMF before electrophoretic experiment, and of the material removed from the pocket wall after the completed separation (Figure 40).

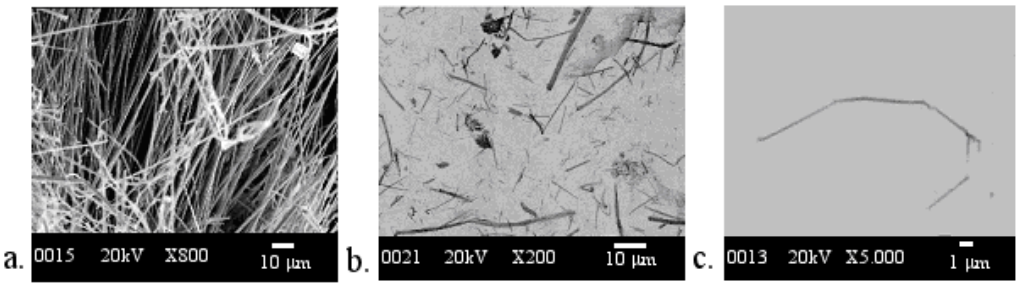

Figure 40: *SEM images of the experiment.* SEM image of $Mo_6S_3I_6$ nanowires as grown (a); of the nanowires dispersed in DMF solution where bundles of $Mo_6S_3I_6$ as well as impurities can be seen (b); of collected nanowires after electrophoresis experiments (c).

We can conclude that the impurities and the large bundles that could not be dispersed were deposited on the bottom of the pockets while the small bundles were deposited on the "positive wall," suggesting a negative charge of the nanowires. To confirm the latter assumption we performed another experiment but with a different pocket geometry. If in the first case the voltage was applied across the pocket, i.e. the shorter wall, now the movement of the material was induced laterally, i.e. on the long side (Figure 41).

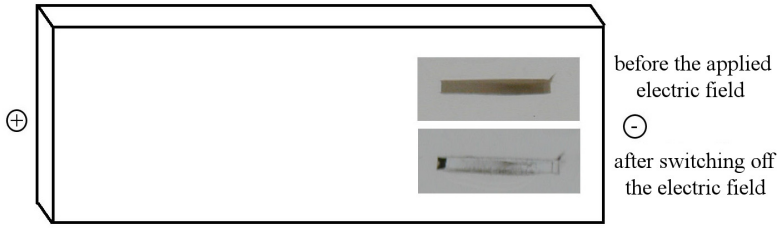

Figure 41: *Electrophoresis experiment.* Image of the solution in the pocket at the beginning of the experiment (top). In the bottom image, a fraction of the nanowires is deposited on the bottom of the pocket and the other on the vertical wall.

As can be clearly seen in the lower pocket in Figure 41 material migrated towards a positive electrode, undoubtedly confirming a negative charge of the nanowires in the solution.

Since the migration through the gel could not be observed, another test was performed. The usual method used for visualizing the electrophoretic experiment in real time is the dyeing of the sample. Under an applied electric field the separated domains of samples with different sizes can be seen due to the attached dye on the sample. In addition, the size of molecules can be estimated by comparing their mobilities in gel electrophoresis with those of standard fragments of known length, i.e. standard ladders.

Electrophoretic experiments were made on dyed $Mo_6S_{9-x}I_x$ nanowires and compared with a standard dyed DNA ladder (GeneRuler™ 100bp DNA Ladders) (Figure 42). DNA was chosen since it has the same negative charge in the solution as our nanowires as well as the same elongated shape, making it an adequate control substance. The DNA ladder is supplied with two dye solutions of xylene cyanol FF (for the upper part of the ladder) and bromophenol blue (for the lower part of the ladder) for visual tracking during migration. The $Mo_6S_{9-x}I_x$ nanowires were dyed in the same manner as the DNA ladder. The electrophoresis was performed under a 80V bias for 90 minutes. Figure 42 shows a schematic of the electrophoretic measurements together with photographs taken before and during the experiment.

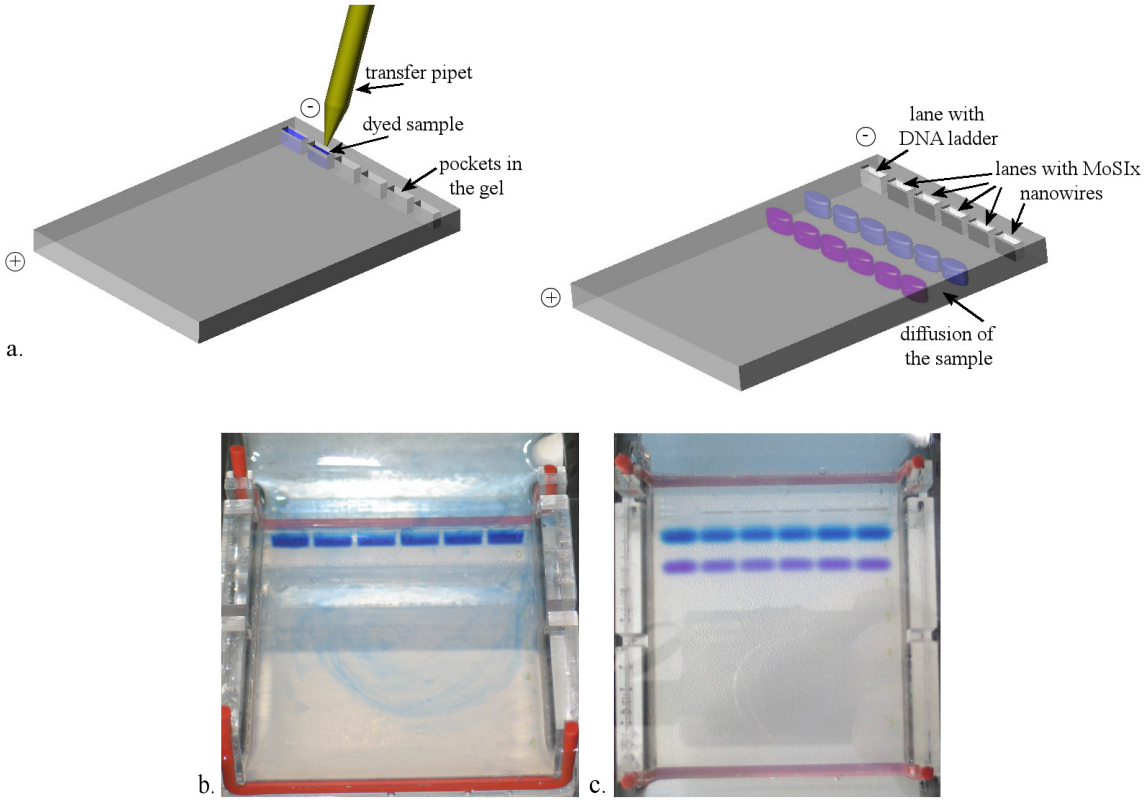

Figure 42: *Electrophoresis experiment with dyed DNA and $Mo_6S_{9-x}I_x$ nanowires.* (a) Schematic of the dyed $Mo_6S_{9-x}I_x$ compared with a standard DNA ladder; (b) a photograph taken before and (c) during the electrophoretic experiment.

After the first minutes of the experiment the DNA ladder could be seen forming. In the case of our sample, the diffusion of bare dye was noticeable as well as the diffusion of nanowires since the pocket walls towards the positive electrode started to become darker due to the deposition of the nanowires (Figure 42c).

Since we did not know if the dye had bound to the nanowires and whether it had also traveled unbound, dye control measurements at the end of the electrophoretic experiment were performed. The gel was preserved in standard EtBr (ethidium bromide) solution for half an hour after the electrophoretic experiment and then photographed with a UV light-box. EtBr intercalates between DNA base pairs and fluoresces under UV light at 312 nm. We hoped that the EtBr would bind to the nanowires and the visualization of the diffusion would be possible. The photograph from Figure 43 shows the standard DNA ladder containing the 11 fragments ranging from 100bp (base-pairs) to 1000bp. In the lanes corresponding to the $Mo_6S_{9-x}I_x$ nanowire solution, however, no signs of diffused nanowires can be seen.

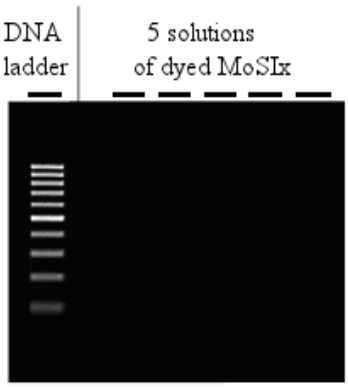

Figure 43*: Photograph of the gel after the experiment finished.* Photograph of the DNA ladder (left). No traces of possibly diffused nanowires can be observed (right).

4.3 Dielectrophoretic manipulation of $Mo_6S_{9-x}I_x$ nanowires

As mentioned previously, dielectrophoresis is the electro-kinetic motion of dielectrically polarized materials in non-uniform electric fields and is currently an active area of research for positioning and orientation or alignment of CNTs and other nanomaterials. In our experiments we used dielectrophoresis for positioning $Mo_6S_3I_6$ nanowires onto Ni wires covered with 99.95% pure Indium.

Experimental approach

Raw material of $Mo_6S_3I_6$ was dispersed in isopropanol (IPA) using an ultrasonic bath for half an hour and left to sediment for one day. The electrodes on which we wanted to attach a single bundle of $Mo_6S_{9-x}I_x$ nanowires were Ni wires coated with In. The coating was performed by immersing the tip of the Ni wires into a droplet of molten In. Upon withdrawing the Ni wires from the In droplet, a layer of In remained on the wire. The rapid cooling of the In and the slow withdrawal of the Ni wires from the droplet enabled us to control the formation of a relatively sharp-end coating as shown schematically in Figure 44. The diameter of the nickel-coated wires was above 100 µm.

Figure 44: *Schematic of the coating process of a Ni electrode wire with pure In.* First, the In is made molten on the tip of a welding machine and the Ni wire is brought close (a). The wire is then immersed in the formed droplet of In (b). With a slow movement the Ni wire is withdrawn from the droplet (c). Upon cooling and due to the slow withdrawing process on the end of the Ni wire, a sharp conical In coating is shaped.

The obtained In-coated Ni electrodes were used further in the dielectrophoretical experiment for the trapping of the $Mo_6S_{9-x}I_x$ nanowires. Two electrodes were brought close together (d≤100 µm) on a glass support and wired up with a serial resistor of 10 MΩ as shown in Figure 45. The circuit was powered either by a DC or AC power supply. For the measurement of the electric current during the experiment, we used an oscilloscope which monitored the drop of voltage across a serial resistor. After switching on the power supply, a droplet of nanowires in IPA dispersion (c=0.05 mg/ml) was applied to the tips. The trapping was performed with an applied DC field of 20V or an applied AC field of 10 V at a frequency of 10 MHz.

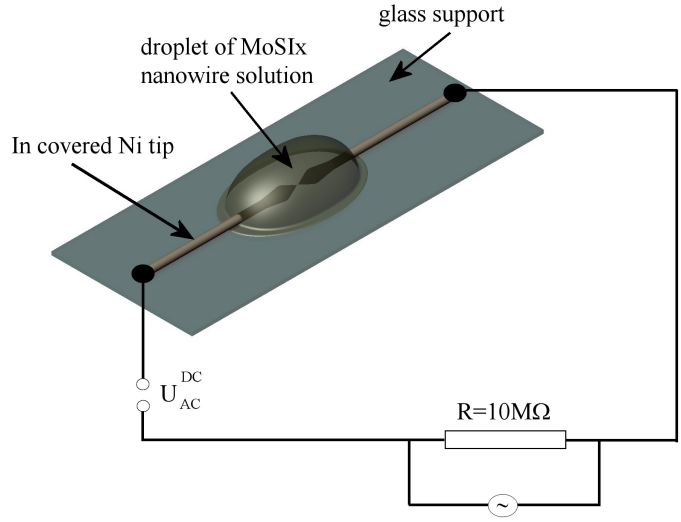

Figure 45: *Schematic diagram of the circuit used for trapping a single bundle of $Mo_6S_3I_6$.*

Experimental results

During the experiment, the drop in voltage across the resistance was measured with an oscilloscope (Figure 47a). A jump in voltage, attributed to the moment when the suspension is applied to the contacts, can be observed in the graph. Almost immediately following that, a bundle of nanowires is trapped on the emitter. The increase in the voltage, indicated in the graph by an arrow, corresponds to the moment in which the bundle is trapped.

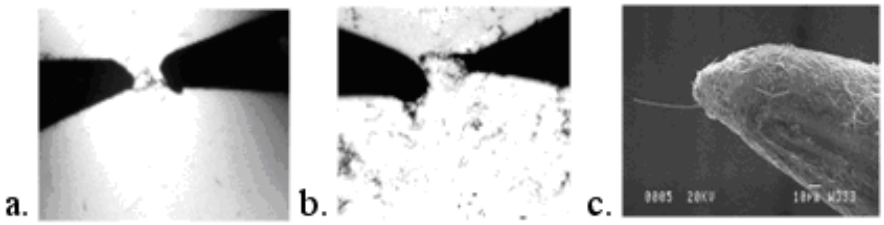

Figure 46: *The visualization of the dielectrophoresis experiment.* Optical microscope image made immediately after the suspension was applied to the contacts (a); optical microscope image made after the solution had dried (b); SEM image showing a single bundle attached to Ni tip (c).

To control and to better understand the experiment, the process was performed under a microscope where we were able to observe the experiment in-situ. When the suspension was applied, nanowire movement towards the positive electrode could be observed until the solution had dried (Figure 46 a and b). Because of the limited resolution of the optical microscope, however, we could not observe the attachment of the bundle. Therefore a SEM image was subsequently taken. A single bundle of $Mo_6S_3I_6$ could then be observed on the tip (Figure 46c).

Once we had obtained a single bundle on the tip we could use it as an emitter for field emission measurements. The results of such measurements are presented in Figure 47b and Figure 47c (Zumer et al., 2005). An I-V curve is plotted together with a Fowler-Nordheim plot for the emitted current. Importantly, during the field emission measurements, the $Mo_6S_3I_6$ bundle did not detach from the tip which suggests that the contact between the $Mo_6S_3I_6$ nanowire and emission is quite strong.

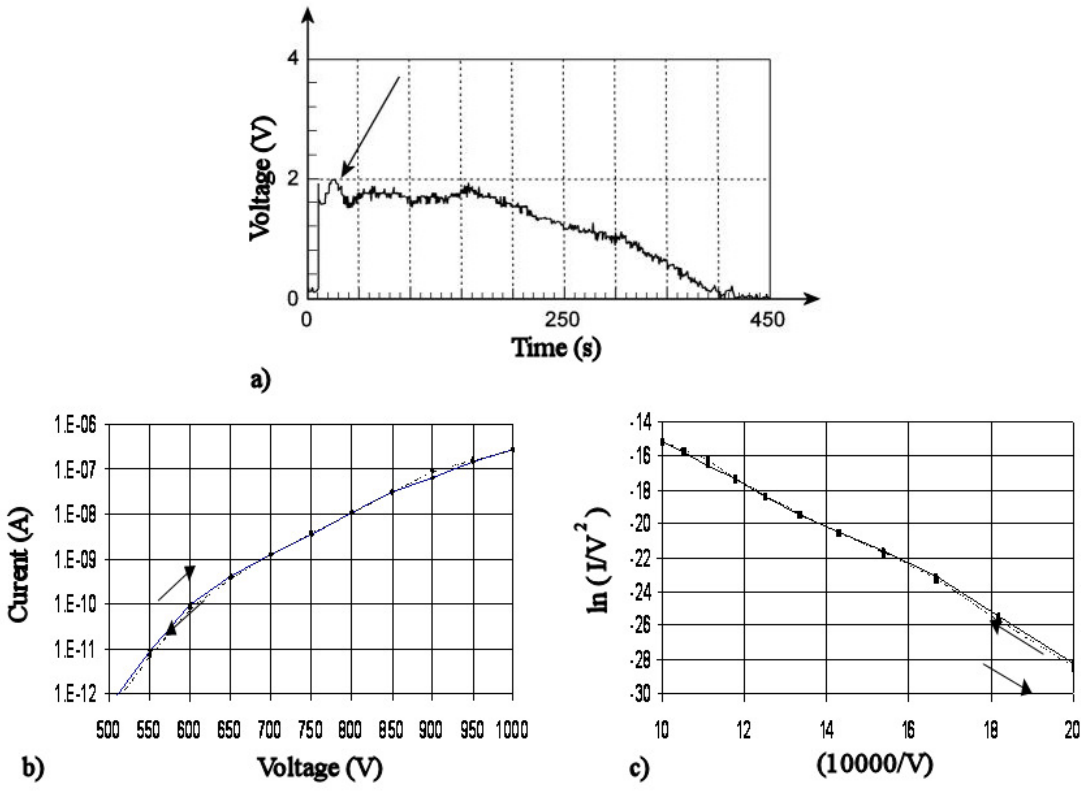

Figure 47: *Drop in voltage across the resistance (a); I-V field emission curve (b); F-N plots (c).*

4.4 Conclusions

Electrophoresis is used for the separation of (bio)molecules on the basis of size and electric charge, for purifying (bio)molecules, or for the analysis of their structures and physical properties. In our experiments electrophoresis has shown the transport of $Mo_6S_{9-x}I_x$ nanowire bundles in solution. Bundles with small diameters travel to the positive electrode while impurities and larger bundles are deposited on the bottom of the gel pocket. Since the diameter of the nanowires is larger then the gel's pores, the diffusion true solution of the nanowires was not possible. In addition, a staining process was done in order to test the mobility of the $Mo_6S_{9-x}I_x$ nanowires further. Dyed standard DNA ladders are usually used as a reference for determining molecules of unknown size. For this our nanowires were dyed in the same way as the DNA ladder and followed by electrophoretic measurements. At the end of the experiment, staining with EtBr was performed in order to observe possible diffusion of the nanowires, since the attachment of the dye to the nanowires was not known. On the photographed gel we were able to observe only the DNA ladder. The observed non-mobility of the nanowires through the gel can be explained by two possible scenarios:

- the nanowires traveled through the gel, but the EtBr did not bond with the nanowires, thus no fluoresce could be observed, falsely implying non-mobility;
- the nanowires did not travel through the gel due to their large diameters.

However, even though the electrophoretic method could not be used to separate $Mo_6S_{9-x}I_x$ nanowires according to diameter, some useful information could be extracted. It was demonstrated that the nanowires carry negative charge in aqueous solutions and that they move in a DC electric field, which can be successfully employed for positioning $Mo_6S_{9-x}I_x$ material or for separating $Mo_6S_{9-x}I_x$ material from impurities.

We have shown dielectrophoresis to be a very good technique for self-assembly of nanowires onto contacts. We have succeeded in obtaining single bundles (up to 10 nm diameter) attached onto indium-coated nickel tips which were then used in field emission measurements. The attachment process was demonstrated to be straightforward and very simple. The point emitters obtained were then used in field emission measurements. The strength of the field emission current from our point emitter was shown to be comparable to the values obtained from SWCNTs. Fowler-Nordheim plots gave a maximum emission current of I_{FE}= 0.8 μA. The fitted data gave a linear dependence in both upward and downward mode (increasing and decreasing the voltage), a good indication that the field emission may be understood as a standard barrier-tunneling mechanism.

5 Solubility of $Mo_6S_{9-x}I_x$ nanowires as a function of the pH of the solution

5.1 Dispersion of nanowires

In general, nanowires and nanotubes are often synthesized in bundles with diameters ranging from several nanometers up to a micron and with different stoichiometries. Moreover, in the case of widespread carbon nanotubes (CNTs), their lack of solubility has raised many problems in the search for their application possibilities. Thus, much effort has been invested in finding the right procedures for nanowire/nanotubes dispersion in different solvents for different applications.

Covalent (Hamon et al., 1999; Rigga et al., 2000) and ionic (Vigolo et al., 2000) modifications have been reported, i.e. dispersion of single-walled nanotubes (SWCNTs), fragments or ropes (rather than individual tubes) in organic media and formation of polymer-nanotube composites. For example, covalent functionalization with a carboxylic acid group (Chen et al., 1998) followed by treatment with thionyl chloride to form an acryl chloride group has been used to improve the solubility of carbon nanotubes. The acid chloride-functionalized SWCNTs are then susceptible to reaction with amines and after four days they can be dispersed into individual nanotubes soluble in organic solvents. Nevertheless, it was observed that the band electronic structure of the native tubes was disrupted by these modifications and in some cases the inherent crystalline structure of the individual tube was severely damaged. The ionic modification is made by dispersing the nanowires in a highly concentrated aqueous solution of sodium dodecyl sulfate (SDS), which adsorbs at the surface of the nanotubes thus improving their solubility.

The efficient purification and length selectivity of CNTs using anionic surfactants such as SDS or nonionic surfactants such as Triton X-100 has already been reported (Liu et al., 1998; Duesberg et al., 1998; Krstic et al., 1998). However, the removal of the surfactants afterwards proved to be problematic, decreasing the range of possible applications. As an alternative, SWCNTs have been dispersed by functionalizing their side-walls with fluorine (Mickelson et al., 1999) and with alkanes (Boul et al., 1999) resulting, however, in the modification of the intrinsic SWCNT properties. Purification techniques in organic solvents (Ausman et al., 2000; Shelimov et al., 1998) were shown to be very productive. By noncovalent functionalization of carboxylic acid groups to SWCNTs, dispersion in common organic solvents was obtained (Chen et al., 2001) with nanotubes of several microns in length and 2-5 nm in diameter. Likewise, it is worth mentioning that organic functionalization (Georgakilas et al., 2002; Liu et al., 2002) can make carbon nanotubes soluble in most organic solvents and even in water.

Wrapping SWCNT in macromolecules such as polyvinyl pyrrolidone (PVP) and polystyrene sulfonate (PSS) (O'Connell et al., 2001) or functionalizing them with monoamine terminated polyethylene oxide (PEO) (Sano et al., 2001) have shown to be effective methods for the solubilization of carbon nanotubes in water. In addition, physical adsorption of long chain polymers (Coleman et al., 2000; Bandyopadhyaya et al., 2002) can be employed for the dispersion of carbon nanotubes. For instance, Nativ-Roth et al. (2007) studied the interaction mechanism between carbon nanotubes and physical adsorbed copolymers. They found that dispersion of SWNT via steric repulsion among physically adsorbed (non-wrapping) block copolymers is applicable to SWNT as well as to MWNT.

Reports have also been published on the functionalization of CNTs with synthetic molecules. For example, dispersion of polyethylene glycol, PEG-attached CNTs, based on the chemical modification of the CNTs (Fernando et al., 2004; Zhao et al., 2005; Lee et al., 2007) or pristine CNTs using PEG-based amphiphilic molecules (Moore et al., 2003; Cohen et al., 2004) have shown to result in stable water solutions.

The II-IV semiconductors are attractive building components for the fabrication of optical and optoelectronic devices, e.g. emitting diodes, solar cells, lasers, etc. Among them CdS nanostructures are

also of great interest due to their high photosensitivity. Thiruvengadathan et al. (2005 and 2007) succeeded in preparing CdS elongated nanostructures of a few microns in length and 3-6 nm in diameter. The dispersion was made in an aqueous solution containing SDS or gum arabic (GA) polymer in glass vials cooled in ice and sonicated under mild (50 W) or harsh (400 W) conditions for different time durations. On the other hand, Hsu et al. (2007) dispersed ZnO nanocrystals in methanol using just an ultrasonic bath.

In past years work has been done on finding the right method for dispersing inorganic $Mo_6S_{9-x}I_x$ nanowires (Nicolosi et al., 2005 and 2006; McCarthy et al., 2007) as well. We have seen in Chapter 3 that these nanowires are easily produced (Vrbanic et al., 2004) and synthesized in long thick bundles. Nicolosi et al. (2005) studied the dispersion properties of nanowires in isopropanol at different initial concentrations (Figure 48). The sedimentation studies were performed by monitoring the transmission of a laser through the center of a sample for over 200 hours. Transmission was then transformed into turbidity using the Lambert-Beer law:

$$I / I_0 = e^{-Tl} \tag{28}$$

where I/I_0 is the transmittance, T is the turbidity and l is the sample length.

They observed that the material contained two insoluble and one soluble phase. Using the sedimentation method, Nicolosi et al. (2005) succeeded in isolating the soluble phase from the insoluble one. TEM (transmission electron microscope) images show that the insoluble phase contains large bundles of $Mo_6S_{9-x}I_x$ nanowires while the soluble phase contains small diameter nanowires (up to 10 nm). Moreover, it could be noticed that the diameter of the bundles decreases with the concentration of the solution.

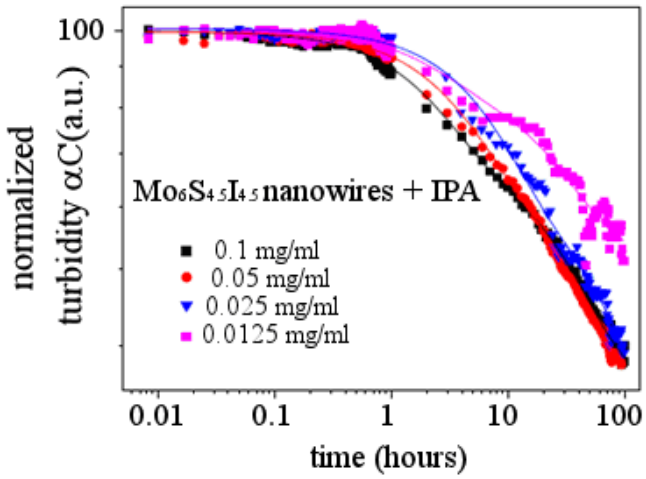

Figure 48: *Sedimentation study as a function of solution concentration (Nicolosi et al., 2005).*

Furthermore, sedimentation studies in different organic solvents have been performed (Nicolosi et al., 2005), demonstrating that the dispersion of $Mo_6S_{9-x}I_x$ nanowires depends dramatically on the solvent used. Figure 49 shows sedimentation curves for all studied solvents, clearly indicating that isopropanol (IPA) and dimethyl formamide (DMF) are by far the best solvents for dispersing the nanowires. From TEM images it was seen that before sedimentation in all solvents both bundles of nanowires and impurities were present, whereas after 100 hours of sedimentation, depending on the solvent, impurities could be found in neither IPA nor DMF.

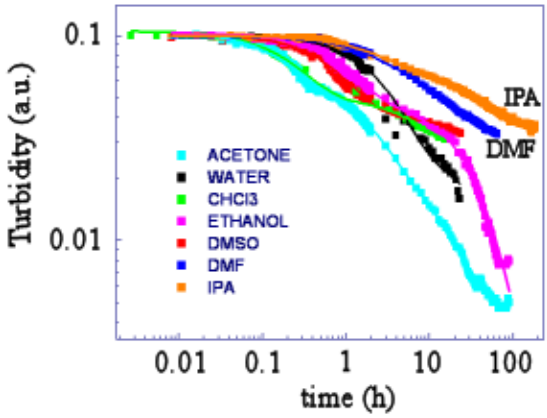

Figure 49: *Sedimentation curves for different organic solvents (Nicolosi et al., 2005).*

5.2 Preparation of the sample

Another possible method for rendering $Mo_6S_{9-x}I_x$ nanowires soluble in solution is by changing the pH of the environment. It has been shown that an assembly of gold (Wang et al., 2007) or Pt (Liu et al., 2005) nanoparticles on nanowires is possible by tuning the pH of the solution. The change in the pH value mainly influences the quantity and distribution of negative charge on the nanoparticle's surfaces. At lower pH values the induced dipole-dipole attraction of the interparticles is so strong that the Au particles self-organize into chains. The increase in the pH values means an increase of the net negative charges on the nanoparticle's surfaces, thus the intensity of the induced dipole-dipole interaction decreases.

Taking into account these observations, we tried to disperse our nanowires in acidic and basic media. Experiments were performed in 1-methyl-2-pyrrolidone (NMP). First, $Mo_6S_{9-x}I_x$ nanowires were dispersed of 0.1 mg/ml, and then the pH value of the $Mo_6S_{9-x}I_x$ solution was adjusted by adding hydrochloric acid (HCl). The exact pH value of the solution was determined using a pH meter.

Sedimentation studies were subsequently carried out. The instrument used is presented in Figure 50. Sedimentation was monitored by measuring the transmission of four lasers through a quartz cuvette containing the sample. The linear transmission is then transformed in turbidity using Lambert-Beer law (Equation 28). More about the theory behind sedimentation process can be read in Nicolosi et al. (2005).

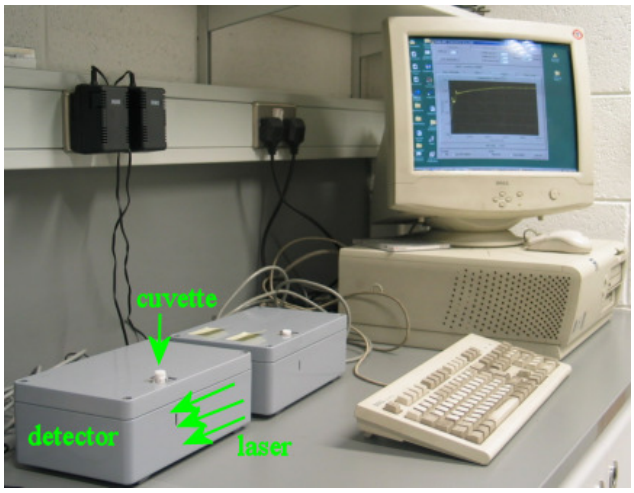

Figure 50: *Apparatus for measuring the sedimentation process of $Mo_6S_{9-x}I_x$ nanowires (Nicolosiet al., 2005).*

5.3 Experimental results

The experimental sedimentation curves can be seen in Figure 51. The experiments were carried out for different pH values: pH was set from 11.4 down to 1.58. It was observed that turbidity tends to decrease till

it reaches a constant value, which represents the turbidity associated with the obtained dispersed material for each pH. For each pH the sedimentation was different and, as can be seen in Figure 51, the curves corresponding to higher pH at the top of the graph represent the best dispersions. We can conclude that with the decreasing pH of the solution, the solubility of the nanowires also decreases.

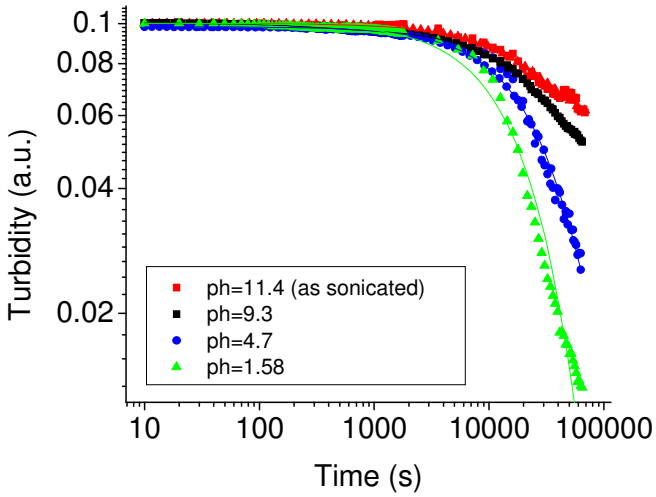

Figure 51: *Sedimentation curves.* $Mo_6S_{9-x}I_x$ nanowires dispersed in NMP at four different pH values.

To determine the composition of the solution, TEM investigation was performed on the $Mo_6S_{9-x}I_x$ nanowires diluted in NMP. A droplet was taken from the top of the solution before the sedimentation and 24 hours afterwards. Before sedimentation in solution both bundles of nanowires and impurities were observed (Figure 52 a and b). The quantity of the impurities from the beginning of the sedimentation started to diminish only after 24 hours (Figure 52 c and d). By the end of the experiment after 4 days, a substantial amount of insoluble phase deposition was observed as the pH value decreased.

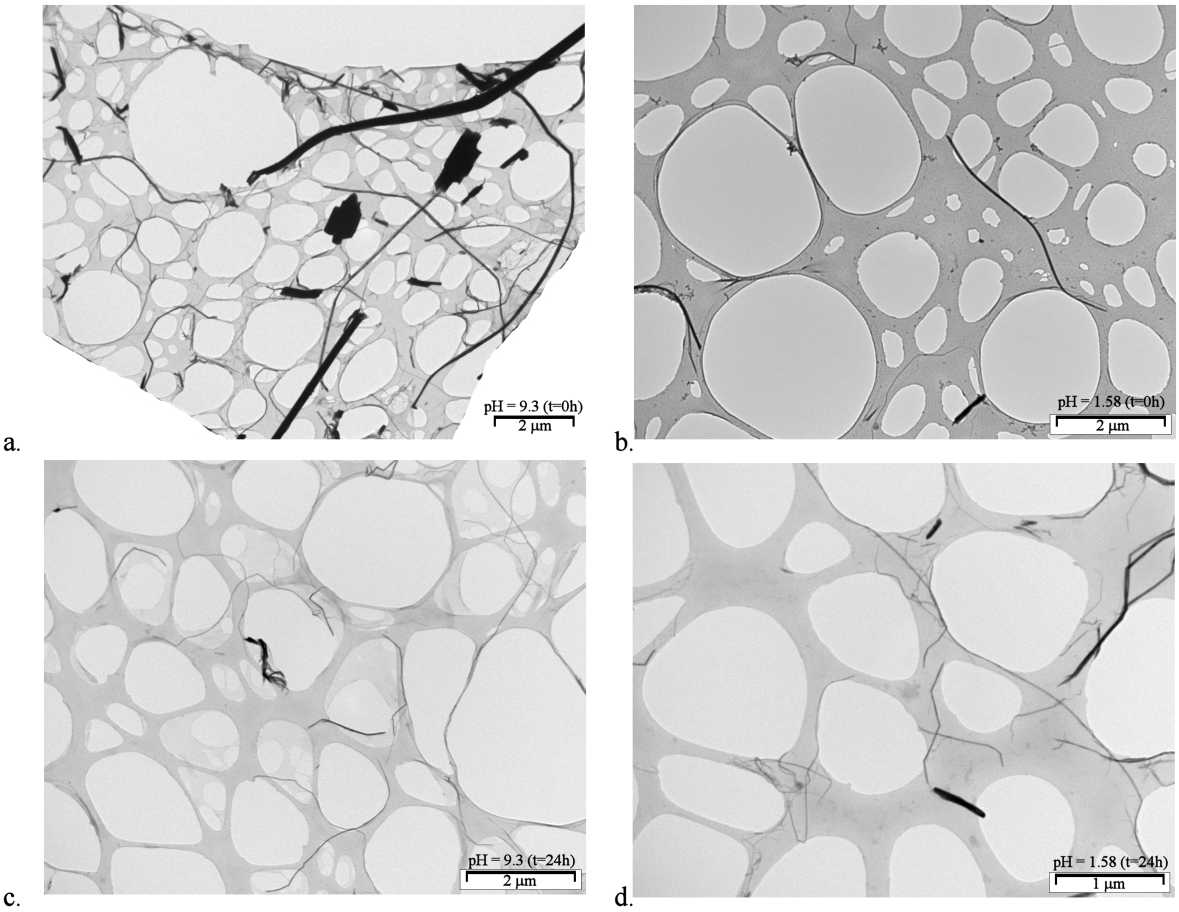

Figure 52: *TEM measurements.* TEM pictures of the dispersed $Mo_6S_{9-x}I_x$ nanowires dispersed in NMP immediately after dispersion (a and b) and after 24 h of sedimentation (c and d) at pH 9.3 and 1.58.

The diameters of the nanowires were also measured. A distribution of the average diameter of the $Mo_6S_{9-x}I_x$ nanowires is presented in Figure 53 for different pH values before the sedimentation process and after 24 hours. It should be pointed out that in the initial solution ($Mo_6S_{9-x}I_x$ nanowires dispersed in NMP) the values of the diameter were between 25 and 50 nm. When HCl was added, the diameter of the nanowires decreased to values below 15 nm, clearly indicating a correlation between the pH and the average nanowire diameter.

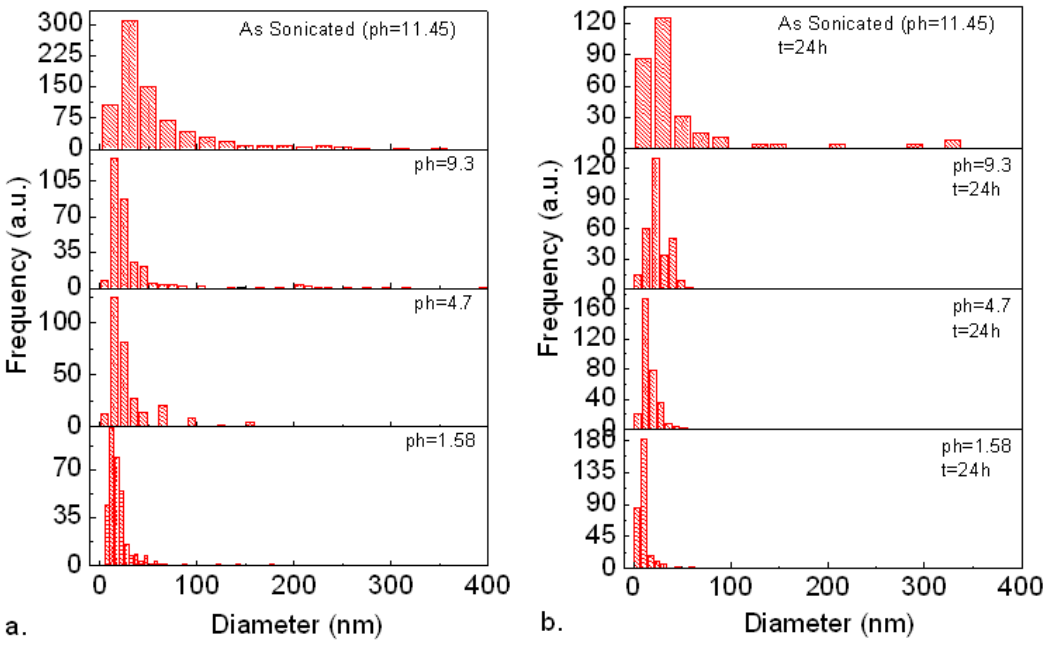

Figure 53: *Diameter distribution.* Diameter distribution of $Mo_6S_{9-x}I_x$ nanowires dispersed in NMP immediately after dispersion (a) and after 24 h of sedimentation (b).

The mean bundle diameter as a function of pH of the solution is shown on Figure 54. An obvious decrease of the diameter is observed as the pH values decreases. Furthermore even after 24 hours the mean diameter of the nanowires in the solution remains the same implicating instantaneous reaction of the nanowires rather then time dependent on a larger scale of several hours.

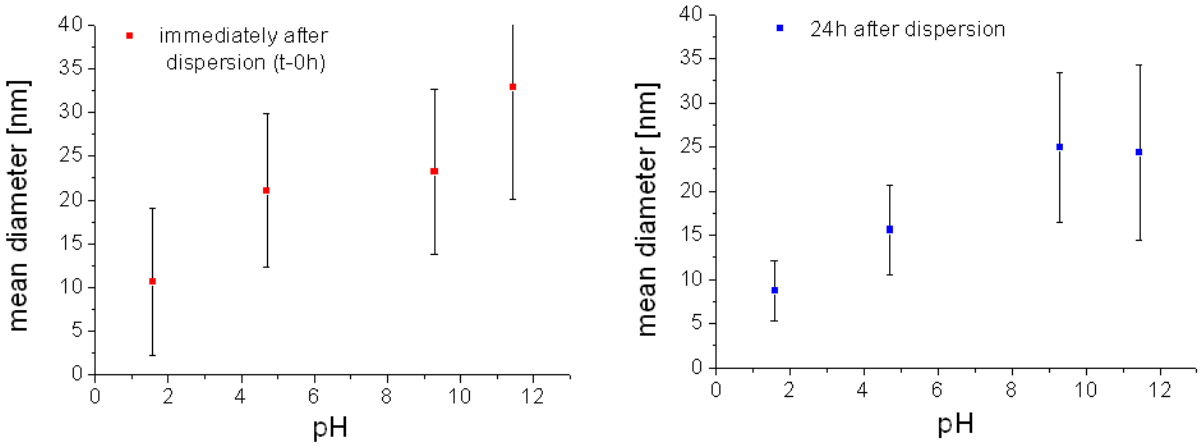

Figure 54: *Mean bunde diameter as a function of the pH of the solution.*

5.4 Conclusions

Following the report of Wang et al. (2007) who succeeded in the self-assembly of gold nanoparticles into long chains just by changing the pH of the media, we performed a sedimentation study in which the pH of the $Mo_6S_{9-x}I_x$ nanowire dispersion was changed in order to debundle the nanowire bundles due to the change in the charge in the solution.

Sedimentation measurements were performed by measuring the turbidity as a function of time. Fitting the experimental curves with the theoretical model we found that the solution consists of insoluble and soluble material. The insoluble sedimented material consists of impurities and large bundles while the stable solution of soluble material consists mainly of thin bundles or even individual nanowires. It was soon clear that the best turbidity curve was for the as-sonicated nanowires in NMP. A decrease in the pH was followed by a decrease of the solubility.

However, the TEM measurements and diameter distribution showed that as the pH decreases towards an

acidic medium, the average diameter of the $Mo_6S_{9-x}I_x$ nanowires also decreases. Moreover, the amount of sedimented material increases as the turbidity curves were showing. The reason for this might lie in the material disintegration upon changing due to the decrease of pH.

6 Functionalization of $Mo_6S_{9-x}I_x$ nanowires with Au colloids

The ability to manipulate the physical, chemical and biological properties of particles, molecules and nanowires allows researchers to design and to use them in disciplines such as nanoengineering, nanoelectronics and nanobioelectronics for drug delivery, as image contrast agents, for diagnostic purposes or as building blocks for the fabrication of nanoscale devices.

6.1 Historical background of Au functionalization

Most of the early studies in the area of metal clusters focused on the preparation of gold colloids in aqueous media (Faraday, 1861; Turkevitch et al., 1951). Colloidal gold particles prepared in an aqueous medium by chemical reduction are usually capped with anions (e.g. citrate) that charge their surface negatively, preventing aggregation (Shipway et al., 2000). More recently, newer methods have been reported for the preparation of stable metal nanoparticles capped with monolayers of organic molecules possessing functional groups such as quaternary ammonium halides, amides, thiols, isothiocyanates, etc. which can often act as stabilizers of nanoparticles. Such monolayer-protected metal clusters are of interest in the design of nanostructured materials.

6.1.1 Synthesis - overview of Au nanoparticles

The simplest and by far the most conventional method of gold nanoparticle (AuNP) synthesis is the aqueous reduction of tetra-chloro-aurate ($H[AuCl_4]$) by sodium citrate reduction (Turkevitch et al., 1951; Handley, 1989) or other reducing agents (Yee et al., 1999). The size of the particles synthesized by citrate reduction can reach 15 nm to 20 nm, depending on the reagent concentration (Yee et al., 1999; Hostetler et al., 1998). Citrate ligands were not the only ones used to stabilize the gold colloids, and in time phosphanes and thiols, owing to their rather strong Au-P and Au-S bonds, were discovered to be excellent stabilizers as well.

Eventually, thiols were shown to be the most important type of stabilizer for gold colloids of any size (Figure 55). The use of thiols leads to the formation of RS^- thiolates that form strong covalent bonds (Au-S). Thus, phosphanes start to be slowly substituted by thiols since the latter ones bind more strongly to the gold. The obtained gold colloids showed to be repeatedly isolated and redissolved in common organic solvents without irreversible aggregation or decomposition. They can be easily handled and functionalized.

The synthesis methods to obtain AuNPs are diverse. One can employ Faraday's two-phase system (Faraday, 1861) which uses thiol ligands. Brust et al. (1995) went further and used p-mercaptophenol to stabilize AuNPs in a single phase system. Many publications subsequently appeared describing the Brust-Schiffrin method for the synthesis of different stable AuNPs (Hostetler et al., 1996). Other ligands containing sulfur, such as xanthates (Tzhayik et al., 2002), disulfides (Porter et al., 1998), di- (Resch et al., 1999), tri- (Felidj et al., 2003) and tetrathiols (Balasubramanian et al., 2002), have also been used successfully as stabilizers.

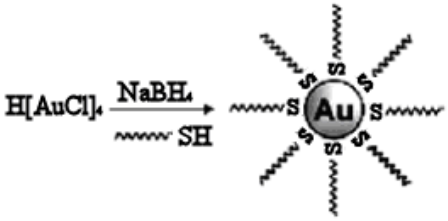

Figure 55: *Schematic of the formation of AuNPs coated with organic shells (Sun et al., 2001).*

A new route for the synthesis of AuNPs is the use of "nano-reaction chambers." Micelles can be the most appropriate kind of such chambers. Moller et al. used diblock co-polymers with regularly organized micelles, in which $AuCl_4$ were transported. The formation of the nanoparticles takes place following a

reduction step with hydrazine or $NaBH_4$ (Spatz et al., 1996). Figure 56 represents a schematic process of the formation of AuNPs in the micelles present in the copolymer structure.

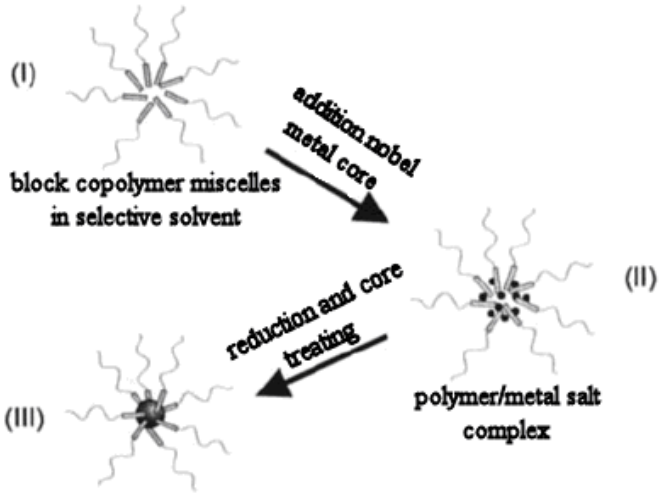

Figure 56: *Formation process of AuNPs in a block of copolymer micelle.* (a) the copolymer micelle; (b) the loaded micelles with the $AuCl_{4;}$ and, (c) the formed single gold nanoparticle in the micelle (Spatz et al., 1996).

Another popular technique that has been used by scientists is the seeding-growth procedure also known as metal-vapor synthesis. Metals consist of atoms, so the simplest way of obtaining nanoparticles is to generate single metal atoms in the gas phase followed by the condensation to nanoparticles. A commonly used technique for metal vapor production is the laser ablation (Mafune et al., 2000; Sibbald et al., 1996; Yeh et al., 1999). An impediment for using this technique is a rather broad nanoparticle size distribution.

Sonochemistry was also used for the synthesis of AuNPs within the pores of silica and for the synthesis of bimetallic Au/Pd particles (Chen et al., 2001). AuNPs have been fabricated via decomposition of $[AuCl(PPh_3)]$ upon reduction in a monolayer at the gas/liquid interface (Khomutov, 2002). The heat treated AuNPs form 2D superlattices with hexagonal packing (Shimizu et al., 2003). The number of procedures for synthesizing AuNPs is enormous, therefore only the most known and used ones have been mentioned above.

6.1.2 Some general properties of Au nanoparticles

Some physical properties

High-resolution transmission electron microscopy (HR-TEM) is by far the most valuable tool for studying nanoparticles' size, distribution and structure, but other methods can be very useful, e.g. scanning tunneling microscopy (STM), atomic force microscopy (AFM), small-angle X-ray scattering (SAXS), laser desorption/ionization mass spectroscopy (LDI-MS) and X-ray diffraction.

Many investigations have shown that gold nanoparticles exhibit either a mono- or a polycrystalline structure of hexagonal close-packed (hcp) atoms. A characteristic of gold colloids is the color, which can vary between light red via purple-red to bluish-red. This effect is caused by the surface plasmon band (SPB), quantitatively described by the Mie theory, a broad absorption band in the visible region around 520 nm. The SPB originates from the collective oscillations of the confined electron gas of the particles (6s electrons of the conduction band for AuNPs) that is correlated with the electromagnetic field of the incoming light.

Mie theory attributes the plasmon band of spherical particles to the dipole oscillations of the free electrons in the conduction band occupying the energy states immediately above the Fermi energy level (Alvarez et al., 1997). The main characteristics of SPB are: a) the position at around 520 nm; b) its sharp decrease with decreasing the core size for AuNPs with 1.4 - 3.2 nm core diameter; and. c) step-like spectral structures indicating transitions to the discrete unoccupied levels of the conduction band (Melinger et al., 2003). Thus, it was found that SPB is absent for gold particles with diameters less than 2 nm as well as for bulk gold. This is due to the lack of quasi delocalized electrons necessary for the interaction with light.

Moreover, SPB maximum and bandwidth do not depend only on the size of the nanoparticles but also on the particle shape, medium dielectric constant and temperature. The refractive index of the solvent has been shown to induce a shift of the SPB (Templeton et al., 2000). With elliptical particles, the SPB is

shifted to higher wavelengths as the spacing between the particles is reduced. The shift is described as an exponential function of the gap between the two particles (Su et al., 2003). Another influential parameter is the core charge. Excess of electronic charge causes a shift of SPB to higher energies, whereas electron deficiency causes shifts to lower energies (Ung et al., 2002).

Of great interest in biophotonics and material science are the fluorescent properties of nanoparticles. Some widely used capping fluorescent groups are pyrenyl (Thomas and Kamat, 2000); polyoctylthiophenyl (Xu and Yanagi, 1999); and, fluorenyl (Dubertret et al., 2001). The ability of the gold surface to bind with specific functional groups has made it suitable for a variety of applications.

Investigation of the electronic properties of gold nanoparticles has also attracted much attention for years. Metal and semiconductor clusters in the nanometer size regime exhibit quantum size behavior. Probably the most used method for studying the electronic structure of the nanoparticles is the measuring of current-voltage (*I-V*) characteristics under different conditions. Measurements at room temperature have shown that the particles exhibit a linear current-voltage response and therefore indicate metallic behavior (Ohm's law) while at low temperature the electronic results were dominated by Coulomb blockade phenomena. The *I-V* curves were found to contain current steps separated by voltage plateaus where each current step represents the addition of a single electron to the particles (Mullen and Ben-Jacob, 1988). However, in order to observe single electron current steps, the junction capacitance *C* must be extremely low, so that the energy necessary to charge the particle with a single electron is large compared with the thermal energy (see Equation 29):

$$E = e^2 / 2C >> kT \tag{29}$$

where *e* is the electron charge, *k* is Boltzmann's constant, *T* is the temperature and *C* is the capacitance of the particle between the electrodes. Thus, with decreasing particle size, C is lowered and the single electron transport (SET) can be observed even at room temperature.

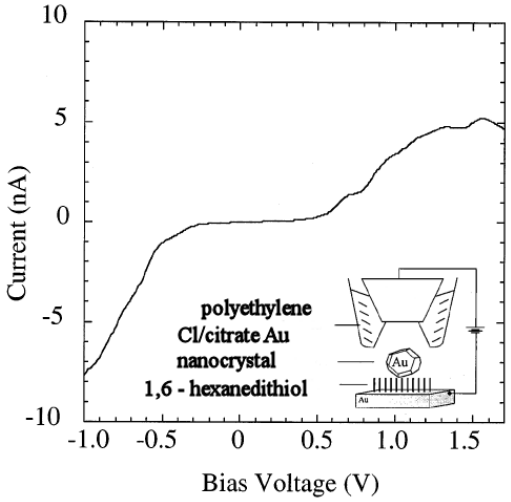

Figure 57: *I-V characteristic of citrated AuNPs showing current steps and voltage plateaus (Brousseau et al., 1998).*

Figure 57 shows a typical *I-V* curve for citrate-capped AuNPs at room temperature (Brousseau et al., 1998). Two well-defined 5 nA current steps and voltage plateaus of 500 mV are observed. The theoretical semi-classical model for single electron tunneling fits the data and gives similar results to previous observations of Andres et al. (1996). Moreover, it was found that by changing the citrate ligands with thiols, the *I-V* characteristic changes significantly. Consequently, the surrounding of a nanoparticle core in a low dielectric shell allows access to important nanoscopic electrical phenomena in relatively complex fluidic environments.

Recently, measurements on $Au_{55}(PPh_3)_{12}Cl_6$ clusters at 7 K under ultra high vacuum (UHV) indicate that the ligands surrounding the AuNPs do not visibly contribute to the tunneling process (Zhang et al., 2003). Moreover, by plotting the differential conductivity d*I*/d*V* as a function of the tunneling bias (Figure 58) the existence of discrete energy levels inside the Au_{55} could be proven.

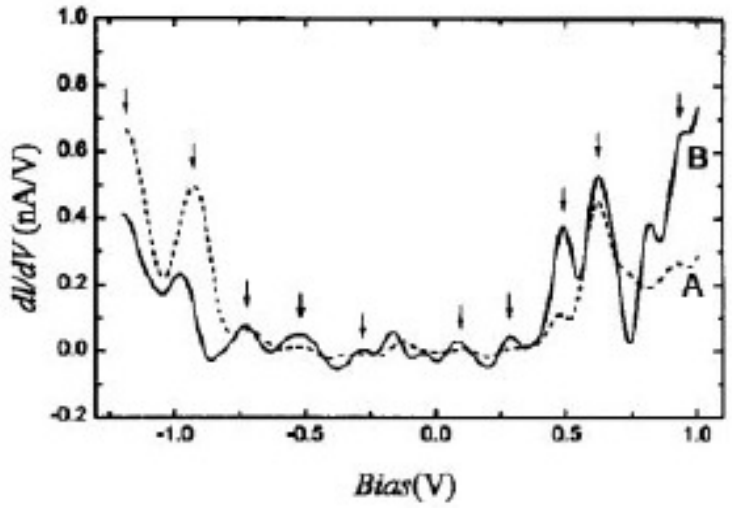

Figure 58: *Differential conductivity vs bias.* Tunneling spectra acquired above the C_6H_5 ligand ring (dashed lines) and next to the ligand ring (solid lines) (Zhang et al., 2003). The arrows indicate the discrete electronic energy levels in the Au_{55} cluster core.

Interesting electrical properties were shown also by regular 2D (two-dimensional) arrangements of gold particles (most of them with size of a few nanometers up to 20 nm) when conductivity measurements were carried out (Torma et al., 2001). The *I-V* characteristics of the layers were shown to exhibit quasi-one-dimensional conduction behavior. Moreover, a temperature dependence of the conductivity has been observed, which can be interpreted by Mott's law for variable range hopping.

The use of nanoclusters in future nanoelectronics has evoked much interest. Progress in the development of well-ordered cluster arrangements has been made during the past year, but much still needs to be learned for producing 3D, 2D or even 1D arrangement routinely and in large amounts.

Some chemical properties

Ligand exchange reactions are a common and much used method to change solubility or to introduce special properties. For instance, the incorporation of 11-mercaptoundecanoic acid gives amphiphilic gold nanoparticles, which are soluble in basic aqueous media but aggregates in acidic media due to the hydrogen-bonding. The control of the particle aggregation was shown to be controllable through the modulation of pH (Simard et al., 2000).

The formation of the water soluble compound $Au_{55}(Ph_2PC_6H_4SO_3Na)_{12}Cl_6$ from $Au_{55}(PPh_3)_{12}Cl_6$ dissolved in dichloromethane is also based on ligand mobility. The property of a carboxylate group to bind with metals has been used to form controllable and reversible assembly of AuNPs monolayer and multilayer films (Zamborini et al., 2000; Wuelfing et al., 2001). Complexes of pyridine-functionalized thiol AuNPs also led to the formation of surface assemblies (Chen et al., 2002). Various other electroactive (Miles and Murray, 2001) and photoactive groups (Sudeep et al., 2002; Kamat, 2002), catalysts (Li et al., 1999) and simple groups such as halides, nitriles, alkenes, and sulfonates were introduced using this ligand-exchange reaction (Warner et al., 2000).

For instance, C_{60} was introduced into AuNPs by nucleophilic addition of 4-aminophenoxide ligands to C_{60} double bonds (Zhu et al., 2003; Liu et al., 2001). This property can be used for the assembly of three-dimensional nanoparticle arrays exhibiting long-range order. Moreover, for the attachment of proteins, peptides and oligonucleotides (Gregori et al., 1997; Alivisatos et al., 1996) on AuNPs for the formation of various building blocks nucleophilic addition of ω-maleimido thiol-AuNPs on a sulfidryl group was used. AuNPs functionalized with sulfo-N-hydroxysuccinimide were shown to react with primary amines, facilitating the attachment of any protein bearing a primary amine to be linked to AuNPs. As the list of ligand exchange reactions is lengthy, only some representative examples have been mentioned above.

6.1.3 Au colloid applications in nanobiology and nanotechnology

Semiconductor and noble metal nanoclusters in the nanometer size regime were shown through the years to

have potential applications in the development of biological nanosensors, optoelectronic nanodevices, etc. (Romero, 2001; Hickman et al., 1991; Chen et al., 1998). The advantages of small nanoparticles are: (a) short-range ordering; (b) enhanced interaction with environment due to the high number of dangling bonds; (c) great variety of the valence band electron structure; and, (d) self-structuring for optimum performance in chemisorption and catalysis.

In recent years the "self-assembly" process has been shown to be a powerful tool for the design of building blocks. The two well-known approaches for self-assembly are the top-down and bottom-up approach. The "top-down" approach methods for nanoscale manipulation have, however, numerous drawbacks, e.g. they do not reach scales below 50 nm in size and have high production costs. Thus, advances in the field of nanotechnology provide an alternate "bottom-up" approach, in which the nanoparticles and the bridging molecular units are assembled together as circuits in nanoelectronics. This technique offers a number of potentially very attractive advantages including experimental simplicity, size domain down to atomic scale, inexpensive fabrication, and 3D organization of building-blocks.

The ability of gold nanoparticles to self-assemble into ordered arrays gives them great potential in silicon memory applications (Kolliopoulou et al., 2003; Paul et al., 2003). For instance, a recent report by Leong et al. (2007) demonstrates combined AuNPs with pentacene to form a new organic memory system. The electronic device has a triple layer structure: on an amine modified silicon substrate AuNPs are mobilized and then covered with pentacene (Figure 59). The gold nanoparticles act as the device's charge-storage elements and their properties are studied using capacitance-voltage and conductance-voltage measurements.

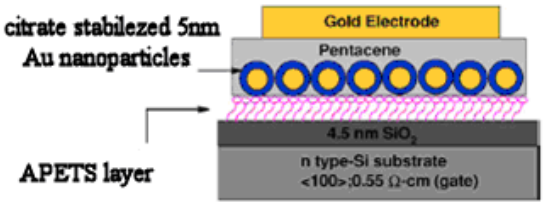

Figure 59: *Schematic of the triple layer organic memory device based on gold nanoparticles (Leong et al., 2007).*

Scientists are also keenly interested in DNA-based sensors used for gene sequence recognition and expression, detection of mutations or polymorphisms, mapping and even for molecular diagnostics. DNA is regarded as a promising construction material because of its recognition capabilities, physicochemical stability and mechanical rigidity. Assemblies of DNA-gold colloids have been prepared by the DNA hybridization-based self-organized pathways. The resulting arrangements have found applications in electronics, optical and laser technology. For example, Mirkin et al. (1996) and Alivisatos et al. (1996) used non-complementary DNA oligonucleotides capped with thiol groups for binding particles to each other or to the surfaces in a controllable fashion. Geometries, such as lines of several particles along DNA strands or gold double- or triple- DNA terminals, have also been produced. On the other hand, Mucic et al. (1998) reported a non-covalent method for the assembly of gold nanoparticles in a network material. By using modified gold nanoparticles with oligonucleotides and complementary oligonucleotide linker to the modified nanoparticles they were able to form two-component networks.

Park et al. (2002) reported a conductivity-based DNA detection using oligonucleotide functionalized AuNPs. In their approach, a small array of short oligonucleotide strands is trapped in the gap between the two electrodes. The target oligonucleotide has complementary recognition elements to the one between the electrodes. Park et al. used the three component sandwich approach, where target DNA is used to bind to functionalized AuNPs with a complementary sequence to the target one. If the target DNA molecules are not present then no gold particles are captured. Capacitance or conductivity measurements can be performed to determine the number of target molecules that filled the gap (Figure 60). By exposing the device to a solution of Ag(I) and hydroquinone (photographic developing solution) the sensitivity of the detection was increased.

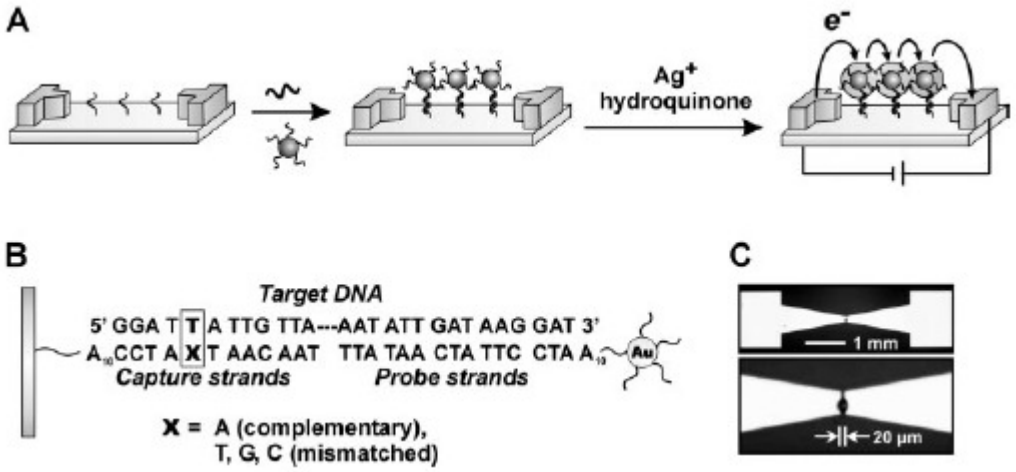

Figure 60: *High sensitivity detection device for DNA molecules.* (a) Scheme showing the construction steps of the DNA detection device; and, (b) sequence of the capturing process: captured DNA oligonucleotide, target oligonucleotide and functionalized AuNPs (Park et al., 2002).

Using the same three layers sandwich approach, Taton and co-workers (Taton et al., 2001) were able to detect two different target sequences in one solution. Thus, 50 and 100 nm AuNPs were functionalized with DNA oligonucleotides (Figure 61). After running the experiment, the array glass slides were observed under microscope and whenever 50 nm gold nanoparticles were attached a green light was observed (542 nm) while whenever 100 nm gold nanoparticles were attached a orange light was observed (583 nm).

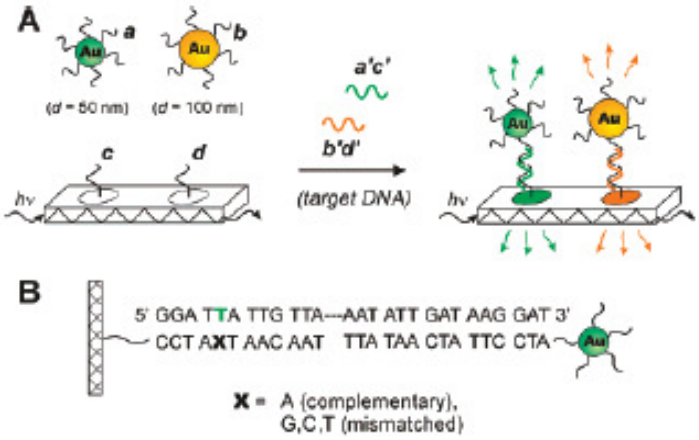

Figure 61: *Schematic of the three layer sandwich of DNA captured arrays, DNA targets and the functionalized gold nanoparticles (Taton et al., 2001).*

Liu and Lu (2003) used gold functionalized DNA enzymes for calorimetric detection of metal ions. They were able to hybridize the nanoparticles into aggregate clusters that have a characteristic blue color. However, in the presence of a specific metal ion like Pb(II), the catalytic DNA will break off individual AuNPs, resulting in a color shift to red. The change of the color depends on the concentration of the contaminant metal ions and can be monitored by UV-spectroscopy. A colorimetric sensor based on functionalized AuNPs was made by Liu and Lu (2006) also for the detection of adenosine and cocaine. The sensor is based on the same principle of disassembly of nanoparticle aggregates exhibiting a very rapid color change. In time, colorimetric detection was shown to be a straightforward method for which scientists showed great interest (Elghanian et al., 1997; Storhoff et al., 1998).

The use of surface plasmon resonance (SPR) method for the detection of molecular binding (Kalyuzhny et al., 2003; Raschke et al., 2004) has been intensely studied. For instance, Nath and Chilkoti (2002) used the SPR method for the design of a biomolecular sensor. They assembled AuNPs on an optically transparent substrate and observed the changes in the absorbance spectrum associated with biomolecular binding to the gold colloids (Figure 62). The formation of the layer of gold particles on the glass will result in the coupling of plasmons of individual particles and would show in the UV-spectra an absorbance at wavelengths of approximately 550 nm. Introducing the proteins, the binding process to the gold nanoparticles is correlated with an increase of absorbance at 550 nm. It was shown also that with the

increase of the solution concentration more proteins are bound and the absorbance increases significantly.

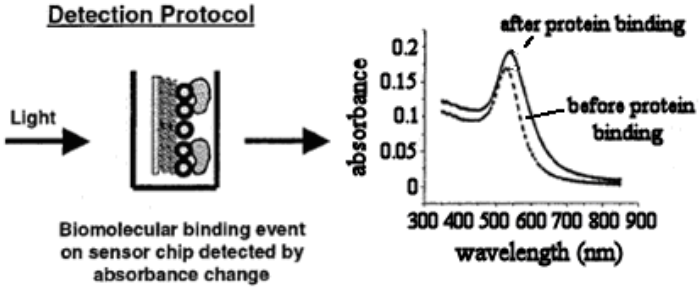

Figure 62: *The principle by which the biomolecular sensor operates (Nath et al., 2004).*

A diffraction based sensor for detecting DNA oligonucleotides was developed by Weld et al. Here, the captured oligonucleotides form a diffraction grating pattern on a silicon wafer. The target oligonucleotides are attached to the AuNPs probes. Illuminating the sample with a laser and measuring the diffraction patterns they were able to determine the hybridization rate of the DNA.

Fuel cell technology is a domain that attracts great attention because it allows the conversion of chemical energy into electricity. Applicability domains of fuel cells are large; among them are low-emission transport systems, stationary power stations, combined heat and power stations, etc. Fuel cells are made up of electrodes, an electrolyte, i.e. a pool of chemicals that bathes the electrodes and fuel, which is used up as the cells produce energy. Like a battery, fuel cells generate a flow of electricity by pushing electrons out from one electrode and receiving them back through a second electrode. At the nanoscale in an aqueous solution, gold-catalyzed chemical reactions vary quickly even at room temperature (Bulushev et al., 2002). Thus, researchers used gold nanotubes on membrane surrounded by water that contained dissolved polyoxometalate, a metal complex that has a high affinity for the electrons. Electricity was produced by catalytic oxidation of carbon monoxide (CO) using the gold catalysts at room temperature. Gold-based alloys also were reported to give very good results by using catalysts for CO oxidation (Cameron et al., 2003).

6.2 Experimental results

We have seen that the self-assembly process plays an important role in the development of nanodevices. In our experiments we demonstrate a new route to recognitive self-assembly of molecular-scale circuits using sulfur-terminated $Mo_6S_{9-x}I_x$ nanowires.

To reproducibly self-assemble a complex circuit based on single molecules, it is essential that the connection junctions between the building blocks exhibit recognitive ability. They should be connectable to diverse entities, such as gold metal surfaces (for connections to the macro world) and biomolecules (for nanosensors, nanoelectrodes, molecular switches), and, most importantly, they must allow branching.

The particular advantage that $Mo_6S_{9-x}I_x$ nanowires have for the development of molecular nanodevices are the S atoms at the end allowing covalent bond formation with gold surfaces or to thiol groups.

6.2.1 Sample preparation

Before self-assembly, $Mo_6S_{9-x}I_x$ nanowires were first annealed at 750 °C in a sulfur atmosphere. Subsequently, the nanowires were ultrasonically debundled in isopropanol (IPA) for one hour in a low power sonification bath. The concentration of the sample was 0.5 mg/ml. After sonification, the solution was left to settle in order to sediment out large bundles. The dispersion from the top of the solution was removed and analyzed with an atomic force microscope (Figure 63a). The 5 nm gold nanoparticles, supplied by British Biocell International, are surrounded by a negative citrate shell. Due to the high concentration of AuNPs in solution, we diluted them in H_2O, the final concentration being $2.5*10^{10}$ part/ml. Afterwards, the AuNPs were also analyzed with an atomic force microscope in order to optimize their concentration and to accurately measure their diameter distribution (Figure 63b).

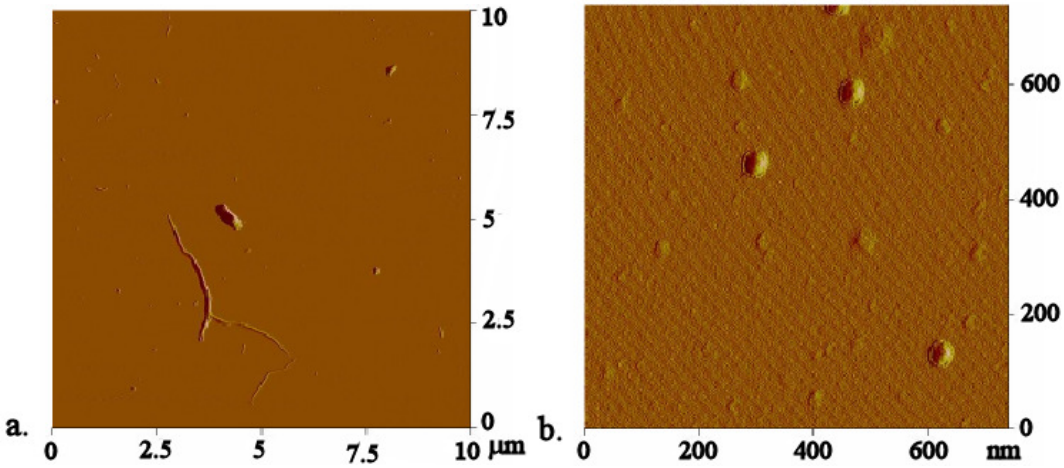

Figure 63: *AFM images.* (a) MoSIx nanowires after dispersion; and, (b) AuNPs after dilution on a mica substrate.

The dispersed $Mo_6S_{9-x}I_x$ nanowires were mixed with the gold colloids in the proportion of 1(nanowires):3(AuNPs). The mixture was left to react for three days and then studied with an AFM.

6.2.2 Atomic force microscope analysis

For the AFM studies, droplets of solution were dried on a mica substrate and then analyzed with a DI Dimension 3100 atomic force microscope in tapping mode. A systematic AFM investigation reveals a large number of gold nanoparticles attached to the ends of $Mo_6S_{9-x}I_x$ nanowires (Figure 64a and Figure 64b). Measurements of height profiles of both the wire and the golden particle were performed. The nanowire measured 1 nm ± 0.2 nm in diameter, (Figure 64d) and the golden particle measured 4.5±0.5 nm in diameter (Figure 64c), which is in perfect agreement with the sizes of single nanowires and of AuNPs in the solution.

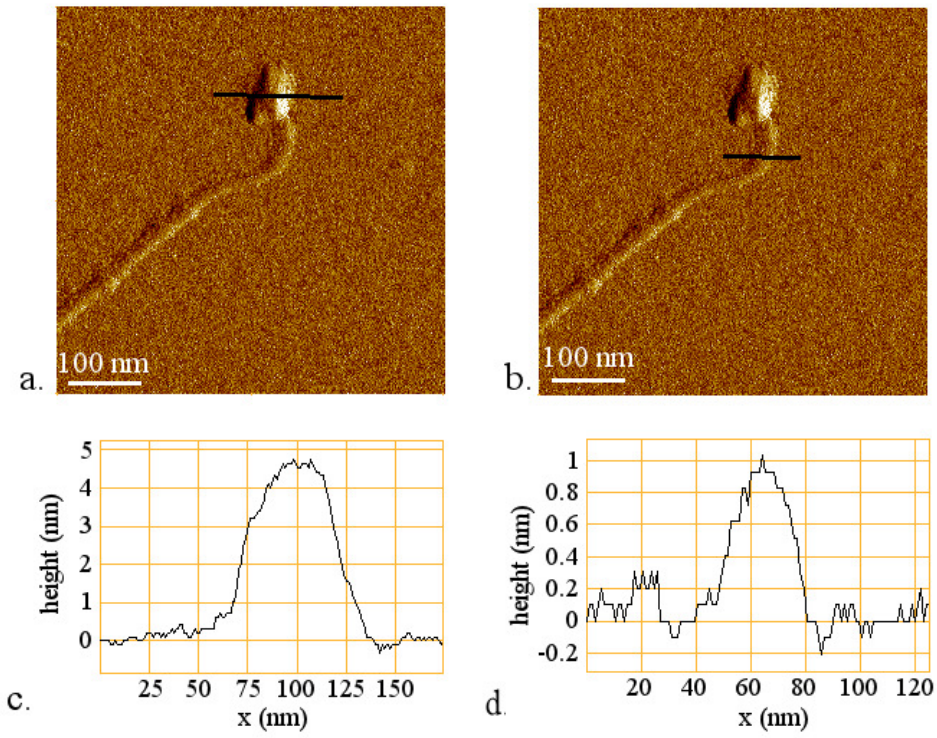

Figure 64: *AFM analysis of the experiment.* AFM images of MoS_xI_y nanowires functionalized with gold particles (a and b), cross section measurements of the individual wire (d), and cross section measurements of the gold particles (c).

We obtained attachment yields of over 50% in water and 10% in IPA (measured by counting the ends of

twenty-one $Mo_6S_{9-x}I_x$ molecular wires MWs (molecular wires) with and without AuNPs attached). In comparison, very few (<5%) AuNPs were observed to be attached to the sides of MWs. Control experiments with silver nanoparticles (supplied by British Biocell International) were performed as well. The $Mo_6S_{9-x}I_x$ nanowires and silver colloid solution were prepared with the same procedure as the gold colloids. After leaving them to react for three days, droplets from the top of the solution were dried on HOPG (highly oriented pyrolytic graphite) substrate. Figure 65 shows where silver colloids are concentrated on the substrate and in the near vicinity of the $Mo_6S_{9-x}I_x$ nanowires. No attachment can be observed at the end or on the lateral parts of the nanowires, suggesting chemical bonds between sulfur terminated nanowires and the gold atoms, ruling out other charge driven connection mechanisms.

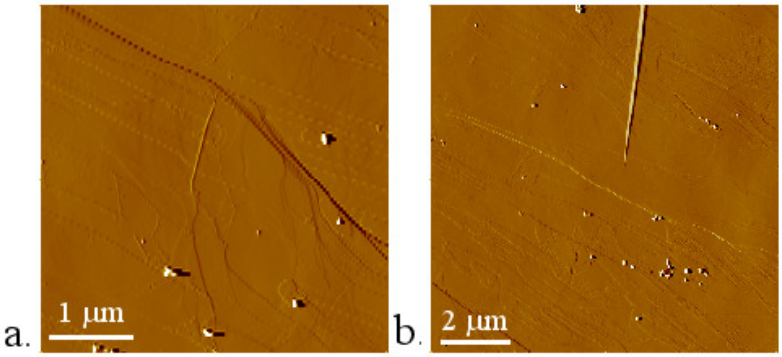

Figure 65: *Control experiment with Ag nanoparticles.* AFM image of $Mo_6S_{9-x}I_x$ nanowires mixed with Ag nanoparticle solution. Noticeable are the Ag nanoparticles concentrated in zones on the mica substrate. Even if the nanoparticles are positioned in the vicinity of the $Mo_6S_{9-x}I_x$ nanowires, no attachment can be seen.

Multiple connections to a single AuNP have also been observed: two or even three MWs attached to a single AuNP were present (Figure 66). The emerging connectivity protocol for self-assembly of larger circuits involves sequential connections of individual components with a yield y_i for each step i, and the maximum final yield approximately equal to the product of all the $Y=\Pi y_i$. The reaction temperature, the choice of the solvent, and the concentration appear as the main control parameters controlling the yield.

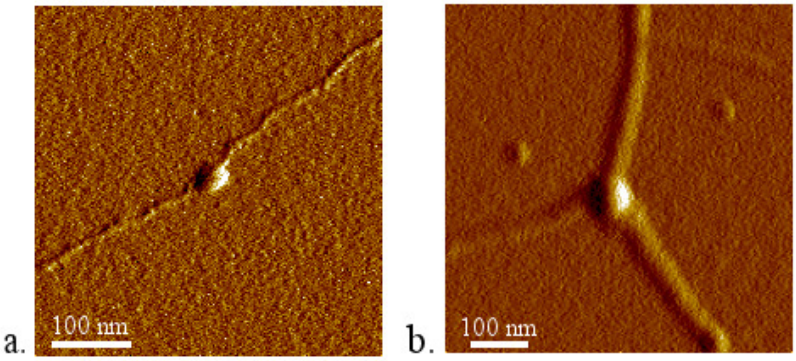

Figure 66: *AFM images of multiple connections to a single AuNP*. it can be seen two (a) or three (b) molecular wires attached to a single AuNP.

Further, in Figure 67a we show a large branched circuit containing a number of AuNP-MW connections. An enlarged image of three thin $Mo_6S_{9-x}I_x$ bundles connected to one AuNP is shown in Figure 67b. The angle between the bundles is 120±5°, and the diameters of the three connecting MWs are d = 1.2, 1.5, and 2 nm as shown in the profile measurements in Figure 67c.

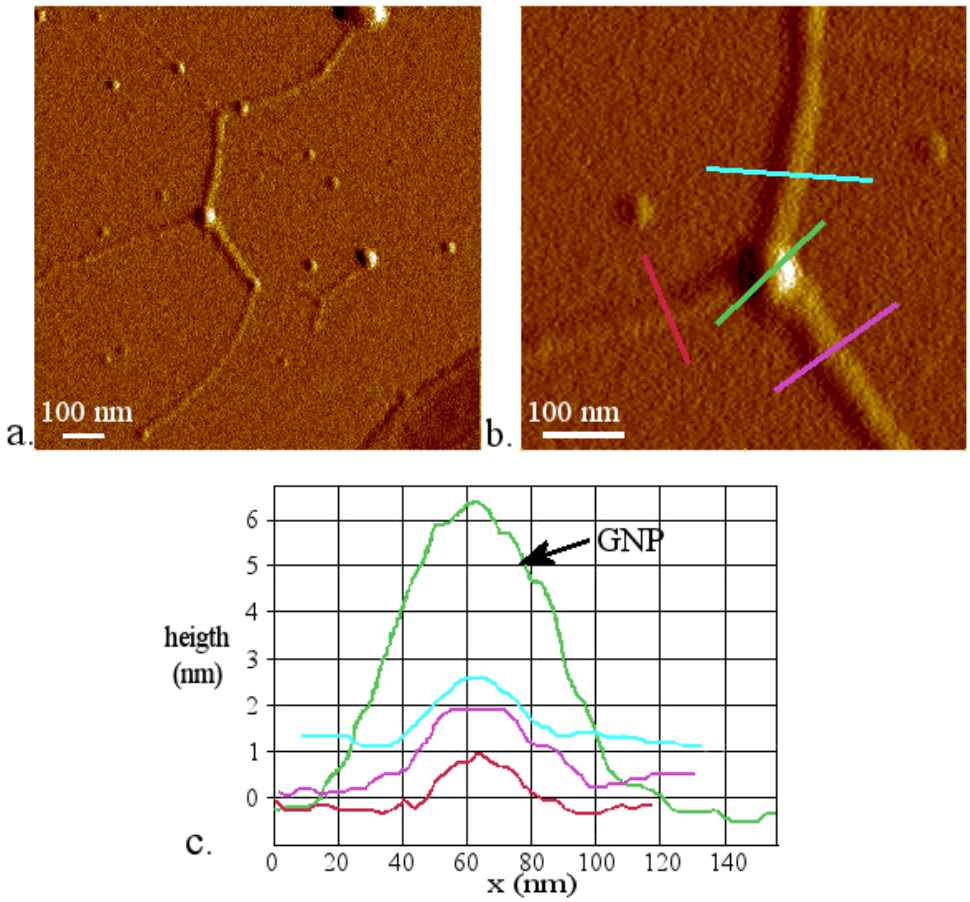

Figure 67: *AFM analysis of a multi-connector.* (a) AFM image of a large branch circuit containing couple of gold colloids; (b) a three-nanowire connection to only one gold particle together with the height profile of each component of the circuit (c).

As mentioned above, connections to gold surfaces may be expected to have more than one covalent bond per MW. The Au atoms on [111] AuNP faces are triangularly arranged, with Au-Au spacing of $d_{Au\text{-}Au}$ = 2.85 Å. $d_{Au\text{-}Au}$ is very close to the Mo-Mo distance $d_{Mo\text{-}Mo}$ = 2.68 Å of Mo atoms at the ends of MoSIx nanowire (Figure 68a). This suggests that the terminal S atoms on the MW ends may easily form three bonds between the Mo atoms in the MW and the Au atoms on the faces of the AuNPs [111] as shown schematically in Figure 68b.

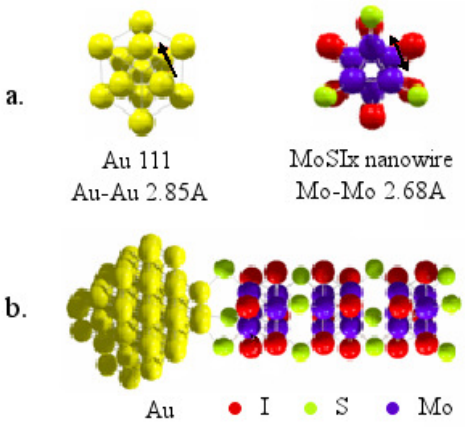

Figure 68: *Schematic of the attachment of $Mo_6S_{9-x}I_x$ nanowires with Au colloids.* (a) represents the atomic arrangements of $Mo_6S_{9-x}I_x$ nanowires and (111) AuNP indicating also the Au-Au and Mo-Mo atom distances while (b) is a schematic of the connection between the gold and the nanowire.

However, the intriguing question is the 120º angle in the three MWs attachment (Figure 69a). It is well known that the Au has a face centered cubic structure (Figure 69b). Truncating the corners of the cube one

can easily obtain a spherical shape close to that of the AuNPs (Figure 69 c and d). The triangular arrangement shown in Figure 69a can be obtained experimentally in two cases:

- projecting to the plane the normals of observed two planes of the type (111) and one plane of the type (100), and
- projecting to the plane the normals of three planes of the type (111).

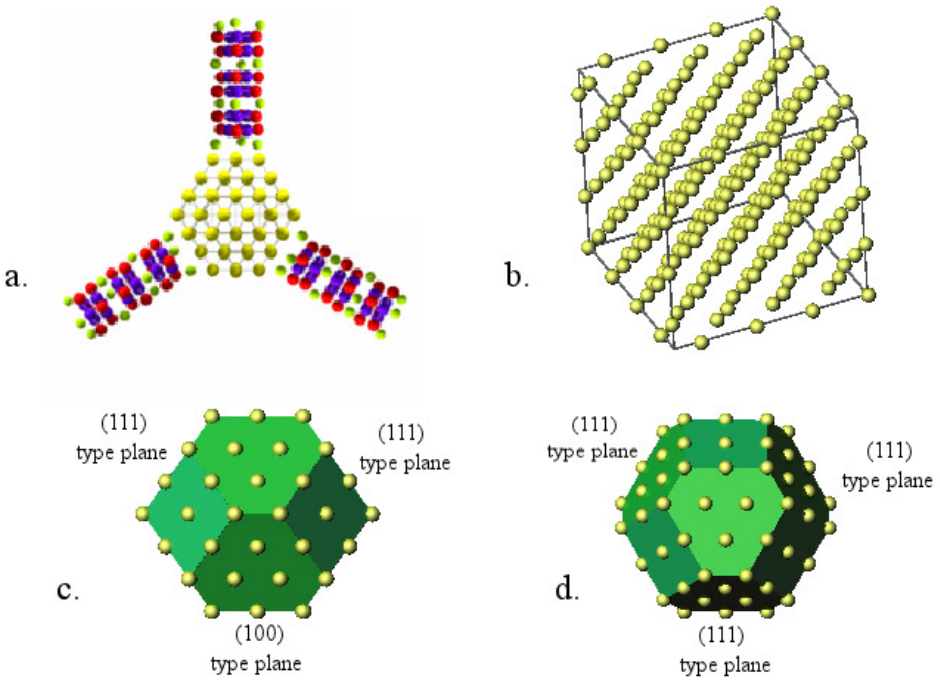

Figure 69: *Triangular arrangement of a three multi-connector.* Schematic of three MWs connected to one AuNP (a) and possible geometries of the bonding between the $Mo_6S_{9-x}I_x$ nanowires and the AuNP (b, c and d).

Larger circuits with five MWs and two AuNPs and the same 120° connectivity pattern have also been observed (such as in Figure 70), suggesting that a favored geometry involves regular AuNP structured nanoparticles.

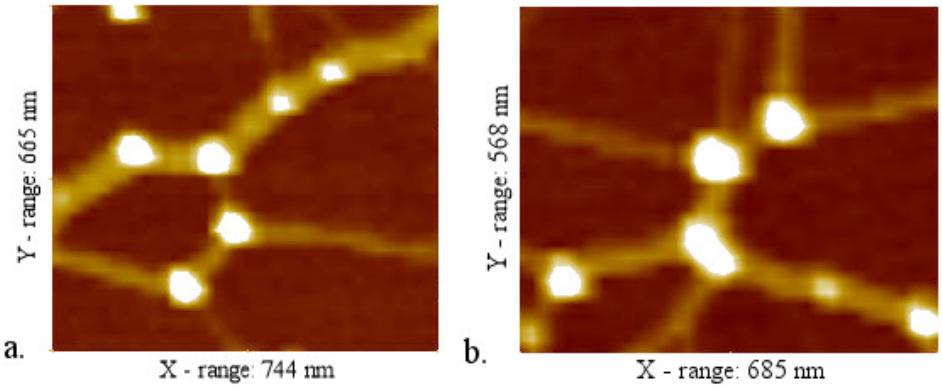

Figure 70: *AFM height image representing multi-terminal circuits with multiple MWs and GNPs.*

A statistical distribution of angles which have been observed is presented in Figure 71. We see that in the case of three MWs connected to a AuNP, the angle between them is centered around 120° and distributed between 100° and 145°. With two MWs connected to a AuNP, the angles are much more widely distributed, ranging from 80° to 180°, larger angles (>120°) occurring more often than the smaller ones (<120°).

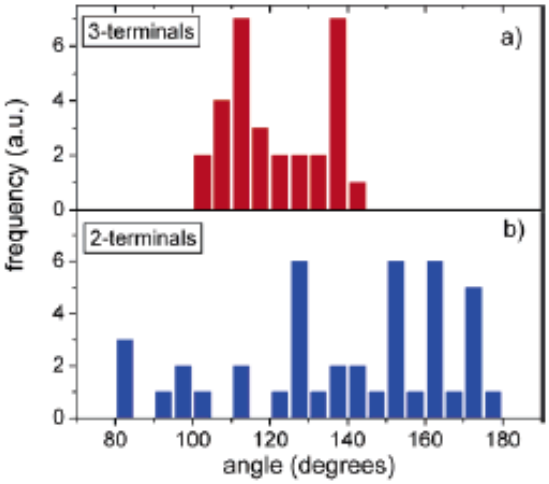

Figure 71: *Angle distribution.* Angle distribution for two terminal connections of $Mo_6S_{9-x}I_x$ nanowires and one AuNP (a) and for three terminal connections of MoSIx nanowires and one AuNP (b).

This affinity for easy functionalization with the gold particles is not shown by all the nanowires. We tried different kinds of stoichiometries of $Mo_6S_{9-x}I_x$ nanowires and some of them were more successful than others (very much depending on the element present in the linking planes). So far, $Mo_6S_3I_6$ and MoS_xI_y nanowires exhibited successful functionalization.

The success of gold attachment to the $Mo_6S_{9-x}I_x$ nanowires brings our attention to the field of biological applications. The next step was to attempt to functionalize proteins with the gold particle already attached to the $Mo_6S_{9-x}I_x$ nanowires. We used thyroglobulin, an iodinated and sulfonated dimeric protein with a high molecular mass (660 kDa) and the major soluble protein of the thyroid gland. Thyroglobulin is stored in the lumen of the thyroid follicles as soluble dimers, tetramers and insoluble multimers, formed through formation of disulfide and dityrosine bonds. This protein can be easily functionalized with Au particles due to its thiol groups. The sample was prepared in one step mixing the dispersed $Mo_6S_{9-x}I_x$ nanowires into water (to ensure the natural environment of the proteins) with the AuNPs and the thyroglobulin. The solution was left to react for three days in a refrigerator, since the proteins at room temperature tend to aggregate. A droplet from the sample was dried on a mica substrate for the investigation with the AFM. To our surprise, the protein was attached directly to the $Mo_6S_{9-x}I_x$ nanowire followed by the gold particle, and not reversed as expected (Figure 72).

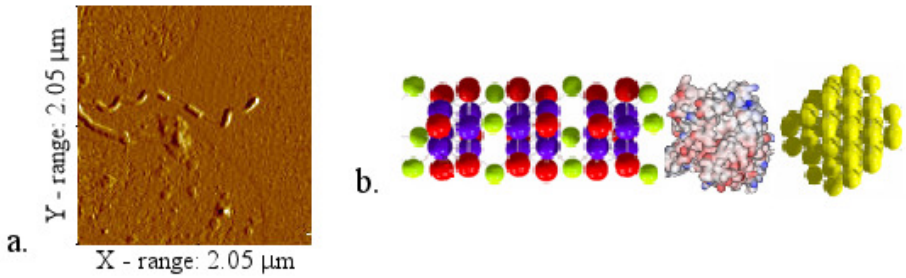

Figure 72: *$Mo_6S_{9-x}I_x$-protein-gold attachment.* AFM image of the system $Mo_6S_{9-x}I_x$ nanowire-protein-gold particle (a); schematic of $Mo_6S_{9-x}I_x$ functionalized with the protein followed by a gold particle (b).

The cross section analysis (Figure 73) confirmed that the protein, which has a diameter ~2 nm, was attached to the 5 nm gold particle. The blue line in the Figure 73 depicts the cross section shown in the Figure 73 b. One possibility of the height cross section interpretation can suggest, from left to right, the zero at the substrate surface followed by a step of ~4 nm corresponding to the nanowire, continuing with a lower step of ~ 2nm attributed to the protein and in the end a step of ~ 7 nm indicating the protein-gold attachment.

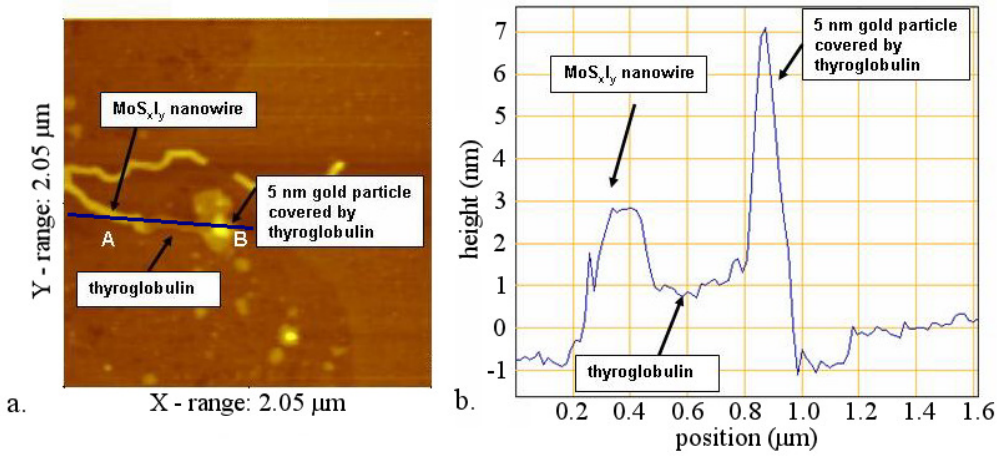

Figure 73: *AFM analysis of the nanowire-protein-gold system.* AFM image of the thyroglobulin protein attached to $Mo_6S_{9-x}I_x$ nanowire and gold nanoparticle in the same time (a); cross section measurement of the protein, wire and the AuNP covered with the protein (b).

6.3 Conclusions

We have demonstrated two possible routes for the construction of larger functional circuits using $Mo_6S_{9-x}I_x$ MWs: through AuNPs and by direct connection to thiolated biomolecules. The two approaches may lead to different possible applications. The use of AuNPs offers the possibility of branching and construction of larger circuits. It is known that AuNPs are protected by a negative shell of citrates so as not to form aggregations. The success of attaching the gold colloids to the nanowires despite the negative surrounding is due to the formation of a covalent bond between Au and S. The control experiments made with AgNPs showed no attachment, which is consistent with our Au-S bond explanation. The repulsion force between the Ag colloids surrounded by the negative shell and the negatively charged nanowires could not be overcome in order to form a stable connection. The distance between Au-Au atoms, being approximately equal to the one between the Mo-Mo atoms, facilitates the bonding with the bridging S atoms present in the structure of the nanowire in geometry close to the one that occurs within the nanowire itself. Moreover, owing to the triangular arrangement of the AuNP clusters, different possible geometries of the bonding between $Mo_6S_{9-x}I_x$ nanowires and AuNPs have been obtained. Connections between two, three or even more nanowires with one, two or more AuNPs have been observed. The angle distribution between the connected nanowires through the AuNPs for terminals with three connectors was shown to be centered at around 120^0 and distributed between 100^0 and 145^0, while for a terminal with two connectors the angles ranged from 80^0 to 180^0.

On the other hand, we have obtained directly connected functional biomolecules as well, which might be used for sensor applications. From the bare mixture of the nanowires, AuNPs and thyroglobulin, a direct connection wire-protein has been obtained with the gold colloid attached to the protein. The sulfur richness of the thyroglobulin surface facilitated a rapid attachment to the nanowires, while the AuNP attached directly to the protein. All the $Mo_6S_{9-x}I_x$ nanowire connections shown here appear to be inherently stable in air and compatible with Si-based technology.

7 Functionalization of $Mo_6S_{9-x}I_x$ nanowires with thyroglobulin protein

Nanowires, nanotubes and nanocrystals have been established as smart building blocks for the development of nanometer-sized electronics and sensing devices. Because of their very high aspect ratio, high electronic conductivity and small size, they offer a series of advantages. However, is still a challenge to devise ways in which appropriate molecular recognition elements can be incorporated. Consequently, nanowires modified with different proteins or oligonucleotides have evoked a great deal of interest.

7.1 A historical overview of bio-functionalization of nanotubes and nanowires

The nano-dimensions, electronic properties, remarkable tensile strength, flexibility and the physico-chemical properties of carbon nanotubes make them an ideal candidate for chemical and biochemical sensing and for nanotechnological applications. A big disadvantage of CNTs is unfortunately their lack of solubility. Thus, numerous attempts have been made for the functionalization of the nanotubes to find a solution for dissolving them in different solvents. For instance, Tanaka et al. (1992) described a method for dissolving SWCNT (single-walled carbon nanotubes) in organic solutions by derivatization with thionyl chloride and octadecyl amine. This approach has opened the way for solution phase chemistry to be carried out on CNTs for the integration of these materials in biological systems. Functionalized carbon nanotubes with proteins (Huang et al., 2002), oligonucleotides (Nguyen et al., 2002; Baker et al., 2002; Hazani et al., 2003; Dwyer et al., 2002), peptides (Pantarotto et al., 2003), etc. have all been successfully reported.

Covalent functionalization of CNTs

DNA molecules offer a great potential as building blocks with all the basic properties necessary for the assembly of nanoscale electronic devices. Linking DNA strands to the nanotubes requires specially prepared DNA strands. Various methods of DNA surface capturing include chemical adsorption, covalent binding, electrostatic attraction, copolymerization and the avidin–biotin affinity system. Hu et al. (2005) functionalized CNTs with molecules containing the thiol group and halogen. The chemical methods for the covalent functionalization of CNTs involve direct fluorination, organic free radical addition, fluorine displacement in fluoro nanotubes producing amino, hydroxyl and carboxyl group terminated derivatives.

Huang et al. (2002) reported that BSA (bovine serum albumin) proteins can be covalently attached to carbon nanotubes via diimide-activated amidation under ambient conditions as can be seen in Figure 74. They observed that the protein sample is colorless in an aqueous buffer solution but, when mixed with the carbon nanotubes, the sample turned dark-colored upon functionalization. For more quantitative measurements the sample was analyzed with an AFM (atomic force microscope). The images suggest that the proteins are immobilized on the walls of the nanotubes.

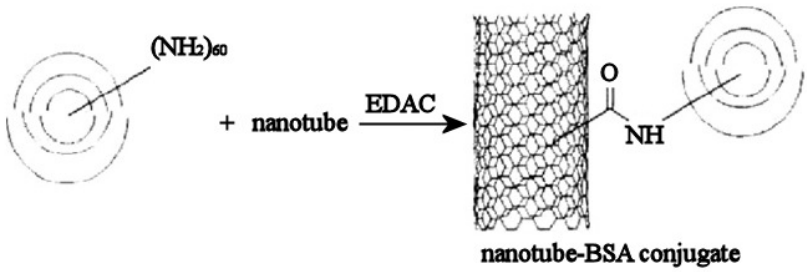

Figure 74: *Covalent functionalization of a carbon nanotube via diimide activated amidation (Huang et al., 2002).*

In time it has been shown that the universal methods for connecting biomolecules to CNTs is diimide-activated amidation by direct coupling of carboxylic acid to proteins as a coupling agent (Jiang et al.,

2004).

Both van der Waals and hydrophobic forces were found to be important for the study of the DNA-CNT interaction (Ito et al., 2003). A simulation performed by Gao et al. (2003) has shown that DNA molecules could be spontaneously inserted into carbon nanotubes (see Figure 75). These mini devices are opening the door to interesting applications and can play an important role in molecular electronics, molecular sensors, electronic DNA and nanotechnology of gene delivery systems.

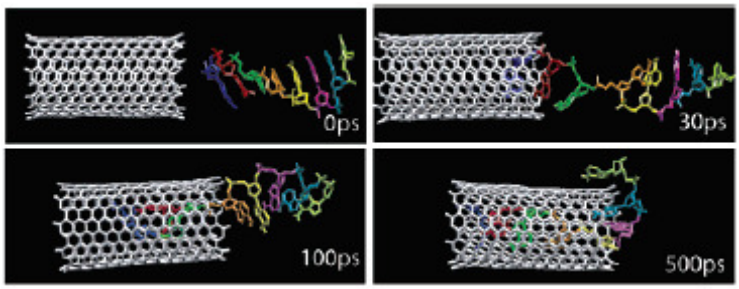

Figure 75: *Simulation of DNA entering a SWCNT (Gaoet et al., 2003).*

Reliable detection of small amounts of DNA/RNA has become of great interest for molecular diagnosis. Electrochemical (EC) techniques have shown great potential in providing solutions to create modern instrumentation for genetic analysis (Kuhr, 2000). For instance, Li et al. (2003) integrated carbon nanotube arrays into electrochemical systems for ultrasensitive chemical and DNA detection. Functionalized nanotube ends with primary amine-terminated oligonucleotide probes were submitted to Ru(bpy)-mediated guanine oxidation method (Sistare et al., 1999). As a result, hybridization of less than a few atom moles of oligonucleotide targets can be easily detected.

The use of enzyme labels to generate electric signals has been extremely useful for ultrasensitive electrochemical bioaffinity assays of proteins and DNA (Caruana and Heller, 1999; Zhang et al., 2003). For instance, Wang et al. (2004) demonstrated the use of carbon nanotubes for dramatic amplification of enzyme-based bioaffinity electrical sensing. The CNT-based amplifiers, loaded with alkaline phosphates enzyme tags, lead to a highly sensitive detection of proteins and DNA. This type of CNT-derived amplification bioassay is expected to open new opportunities for medical diagnostics and protein analysis.

The covalent modification of nanotube tips enables the straightforward creation of well-defined probes sensitive to specific intermolecular interactions that define the properties of many chemical and biological systems. It is believed that functionalized nanotube tips will prove especially useful for imaging self-assembled polymeric and biological materials. For instance Wong et al. (1998) studied the ligand-receptor interaction of biotin-streptavidin using covalently modified carbon nanotubes. Biotin was covalently linked to the nanotube and force-displacement measurements were performed on streptavidin immobilized on a mica surface. The functionalized nanotube tips usually show only single binding events of 200 pN as can be seen in Figure 76.

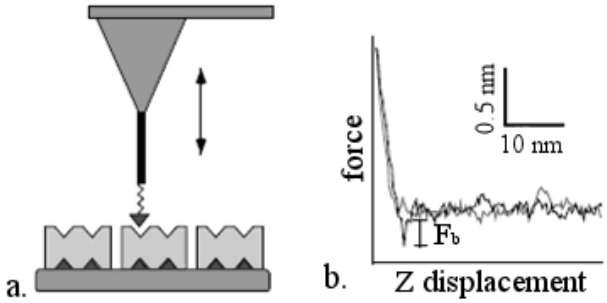

Figure 76: *Covalently functionalized nanotubes with biotin as biological probe.* (a) Schematic of modified carbon nanotubes with biotin interacting with streptavidin protein immobilized on a mica substrate; and (b) force-displacement curve showing the binding force of approximately 200 pN (Wong et al., 1998).

Functionalization of carbon nanotubes with biomolecules was also used for the self-assembly of carbon nanotubes into functional devices and circuits. Keren et al. (2003) used DNA biological recognition for the self-assembly of carbon nanotube-based electronics. Figure 77a shows an atomic force microscope of the DNA/SWCNT assembly. The white arrow indicates the streptavidin-coated SWCNT bound to a RecA-coated 500-base-long ssDNA localized at the homologous site in the middle of a scaffold λ-DNA molecule.

The obtained assembly was connected via e-beam lithography to electrodes and electrical measurements under ambient conditions were performed (Figure 77b).

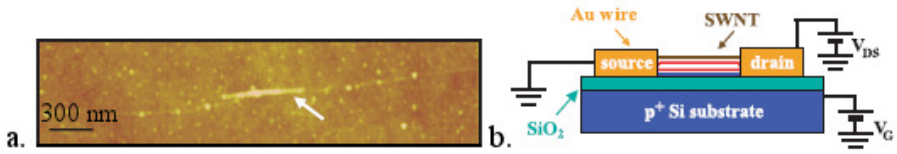

Figure 77: *Carbon nanotube-based electronics.* (a) Atomic force microscope image of a conductive SWCNT coated with streptavidin and connected at both ends to a λ-DNA scaffold (Keren et al., 2003); and (b) schematic representation of the electrical measurements circuit (Keren et al., 2003).

Carbon nanotube field effect transistors (CNTFETs) incorporating biotin-functionalized nanotubes have been successfully used for the sensing of streptavidin (Star et al., 2003). The carbon nanotubes were covered with a polymer coating that has hydrophilic properties on which biotin can be covalently attached (Figure 78). Upon electrical measurements a significant change can be seen as the streptavidin binds to the biotin-functionalized carbon nanotube.

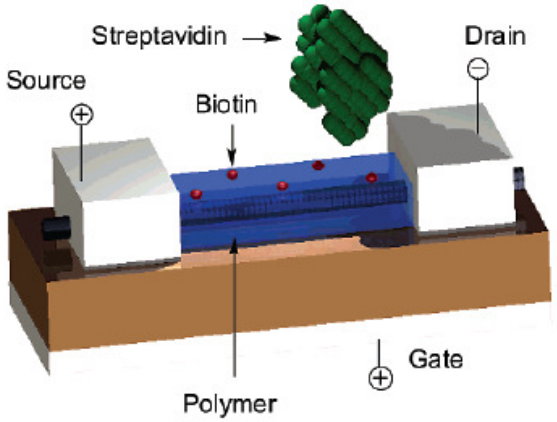

Figure 78: *CNTFET with biotin functionalized SWCNT for the sensing of streptavidin (Star et al., 2003).*

Noncovalent functionalization of CNT

Another way to functionalize carbon nanotubes is by noncovalent binding. This method is of particular interest because it allows carbon nanotubes to preserve their sp^2 structure and thus their electronic characteristics. The noncovalent interaction is based on van der Waals forces or π-π stacking and it is controlled by thermodynamics. Multi-walled carbon nanotubes covered by DNA (Guo et al., 1998), supramolecular conjugates of nanotubes covered by DNA, and DNA molecules inserted endohedrally into nanotubes (Okada et al.,2006) are some examples of noncovalently bonded composites.

Azamian et al. (2002) have shown that it is possible to adsorb a variety of metalloproteins and enzymes on oxidized, purified and vacuum-annealed single-walled carbon nanotubes in aqueous solution (Figure 79). They conducted experiments in the presence and in the absence of a coupling reagent (EDC) to prove that the bond between the nanotubes and the proteins is noncovalent.

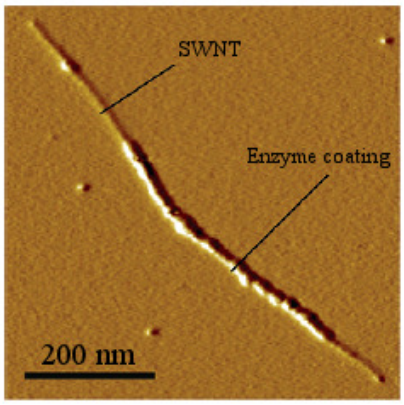

Figure 79: *AFM image of a protein-modified SWCNT taken by Azamian et al. (2002).*

A simple method for noncovalent functionalization of nanotubes has been proposed also by Chen et al. (2001). Their method involves a bifunctional molecule, 1-pyrenebutanoic acid and succinimidyl ester (Prakash et al., 2006). Successful attachment of both ferritin and streptavidin onto SWCNTs was observed under a transmission electron microscope (Figure 80). This method may offer the means of obtaining stable suspensions of functionalized SWNTs in solutions and introduce the possibility of self-assembly of nanotubes with unperturbed sp^2 structures and electronic properties.

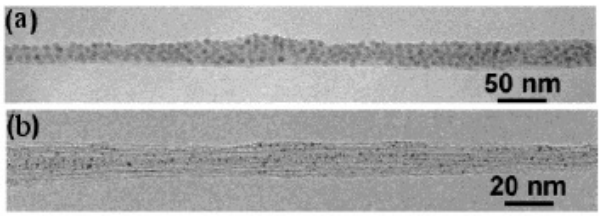

Figure 80: *TEM image of functionalized SWCNT with ferritin (a) and streptavidin (b) (Chen et al., 2001).*

If initially research was concentrated on functionalizing CNTs with small biomolecules (~60 kDa), to be of particular importance in biomedical nanotechnology it has shifted to larger proteins (~150 kDa). In a recent study, Teker et al. (2006) used functionalized carbon nanotubes with antibodies (Figure 81) for detecting overexpressed cell surface receptors in breast cancer cells and for drug delivery. Electronic transport properties of carbon nanotubes have shown a decrease in conductance upon adsorption of antibodies on the surface of the nanotubes.

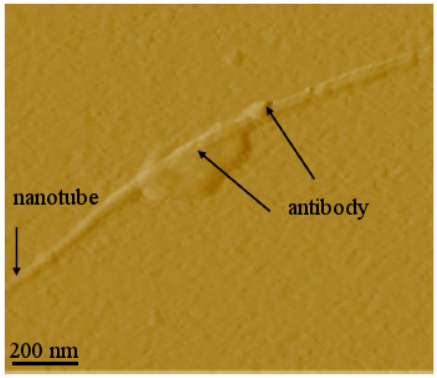

Figure 81: *AFM image of CNT functionalized with antibodies (Teker et al., 2006).*

The solubility of carbon nanotubes in polymers in aqueous solutions has been studied for years using adsorption of surfactants. Recent studies have shown that the solubility of carbon nanotubes can be drastically improved also through functionalization with biomolecules such as single-stranded DNA (Zheng et al., 2003), polysaccharides (Numata et al., 2005), peptides (Ortiz et al., 2005), etc. For instance, Karajanagi et al. (2006) used a number of proteins of different sizes and structures for the solubility of HiPco SWNTs in water. Characterization methods such as UV-Vis spectroscopy, Raman spectroscopy and atomic force microscopy were used for the analysis of solutions. High dispersability and debundling of

SWCNTs was obtained by Nepal and Geckeler (2006) as well, but this time using lysozyme. By merely changing the pH value it was observed that the nanotubes can be highly dispersed or can form aggregates. This result has great potential in the design of solution-based optical pH sensors.

The immobilization of streptavidin on CNTs has been reported as the key approach for the controlled deposition of carbon wires on specific surfaces. To prevent the nonspecific adsorption of streptavidin, CNTs have been decorated noncovalently by a surfactant/polymer mixture. Scientists have shown that specific binding of the protein can be achieved by cofunctionalization of the CNTs with biotin, a molecule which exhibits extremely high affinity to streptavidin.

Concerning biosensor technology, glucose oxidase, an enzyme which catalyzes the oxidation of glucose, has been immobilized onto the surface of CNTs (Wang et al., 2003; Tang et al., 2004) and was extensively used in clinical tests. The nanotube-enzyme conjugate was integrated on a carbon electrode for voltammetric detection of glucose, resulting in an increase of the catalytic response of more than 10 times due to the presence of conducting CNT. Other examples of such electrochemical biosensors concern the hemoglobin system (Cai and Chen, 2004; Zhao et al., 2003) for hydrogen peroxide detection, the myoglobin composite for nitric oxide (Zhao et al., 2003; Zhang et al., 2005) or hydrogen peroxide (Zhao et al., 2004) detection, the hemin conjugate for oxygen gas sensing (Ye et al., 2004), the microperoxidase-11 system for oxygen reduction (Liu et al., 2005), the cholesterol esterase system for blood analysis (Li et al., 2005) and the horseradish peroxides system for hydrogen peroxide reduction (Zhao et al., 2002).

Functionalization of other nanowire types with biomolecules

Carbon nanotubes are not the only promising materials for the functionalization with biomolecules for applications in bionanotechnology. Searson's group (Salem et al., 2004) used biotin-avidin to direct the end-to-end assembly of Au/Pt/Au multisegment nanowires. The biotin/avidin linkage is one of the strongest known biological interactions and has been used for the assembly of single-component gold nanoparticles (Mann et al., 2000; Salem et al., 2003) and nanorods (Caswell et al., 2003). Searson has shown that by changing the length of the gold segment the number of nanowires connected at each node can be controlled.

Another method for the assemblies of superstructures is the use of antigen-antibody interactions. Wang et al. (2005) demonstrated that by using this method aqueous CdTe nanowires can be assembled into crossbar and end-to-side connections. Studies performed with the help of a conductive AFM demonstrated that the junction points between the NW are nonconducting, thus impeding the charge transport between the wires.

An interesting material due to its high environmental stability, electronic conductivity, ion exchange capacity, and biocompatibility is polypyrrole (Ppy). These properties have made Ppy a popular constituent of planar electrochemical biosensors. Hernandez et al. (2004) used functionalized Au/Ppy/Au nanowires loaded with avidin and streptavidin proteins (see Figure 82) for the development of nanoscale biosensors and assemblies.

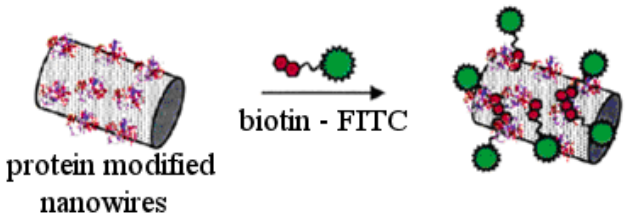

Figure 82: *Schematic of the functionalization process of Au/Ppy/Au nanowires with biotin protein.*

Boron-doped silicon nanowires (SiNW) field effect transistors were modified into biomolecular nanosensors (Cui et al., 2001; Patolsky et al., 2004). Functionalizing SiNWs with biotin, the ligand-receptor binding of biotin-streptavidin was studied through electrical measurements. An increase was observed in the conductance of biotin-modified SiNW to a constant value upon addition of streptavidin. The concept of using NW FETs modified with receptors or ligands for specific detection can be developed in many directions. Using also Si nanowires, Hahm and Lieber (2004) succeeded in real-time detection of DNA and DNA mismatches. They have shown that Si nanowire sensors functionalized with peptide nucleic acid (PNA) receptors can distinguish between wild type and mutant oligonucleotide sequences. Taking these results into consideration, it should be possible to extend this approach to the detection of other

genetic markers of diseases.

Another interesting type of nanowire structure that could be a good candidate for the manufacturing of future generation nanobiosensors are the metal oxide nanowires such as In_2O_3 nanowires (Curreli et al., 2005; Tang et al., 2005) or ZnO (Kim et al., 2006). Li et al. (2005) proposed a complementary detection system of prostate specific antigen (PSA) based on n-type In_2O_3 nanowires and SWNT (PSA is an oncological marker for the presence of prostate cancer). For this, Li first covalently attached antibodies to the nanowire surface via a succinimidyl linking molecule and then combined the In_2O_3 nanowires with SWCNTs for the detection of PSA, which revealed complementary electrical response upon PSA binding (Figure 83).

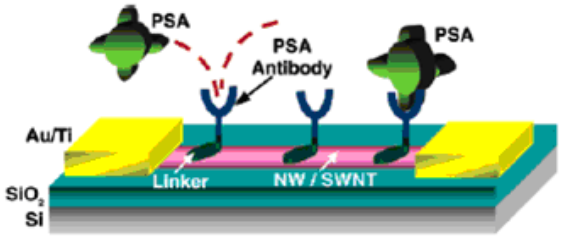

Figure 83: *Schematic of the detection device of In_2O_3 nanowire/SWCNT (Li et al., 2005).*

7.2 AFM force measurements: theoretical and experimental considerations

The number of applications for AFM has increased since its invention in 1986 to the point where it has been adopted in many fields of nanoscience and nanobiotechnology. It provides the ability to view and understand events as they occur at the molecular level, which increases our understanding of how systems work and leads to new discoveries in a wide range of fields including life science, materials science, electrochemistry, polymer science, biophysics, nanotechnology, and biotechnology.

We have described above that the self-assembly approach is a straightforward method for manufacturing nanodevices for bionano- or nanotechnological applications. Understanding how molecular recognition works or investigating the electrical, mechanical and chemical properties of nanowires and the contact connecting two different entities for developing molecular electronic devices is therefore of immense interest. The development of the atomic force microscope (AFM) has opened new perspectives for the investigation of surfaces at high lateral and vertical resolution. The AFM has several properties that make it an ideal tool for measuring intermolecular forces: theoretical force sensitivity in the order of 10^{-14} N, displacement sensitivity of 0.01 nm, contact areas as small as 10 nm^2, and the ability to operate under physiological conditions.

Force-distance curves have been employed for the study of numerous material properties and for the characterization of all known types of surface forces. AFM force-distance curves are routinely used in several kinds of measurement, for the determination of elasticity, Hamaker constant, surface charge densities, and degrees of hydrophobicity. The essential part of the AFM is the cantilever which contains the tip (see more details about AFMs in Chapter 2). While the tip is scanning the sample, the cantilever deflects upon encountering differences in the surface height. Focusing a laser beam on the back side of the cantilever upon its deflection, the laser is reflected and detected by means of a position sensor. The deflection of the cantilever is detected from the reflection of the laser, focused on the end of the cantilever and reflected on a photodiodes.

The first reports of attempts to interpret force-distance curves and related information appeared in 1989-1990. The force-distance curves were divided into four regions (Figure 84): the non-contact line, where the tip is far from the sample and thus no interaction is detected (region I); next, the tip is closely approaching the surface until it is jumping-to-contact due to van der Waals forces (region II); after contact and by approaching the tip closer to the surface, a positive deflection of the cantilever arises due to repulsive forces. This is the contact region of the force curve (region III), where elastic properties of the sample can be measured; finally, throughout the withdrawing process the cantilever follows the approaching behavior as it returns, but due to the adhesion forces between the tip and the sample it starts to deflect negatively until the contact breaks (region IV).

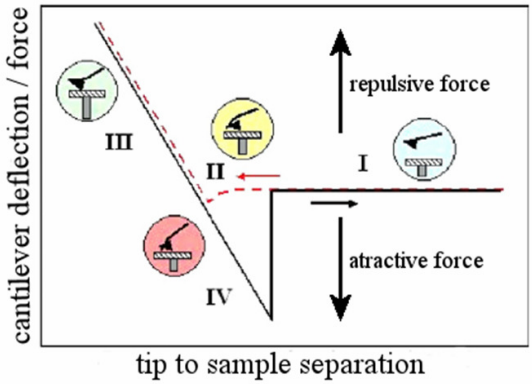

Figure 84: *Typical force-distance curve showing the different regions of the approaching and withdrawing processes of the tip to and from the surface.*

Theoretical considerations

Over time, several theories have described the tip-sample interaction. At the beginning, both the tip and the sample were considered to be continuous elastic media. Differences in the relations between the applied force F and the contact radius a or the deformation δ (see Figure 85) were found to be caused by the adhesion. The most developed theories that studied these differences were proposed by Hertz (Hertz, 1882), DMT (Dejaguin-Muller-Toporov) (Johnson et al., 1971), and JKR (Johnson-Kendall-Roberts) (Derjaguin et al., 1975 and 1983).

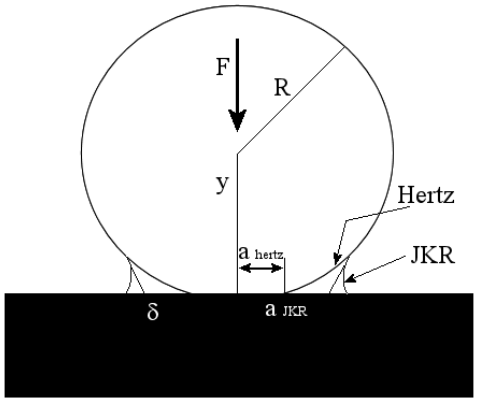

Figure 85: *The interactions between an elastic sphere and a flat surface.* F is the loading force, R the radius of the sphere, y the distance from the center of the contact area, δ the penetration depth, a_{Hertz} and a_{JKR} are the contact radius following the Hertz and JKR theories.

The Hertz model does not take into account the adhesion of the sample while the other two theories can be applied in the case of small tips and stiff samples (DMT) or large tips and soft samples (JKR). In the Hertz theory, the adhesion force is much smaller than the maximum load, whereas in the other two theories, the thermodynamic (Dupre) work of adhesion W can be calculated from the jump-to-contact region if the radius R of the tip is known. Furthermore, the contact area can be calculated as a function of Young's modulus E while the deformation of the sample can be measured from the contact regime. For a better view of all the parameters, Table 3 presents the relations between a, δ and the adhesion force for all three theories.

Table 3 *Summary of the equation of contact radius a, deformation of the sample δ and adhesion force F_{adh} calculated from the three commonly used theories which explain tip-sample interaction, W is the adhesion work per unit area, E_{tot} is reduced Young's modulus, F is the force exerted by the tip on the surface.*

	Hertz	DMT	JKR
a	$\sqrt[3]{\frac{RF}{E_{tot}}}$	$\sqrt[3]{\frac{R}{E_{tot}}\left(F+2\pi RW\right)}$	$\sqrt[3]{\frac{R}{E_{tot}}\left(F+3\pi RW+\sqrt{6\pi RWF+\left(3\pi RW\right)^2}\right)}$
δ	$\frac{a^2}{R}=\left(\frac{F^2}{RE_{tot}^2}\right)^{1/3}$	$\frac{a^2}{R}=\frac{\left(F+2\pi RW\right)^{2/3}}{\sqrt[3]{RE_{tot}^2}}$	$\frac{a^2}{R}-\frac{2}{3}\sqrt{\frac{6\pi Wa}{E_{tot}}}$
F_{adh}	0	$2\pi RW$	$\frac{3\pi RW}{2}$

Later, in 1992, Maugis et al., following the Dugdale model (Dugdale, 1960), proposed that adhesion be considered as a constant additional stress present around the contact area. Moreover, he proposed that all the material properties be described by the dimensionless parameter λ:

$$\lambda=\frac{2.06}{z_0}\sqrt[3]{\frac{RW^2}{\pi K^2}} \tag{30}$$

where z_0 is a typical atomic diameter., Following Maugis' theory, one can observe a continuous transition from the DMT theory to the JKR theory. Nowadays, this theory is the only general theory fully describing the elastic deformation of the samples.

However, in all the above theories, the shape of the tip was considered to be spherical. In contrast, Sneddon et al. (1965) developed another theory which takes into consideration a punch as a tip and describes the force-distance relationship as a power law:

$$F=\alpha\delta^n \tag{31}$$

where, α and n are constant, with n being 1 for a flat cylinder, 2 for cones and 1.5 for spheres and paraboloids.

When talking about soft samples, e.g. biomolecules, polymers, etc., plastic deformations might take place, thus the before mentioned theories do not apply to this type of tip-sample interaction. In the presence of plastic deformations, the approaching and withdrawing curves present a hysteresis. It is seen that upon retraction of the tip, the sample does not regain its shape. As a result, the AFM is employed as an indenter in such experiments, and force-displacement curves are not of primary interest. The measurements are focused on the results of a given indentation, i.e. on the shape of the indented hole and not on the dependence of the deformation on the load. A review of this experiment was published recently by van Landingham et al. (2001).

Experimentally, Burnham and Colton (1989) were the first to deal with the elasto-plastic properties of the materials using the AFM. In view of Hertzian theory, a good agreement with the experiments was obtained for Young's modulus of an elastometer, HOPG (highly ordered pyrolytic graphite) and gold. Radmacher et al. (1994), on the other hand, measured the indentation of Si_3N_4 tip on a lysozyme adsorbed on a mica substrate. He also found a good agreement between the experimental results and Hertzian theory. Moreover, he showed that through the acquisition of force-distance curves one can distinguish between two materials, e.g. between lysozyme and mica surface (Figure 86).

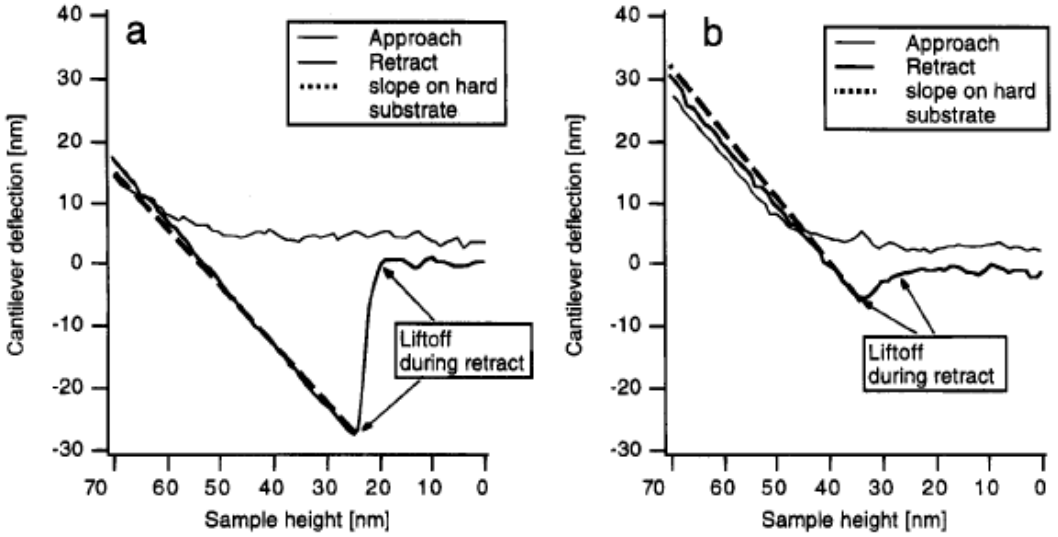

Figure 86: *Force spectroscopy on mica substrate (a) and on lysozyme aggregate (b) taken by Radmacher et al. 1994.*

In the case of polymers, for the determination of the elastic properties the Hertz model is usually employed (Matzelle et al., 2003; Mermut et al., 2003) due to the low adhesion, but in some cases JKR (Lubarsky et al., 2004) and Maugis theory (Sun et al., 2004) can also offer good results. For thin deformable films the effect of the surface cannot be neglected (Dimitriadis et al., 2002, Shulha et al., 2004). Consequently, indentation is limited to depths much less than the total thickness of the sample in order to eliminate substrate influence.

More information about the attractive forces between the tip and the sample can be extracted from jump-to-contact as well as from jump-off-contact events. In order to evaluate these attraction forces one must know the force law and the shape of the tip. The jump-to-contact regime can be predicted by either JKR or Maugis theories. In AFM measurements, the jump-to-contact instability is governed by the stiffness of the cantilever relative to the long-range tip-sample forces. Pethica and Sutton (1988) have shown that there is a minimum separation of approximately 1-2 Å below which the jump-to-contact is present regardless of the rigidity of the tip. This instability is due to the fact that at some small enough separation, the gradient of the surface forces exceeds the gradient of the elastic restoring force of the cantilever. In the case of the jump-off-contact regime, features of the force-distance curves are related to the sample surface energies, e.g. material stiffness and adhesion, all well explained by the Maugis theory.

Measurements of forces

As previously mentioned, the interaction between the tip and the sample arises from one or more forces acting between them (Figure 87). For a simplified approach between two hard surfaces in the absence of any long range interactions, van der Waals forces will dominate. These forces appear in the approaching process as a downward deflection just prior to contact. The van der Waals forces between atoms/molecules are the sum of three different forces, all proportional with $1/r^6$, where r is the distance between the atoms or molecules. The three forces are: the orientation or Keesom force, the induction or Debye force and the dispersion or London force.

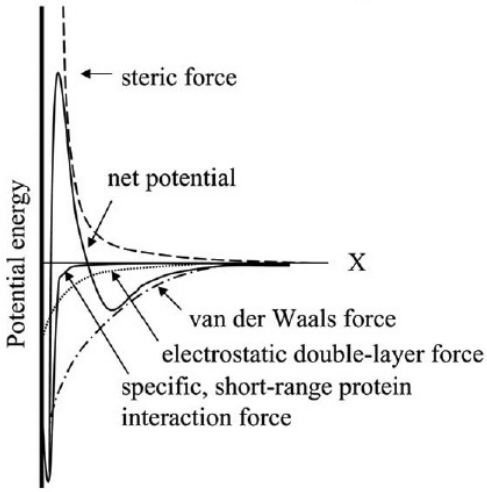

Figure 87: *Different possible interactions between the tip and the surface.*

The Keesom force originates from the angle-averaged dipole-dipole interaction and is written as:

$$w_K(r) = -\frac{u_1^2 u_2^2}{3(4\pi\varepsilon_0\varepsilon)^2 k_B T r^6} = -\frac{C_K}{r_6} \tag{32}$$

where u_1 and u_2 are the dipole moments of the molecules, ε the dielectric constant of the medium, k_B Boltzmann's constant and T the temperature.

The Debye force is the angle-averaged dipole-induced dipole interaction, between two atoms or molecules:

$$w_D(r) = -\frac{u_1^2 \alpha_{02} + u_2^2 \alpha_{01}}{(4\pi\varepsilon_0\varepsilon)^2 r^6} = -\frac{C_D}{r^6} \tag{33}$$

where α_{01} and α_{02} are the electronic polarizabilities of the molecules.

The dispersion force has the highest contribution to van der Waals forces. It acts between all atoms/molecules (a distance ranging from 2 Å up to 10 nm). It is the dipole-induced dipole interaction and is of quantum-mechanical origin:

$$w_L(r) = -\frac{3}{2}\frac{\alpha_{01}\alpha_{02}}{(4\pi\varepsilon_0)^2 r^6}\frac{(h\nu_1)(h\nu_2)}{h\nu_1 + h\nu_2} = -\frac{C_D}{r^6} \tag{34}$$

where $h\nu_1$ and $h\nu_2$ are the first ionization potentials of the molecules and h is Planck's constant. The Keesom and Debye forces are acting between polar molecules while the dispersion contribution acts between every molecule.

However, for molecules of dielectric constants ε_1 and ε_2 in a medium of dielectric constant ε_3 and using Clausius-Mossotti expression (Equation 35) McLachland et al. obtained different expressions for the van der Waals forces:

$$\alpha_{ecs}(\nu) = 4\pi\varepsilon_0\varepsilon_3(\nu)\frac{\varepsilon_1(\nu) - \varepsilon_3(\nu)}{\varepsilon_1(\nu) + 2\varepsilon_3(\nu)} R_m^3 \tag{35}$$

where α_{ecs} is the excess polarizability and R_m is the molecule radius. A more general introduction regarding van der Waals forces is given in Israelachvili et al. (1992).

In order to model the interaction which takes place in the AFM, it is necessary to consider macroscopic bodies. Thus, in the case of two interacting spheres of radii R_1 and R_2 at the distance D (Figure 88), the

force $F(D)$ can be obtained by integrating over small circular sections of surface $2\pi x dx$ on both spheres (Israelachvili 1992):

$$F(D) = \int_{D}^{x} 2\pi x f(Z) dx \tag{36}$$

where $f(Z)$ is the normal force per unit area. From Chord theorem $x^2 \sim 2R_1 z_1 = 2R_2 z_2$ and

$$Z = D + z_1 + z_2 = D + \frac{x^2}{2}\left(\frac{1}{R_1} + \frac{1}{R_2}\right) \tag{37}$$

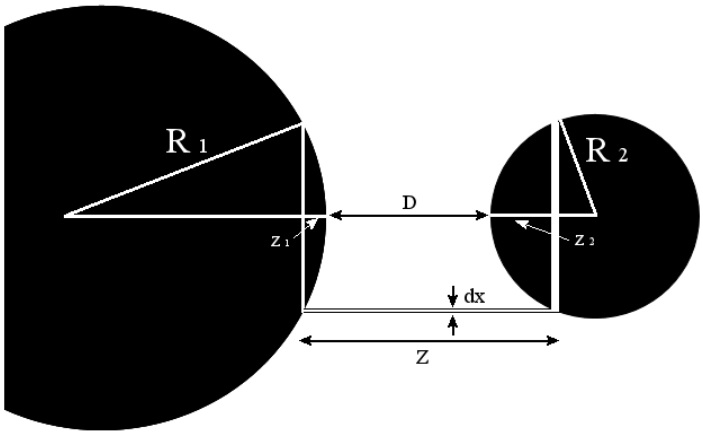

Figure 88: *Schematic of two interacting spheres.* The two spheres of radius R_1 and R_2 are at distance D. The force is integrated over small circular sections of radius x and height dx at distances $Z=D+z_1+z_2$.

and hence

$$dZ = \left(\frac{1}{R_1} + \frac{1}{R_2}\right) x dx \tag{38}$$

Thus the force can be expressed as:

$$f(D) = \int_{D}^{x} 2\pi \frac{R_1 R_2}{R_1 + R_2} f(Z) dZ = 2\pi \frac{R_1 R_2}{R_1 + R_2} W(D) \tag{39}$$

where $W(D)$ is the interaction potential between two flat surfaces. Equation 39 is known as the Derjaguin approximation and it is valid when the interaction range and the separation D are much smaller than R_1 and R_2. The different expressions of the force for common geometries can be seen in Table 4.

Table 4 *The summary of the van der Waals law forces for different geometries.*

geometry	force
Two flat surfaces	$f = -\frac{A_H}{6\pi D^3}$ per unit area
Two spheres	$f = -\frac{A_H}{6D^2}\frac{R_1 R_2}{R_1 + R_2}$
Sphere-flat surface	$f = -\frac{A_H R}{6D^2}$
Cone-flat surface	$f = -\frac{A_H \tan g^2\theta}{6D}$
Paraboloid-flat surface	$f = -\frac{A_H}{12D^2}\frac{l_{xy}^2}{l_z}$
Cylinder-flat surface	$f = -\frac{A_H R^2}{6D^3}$

It is noticeable that all the interaction laws depend on the Hamaker constant A_H which includes all physico-chemical information:

$$A_H = \pi^2 C \rho_1 \rho_2 \tag{40}$$

in which C is the constant in the atom-atom pair potential and ρ_1 and ρ_2 are the numbers of atoms per unit volume.

In reality a thin layer of water vapor often adsorbs on the sample surface, creating a meniscus that in turn creates additional capillary forces. Such a water layer barely affects attractive forces, whereas it prevents the tip from jump-off-contact from the surface due to its high surface energy. The Laplace pressure of the liquid meniscus is given by:

$$P = \gamma_L \left(\frac{1}{R_1} + \frac{1}{R_2} \right) \tag{41}$$

in which γ_L is the surface energy of the liquid and R_1 and R_2 are the two radii that define the liquid meniscus (see Figure 89).

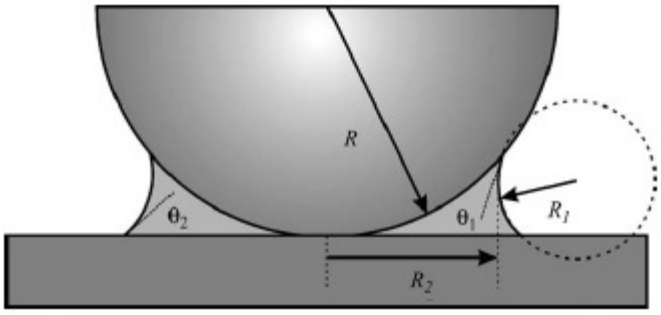

Figure 89: *Schematic of the meniscus formed between the AFM tip and the sample.*

The resulting capillary force F_{cap} between a plate and a sphere with radius R has been calculated by O'Brien and Hermann to be:

$$F_{cap} = 2\pi R\gamma_L(\cos\theta_1 + \cos\theta_2) \tag{42}$$

where the parameters θ_1 and θ_2 are the contact angles between the two surfaces and the liquid.

Recently Gao et al. (1997) have calculated formulas for different tip geometries. More elaborate theories to describe the meniscus forces have been developed in recent years by Lazzer et al. (1999) and Stiffer et al. (2000).

Measurements of Coulomb forces can be employed for studying the tip's shape. Hao et al. (1999) have studied these forces by modeling the tip first with a sphere and then with a cone. The resulting forces were:

$$F_{sp} = \pi\varepsilon_0 V^2 \frac{R}{D} \quad \text{(R/D»1)} \tag{43}$$

$$F_{sp} = \pi\varepsilon_0 V^2 \left(\frac{R}{D}\right)^2 \quad \text{(R/D«1) - spherical tip} \tag{44}$$

$$F_C = \frac{\lambda_0^2}{4\pi\varepsilon_0}\ln\left(\frac{L}{4D}\right) \text{ - conical tip} \tag{45}$$

where V is the voltage difference between the tip and the sample, R the radius of the sphere, D is the tip-sample distance and L is the cone length.

The tip-sample interaction was studied also in liquid media. The commonly encountered forces between tip and sample are electrostatic double-layer (arising because of surface charges at interfaces), solvation forces (arising whenever liquid molecules are ordered in discrete layers between two surfaces), repulsive hydration forces (arising between hydrophilic surfaces), hydrophobic attractive forces (arising between two hydrophobic surfaces), and steric forces (arising when the interaction surfaces are spatially diffuse).

Likewise of great interest are the specific forces. These are noncovalent forces that generate very strong adhesion between molecular groups. The term "specific" refers to all forces that are present only between a specific pair of molecules. Most of these forces arise at the interaction between biological molecules. In order to measure the specific forces one has to functionalize the AFM tip with molecules of interest.

Some experimental results

The unique capability of the AFM to acquire forces locally and with high sensitivity makes it possible to obtain information about the interaction of a single molecular pair.

Adhesion of proteins to the surfaces is important in biology and for medical and industrial applications. Snellings et al. (2000) have found reduced adhesion of human serum albumin (HAS) coated tips to surfaces coated with PEG (polyethylene glycol) polymer brushes. PEG materials are considered as biocompatible coatings for biomedical devices. It was found, following the introduction onto bare gold sensor chips by either spin coating or chemisorption, that the incorporation of hydrophilic PEGs significantly reduced the

protein affinity at the polymer interfaces.

Sethuraman et al. (2004) studied protein adhesion surfaces functionalized with different end groups using colloid probes coated with proteins (ribonuclease A, lysozyme, bovine serum albumin (BSA), immunoglobulin, g-globulins, pyruvate kinase, and fibrinogen). Adhesion increased with wettabilities of the surfaces and the self-adhesion of proteins increased with protein size. As has been noticed by others (Oberhauser et al., 2001; Gergely et al., 2000) step-like behavior exhibiting large jump-off-contact distances suggests that the proteins are stretched and most likely partially or fully denatured.

Adhesion in aqueous buffer solution between AFM probes functionalized with BSA was employed to recognize liposome adsorption on dextran-coated surface plasmon sensor chips (Erb et al., 2000). Analysis of the maximal adhesive force and adhesion energy reveals a stronger interaction between BSA and the dextran matrix compared to the lipid covered surfaces. It could be concluded that the sensor chip surface becomes completely covered by lipid when injecting lipid vesicles.

Another growing field in biological applications is the use of the AFM as a nanomechanical sensor that allows probing of the mechanical properties of cells. A first measurement of the mechanical properties of animal tissue by AFM force–distance curves was done by Tao et al. in 1992 on a section of hydrated cow tibia. Bones have rather complicated but well-organized structures. The relationship between their structures and elastic properties is still not well understood. However, Tao has demonstrated that quantitative data on the elastic properties of a biological composite can be obtained with unprecedented resolution. First single cells studies in 1993 by Weisenhorn et al. gave values of 0.013–0.15 MPa for the elastic modulus of lung cancer cells.

A comparison of the elastic properties of normal human epithelial cell lines (Hu609 and HCV29) and three cancerous ones (Hu456, T24, BC3726) have shown that healthy cells have a Young's modulus of about one order of magnitude higher than cancer cells (Lekka et al., 1999). Quantitatively determined differences in the elastic properties between normal and cancerous cells were attributed to possible changes in cytoskeleton organization due to oncogenic transformation. Adhesion of cells to surfaces is of critical importance in many medical, biological and industrial applications. Biocompatibility of implants and formation of biofilms on surfaces (films made up of cells, having in part different properties from isolated cells) (Beech et al., 2002) are closely related to this issue.

Another mechanism for the adhesion can be the specific receptor–ligand interaction (Leckband et al., 2000). In many examples, such as hormone binding to cell surface receptors and drug targeting, the surface microenvironment can alter the apparent kinetics/thermodynamics of protein recognition events. In such cases, the force profiles that control receptor binding are superpositions of specific receptor-ligand interactions and nonspecific forces between the soluble ligand and the substrate. Discrete measurements of the force-distance curves can identify the different forces that govern protein interactions at surfaces.

Measurements of mechanically induced unfolding have been done in the past years by many groups (Jeon et al., 1991; Rief et al., 1997). The AFM measurements exhibited periodic spikes in the force-extension curves that were attributed to the reversible unfolding transitions of the individual domains. The sharpness of the peaks suggests a protein unfolding by a two-state mechanism. Tskhovrebova et al. (1997) have done mechanical experiments on single molecules of titin protein to determine their visco-elastic properties. Applying high forces they obtained an unfolding of the immunoglobulin and fibronectin domains.

Clausen-Schaumann et al. (2000) examined stretching and the mechanical stability of the DNA double helix. They have performed measurements of AFM functionalized tips with double-stranded DNA molecules on a gold surface and shown that if individual DNA double strands are mechanically overstretched, the double helix splits into single strands that, depending on the attachment of the two strands to the mechanical actuators and on the number of single-strand breaks in the molecule, may recombine to the double-helical conformation upon relaxation of the molecule. The force on which this splitting occurs depends on the pulling velocity, the ionic strength and the temperature as well as on the DNA sequence.

Measurements of bond-rupture forces as a function of the force loading rate, known as dynamic force spectroscopy, have been performed in several biological systems using AFM. For instance, Lo et al. (2001) have analyzed dynamic force spectra of biotin-streptavidin interactions over a range of loading rates. They observed linear relationships between the unbinding force and the log of the loading rate.

Krautbauer et al. (2000) used single molecule force spectroscopy to characterize DNA-small molecule interactions. Binding of cisplatin and ethidium bromide to duplex DNA produced marked changes in its mechanical properties as compared to untreated molecules. These changes strongly depend on the sequence of the stretched molecules. Lioubashevski et al. (2001) measured hybridization forces between PNA (peptide nucleic acids) and DNA and detected single-base mismatches. The adhesion force between

double-stranded PNA/PNA molecules was 1.8 times larger than double-stranded DNA/PNA. Cocco et al. (2001) developed models for the mechanical unzipping of DNA under the conditions used in typical force spectroscopy experiments.

Marszalek et al. (2001) used single molecule force spectroscopy to identify the components in mixtures of polysaccharides. Using the elasticity of the various polysaccharides as a fingerprint, the force spectra obtained were related to the conformation of the pyranose ring and the type of glycosidic linkages. Their approach allows the identification of individual polysaccharide molecules.

Van der Aa et al. (2001) have used force spectroscopy and microscopy measurements for macromolecular stretching at the surface of living cells. The surface of dormant spores exhibited no surface adhesion while the germinating spores exhibited adhesion forces of up to 5.4 N. Adhesive interactions were attributed to the stretching of polysaccharides on the cell surface.

Instead of taking force-distance curves only on selected points of the sample, one can also acquire curves in every point corresponding to a pixel of the AFM image. Since the tip is scanned not only along the surface but also travels in the Z-direction perpendicular to the surface, the term "force-volume mode" has been attributed to this operational mode. From the array of force-distance curves the spatial variation of interactions throughout the sample surface can be obtained. This is usually done by post-processing the force data, resulting in two-dimensional maps of physico-chemical sample properties. A considerable number of studies using the force volume mode have been performed in the biological field. The ability to resolve specific interactions as antibody-antigen binding between AFM tip and sample surface have been already reported (Stroh et al., 1996). Measurements of biotin-streptavidin (Ludwig et al., 1997), ferritin-anti-ferritin (Allen et al., 1998), and thymine and adenine (Ijiro et al., 2002) have also been performed using force-volume mode. Radmacher et al. (1996) have mapped force-distance curves on human platelets showing differences between the substrate and the cells mainly due to elasticity.

7.3 Experimental results

Inspired by the results of previous research on nanowire functionalization, we attempted to test the connectivity of our inorganic $Mo_6S_{9-x}I_x$ nanowires. We were mainly interested in biofunctionalization since our nanowires contain sulfur, raising the possibility of agile biomaterial connectivity. Moreover, sulfur-based chemistry allows binding with gold, opening the gate to enormous possibilities not only in the field of functionalization, but also in the wider areas of research, especially for sensory applications.

Our experiments were focused on functionalizing $Mo_6S_{9-x}I_x$ nanowires with two different types of proteins and to study their connectivity with the help of the AFM. The functionalization was made on two types of nanowires: $Mo_6S_3I_6$ raw material and $Mo_6S_3I_6$ rich in S. The sulfonation was performed by annealing the as-synthesized material in an S atmosphere at 700 °C. Subsequently, for the functionalization process we dispersed the $Mo_6S_{9-x}I_x$ nanowires in distilled water for one hour in a low power ultrasound bath and left it to sediment for one day. The proteins used were thyroglobulin (Tg) and green fluorescent protein (GFP).

7.3.1 $Mo_6S_{9-x}I_x$ nanowires functionalized with proteins: sample preparation

Nanowire-Tg conjugates were produced by mixing 0.8 μg/ml of thyroglobulin (reduced with 10 mM dithiothreitol DTT or intact) and 0.1 mg/ml of $Mo_6S_3I_6$ nanowires. The conjugates were left to react overnight at 4°C. Nanowire-GFP conjugates were produced by mixing 0.4 μg/ml of GFP-Cys mutant (reduced with 10 mM dithiothreitol DTT or intact) and 0.1 mg/ml of $Mo_6S_3I_6$ nanowires. The conjugates were left to react overnight at 4°C. They were further purified by Percoll gradient centrifugation. A step gradient was prepared with 1.15 ml undiluted Percoll, 1.15 ml Percoll diluted 1:2 and 1.7 ml Percoll diluted 1:10. Centrifugation was performed for two hours at 20000 g with a TST 60-4 rotor in a Centrikon T-2070 ultracentrifuge (Kontron Instruments). The GFP-Cys-nanowire conjugates were collected at the interface between 10% and 50% Percoll. The conjugates were subjected to a 1.5-hour centrifugation at 100000 g using the same rotor as described above to remove Percoll from the sample.

From the resulting solutions a drop from the top was taken, deposited on HOPG substrate and investigated with the AFM (Figure 90). We can see that the functionalization process for the two types of $Mo_6S_{9-x}I_x$ nanowires is very different. We observe that raw, as-synthesized nanowires are always functionalized with proteins only at the ends (Figure 90a and c), whereas in the case of $Mo_6S_{9-x}I_x$ nanowires rich in S the protein seems to cover the wire along the entire length (Figure 90b), which would be consistent with our expectations.

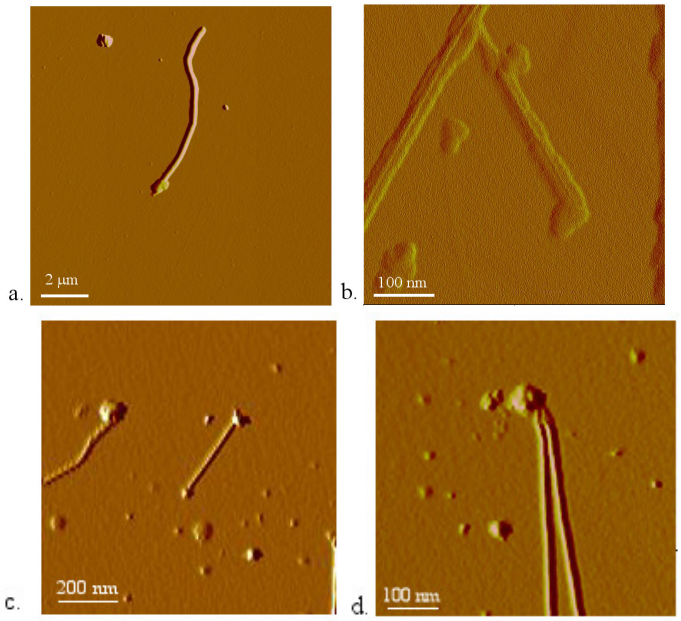

Figure 90: *AFM tapping mode images of two types of $Mo_6S_{9-x}I_x$ nanowires*. As-synthesized (a) and rich in S (b) functionalized with Tg. The (c) and (d) images shows a functionalized $Mo_6S_{9-x}I_x$ nanowire raw material with GFP.

Reproducible results have been observed. Figure 91is a gallery of images showing protein aggregation attached to the end of the nanowires.

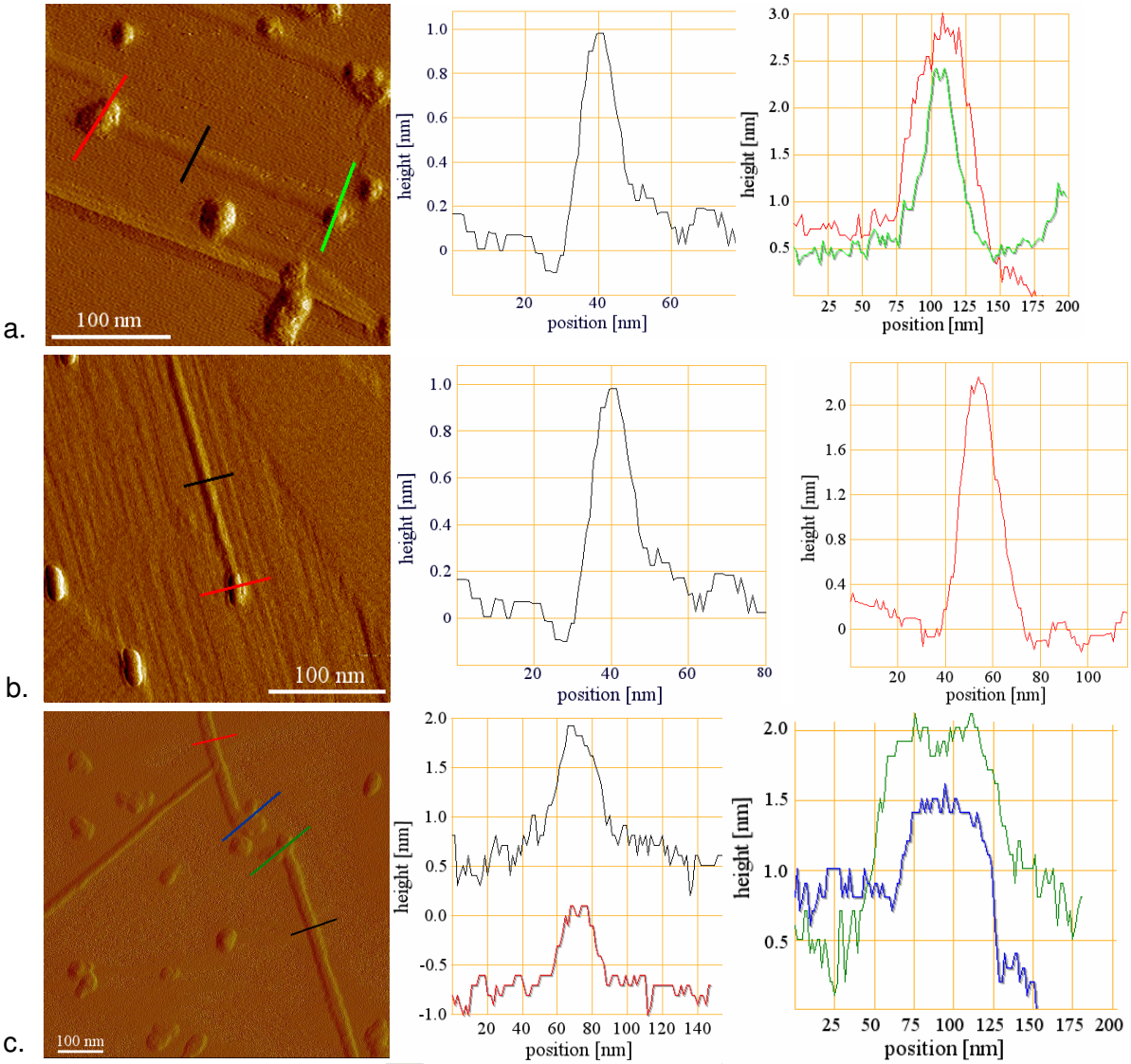

Figure 91: *Image gallery of thyroglobulin protein attached to nanowire ends.* From the profile analysis individual nanowires having a diameter of about 1 nm can be observed, while the proteins are present in aggregations with diameters of between 1nm and 2.5 nm.

7.3.2 AFM force measurements

To confirm the wrapping of the sulfonated nanowires with thyroglobulin, we used AFM to perform force measurements. These experiments were carried out as described in section 7.2 by monitoring the deflection of the cantilever as the tip is approaching or withdrawing from the sample. The general introduction to the interaction between the tip and the sample in section 7.2 leads to the conclusion that different substrates exhibit different interactions with the tip, resulting in different force-distance curves. In other words, we can say that the force-curves for each material have a unique shape, some sort of fingerprint due to its unique interaction with the tip. Obtaining force-distance curves at specific reference points we hoped to confirm the presence of functionalized nanowires and to find an easy way to distinguish between the bare nanowire and the one wrapped with the protein. In order to do this we first performed force-measurement curves to find the fingerprint of each component: the substrate (in our case HOPG), the protein and the nanowire. Figure 92a represents the typical shape of the force curves on HOPG. The small displacement of the withdrawing curve present in the contact-line of the approaching curve has also been achieved in the results obtained by Patil et al. (2002) who proposed that the friction effect between the HOPG substrate and the AFM SiN tip causes this hysteresis behavior.

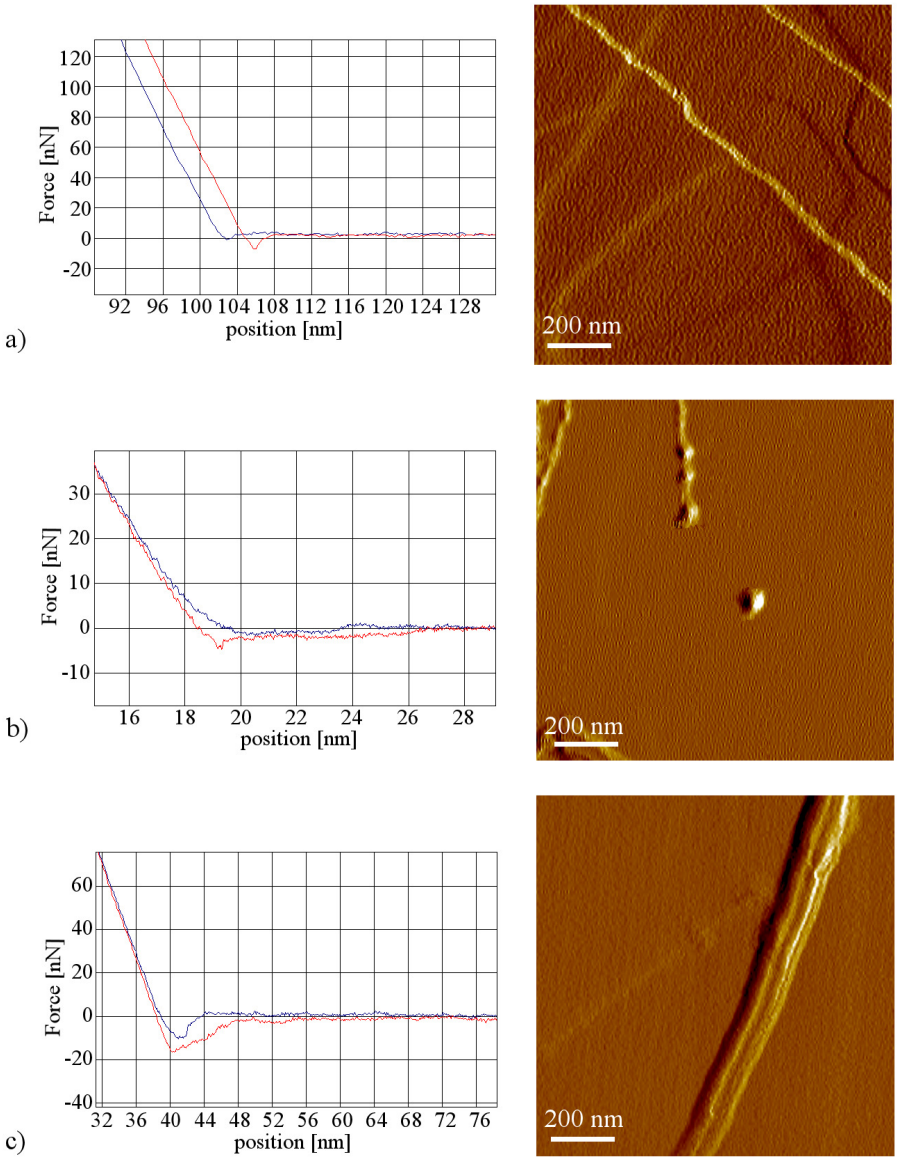

Figure 92: *AFM force measurements.* Obtained force-distance curves and AFM pictures of HOPG substrate (a), of the $Mo_6S_{9-x}I_x$ nanowires on HOPG substrate (b) and of thyroglobulin deposit on HOPG substrate (c).

Figure 92b represents the force curves for the $Mo_6S_{9-x}I_x$ nanowire deposit on a HOPG substrate. In this case no hysteresis is present and the approaching curve could be assigned to van der Waals interaction between the tip and the sample. However, the drop upon withdrawing might occur due to some binding forces between the tip and the nanowire or to the adhesion forces (since we were working in ambient atmosphere a thin layer of water on the sample was always present). In the case of the protein deposit on HOPG substrate, the shape of the force curve is considerably different. The protein is positively charged, so the repulsion interaction is anticipated upon approaching. This can be seen in the force-distance curves (Figure 92c) where we notice the lack of a pronounced jump-to-contact event. Upon withdrawing the jump-off-contact process is attributed to the sensitivity of the HOPG substrate beneath. The withdrawing curve resembles the one for the bare HOPG substrate but is not as pronounced as was proposed by D. Kim et al. (2002).

Having the fingerprints of each individual material present in our experiments, we could measure force-distance curves on the $Mo_6S_{9-x}I_x$ nanowires assumed to be completely wrapped. A slow approach of the AFM tip on the covered nanowire results in the bending of the cantilever upon contact with the sample. The obtained force-distance curve shows the fingerprint of the thyroglobulin in the approaching process, the withdrawing curve, however, is typical for the $Mo_6S_{9-x}I_x$ nanowires that the tip is sensing beneath the protein (Figure 93a) (the same phenomenon observed also in the case of the protein on bare HOPG substrate).

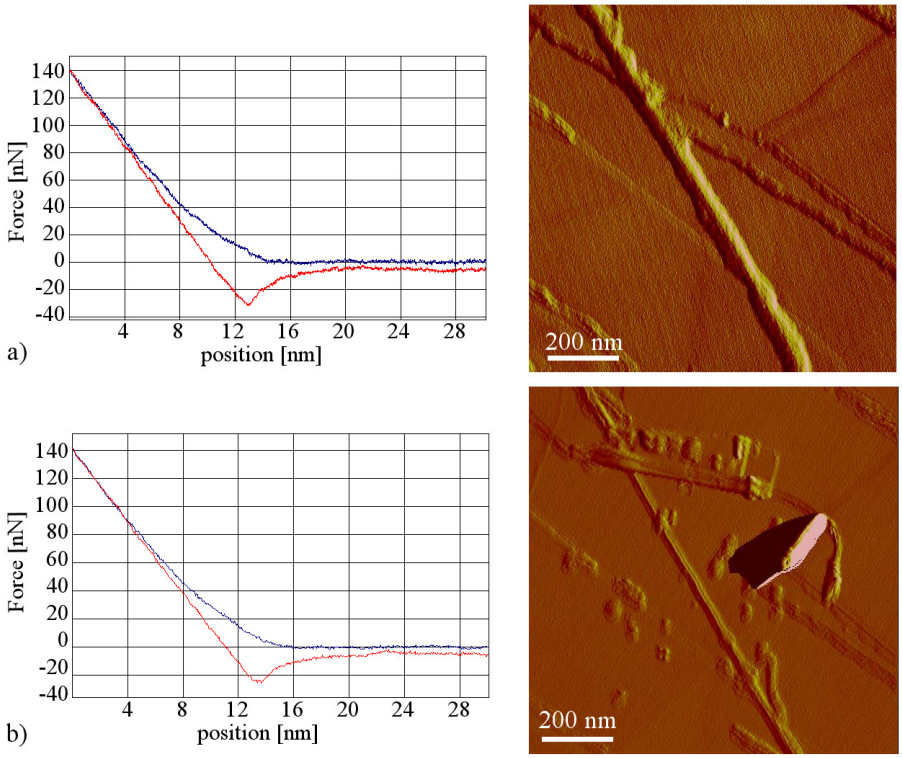

Figure 93: *Force-distance curves and AFM images of a fully wrapped $Mo_6S_{9-x}I_x$ nanowire with thyroglobulin (a) and of an unwrapped nanowire after measurement (b).*

By increasing the force upon the $Mo_6S_{9-x}I_x$ nanowires the process terminates with the unwrapping of the nanowire from the protein (Figure 93b). What is surprising is that the unwrapping is complete and we do not have just local damage (in Figure 93b the remaining protein can be seen after the experiment is finished).

To avoid irreversible damage to the wrapped $Mo_6S_{9-x}I_x$ nanowire, force-volume measurements at room temperature were performed as well. Instead of taking force-distance curves only at selected points in the sample, in force-volume measurements one can acquire force-distance curves on every point corresponding to a pixel of the AFM image.

In the first step, we used a tapping-mode AFM to study the surface topography of functionalized nanowires to allow identification of feature characteristics (Figure 94).

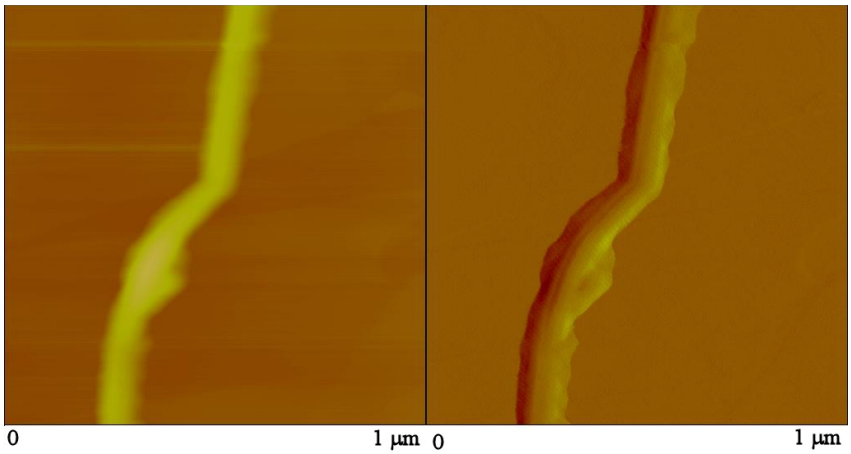

Figure 94: *Tapping-mode AFM image of $Mo_6S_{9-x}I_x$ nanowire wrapped with thyroglobulin before performing force-volume measurements.*

Further force-volume experiments were performed by recording the force curves at individual pixel points in an AFM image. Adhesion measurements in force-volume mode were carried out in an array of 64 x 64 forces versus distance curves uniformly distributed over an area of $1\mu m^2$, tip velocity of ~1 µm/s and a

constant applied force of 2.32 nN. A typical force-volume image is presented in Figure 95. On the left is the height image of the wrapped nanowire obtained by the force-volume measurements. The resolution of the image is low due to the few points taken per line. On the other hand, on the right, the corresponding force-volume image based on the retract (adhesion) forces can be seen. Clearly, the topographical features in the height image directly correspond to different tip-force interactions with the surface in the force-volume image. Typical force curves of the wrapped $Mo_6S_{9-x}I_x$ nanowire (A), thyroglobulin (B) and HOPG substrate (C) are shown in the force plot. The force curve of the wrapped nanowires (A) shows a soft adhesion jump, whereas for the thyroglobulin and HOPG substrate (B and C) the tip adheres to a much greater extent. For the wrapped nanowires the soft adhesion force is due to the fact that the tip feels only the proteins that cover the nanowire, the significant layer of protein overcoming the influence of the nanowire beneath. However, in the case of the thyroglobulin close to the HOPG and the substrate itself, the adhesion forces are much stronger.

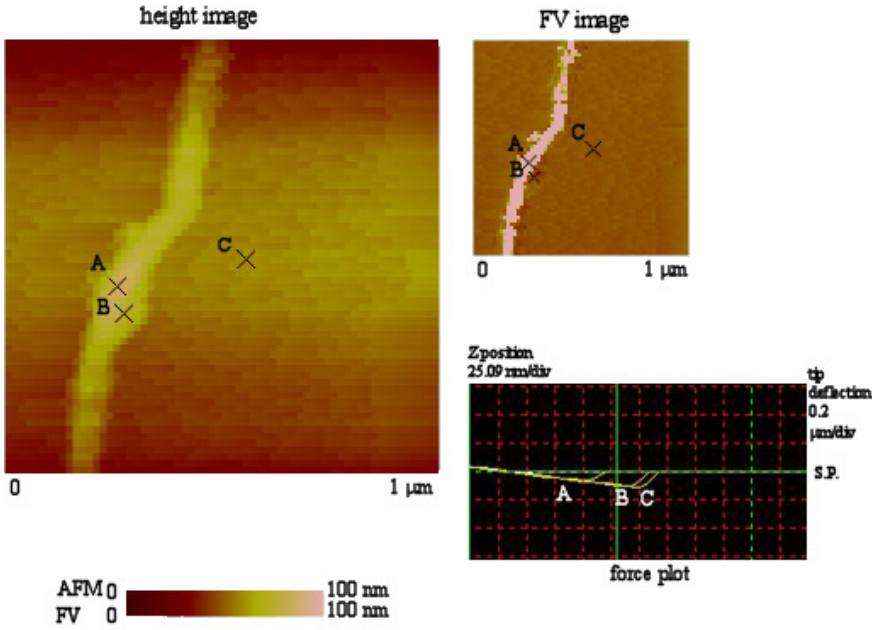

Figure 95: *Force volume mapping of wrapped $Mo_6S_{9-x}I_x$ nanowires with thyroglobulin protein.*

7.4 Conclusions

We have demonstrated a straightforward method for the functionalization of $Mo_6S_{9-x}I_x$ nanowires with thyroglobulin. Using different nanowires, we observed that the proteins can attach themselves at the ends of the nanowires (for the as-synthesized material) or it can cover them entirely (for $Mo_6S_{9-x}I_x$ nanowires rich in S). The functionalization was shown to be successful for both thyroglobulin and green fluorescent protein. The richness in S on the surface of the proteins made the functionalization of the nanowires straightforward.

The AFM force–distance measurements emerged as a useful experiment to confirm the two possible functionalizations. We found that each material has its own fingerprint, providing us with the possibility of distinguishing between HOPG substrate, protein and $Mo_6S_{9-x}I_x$ nanowire. It has been seen that upon approaching, the tip experiences a repulsive force due to the positive charge of the protein, while the withdrawing process is governed by the strong attractive forces felt from the HOPG substrate beneath.

On the other hand, the force-curves in the case of the nanowires are completely different. Owing to the van der Waals forces, the tip jumps-to-contact in a first step on approach until a true contact is made upon application of increased force to the cantilever. In the withdrawing process the pronounced jump-off-contact seen in the force-curves is attributed to strong adhesion forces. Similar force-curves were also measured for the HOPG with the difference of a hysteresis presence in the contact regime due to the friction between the HOPG and the AFM tip.

Knowing the shape of the force curve we performed measurements on $Mo_6S_{9-x}I_x$ nanowires covered entirely with thyroglobulin. We observed that increased force on the cantilever unwraps the protein completely from the nanowire. Upon approaching the force-curves exhibit a typical behavior for proteins, i.e. a repulsion force felt by the tip preventing a jump-to-contact event is observed. On the other hand, in

the withdrawing process the van der Waals forces from the nanowires were strongly felt by the tip, yielding a pronounced jump-off-contact drop. By increasing the force on the cantilever, the protein is scattered from the nanowire resulting in a total unwrapping. The clear distinction between different materials, based on force measurement curves, opens the way to reliable and high-yield functionalization studies of $Mo_6S_{9-x}I_x$ nanowires.

For avoiding the unwrapping and for a clearer interpretation of the measurements, force-volume mapping was performed. Due to the significant covering of the nanowire with thyroglobulin, upon retraction the tip senses only the protein with no influence from the nanowire beneath, thus the jump-of-contact event is small. The situation is completely different when taking the HOPG substrate and the thyroglobulin close to it into consideration. In both cases the retracting curve shows strong adhesion forces normal for the substrate and as well as for the protein due to the sensing force from the substrate beneath. In conclusion we can say that the AFM in our measurements was shown to be an excellent tool not only for the visualization of our samples, but also for their subsequent interpretation.

8 Overall conclusions

The new class of inorganic nanowires synthesized in 2002, i.e. $Mo_6S_{9-x}I_x$ nanowires, has proved to be of immense interest due to their striking physical and chemical properties. Numerous experiments have been performed in order to extract some of their basic properties, of which many still remain hidden. Our work was focused on studying the properties of these nanowires for possible applications in nanotechnology and nanobiotechnology.

In the first part (di)electrophoresis techniques were employed for the manipulation and separation of $Mo_6S_{9-x}I_x$ nanowires. With the help of electrophoresis it was shown that the $Mo_6S_{9-x}I_x$ nanowires are negatively charged. A net movement of the nanowires towards the positive electrode was observed, yet no diffusion through the gel was noticed. Staining the nanowires with typical dyes for DNA observation also could not reveal any eventual nanowire traveling through the gel. This could be due to the lack of bonding between the dyes and the nanowires. Thus, only the diffusion of the bare dyes was detected, without a noticeable trace of nanowire movement. Even EtBr staining did not show any traces of nanowire diffusion, again possibly due to the lack of successful nanowire bonding. On the other hand, no travel of the nanowires through the gel could be the consequence of their long lengths and rapid agglomeration in the sample solution. The nanowires tend to entrap themselves in large meshes, webs or networks that completely block the pores, disabling the eventual single nanowires from even leaving the pocket and entering the gel. In addition, large diameter nanowires contribute to this pore stuffing effect, single-handedly blocking the pores. Even though the nanowire diffusion was not observed, the experiment yielded the undisputable fact that the charge of the nanowire in aqueous solution is negative. This creates new possibilities to chemical functionalization of these materials. In comparison to relatively inert carbon nanotubes that show very little chemical compatibilities in common solvents, our material exhibits intrinsic solubility in various solvents that, together with charging the solution, enables rich and straightforward chemistry. Moreover, the solubility in water gives us a unique route to biofunctionalization and biochemistry, laying the foundation for nanotechnology and biological sciences on the cellular level.

We successfully used dielectrophoresis also for the self-assembled manufacture of nanowires terminated with nickel/indium field emission tips. Interestingly, the performance of our inorganic nanowires was comparable with the reported emission properties of SWCNTs, making our material a strong, sound alternative for field emission applications. The maximum measured current of 0.8 μA driven by barrier-tunneling mechanism and the stability of tips over several hours could launch these novel composites into the high-tech industry of new generation display boards, electronic microscopy and electronic lithography.

Our pursuit of basic chemical and physical properties led us from sample preparation methods in different solvents and pHs to the testing of chemical reactivity implemented in terms of functionalization capabilities with chosen microparticles. It emerged that the best solubility of the sample and stability of the particles was achieved in a neutral pH, simplifying the chemical reaction as well as deploying an arsenal of possible functionalizing entities. Solvent charging along with sulfur arrangement on distances nearing gold lattice distances in the basic construction of the compound raised the hope of possible connectivity with gold nanoparticles. As anticipated, our direct route of attachment proved to be a successful one. Since sequential chemical modification of AuNPs on the nanowires could give rise to many interesting compounds, new nanoelements with remarkable electrical properties could be manufactured. This exciting fact makes the material for multifunctional posterior chemical treatment, enabling us to produce templates for possible nanoelectronic building blocks in a controlled manner. Along with individual nanowire attachment, the AuNP functionalization also yielded multi terminal connections and even networks with the AuNP links between the wires. These self-assembled structures are by themselves fascinating and exciting systems whose properties may facilitate a new generation of logic circuits, chips, controllers, and sensors.

Encouraged by the AuNP functionalization we then attempted more complex attachment with sulfur or thiol-containing biomolecules, i.e. with proteins. The basic idea was again based on favorable sulfur gold chemistry using AuNP as mediators between the nanowire and the sulfur-rich protein molecule. To our surprise, the protein attached on the ends directly to the nanowire omitting AuNP altogether. This stunning result was of course confirmed in the attempt to connect nanowires and protein directly, namely without

AuNP in the solution. Moreover, our experiment with sulfur-rich nanowires yielded nanowires completely wrapped with protein, implying the crucial role of sulfur in the attachment procedure. Our sensitive and nondestructive AFM analysis reliably identified the individual building blocks of the nanowire—the AuNP/protein complex—based on predetermined force-curve fingerprints for each component. This vivid connectivity could be the base for implementation of biomolecules in electronic circuits, potentially revolutionizing medicine especially in diagnostics with a new generation of maximum sensitivity biosensors at the level of single molecules.

The presented work reveals some interesting and intriguing properties of inorganic $Mo_6S_{9-x}I_x$ nanowires. Along with compatibility with a variety of common solvents, especially with aqueous solutions, this compound also exhibits rich chemical properties, as demonstrated by successful attachment of AuNPs and especially protein biomolecules. Likewise, their performance as electron field emitters cannot be neglected since their stability implies favorable electronic properties, making them adequate for integration into electronic circuits. This unique “all-in-one” nanocompound, due to its straightforward processing, high connectivity, and excellent biocompatibility, can thus join the elite group of potential future materials for novel applications in the burgeoning field of nanotechnology.

9 Acknowledgements

I would like to thank ***Prof.Dr. Dragan Mihailovic*** for accepting and giving me the opportunity to work in his group, the Department for Complex Matter at the Josef Stefan Institute and to make my Ph.D. research. I want to thank for all the support and encouragements that he gave me for the entire time spend in his group. I have learned a lot and I progressed considerably under his supervision. Thank you very much.

A special thank to ***Dr. Hartmut Stadler*** from the Veeco Instruments GmbH, for all the patience that had with me. Thank you for your guiding and help in atomic force microscope measurements. Thanks for the prompt answers and for all the detailed e-mail. It helped me a lot in understanding and in making AFM experiments. Lots of thanks also to ***Dr. Sasa Jenko Kokalj*** for all the collaborations. Without you part of my Ph.D. would not be done. Thanks for all the samples which you provided me with and for your understanding. Good luck in your new job and lots of happiness.

I would like to acknowledge also the group of ***Prof.Dr. Werner J. Blau*** especially ***Prof.Dr. Jonathan N. Coleman*** and ***Dr.V. Nicolosi*** for the opportunity to make a part of my experiments in their laboratories. Also I would like to thank to ***Prof.Dr. Malcom Green*** *and* ***Dr. Jeremy Sloan*** for the occasion given to work in their microscopy laboratories. Acknowledgment also for the *European Union* for the financial support through the *NANOTEMP Network*.

A special thank is going now to my colleagues, this are ***Marko Uplaznik, Damjan Vengust, Jure Strle, Damjan Dvorsek, Primos Kusar*** for all the help and for the good times that we spent. You are all great and thank you for all the fun that I had here. ***Jure***, thanks for the patience that you had for reading my thesis and also for all those small "tricks" that you did at my computer or desk (I'm referring to the game with the glasses, the doll that I have there, the kinder surprises and not to forget, more recently, with the web camera). Every day when seeing something what you have done it was making me laugh so much. ***Marko***, thank you also for everything: for reading the thesis, for not getting angry when screaming at you thinking that you exaggerate with the corrections (which by the way were not exaggerated), thank you for all the pictures that you made for me to put in the thesis. Thank you also for the great time that we had everywhere and for supporting me when thinking that is no way out anymore. And moreover, thanks for the great time that we had in Bucharest and hope that you will come also in summer, this time to see the sea side.

I would like further to thank to my friends from Bucharest: ***Gabitz, Mihu, Cristinuca, Irinuca, Nirvana*** and the others. You are the best and "merci pentru bautele pe care le-am tras cand ne-am vazut. Chiar daca nu am reusit in fiecare an sa ne intalnim imi pare super bine ca am reusit sa tinem legatura prin net. Pupici multi la toate." And be prepared for when I came back cos we have to celebrate, hahahahaha. Thanks also to the Romanian friends that I made in Slovenia: ***Elena, Luminita,*** and the others. ***Elena***, thank you for all the excursions that we made and for all the talks that we had. ***Lumi***, thank you also for everything, specially for the time that we were spending in the shops to buy stuff for my niece.

Special thanks also to "***ShAlex***": even if we knew each other now, at the end of my time here in Slovenia, I had great time with you and I will never forget the wild parties that we had. We are both party girls and I am glad to know you. You are the best.

Thanks also to the group from Bucharest from INFLPR where I worked before coming in Slovenia to make my Ph.D. Thanks to my boss ***Morjan*** for welcoming me always with open arms every time when I visited them and for everything that I learned from him and from his group. Thanks to ***Mr Voicu***, ***Mrs Alexandrescu***, ***Florin***, ***Sandu***, ***Iulia***, ***Claudiu***, ***Mr. Petrica*** and ***Mr. Popovici*** for not forgetting me, for all that I have learned from them and for the good time that we had when we met. ***Monica*** and ***Lavinia***, even if I did not have the occasion to know you better because you came in the group after I left, thank you for reminding me about the bureaucratic part and taking care off all the papers. Thanks a lot.

Finally I would like to greatly thank to my family for all the support and encouragements given to me. Thank you for your trust in me and for all your understanding. ***Sis***, ***mom***, ***dad*** you are the best family ever. "Mama si tata, multumesc pentru tot suportul pe care mi l-ati dat si pentru toata increderea avuta in mine. Dupa toate discutiile pe care le-am avut pe messenger sau skype, cu orele cate odata, ma relaxam si nu mai eram asa de nervoasa. Multumesc inca o data pentru tot." Sis and Luci, what shall i thank you for? I think that you know already. "Merci pentru super nepotica pe care mi-ati dat-o, e o dulceata. Merci pentru toate petrecerile de revelion pe care le-am facut la voi si pentru toate petrecerile de-altfel pe care le-ati dat. Ca de

obicei sunt cele mai reusite, hahahahaha. Merci si pentru ca m-ati ascultat de fiecare data cand am avut chef de o vorba si am avut nevoie de un umar pe care sa ma plang. Gata, asta este tot, ca sa nu dau in latura cealalta, ☺”.

10 References

van der Aa, B.C.; Michel, R.M.; Asther, M.; Zamora, M.T.; Rouxhet, P.G.; Dufrene, F. Stretching cell surface macromolecules by atomic force microscopy. *Langmuir* **17** (11), 3116 (2001).

Aharonovich, I.; Tamir, S.; Lifshitz, Y. Growth of SiO_x nanowires by laser ablation *Nanotechnology* **19**, 065608 (2008).

Allen, S.; Chen, X; Davies, J.; Davies, M.C.; Dawkes, A.C.; Edwards, J.C.; Roberts, C.J.; Tendler, S.J.B.; Williams, P.M. The application of force microscopy to immunodiagnostic systems: imaging and biomolecular adhesion measurements. *Apply Phys A* **66**, S255 (1998).

Alivisatos, A.P.; Johnsson, K.P.; Peng, X.; Wilson, T.E.; Loweth, C.J.; Bruchez Jr, M.P.; Schultz, P.G. Organization of 'nanocrystal molecules' using DNA. *Nature* **382**, 609 (1996).

Alvarez, M.M.; Khoury, J.T.; Khoury, J.T.; Schaaff, T.G.; Shafigullin, M.N.; Vezmar, I.; Whetten, R.L. Optical absorption spectra of nanocrystal gold molecules. *J Phys Chem B* **101**(19), 3706 (1997).

Andres, R.P.; Bein, T.; Dorogi, M.; Feng, S.; Henderson, J.I.; Kubiak, C.P.; Mahoney, W.; Osifchin, R.G.; Reifenberger, R. "Coulomb Staircase" at room temperature in a self-assembled molecular nanostructure. *Science* **272**, 1323 (1996).

Arnaud, I.; Abid, J.-P.; Abid, J.P.; Roussel, C.; Girault, H.H. Size-selective separation of gold nanoparticles using isoelectric focusing electrophoresis. (IEF) *Chem Commun* **6**, 787 (2005).

Asbury, C.L.; van den Engh, G. Trapping of DNA in nonuniform oscillating electric fields. *Biophy J* **74**, 1024 (1998).

Ausman, K.D.; Piner, R.; Lourie, O.; Ruoff, R.S.; korobov, M. Organic solvent dispersion of single-walled carbon nanotubes: toward solutions of pristine nanotubes. *J Phys Chem B* **104**(38), 8911 (2000).

Azamian, B.R.; Davis, J.J.; Coleman, K.S.; Bagshaw, C.B.; Green, M.L.H. Bioelectrochemical single-walled carbon nanotubes. *J Am Chem Soc* **124**(43), 12664 (2002).

Awdeh, Z.L.; Williamson, A.R.; Askonas, B.A. Isoelectric focusing in polyacrylamide gel and its application to immunoglobulins. *Nature* **219**, 66 (1968).

Bai, J.; Qin, Y.; Jiang, C.; Qi, L. Polymer-controlled synthesis of silver nanobelts and hierarchical nanocolumns *Chem.Mater.* **19**(14), 3367 (2007).

Baik, J.M.; Schierhorn, M.; Moskovits, M. Fe nanowires in nanoporous alumina: geometric effect versus influence of pore walls *J.Chem.Phys.Chem. C* **112**(7), 2252 (2008).

Baker, S.E.; Cai, W.; Lasseter, T.L.; Weidkamp, K.P.; hamers, R.J. Covalently bonded adducts of deoxyribonucleic acid (DNA) oligonucleotides with single-wall carbon nanotubes: synthesis and hybridization. *Nano Lett* **2**(12), 1413 (2002).

Balasubramanian, R.; Kim, B.; Tripp, S.L.; Wang, X.; Lieberman, M.; Wei, A. Dispersion and stability studies of resorcinarene-encapsulated gold nanoparticles. *Langmuir* **18**(9), 3676 (2002).

Bandyopadhyaya, R.; Nativ-Roth, E.; Regev, O.; Yerushalmi-Rozen, R. Stabilization of individual carbon nanotubes in aqueous solutions. *Nano Lett* **2**(1), 25 (2002).

Bars, O.; Guillevic, J.; Grandjean, D. Étude structurale de combinaisons sulfurées et séléniées du molybdène: I. Structure cristalline de Mo_3Se_4. *J Solid State Chem* **6**(1), 48 (1973).

Bauer, J. Electrophoretic separation of cells. *J. Chrom: Biomed Appl* **418**(17), 359-83 (1987).

Beech, I.B.; Smith, J.R.; Steele, A.A.; Penegar, I.; Campbell, S.A. The use of atomic force microscopy for studying interactions of bacterial biofilms with surfaces. *Coloidsl Surf B* **23**(2-3), 231 (2002).

Bercic, B.; Pirnat, U.; Kusar, P.; Dvorsek, D.; Mihailovic, D. Transport properties of $Mo_6S_3I_6$ nanowire networks. *App Phy Lett* **88**, 173103 (2006).

Bergmann, G.; Rainer, D. The sensitivity of the transition temperature to changes in alpha2 F(omega). *Z Physik* **263**, 59 (1973).

Bernaerts, D.; Amelinckx, S.; van Tendeloo, G.; van Landuyt, J. Microstructure and formation mechanism of cylindrical and conical scrolls of the misfit layer compounds $PbNbS_{2n+1}$. *J Cryst Growth* **172**, 433 (1997).

Bennett, J.; Scott, K.J. Quantitative staining of fraction I protein in polyacrylamide gels using Coomassie brilliant blue. *Analyt Biochem* **43**(1), 173 (1971).

Bethune, D.S.; Kiang, C.H.; de Vries, M.S.; Gorman, G.; Savoy, R.; Vazquez, J.; Beyers, R. Cobalt-catalysed growth of carbon nanotubes with single-atomic-layer walls. *Nature* **363**, 605 (1993).

Bhatt, K.H.; Velev, O.D.Control and modeling of the dielectrophoretic assembly of on-chip nanoparticle wires. *Langmuir* **20**(2), 467 (2004).

Bishop, D.H.; Claybrook, J.R.; Spiegelman, S. Electrophoretic separation of viral nuclei acids on polyacrylamide gels. *J Mol Biol* **26**(3), 373 (1967).

Binnig, G.; Rohrer, H.; gerber, Ch.; Weibel, E. Surface studies by scanning tunneling microscopy. *Phys Rev Lett* **49**(1), 57 (1982).

Binnig, G.; Quate, C.F.; Gerber, Ch. Atomic force microscopy. *Phys Rev Lett* **56**(9), 930 (1986).

Boul, P.J.; Liu, J.; Mickelson, E.T.; Huffman, C.B.; Ericson, L.M.; Chiang, I.W.; Smith, K.A.; Colbert, D.T.; Hauge, R.H.; Margrave, J.L.; Smalley, R.E. Reversible sidewall functionalization of buckytubes. *Chem Phys Lett* **310**, 367 (1999).

Brousseau, L.C.; Marinakos, S.M.; Novak, J.P.; feldheim, D.L. Electronic properties of single Au nanocrystals and synthesis of 1-dimensional nanocrystal arrays. *Cryst Engineer* **1**(2), 129-37 (1998).

Brown, F.C.; Bunker, B.A.; Ginsberg, D.M.;Miller, T.J.; Miller, W.M.; Stern, E.A. X-ray-edge studies and photoemission of $Mn_xSn_{1-x}Mo_6S_8$. *Phys Rev B* **34**(11), 7698 (1986).

Brust, M.; Fink, J.; Bethell, D.; Schiffrin, D.J.; Kiely, C. Synthesis and reactions of functionalized gold nanoparticles. *J Chem Soc, Chem Commun* 1655 (1995)

Buffat, Ph.; Borel, J.-P. Size effect on the melting temperature of gold particles. *Phys Rev A* **13**(6), 2287 (1976).

Bulushev, D.A.; Kiwi-Minsker, L.; yuranov, I.; Suvorova, E.I.; Buffat, P.A.; Renken, A. Structured Au/FeOX/C catalysts for low-temperature CO oxidation. *J Catalys* **210**, 149 (2002).

Burnham, N.A.; Colton, R.J. Measuring the nanomechanical properties and surface forces of materials using an atomic force microscope. *J Vac Sci Technol A* **7**(4), 2906 (1989).

Busbee, B.D.; Obare, S.O.; Obare, O.; Murphy, C.J. An improved synthesis of high-aspect-ratio gold nanorods. *Adv Mater* **15**(5), 414 (2003).

Bush, C.N.; Holmes, D.S. The use of agar gel electrophoresis of DNA. *Analyt Biochem* **119**(1), 164 (1982).

Butt, H.-J. Measuring local surface charge densities in electrolyte solutions with a scanning force microscope. *Biophys Journal* **63**, 578 (1992).

Cai, C.; Chen, J. Direct electron transfer of glucose oxidase promoted by carbon nanotubes. *Analyt Biochem* **332**, 75 (2004).

Cameron, D.; Holliday, R.; Thompson, D. Gold's future role in fuel cell systems. *J Power Sources* **118**, 298 (2003).

Cappella, B.; Dietler, G. Force-distance curves by atomic force microscopy. *Surface Science Reports* **34**, 1 (1999).

Caruana, D.J.; Heller, A. Enzyme-amplified amperometric detection of hybridization and of a single base pair mutation in an 18-base oligonucleotide on a 7 µm-diameter microelectrode. *J Am Chem Soc* **121**, 769 (1999).

Cassou, M.L.; Tovar, E.G. Primitive model electrophoresis. *J Colloid Interface Sci* **239**, 285 (2001).

Caswell, K.K.; Wilson, J.N.; Bunz, U.H.F.; Murphy, C.J. Preferential end-to-end assembly of gold nanorods by biotin-streptavidin connectors. *J Am Chem Soc* **125**, 13914 (2003).

Cerrina, F.; Marrian, C. A path to nanolithography *MRS Bull.* **21**(12), 56 (1996).

Chen, H.; Lu, H.; Nie, Y.; Zhang, J.; Zhang, M.; Dai, Q.; Gao, S.; Kan, S.; Li, D.; Zou, G. The fabrication of Te nanowires with different orientations by vacuum vapor deposition *Phys.Lett. A* **362**(1), 61 (2007).

Chen, J.; Deng, S.Z.; Chen, J.; She, J.C.; Xu, N.S. Preparation and characterization of nanostructured film of graphitized diamond crystallites for field electron emission. *J Appl Phys* **94**(8), 5429 (2003).

Chen, J.; Hamon, M.A.; Hu, H.; Chen, Y.; Rao, A.M.; Eklund, P.C.; Haddon, R.C. Solution properties of single-walled carbon nanotubes. *Science* **282**, 95 (1998).

Chen, J.; Li, S.L.; Tao, Z.L.; Gao, F. Low-temperature synthesis of titanium disulfide nanotubes. *Chem Commun* 980 (2003).

Chen, J.; Rao, A.M.; Lyuksyutov, S.; Itkis, M.E.; Hamon, M.A.; Hu, H.; Cohn, R.W.; Eklund, P.C.; Colbert, D.T.; Smalley, R.E.; Haddon, R.C. Dissolution of full-length single-walled carbon nanotubes. *J Phys Chem B* **105**(13), 2525 (2001).

Chen, R.J.; Zhang, Y.; Wang, D.; Dai, H. Noncovalent sidewall functionalization of single-walled carbon nanotubes for protein immobilization. *J Am Chem Soc* **123**(16), 3838-39 (2001).

Chen, S.; Ingram, R.S.; Hostetler, M.J.; Pietron, J.J.; Murray, R.W.; Schaaff, T.G.; Khoury, J.T.; Alvarez, M.M.; Whetten, R.L. Gold nanoelectrodes of varied size: transition to molecule-like charging. *Science* **280**, 2098 (1998).

Chen, S.; Pei, R.; Zhao, T.; Dyer, D.J. Gold Nanoparticle Assemblies by Metal Ion-Pyridine Complexation and Their Rectified Quantized Charging in Aqueous Solutions. *J Phys Chem B* **106**(8), 1903 (2002).

Chen, W.; Cai, W.P.; Liang, C.H.; Zhang, L.D. Synthesis of gold nanoparticles dispersed within pores of mesoporous silica induced by ultrasonic irradiation and its characterization. *Mater Res Bull* **36**(1-2), 335 (2001).

Chen, W.; Cai, W.P.; Zhang, L.; Wang, G; Zhang, L. Sonochemical processes and formation of gold nanoparticles within pores of mesoporous silica. *J Colloid Surf Sci* **238**, 291 (2001).

Cheng, B.; Samulski, E.T. Fabrication and characterization of nanotubular semiconductor oxides In_2O_3 and Ga_2O_3. *J Mater Chem* **11** 2901 (2001).

Chevrel, R.; Potel, M.; Sergent, M.; Decroux, M.; Fischer, O. One-dimensional condensation of Mo6 octahedral clusters: A new cluster, Mo_{12}, and a new building block, $Mo_{12}S_{14}$, in $M_2Mo_9S_{11}$. *J Solid State Chem* **34**(2), 247 (1980).

Chevrel, R.; Sergent, M.; Prigent, J. Sur de nouvelles phases sulfurees ternaries du molybdene. *J Solid State Chem* **3**(4), 515 (1971).

Chevrel, R.; Sergent, M.; seeber, B.; Fischer, O.; Gruttner, A.; Yvon, K. New ternary Mo(II)-compounds $In_xMo_{15}S_{19}$ containing Mo_6Se_8 and Mo_9Se_{11} units. *Mat Res Bull* **14**(4), 567 (1979).

Chiari, M.; Dell'Orto, N.; casella, L. Separation of organic acids by capillary zone electrophoresis in buffers containing divalent metal cation. *J Chromat A* **745**(1-2), 93 (1996).

Chopra, N.G., R.G. Luyken, et al. (1995). "*Boron nitride nanotubes.*" Science **269**: 966- 67.

Clausen-Schaumann, H.; Rief, M.; Tolksdorf, C.; Gaub, H.E. Mechanical stability of single DNA molecules. *Biophys J* **78**(4), 1997 (2000).

Cleveland, D.W.; Fischer, S.G.; Kirschner, M.W.; Laemmli, U.K. Peptide mapping by limited proteolysis in sodium dodecyl sulfate and analysis by gel electrophoresis. *J Biol Chem* **252**(3), 1102 (1977).

Cocco, S.; Monasson, R.; Marko, J.F. Force and kinetic barriers to unzipping of the DNA double helix. *Proc Natl Acad Sci USA* **98**(13), 8608 (2001).

Cohen, R.S.; Kalisman, Y.L.; Nativ-Roth, E.; Yerushalmi-Rozen, R. Generic approach for dispersing single-walled carbon nanotubes: the strength of a weak interaction. *Langmuir* **20**(15), 6085 (2004).

Coleman, J.N.; Dalton, A.B.; Curran, S.; Rubio, A.; Davey, A.P.; Drury, A.; McCarthy, B.; Lahr, B.; Ajayan, P.M.; Roth, S.; Barklie, R.C.; Blau, W.J. Phase separation of carbon nanotubes and turbostratic graphite using a funtional organic polymer. *Adv Mater* **12**(3), 213 (2000).

Collet, J.; Baguna, J. Optimizing a method of protein extraction for two-dimensional electrophoretic separation of proteins from planarians. *Electrophoresis* **14**(1), 1054 (1993).

Cui, Y.; Wei, Q.; Park, H.; Lieber, C.M. Nanowire nanosensors for highly sensitive and selective detection of biological and chemical species. *Science* **293**, 1289 (2001).

Curreli, M.; Li, C.; Sun, Y.; Lei, B.; Gundersen, M.A.; Thompson, M.E.; Zhou, C. Selective functionalization of In_2O_3 nanowire mat devices for biosensing applications. *J Am Chem Soc* **127**(19), 6922 (2005).

Dagata, J.A. Device fabrication by scanned probe oxidation *Science* **270**, 1625 (1995).

Debye, P.; Huckel, E. Zur Theorie der Elektrolyte. *Physik Zeitschr* **24**, 185 (1923).

Deng, C.; Sigmon, T.W.; Giust, G.K.; Wu, J.C.; Wybourne, M.N. Novel scheme to fabricate SiGe

nanowires using pulsed ultraviolet laser induced epitaxy *J.Vacc.Scien.Tech. A* **14**(3), 1860 (1996).

Derjaguin, B.V.; Muller, V.M.; Toporov, Y.P. Effect of contact deformations on the adhesion of particles. *J Colloid Interf Sci* **53**(2), 314 (1975).

Derjaguin, B.V.; Muller, V.M.; Toporov, Y.P. On two methods of calculation of the force of sticking of an elastic sphere to a rigid plane. *Colloids Surf* **7**(3), 251 (1983).

Deutsh, J.M.; Madden, T.L. Theoretical studies of DNA during gel electrophoresis. *J Chem Phys* **90**(4), 2476 (1989).

Diezel, W.; Kopperschlager, G.; Hofmann, E. An improved procedure for protein staining in polyacrylamide gels with a new type of Coomassie brilliant blue. *Analyt Biochem* **48**(2), 617 (1972).

Dimitriadis, E.K.; Horkay, F.; Maresca, J.; Kachar, B.; Chadwick, R.S. Determination of elastic moduli of thin layers of soft material using the atomic force microscope. *Biophys J* **82**, 2798 (2002).

Dloczik, L.; Engelhardt, R.; Emst, K.; Fiechter, S.; Sieber, I.; Konenkamp, R. Hexagonal nanotubes of ZnS by chemical conversion of monocrystalline ZnO columns. *Appl Phys Lett* **78**(23), 3687 (2001).

Doorn, S.K.; Fields, R.E.; Hu, H.; Hamon, M.A.; Haddon, R.C.; Selegue, J.P.; Majidi, V. High resolution capillary electrophoresis of carbon nanotubes. *J Am Chem Soc* **124**(12), 3169 (2002).

Dubertret, B.; Calame, M.; Libchaber, A.J. Single-mismatch detection using gold-quenched fluorescent oligonucleotides. *Nat Biotechnol* **19**, 365 (2001).

Duesberg, G.S.; Graupner, R.; Downes, P.; Minett, A.; Ley, L.; Roth, S.; Nicoloso, N. Hydrothermal functionalisation of single-walled carbon nanotubes. *Synthetic Metals* **142**(1-3), 263 (2004).

Duesberg, G.S.; Muster, J.; Krstic, V.; Roth, S. Chromatographic size separation of single-wall carbon nanotubes. *Appl Phys A* **67**, 117 (1998).

Dugdale, D.S. Yielding of steel sheets containing slits. *J Mech Phys Solids* **8**, 100 (1960).

Dwyer, C.; Guthold, M.; Falvo, M.; Washburn, S.; Superfine, R.; Erie, D. DNA functionalized single-walled carbon nanotubes. *Nanotechnology* **13**, 601 (2002).

Elghanian, R.; Storhoff, J.J.; Mucic, R.C.; Letsinger, R.L.; Mirkin, C.A. Selective colorimetric detection of polynucleotides based on the distance-dependent optical properties of gold nanoparticles. *Science* **277**, 1078 (1997).

Erb, E.M.; Chen, X.; Allen, S.; Roberts, C.J.; Tendler, S.J.B.; Davies, M.C.; Forsen, S. Characterization of the surfaces generated by liposome binding to the modified dextran matrix of a surface plasmon resonance sensor chip. *Anal Biochem* **280**(1), 29 (2000).

Eychmuller, A.; Katsikas, L.; Weller, H. Photochemistry of semiconductor colloids. Size separation of colloidal CdS by gel electrophoresis. *Langmuir* **6**(10), 1605 (1990).

Fangman, W.L. Separation of very large DNA molecules by gel electrophoresis. *Nucleic Acids Research* **5**(3), 653 (1978).

Faraday, M. Experimental relations of gold (and other metals) to light. *Philos Trans R Soc Lond* **151**, 183 (1861).

Favier, F.; Walter, E.C.; Zach, M.P.; Benter, T.; Penner, R.M. Hydrogen sensors and switches from electrodeposited palladium mesowire arrays. *Science* **293**, 2227 (2001).

Feldman, Y.; Wasserman, E.; Srolovitz, D.J.; Tenne, R. High rate gas phase growth of MoS_2 nested inorganic fullerene-like and nanotubes. *Science* **267**, 222 (1995).

Felidj, N.; Aubard, J.; Levi, G.; Krenn, J.R.; Hohenau, A.; Schider, G.; Leitner, A.; Aussenegg, F.R. Optimized surface-enhanced raman scattering on gold nanoparticles arrays. *Appl Phys Lett* **82**(18), 3095 (2003).

Fernando, S.; Lin, Y.; Sun, Y.P. High aqueous solubility of functionalized single-walled carbon nanotubes. *Langmuir* **20**(11), 4777 (2004).

Fischer, O. Chevrel phases: superconducting and normal state properties. *Appl Phys* **16**(1), 1 (1978).

Fischer, O.; Jones, H.; Bongi, G.; Sergent, M.; Chevrel, R. Measurements of critical fields up to 500 kG in the ternary molybdenum sulphides. *J Phys C: Solid State Phys* **7**(24), L450 (1974).

Foner, S.; McNiff, E.J.; Alexander, E.J. 600kG superconductors. *Phys Lett A* **49**(4), 269 (1974).

Foss, C.A.; Tierney, M.J.; Martin, C.R. Template synthesis of infrared transparent metal microcylinder: comparison of optical properties with the predictions os effective medium theory *J.Phys.Chem.* **96**(22), 9001 (1992).

Furuta, N.; Ohasi, Y.; Itinose, H.; Igarashi, Y. Kinetics of vapor-grown tellurium whiskers *Jap.J.Appl.Phys.* **14** (7), 929 (1975).

Galvan, D.H.; Kim, J.H.; Maple, M.B.; Avalos-Borja, M.; Adem, E. Formation of $NbSe_2$ nanotubes by electron radiation. *Fullerene Sci Technol* **8**(3), 143 (2000).

Gao, C. Theory of menisci and its applications. *Appl Phys Lett* **71**(13), 1801 (1997).

Gao, H.; Kong, Y.; Cui, D.; Ozkan, C.S. Spontaneous insertion of DNA oligonucleotides into carbon nanotubes. *Nano Lett* **3**(4), 471 (2003).

Garg, A.; Sinnott, S.B. Effect of chemical functionalization on the mechanical properties of carbon nanotubes. *Chem Phys Lett* **295**, 273 (1998).

Gates, B.; Yin;Y.; Xia, Y. A solution phase approac to the synthesis of uniform nanowires of crystalline selenium with lateral dimensions in the range of 10-30 nm *J.AM.Chem.Soc.* **122**(50), 12582 (2000).

Gates, B.; Mayers, B.; Grossman, A.; Xia, Y. A sonochemical approach to the synthesis of crystalline selenium nanowires in solutions and on solid supports *Adv. Mater.* **14**(23), 1749 (2002).

Georgakilas, V.; Kordatos, K.; Prato, M.; Guldi, D.M.; Holzinger, M.; Hirsch, A. Organic functionalization of carbon nanotubes. *J Am Chem Soc* **124**(5), 760 (2000).

Gergely, C.; Voegel, J.C.; Schaaf, P.; Senger, B.; Maaloum, M.; Horber, J.K.H.; Hemmerle, J. Unbinding process of adsorbed proteins under external stress studied by atomic force microscopy spectroscopy. *J Proc Natl Acad Sci USA* **97**(20), 10802 (2000).

Ghosh, P.; Kahaly, M.U.; Waghmare, U.V. Atomic and electronic structures, elastic properties and optical conductivity of bulk Te and Te nanowires: a first principle study *Phys,Rev. B* **75**(24), 245437 (2007).

Gibson, J.M. Reading and writing with electron beams *Phys. Today* **50**(10), 56 (1997).

Givargizov, E.I. Fundamental aspects of VLS growth *J.Crystal Growth* **3**, 20-30 (1975).

Golden, J.H.; DiSalvo, F.J.; Frechet, J.M.J. Ordered conducting films of the inorganic polymer $(LiMo_3Se_3)n$ cast from solution *Chem. Mater.* **7**(1), 232 (1995).

Golden, J.H.; DiSalvo, F.J.; Frechet, J.M.J.; Silcox, J.; Thomas, M.; Elman, J. Subnanometer wires isolated in a polymer matrix by fast polymerization *Science* **273**, 782 (1996).

Green, N.G.; Morgan, H. Dielectrophoretic separation of nano-particles. *J Phys D: Appl Phys* **30**(11), L41 (1997).

Green, N.G.; Morgan, H. Dielectrophoretic investigations of sub-micrometre latex spheres. *J Phys D: Appl Phys* **30**(18), 2626 (1997).

Green, N.G.; Morgan, H.; Milner, J.J. Manipulation and trapping of sub-micron bioparticles using dielectrophoresis. *J Bioch Biophys Meth* **35**(2), 89 (1997).

Greenaway, D.L.; Nitsche, R. Preparation and optical properties of group IV-VI_2 chalcogenides having the CdI_2 structure. *J Phys Chem Solids* **26**(9), 1445 (1965).

Greenspan, P.; Gutman, R.L. Detection by nile red of agarose-gel electrophoresed native and modified low-density-lipoprotein. *Electrophoresis* **14**(1), 65 (1993).

Gregori, L.; Hainfeld, J.F.; Simon, M.N.; Goldgaber, D. Binding of amyloid β protein to the 20 S proteasome. *J Bio Chem* **272**(1), 58 (1997).

Greytak, A.B.; Lauhon, L.J.; Gudiksen, M.S.; Lieber, C.M. Growth and transport properties of complementary germanium nanowires field-effect transistors *Appl.Phys.Lett.* **84**(21), 4176 (2004).

Guo, Z.; Sadler, P.J.; Tsang, S.C. Immobilization and visualization of DNA and proteins on carbon nanotubes. *Adv Mater* **10**(9), 701 (1998).

Hacohen, Y.R.; Grunbaum, E.; Tenne, R.; Sloan, J.; Hutchison, J.L. Cage structures and nanotubes of $NiCl_2$. *Nature* **395**, 336 (1998).

Hahm, J.-I.; Lieber, C.M. Direct ultrasensitive electrical detection of DNA and DNA sequence variations using nanowire nanosensors. *Nano Lett* **4**(1), 51 (2004).

Hamada, N.; Sawada, S.; Oshiyama, A. New one-dimensional conductors: graphitic microtubules. *Phys Rev Lett* **68**(10), 1579 (1992).

Hamon, M.A.; Chen, J.; Hu, H.; Chen, Y.; Itkis, M.E.; Rao, A.M.; Eklund, P.C.; Haddon, R.C. Dissolution of single-walled carbon nanotues. *Adv Mater* **11**(10), 834 (1999).

Han, C.C.; Bai, M.Y.; Lee, J.T. A new and easy method for making Ni and Cu microtubules and their regular assembled structures. *Chem Mater* **13**(11), 4260 (2001).

Hannig, K. New aspects in preparative and analytical continous free-flow cell electrophoresis. *Electrophoresis* **3**(5), 235 (1982).

Hao, H.W., Baro, A.M.; Saenz, J.J. Electrostatic and contact forces in force microscopy. *J Vac Sci Technol B* **9**(2), 1323 (1991).

Hazani, M.; Naaman, R.; Hennrich, F.; Kappes, M.M. Confocal fluorescence imaging of DNA-functionalized carbon nanotubes. *Nano Lett* **3**(2), 153 (2003).

He, J.H.; Wu, T.H.; Hsin, C.L.; Chen, L.J.; Wang, Z.L. Synthesis of Si-Ge oxide nanowires via the transformation of Si-Ge thin films with self-assembled Au catalysts Electrochem. *Solid-State Lett.* **8**(10), G254 (2005).

Heinz, W.F.; Hoh, J.H. Spatially resolved force spectroscopy of biological surfaces using the atomic force microscope. *Nanotechnology* **17**, 143 (1999).

Hernandez, B.A.; Chang, K.S.; Chang, K.S.; Fisher, E.R.; Dorhout, P.K. Sol-gel template synthesis and characterization of BaTiO3 and PbTiO3 nanotubes. *Chem Mater* **14**(2), 480 (2002).

Hernandez, R.M.; Richter, L.; Semancik, S.; Sranick, S.; Mallouk, T.E. Template fabrication of protein-functionalized gold-polypyrrole-gold segmented nanowires. *Chem Mater* **16**(18), 3431 (2004).

Hertz, H.; Reine, J. On the contact of elastic bodies. *Angew Math* **92**, 156 (1882).

Hickman, J.J.; Ofer, D.; Laibinis, P.E.; Whitesides, G.M.; Wrighton, M.S. Molecular self-assembly of two-terminal, voltammetric microsensors with internal references. *Science* **252**, 688 (1991).

Holzel, R.; Calander, N.; Chiragwandi, Z.; Willander, M.; Bier, F.F. Trapping single molecules by dielectrophoresis. *Phys Rev Lett* **95**(12) 128102 (2005).

Hor, Y.S.; Welp, U.; Ito, Y.; Xiao, Z.L.; Patel, U.; Mitchell, J.F.; Kwok, W.K.; Crabtree, G.W. Superconducting $NbSe_2$ nanowires and nanoribbons converted from $NbSe_3$ nanostructures *Appl.Phys.Lett.* **87**(14), 142506 (2005).

Hostetler, M.J.; Wingate, J.E.; Zhong, C.J.; Harris, J.E.; Vachet, R.W.; Clark, M.R.; Londono, J.D.; Green, S.J.; Stokes, J.J.; Wignall, G.D.; Glish, G.L.; Porter, M.D.; Evans, N.D.; Murray, R.W. Alkanethiolate gold cluster molecules with core diameters from 1.5 to 5.2 nm: core and monolayer properties as a function of core size. *Langmuir* **14**(1), 17 (1998).

Hostetler, M.J.; Green, S.J.; Stokes, J.J.; Murray, R.W. Monolayers in three dimensions: synthesis and electrochemistry of ω-functionalized alkanethiolate-stabilized gold cluster compounds. *J Am Chem Soc* **118**(17), 4212 (1996).

Hoyer, P. Formation of a titanium dioxide nanotube array. *Langmuir* **12**(6), 1411 (1996).

Hsu, W.K.; Zhu, Y.Q.; Boothroyd, C.B.; Kinloch, I.; Trasobares, S.; Terrones, H.; Grobert, N.; Terrones, M.; Escudero, R.; Chen, G.Z.; Colliex, C.; Windle, A.H.; fray, D.J.; Kroto, H.W.; Walton, D.R.M. Mixed-phase $W_xMo_yC_zS_2$ nanotubes. *Chem Mater* **12**(12), 3541 (2000).

Hsu, S.-C.; Whang, W.-T.; Hung, C.H. Large scale fabrication of ZnO nanocrystals by a simple two-step evaporation oxidation approach. *Mater Charact* **58**, 401 (2007).

Hu, W.B.; Zhu, Y.Q.; Hsu, W.K.; Chang, B.H.; Terrones, M.; Grobert, N.; Terrones, H.; Hare, J.P.; Kroto, H.W.; Walton, D.R.M. Generation of hollow crystalline tungsten oxide fibres. *Appl Phys A* **70**, 231 (2000).

Hu, J.; Bando, Y.; Liu, Z. Synthesis of gallium-filled gallium oxide-zinc oxide composite coaxial nanotubes. *Adv Mater* **15**(12), 1000 (2003).

Hu, J.; Shi, J.; Li, S.; Qin, Y.; Guo, Z.X.; Song, Y.; Zhu, D. Efficient method to functionalize carbon nanotubes with thiol groups and fabricate gold nanocomposites. *Chem Phys Lett* **401**, 352 (2005).

Huang, T.K.; Cheng, T.H.; Yen, M.Y.; Hsiao, W.H.; Wang, L.S.; Chen, F.R.; Kai, J.J.; Lee, C.Y.; Chiu, H.T. Growth of Cu nanobelt and Ag belt-like materials by surfactant-assisted galvanic reductions *Langmuir* **23**(10), 5722 (2007).

Huang, W.; Taylor, S.; Fu, K.; Lin, Y.; Zhang, D.; Hanks, T.W.; Rao, A.M.; Sun, Y.P. *Attaching proteins to carbon nanotubes via diimide-activated amidation. Nano Lett* **2**(4), 311 (2001).

Huckel, E. *Physik Zeitsch.* **25**: 204 (1924).

Hughes, M.P.; Morgan, H. Dielectrophoretic trapping of single sub-micrometre scale bioparticles. *J Phys D: Appl Phys* **31**(17), 2205 (1998).

Hummelgard, M.; Olin, H.; Vengust, D.; Dvorsek, D.; Mihailoviv, D. High conductivity observed in $Mo_6S_3I_6$ molybdenum-based nanowire-bundles by in-situ TEM-SPM technic. in press (2007).

Iijima, S. Helical microtubules of graphitic carbon. *Nature* **354**, 56 (1991).

Iijima, S.; Ichihashi, T. Single-shell carbon nanotubes of 1-nm diameter. *Nature* **363**, 603 (1993).

Ijiro, K.; Sunami, H.; Arai, K.; Matsumoto, J.; Karthaus, O.; Kraemer, S.; Mittler, S.; Nishi, N.; Juskowiak, B.; Takenaka, S.; Knoll, W.; Shimomura, M. Base-pair mapping by chemical force microscopy on nucleobase self-assembled monolayers. *Coll Surf A* 198-200, 677 (2002).

Ishigami, M.; Sau, J.D.; Aloni, S.; Cohen, M.L.; Zettl, A. Observation of the giant stark effect in boron-nitride nanotubes. *Phys Rev Lett* **94**, 056804 (2005).

Issi, J.-P.; Langer, L.; Heremans, J.; Olk, C.H. Electronic properties of carbon nanotubes: experimental results. *Carbon* **33**(7), 941 (1995).

Ito, T.; Sun, L.; Crooks, R.M. Observation of DNA transport through a single carbon nanotube channel using fluorescence microscopy. *Chem Commun* 1482 (2003).

Jana, N.R.; Gearheart, L.; Murphy, C.J. Wet chemical syntheis of high aspect ratio cylindrical gold nanorods *J.Phys.Chem. B* **105**, 4065 (2001).

Jeon, S.I.; Lee, J.H.; Andrade, J.D.; de Gennes, P.G. Protein-surface interactions in the presence of polyethylene oxide: simplified theory. *J Coll Inter Sci* **142**(1), 149 (1991).

Jiang, K.; Schadler, L.S.; Siegel, R.W.; Zhang, X.; Zhang, H.; Terrones, M. Protein immobilization on carbon nanotubes via a two-step process of diimide-activated amidation. *J Mater Chem* **14**, 37 (2004).

Jiang, X.; Xie, Y.; Lu, J.; Zhu, L.; He, W.; Qian, Y. Synthesis of novel nickel sulfide layer-rolled structures. *Adv Mater* **13**(16), 1278 (2001).

Jie, J.; Wang, G.; Wang, Q.; Chen, Y.; Han, X.; Wang, X.; Hou, J.G. Synthesis and characterization of aligned ZnO nanorods on porous aluminum oxide template *J.Phys.Chem. B* **108**(32), 11976 (2004).

Jo, S.H.; Lao, J.Y.; Ren, Z.F.; Farrer, R.A.; Baldacchini, T.; Fourkas, J.T. Field emission studies on thin films of zinc oxide nanowires *Appl.Phys.Lett.* **83**(23), 4821 (2003).

Johnson, P.H.; Grossman, L.I. Electrophoresis of DNA in agarose gels. Optimizing separations of conformational isomers of duple and single-stranded DNAs. *Biochem* **16**(19), 4217 (1977).

Johnson, K.L.; Kendall, K.; Roberts, A.D. Surface energy and the contact of elastic solids. *Proc R Soc Lond A* **324**, 301 (1971).

Joly-Pottuza, L.; Dassenoya, F.; Martin, J.M.; Vrbanic, D.; Mrzel, A.; Mihailovic, D.; Vogel, W.; Montagnac, G. Tribological properties of Mo–S–I nanowires as additive in oil. *Tribology Letters* **18**(3), 385 (2005).

Jorgenson, J.W.; Lukacs, K.D. Zone electrophoresis in open-tubular glass capillaries. *Anal Chem* 53: 1298 (1981).

Joy, D.C. Beam interactions, contrast and resolution in the SEM. *J Microsc* **136**, 241 (1984).

Jung, S.I.; Choi, J.S.; Shim, H.C.; Kim, S.; Jo, S.H.; Lee, C.J. Fabrication of probe-type carbon nanotubes point emitters. *Appl Phys Lett* **89**, 233108 (2006).

Kahaly, M.U.; Ghosh, P.; Narasimhan, S.; Waghmare, U.V. Size dependence of structural, electronic, elastic and optical properties of selenium nanowires: a first-principles study *The J.Chem.Phys.* **128**(4), 044718 (2008).

Kakutani, T.; Shibatani, S.; Sugai, M. Electrorotation of non-spherical cells: theory for ellipsoidal cells with an arbitrary number of shells. *Bioelectrochem Bioenerg* **31**(2), 131 (1993).

Kalyuzhny, G.; Schneeweiss, M.A.;Shanzer, A.; Vaskevich, A.; Rubinstein, I. Differential plasmon spectroscopy as a tool for monitoring molecular binding to ultrathin gold films. *J Am Chem Soc* **123**(13), 3177 (2003).

Kamat, P.V. Photophysical, photochemical and photocatalytic aspects of metal nanoparticles. *J Phys Chem B* **106**(32), 7729 (2002).

Karajanagi, S.S.; Yang, H.; Asuri, P.; Sellitto, E.; Dordick, J.S.; Kane, R.S. Protein-assisted solubilization of single-walled carbon nanotubes. *Langmuir* **22**(4), 1392 (2006).

Keren, K.; Berman, R.S.; Buschstab, E.; Sivan, U.; Braun, E. DNA-templated carbon nanotube field-effect transistor. *Science* **302**, 1380 (2003).

Khomutov, G.B. Two-dimensional synthesis of anisotropic nanoparticles. *Colloids Surf* **202**(2-3), 243

(2002).

Khoo, K.H.; Mazzoni, M.S.C.; louie, S.C. Tuning the electronic properties of boron nitride nanotubes with transverse electric fields: a giant dc Stark effect. *Phys Rev B* **69**: 201401 (2004).

Kim, D.T.; Blanch, H. W.; Radke, C.J. Direct imaging of lysozyme adsorption onto mica by atomic force microscopy. *Langmuir* **18**(15), 5841 (2002).

Kim, J.S.; Park, W.; Lee, C.H.; Yi, G.C. ZnO nanorod biosensor for higly sensitive detection of specific protein binding. *J Korean Phys Soc* **49**(4), 1635 (2006).

Kodre, A.; Gomilsek, J.P.; Arcon, I.; Meden, A.; Mihailovic, D. Specific EXAFS tools in analysis of MoSI nanowires. *Acta Chim Slov* **53**, 13 (2006).

Kolliopoulou, S.; Dimitrakis, P.; Normand, P.; Zhang, H.L.; Cant, N.; Evans, S.D.; Paul, S.; Pearson, C.; Molloy, A.; Petty, M.C.; Tsoukalas, D. Hybrid silicon–organic nanoparticle memory device. *J Appl Phys* **94**(8), 5234 (2003).

Kohn, J. A cellulose acetate supporting medium for zone electrophoresis. *Clin Chem Acta* **2**, 297 (1957).

Hong, S.; Zhu, J.; Mirkin, C.A. Multiple ink nanolithography: toward a multiple-pen nano-plotter *Science* **286**, 523 (1999).

Kovtyukhova, N.I.; Martin, B.R.; Mbindyo, J.K.N.; Smith, P.A.; Razavi, B.; Mayer, T.S.; Mallouk, T.E. Layer-by-layer assembly of rectifying junctions in and on metal nanowires. *J Phys Chem B* **105**(37), 8762 (2001).

Krautbauer, R.; Clausen-Schaumann, H.; Gaub, E.H. Cisplatin changes the mechanics of single DNA molecules. *Anges Chem Int Ed* **39**(21), 3912 (2000).

Kretschemer, R.; Fritzsche, W. Pearl chain formation of nanoparticles in microelectrode gaps by dielectrophoresis. *Langmuir* **20**(26), 11797 (2004).

Kroto, H.W.; Heath, J.R.; O'Brien, S.C.; Curl, R.F.; Smalley, R.E. C_{60}: buckminsterfullerene. *Nature* **318**, 162 (1985).

Krstic, V.; Duesberg, G.S.; Muster, J.; Burghard, M.; Roth, S. Langmuir-blodgett films of matrix-dilluted single-walled carbon nanotubes. *Chem Mater* **10**(9), 2338 (1998).

Krupke, R.; Hennrich, F.; Lohneysen, H.; Kappes, M.M. Separation of metallic from semiconducting single-walled carbon nanotubes. *Science* **301**, 344 (2003).

Krupke, R.; Hennrich, F.; Kappes, M.M.; Lohneysen, H. Surface conductance induced dielectrophoresis of semiconducting single-walled carbon nanotubes. *Nano Lett* **4**(8), 1395 (2004).

Krupke, R.; Linden, S.; Rapp, M.; Hennrich, F. Thin films of metallic carbon nanotubes prepared by dielectrophoresis. *Adv Mater* **18**, 1468 (2006).

Kuhr, W.G. Electrochemical DNA analysis comes of age. *Nature Biotech* **18**, 1042 (2000).

Kumar, T.S.K.; Raman, B.; Rao, Ch.M. Fluorescent staining fro proteins on polyacrylamide gels with 5-dimethylamino-1-naphthalenesulfonyl chloride (dansyl chloride). *J Biochem and Biophys Methods* **30**(1), 79 (1995).

van Landingham, M.R.; Villarrubia, J.S.; Guthrie, W.F.; Meyers, G.F. Nanoindentation of polymers: an overview. *Macrom Symp* **167**(1), 15 (2001).

de. Lazzer, A.; Dreyer, M.; Rath, H.J. Particle-surface capillary forces. *Langmuir* **15**(13), 4551 (1999).

Law, M.; King, H.; Messer, B.; Kim, F.; Yang, P. Photochemical sensing of NO_2 with SnO_2 nanoribbon nanosensors at room temperature. *Angew Chem Int Ed* **41**(13), 2405 (2002).

Law, M.; Kind, H; Messer, B.; Kim, F.; Yang, P. Photochemical sensing of NO_2 with SnO_2 nanoribbon nanosensors at room temperature *Angew.Chem.Int.Ed.* **41**(13), 2405-2408 (2002).

Law, M.; Greene, L.E.; Johnson, J.C.; Saykally, R.; Yang, P. Nanowire dye-sensitized solar cells *Nat.Mater.* **4**, 455 (2005).

Leckband, D. Measuring the forces that control protein interactions. *Annu Rev Biophys Biomol Struct* **29**, 1 (2000).

Lee, C.J.; Lee, T.J.; Lyu, S.C.; Zhang, Y.; Ruh, H.; Lee, H.J. Field emission from well-aligned zinc oxide nanowires grown at low temperature *Appl.Phys.Lett.* **81**(19), 3648 (2002).

Lee, D.J.; Park, J.Y.; Yun, Y.S.; Hong, Y.S.; Moon, J.H.; Lee, B.T.; Kim, S.S. Comparative studies on the growth behavior of ZnO nanorods by metalorganic chemical vapor deposition depending on the type of substrate *J.Crystal Growth* **276**(3-4), 458 (2005).

Lee, J.U.; Huh, J.; Kim, K.H.; Park, C.; Jo, W.H. Aqueous suspension of carbon nanotubes via non-covalent funtionalization with oligothiophene-terminated poly(ethylene glycol). *Carbon* **45**, 1051 (2007).

Lekka, M.; Laidler, P.; Gil, D.; Lekki, J.; Stachura, Z.; Hrynkiewicz, A.Z. Elasticity of normal and cancerous human bladder cells studied by scanning force microscopy. *Eur Phys J* **28**(4), 312 (1999).

Leong, W.L.; Lee, P.S.; Mhaisalkar, S.G.; Chen, T.P.; Dodabalapur, A. Charging phenomena in pentacene-gold nanoparticle memory device. *Appl Phys Lett* **90**, 042906 (2007).

Li, C.; Curreli, M.; Lin, H.; Lei, B.; Ishikawa, F.N.; Datar, R.; Cote, R.J.; Thompson, M.E.; Zhou, C. Complementary detection of prostate-specific antigen using In_2O_3 nanowires and carbon nanotubes. *J Am Chem Soc* **127**(36), 12484 (2005).

Li, G.; Liao, J.M.; Hu, G.Q.; Ma, N.Z.; Wu, P.J. Study of carbon nanotube modified biosensor for monitoring total cholesterol in blood. *Biosen Bioelectr* **20**, 2140 (2005).

Li, H.; Luk, Y.-Y.; Mrksich, M. Catalytic Asymmetric Dihydroxylation by Gold Colloids Functionalized with Self-Assembled Monolayers. *Langmuir* **15**(15), 4957 (1999).

Li, J.; Ng, H.T.; Cassell, A.; Fan, W.; Chen, H.; Ye, Q.; Koehne, J.; Han, J.; Meyyappan, M. Carbon nanotube nanoelectrode array for ultrasensitive DNA detection. *Nano Lett* **3**(5), 597 (2003).

Li, S.H.; Zhu, X.F.; Zhao, Y.P. Carbon assisted growth of SiO_x nanowires *J.Phys.Chem. B* **108**(44), 17032-17041 (2004).

Li, Y.; Wang, J.; Deng, Z.; Wu, Y.; Sun, X.; Yu, D.; Yang. P. Bismuth nanotubes: a rational low-temperature synthetic route. *J Am Chem Soc* **123**, 9904 (2001).

Lin, A.P.; Mou, C.Y.; Liu, S.B. Formation of mesoporous silica nanotubes. *Adv Mater* **12**(2), 103 (2000).

Link, S.; Burda, C.; Mohamed, M.B.; Nikoobakht, B.; El-Sayed, M.A. Femtosecond transient-absorption dynamics of colloidal gold nanorods: shape independence of the electron-phonon relaxation time. *Phys Rev B* **61**(9), 608690 (2000).

Lioubashevski, O.; Patolsky, F.; Willner, I. Probing of DNA and single-base mismatches by chemical force microscopy using peptide nucleic acid modified sensing tips and functionalized surfaces. *Langmuir* **17**(17), 5134 (2001).

Liu, J.; Abid, S.; Hail. M.E.; Lee, M.S.; Hungeland, J.; Zein, N. Use of affinity capillary electrophoresis for the study of protein and drug interactions. *The Analyst* **123**(7), 1455 (1998).

Liu, J.; Alvarez, I.; Ong, W.; Kaifer, A.E. Network aggregates formed by C_{60} and gold nanoparticles capped with γ-cyclodextrin hosts. *Nano Lett* **1**(2), 57 (2001).

Liu, J.; Lu, Y. A colorimetric lead biosensor using DNAzyme-directed assembly of gold nanoparticles. *J Am Chem Soc* **125**(22), 6642 (2003).

Liu, J.; Lu, Y. Fast colorimetric sensing of adenosine and cocaine based on a general sensor design involving aptamers and nanoparticles. *Angew Chem Int Ed* **45**, 90 (2006).

Liu, L.Q.; Guo, Z.X.; Dai, L.M. Organic modification of carbon nanotubes. *Chin Scienc Bull* **47**(6), 441 (2002).

Liu, J.; Raveendran, P.; Qin, G.; Ikushima, Y. Self-assembly of $\beta_{\text{-D}}$ glucose-stabilized Pt nanocrystals into nanowire-like structures. *Chem Commun* 2972 (2005).

Liu, J.; Rinzler, A.G.; Dai, H.; Hafner, J.H.; Bradley, R.K.; Boul, P.J.; Lu, A.; Iverson, T.; Shelimov, K.; Huffman, C.B.; Rodriguez-Macias, F.; Shon, Y.-S.; Lee, T.R.; Colbert, D.T.; Smalley, E.R. Fullerene pipes. *Science* **280**, 1253 (1998).

Liu, Y.; Wang, M.; Zhao, F.; Xu, Z.; Dong, S. The direct electron transfer of glucose oxidase and glucose biosensor based on carbon nanotubes/chitosan matrix. *Biosens Bioelectr* **21**(6), 984 (2005).

Liu, Z.; Li, S.; Yang, Y.; Peng, S.; Hu, Z.; Qian, Y. Complex surfactant assisted hydrothermal route to ferromagnetic nickel nanobelts *Adv.Mater.* **15**(22), 1946 (2003).

Lo, Y.-S.; Zhu, Y.-J.; Beebe Jr., T.P. Loading-rate dependence of individual ligand-receptor bond-rupture forces studied by atomic force microscopy. *Langmuir* **17**(12), 3741 (2001).

Loiseau, A.; Williame, F.; Demoncy, N.; Hug, G.; Pascard, H. Boron nitride nanotubes with reduced numbers of layers synthesized by arc discharge. *Phys Rev Lett* **76**(25), 4737 (1996).

Lu, C.Y.; Chang, S.J.; Chang, S.P.; Lee, C.T.; Kuo, C.F.; Chang, H.M.; Chiou, Y.Z.; Hsu, C.L.; Chen, I.C. Ultraviolet photodetectors with ZnO nanowires prepared on ZnO: Ga/glass templates *Appl.Phys.Lett.*

89(15), 153101 (2006).

Lubarsky, G.V.; Davidson, M.R.; Bradley, R.H. Elastic modulus, oxidation depth and adhesion force of surface modified polystyrene studied by AFM and XPS. *Surf Sci* **558**, 135 (2004).

Ludwig, M.; Dettmann, W.; Gaub, H.E. Atomic force microscope imaging contrast based on molecular recognition. *Biophys J* **72**, 445 (1997).

Mafune, F.; Kohno, J.; Takeda, Y.; Kondow, T. Formation and size control o silver nanoparticles by laser ablation in aqueous solution. *J Phys Chem B* **104**(39), 9111 (2000).

Maniatis, T.; Jeffrey, A.; van de Sande, H. Chain length determination of small double- ans single-stranded DNA molecules by polyacrylamide gel electrophoresis. *Biochemisty* **14**(17), 3787 (1975).

Mann, S.; Shenton, W.; Li, M.; Connolly, S.; Fitzmaurice, D. Biologically programmed nanoparticle assembly. *Adv Mater* **12**(2), 147 (2000).

Marezio, M.; Dernier, P.D.; Remeika, J.P.; Corenzwit, E.; Matthias, B.T. Superconductivity of ternary sulfides and the structure of $PbMo_6S_8$. *Mater Res Bul* **8**(6), 657 (1973).

Margulis, L.; Saltra, G.; Tenne, R. Nested fullerene-like structure. *Nature* **365**, 113 (1993).

Markx, G.H.; Huang, Y.; Zhou, X.F.; Pethig, R. Dielectrophoretic characterization and separation of microorganisms. *Microb* **140**(3), 585 (1994).

Marszalek, P.E.; Li, H.; Fernandez, J.M. Fingerprinting polysaccharides with single-molecule atomic force microscopy. *Nature Biotech* **19**, 258 (2001).

Martinez-Gomez, M.A.; Sagrado, S.; Villanueva-Camanas, R.M.; Medina-Hernandez, M.J. Characterization of basic drug-human serum protein interactions by capillary electrophoresis. *Electrophoresis* **27**(17), 3410 (2006).

Marszalek, P.E.; Greenleaf, W.J.; Li, H.; Oberhauser, A.F.; Fernandez, J.M. Atomic force microscopy captures quantized plastic deformation in gold nanowires *PNAS* **97**(12), 6282-6286 (2000).

Matthias, B.T.; Marezio, M.; Corenzwit, E.; Cooper, A.S.; Barz, H.E. High-temperature superconductors, the first ternary system. *Science* 175, 1465 (1972).

Matsui, S.; Ochiai, Y. Focused ion-beam applications to solid state devices *Nanotechnology* **7**(3), 247 (1996).

Matzelle, T.R.; Geuskens, G.; Kruse, N. Elastic properties of poly(N-isopropylacrylamide) and poly(acrylamide) hydrogels studied by scanning force microscopy. *Macromolecules* **36**(8), 2926 (2003).

Maugis, D. Adhesion of spheres: the JKR-DMT transition using a dugdale model. *J Coll Int Sci* **150**(1), 243 (1992).

Mayers, B.; Xia, Y. Formation of tellurium nanotubes through concentration depletion at the surfaces of seeds. *Adv Mater* **14**(4), 279 (2002).

McCarthy, D.N.; Nicolosi, V.; Vengust, D.; Mihailovic, D.; Compagnini, G.; Blau, W.J.; Coleman, J.N. Dispersion and purification of $Mo_6S_3I_6$ nanowires in organic solvents. *J Appl Phys* **100**, 014317 (2007).

Meden, A.; Kodre, A.; Gomilsek, J.P., Arcon, I.; Vilfan, I.; ;Vrbanic, D.; Mrzel, A.; Mihailovic, D. Atomic and electronic structure of $Mo_6S_{9-x}I_x$ nanowires. *Nanotehnology* **16**, 1578 (2005).

Melinger, J.S.; Kleiman, V.D.; McMorrow, D.; Grohn, F.; Bauer, B.J.; Amis, E. Ultrafast dynamics of gold-based nanocomposite materials. *J Phys Chem A* **107**(18), 3424 (2003).

Mendelev, M.I.; Srolovitz, D.J.; Safran, S.A.; Tenne, R. Equilibrium structure of multilayer van der Waals films and nanotubes. *Phys Rev B* **65**, 075402 (2002).

Mermut, O.; Lefebvre, J.; Gray, D.G.; Barrett, C.J. Structural and mechanical properties of polyelectrolyte multilayer films studied by AFM. *Macromolecules* **36**(23), 8819 (2003).

Messer, B.; Song, J.H.; Huang, M.; Wu, Y.; Kim, F.; Yang, P. Surfactant-induced mesoscopic assemblies of inorganic molecular chains *Adv. Mater.* **12**(20), 1526 (2000).

Meyer, E.; Heinzelmann, H.; Grutter, P.; Jung, Th.; Hidber, H.R.; Rudin, H.; Guntherodt, H.J. Atomic force microscopy for study of tribology and adhesion. *Thin Solid Films* **181**(1-2), 527 (1989).

Meyers, J.A.; Sanchez, D.; Elwell, L.P.; Falkow, S. Simple agarose gel electrophoretic method for the identification and characterization of plasmid deoxyribonucleic acid. *J Bacteriol* **127**(3), 1529 (1976).

Michalski, W.P.; Shiell, B.J. Strategies for analysis of electrophoretically separated proteins and peptides. *Analy Chimic Acta* **383**, 27 (1999).

Michov, B.M. Radically simplifying the Henry function. *Electrophoresis* **9**, 199 (1988).

Mickelson, E.T.; Chiang, I.W.; Zimmerman, J.L.; Boul, P.J.; Lozano, J.; Liu, J.; Smalley, R.E.; Hauge, R.H.; Margrave, J.L. Solvation of fluorinated single-wall carbon nanotubes in alcohol solvents. *J Phys Chem B* **103**(21), 4318 (1999).

Mikkers, F.E.P.; Everaerts, F.M.; Verheggen, Th.P.E.M. Concentration distribution in free zone electrophoresis. *J Chrom* **169**, 1 (1979).

Miles, D.T.; Murray, R.W. Redox and double-layer charging of phenothiazine functionalized monolayer-protected clusters. *Anl Chem* **73**(5), 921 (2001).

Milosevic, I.; Vukovic, T.; Damnjanovic, M.; Nikolic, B. Symetry properties of the transition metal dichalcogenide nanotubes. *Eur Phys J B* **17** (4), 707 (2002).

Mintmire, J.W.; Dunlap, B.I.; White, C.T. Are fullerene tubules metallic? *Phys Rev Lett* **68**(5), 631 (1992).

Mirkin, C.A.; Letsinger, R.L.; Mucic, R.C.; Storhoff, J.J. A DNA-based method for rationally assembling nanoparticles into macroscopic materials. *Nature* **382**, 607 (1996).

Moore, V.C.; Strano, M.S.; Haroz, E.H.; Hauge, R.H.; Smalley, R.E. Individually suspended single-walled carbon nanotubes in various surfactants. *Nano Letters* **3**(10), 1379 (2003).

Morgan, H.; Green, N.G. Dielectrophoretic manipulation of rod-shaped viral particles. *J Electrost* **42**(3), 279 (1997).

Morgan, H.; Hughes, M.P.; Green, N.G. Separation of submicron bioparticles by dielectrophoresis. *Biophy J* **77**, 516 (1999).

Mossotti, O.F. Discussione analitica. *Mere Soc Ital* **14**, 49 (1850).

Mourzina, Y.; Steffen, A.; Kalyagin, D.; Carius, R.; Offenhausser, A. Cappilary zone electrophoresis of amino acids on a hybrid poly(dimethylsiloxane)-glass chip. *Electophoresis* **26**(9), 1849 (2005).

Mucic, R.C.; Storhoff, J.J.; Mirkin, C.A.; Letsinger, R.L. DNA-directed synthesis of binary nanoparticle network materials. *J Am Chem Soc* **120**(48), 12674 (1998).

Mullen, K.; Ben-Jacob, E.; Jaklevic, R.C.; Schuss, Z. I-V characteristics of coupled ultrasmall-capacitance normal tunnel junctions. *Phys Rev B* **37**(1), 98 (1998).

Muller, T.; Gerardino, A.; Schnelle, T.; Shirley, S.G.; Bordoni, F.; de Gasperis, G.; Leoni, R.; Fuhr, G. Trapping of micrometre and sub-micrometre particles by high-frequency electric fields and hydrodynamic forces. *J Phys D: Appl Phys* **29**, 340 (1996).

Muys, J.; Alkaisi, M.M.; Evans, J.J.; Nagase, J. Biochip: cellular analysis by atomic force microscopy using dielectrophoretic manipulation. *Japan J Appl Phys* **44**(7B), 5717 (2005).

Nath, N.; Chilkoti, A. A colorimetric gold nanoparticle sensor to interrogate biomolecular interactions in real time on a surface. *Anal Chem* **74**(3), 504 (2002).

Nath, M.; Rao, C.N.R. $MoSe_2$ and WSe_2 nanotubes and related structures. *Chem Commun* 2236 (2001).

Nath, M.; Rao, C.N.R. New metal disulfide nanotubes. *J Am Chem Soc* **123**(20), 4841 (2001).

Nath, M.; Mukhopadhyay, K.; Rao, C.N.R. $Mo_{1-x}W_xS_2$ nanotubes and related structures. *Chem Phys Lett* **352**, 163 (2002).

Nath, M.; Rao, C.N.R. Nanotubes of group 4 metal disulfide. *Angew Chem Int Ed* **41**(18), 3451 (2002).

Nativ-Roth, E.; Shvartzman-Cohen, R.; Bounoiux, C.; Florent, M.; Zhang, D.; Szleifer, I.; Yerushalmi-Rozen, R. Physical adsorption of block copolymers to SWNT and MWNT: a nonwrapping mechanism. *Macromol* **40**(10), 3676 (2007).

Nepal, D.; Geckeler, K.E. pH-sensitive dispersion and debundling of single- walled carbon nanotubes: lysozyme as a tool. *Small* **2**(3), 406 (2006).

Nguyen, C.V.; Delzeit, L.; Cassell, A.M.; Li, J.; Han, J.; Meyyappan, M. Preparation of nucleic acid functionalized carbon nanotube arrays. *Nano Lett* **2**(10), 1079 (2002).

Nicolosi, V.; Vrbanic, D.; Mrzel, A.; McCauley, J.; O'Flaherty, S.; Mihailovic, D.; Blau, W.J.; Coleman, J.N. Solubility of $Mo_6S_{4.5}I_{4.5}$ nanowires. *Chemical Physics Letters* **401**, 13 (2005).

Nicolosi, V.; Vrbanic, D.; Mrzel, A.; McCauley, J.; O'Flaherty, S.; McGuinness, C.; Compagnini, G.; Mihailovic, D.; Blau, W.J.; Coleman, J.N. Solubility of $Mo_6S_{4.5}I_{4.5}$ nanowires in common solvents: a sedimentation study. *J Phys Chem B* **109**, 7124 (2005).

Nicolosi, V.; Vengust, D.; Mihailovic, D.; Blau, W.J.; Coleman, J.N. Debundeling by dilution: observation

of significant populations of individual MoSI nanowires in high concentration dispersions. *Chem Phys Lett* **425**(1-3), 89 (2006).

Niederberger, M.; Muhr, H.J.; Krumeich, F.; Bieri, F.; Gunther, D.; Nesper, R. Low-cost synthesis of vanadium oxide nanotubes via two novel non-alkoxide routes. *Chem Mater* **12**(7), 1995 (2000).

Nishhi, H. Capillary electrophoresis of drugs: current status in the analysis of pharmaceuticals. *Electrophoresis* **20**(15-16), 3237 (1999).

Numata, M.; Asai, M.; Kaneko, K.; Bae, A.H.; Hasegawa, T.; Sakurai, K.; Shinkai, S. Inclusion of cut and as-grown single-walled carbon nanotubes in the helical superstructure of schizophyllan and curdlan (β-1,3-glucans). *J Am Chem Soc* **127**, 5875 (2005).

Oana, H.; Ueda, M.; Washizu, M. Visualization of a specific sequence on a single large DNA molecule using fluorescence microscopy based on a new DNA-stretching method. *Biochem Biophys Res Commun* **265**(1), 140 (1999).

Oberhauser, A.F.; Hansma, P.K.; Carrion-Vasquez, M.; Fernandez, M. Stepwise unfolding of titin under force-clamp atomic force microscopy. *J Proc Natl Acad Sci USA* **98**(2), 468 (2001).

O'Connell, M.J.; Boul, P.; Ericson, L.M.; Huffman, C.; Wang, Y.; Haroz, E.; Kuper, C.; Tour, J.; Ausman, K.D.; Smalley, R.E. Reversible water-solubilization of single-walled carbon nanotubes by polymer wrapping. *Chem Phys Lett* **342**, 265 (2001).

Odermatt, R.; Fischer, O.; Jones, H.; Bongi, G. Upper critical fields of some ternary molybdenum sulphides. *J Phys C: Solid State Phys* **7**(1), L13 (1974).

Ogston, A.G. The spaces in a uniform random suspension of fibres. *Trans Faraday Soc* **54**, 1752 (1958).

Okada, T.; Kaneko, T.; Hatakeyama, R.; Tohji, K. Electrically triggered insertion of single-stranded DNA into single-walled carbon nanotubes. *Chem Phys Lett* **417**(4-6), 288 (2006).

Ortiz-Acevedo, A.; Xie, H.; Dalton, A.B.; Baughman, R.H.; Draper, R.K.; Musselman, I.H.; Dieckmann, G.R. Diameter-selective solubilization of single-walled carbon nanotubes by reversible cyclic peptides. *J Am Chem Soc* **127**(26), 9512 (2005).

Pan, Z.W.; Dai, Z.R.; Wang, Z.L. Nanobelts of semiconducting oxides *Science* **291**, 1947 (2001).

Pantarotto, D.; Partidos, C.D.; Graff, R.; Hoebeke, J.; Briand, J.P.; Prato, M.; Bianco, A. Synthesis, structural sharacterization, and immunological properties of carbon nanotubes functionalized with peptides. *J Am Chem Soc* 125, 6160 (2003).

Park, S.J.; Taton, T.A.; Mirkin, C.A. Array-based electrical deetction of DNA with nanoparticle porbes. *Science* **295**, 1503 (2002).

Patil, S.; Dharmadhikari, C.V. Investigation of the electrostatic forces in scanning probe microscopy at low bias voltages. *Surf Interface Anal* **33**, 155 (2002).

Paul, S.; Pearson, C.; Molloy, A.; Cousins, M.A.; Green, M.; Kolliopoulou, S.; Dimitrakis, P.; Normand, P.; Tsoukalas, D.; Petty, M.C. Langmuir-blodgett film deposition of metallic nanoparticles and their application to electronic memory structures. *Nano Lett* **3**(4), 533 (2003).

Peng, Y.; Meng, Z.; Zhong, C.; Lu, J.; Xu, L.; Zhang, S.; Qian, Y. $Cu_{5.5}FeS_{6.5}$ nanotubes – a new kind of ternary sulfide nanotubes. *New J Chem* **25**, 1359 (2001).

Perrin, A.; Chevrel, R.; Sergent, M.; Fischer, O. Synthesis and electrical properties of new chalcogenide compounds containing mixed $(Mo,Me)_6$ octahedral clusters (Me=Ru or Rh). *J Soild State Chem* **33**, 43 (1980).

Perrin, A.; Sergent, M.; Fischer, O. New compounds of the type $Mo_2Re_4X_8$ (M=S, Se) containing octahedral Mo_2Re_4. *Mater Res Bull* **13**(4), 259 (1978).

Petersen, L.S.; Ballou, N.E. Separation of micrometer-size oxide particles by capillary zone electrophoresis. *J Chromatogr* **834**, 445-52 (1999).

Pethica, J.B.; Sutton, A.P. On the stability of a tip and flat at very small separations. *J Vac Sci Technol A* **6**(4), 2490 (1988).

Pohl, H.A. The motion and precipitation of suspensoids in divergent electric fields. *J Appl Phys* **22**(7), 869 (1915).

Poinsot, V.; Lacroix, M.; Maury, D.; Chataigne, G.; Feurer, B.; Couderc, F. Recent advances in amino acid analysis by capillary electrophoresis. *Electrophoresis* **27**(1), 176 (2006).

Porter, L.A.; Ji, J.D.; Westcott, S.L.; Graupe, M.; Czernuszewicz, R.S.; Halas, N.J.; Lee, T.R. Gold and

silver nanoparticles functionalized by the adsorption of dialkyl disulfides. *Langmuir* **14**(26), 7378 (1998).

Prakash, R.; Superfine, R.; Washburn, S.; Falvo, M.R. Funtionalization of carbon nanotubes with proeins and quantum dots in aqueous buffer solutions. *App Phys Lett* **88**, 063102 (2006).

Pu, L.; Bao, X.; Zou, J.; Feng, D. Individual alumina nanotubes. *Angew Chem Int Ed* **40**(8), 1490 (2001).

Qian, L.; Teng, F.; Jin, Z.S.; Zhang,Z.J.; Zhang, T.; Hou, Y.B.; Yang, S.Y.; Xu, X.R. Improved optoelectronic characteristics of light-emitting diodes by using a dehydrated nanotube titanic acid (DNTA)-polymer nanocomposite. *J Phys Chem B* **108**(37), 13928 (2004).

Qin, C.; Goncher, G.; Solanki, R.; Jordan, J. SiGe nanowire growth and characterization *Nanotechnology* **18**, 075302 (2007).

Qin, D.; Zhou, J.; Luo, C.; Liu, Y.; Han, L.; Cao, Y. Surfactant-assisted synthesis of size-controlled trigonal Se/Te alloy nanowires *Nanotechnology* **17**, 674 (2006).

Radmacher, M.; Fritz, M.; Cleveland, J.P.; Walters, D.A.; Hansma, P.K. Imaging adhesion forces and elasticity of lysozyme adsorbed on mica with the atomic force microscope. *Langmuir* **10**(14), 3809 (1994).

Radmacher, M.; Fritz, M.; Kacher, C.M.; Cleveland, J.P.; Hansma, P.K. Measuring the viscoelastic properties of human platelets with the atomic force microscope. *Biophys J* **70**, 556 (1996).

Rao, C.N.R.; Govindaraj, A.G.; Deepak, F.L.; Gunari, N.A.; Nath, M. Surfactant-assisted synthesis of semiconductor nanotubes and nanowires. *Appl Phys Lett* **78**(13), 1853 (2001).

Raymer, D.M.; Smith, D.E. A simple system for staining protein and nucleic acid electrophoresis gels. *Electrophoresis* **28**(5), 746 (2007).

Raymond, S.; Weintraub, L. Acrylamide gel as a supporting medium for zone electrophoresis. *Science* **130**, 711 (1995).

Remskar, M.; Skraba, Z.; Cleton, F.; Sanjines, R.; Levy, F. MoS_2 as microtubes. *Appl Phys Lett* **69**(3), 351 (1996).

Remskar, M.; Skraba, Z.; Stadelmann, P.; Levy, F. Structural stabilization of new compounds: MoS_2 and WS_2 micro- and nanotubes alloyed with gold and silver. *Adv Mater* **12**(11), 814 (2000).

Resch, R.; Baur, C.; Bugacov, A.; Koel, B.E.; Echtarnach, P.; Madhukar, A.; Montoya, N.; Requicha, A.A.G.; Will, P. Likning and manipulation of gold multinanoparticle structures using dithiols and scanning force microscopy. *J Phys Chem B* **103**(18), 3647 (1999).

Rief, M.; Gautel, M.; Oesterhelt, F.; Fernandez, J.M.; Gaub, H.E. Reversible unfolding of individual titin immunoglobulin domains by AFM. *Science* **276**, 1109 (1997).

Riggs, J.E.; Guo, Z.; Carroll, D.L.; Sun, Y.P. Strong luminescence of solubilized carbon nanotubes. *J Am Chem Soc* **122**(24), 5879 (2000).

Romero, P.G. Hybrid organic-inorganic materials – in search of synergic activity. *Adv Mater* **13**(3), 163 (2001).

Saito, R.; Fujita, M.; Dresselhaus, G.; Dresselhaus, M.S. Electronic structure of chiral graphene tubules. *Appl Phys Lett* **60**(18), 2204 (1992).

Saito, N.; Haneda, H.; Sekiguchi, T.; Ohashi, N.; Sakaguchi, I.; Koumoto, K. Low-temperature fabrication of light-emitting zinc oxide micropatterns using self-assembled monolayers *Adv.Mater.* **14**(6), 418 (2002).

Salem, A.K.; Rose, F.R.A.J.; Oreffo, R.O.C.; Yang, X.; Davies, M.C.; Mitchell, J.R.; Roberts, C.J.; Stolnik-Trenkic, S.; Tendler, S.J.B.; Williams, P.M. Porous polymer and cell composites that self-assemble in situ. *Adv Mater* **15**(3), 210 (2003).

Salem, A.K.; Chen, M.; Hayden, J.; Leong, K.W.; Searson, P.C. Directed assembly of multisegment Au/Pt/Au nanowires. *Nano Lett* **4**(6), 1163 (2004).

Sander, M.S.; Tan, L.S. Nanoparticle arrays on surfaces fabricated using anodic alumina films as templates *Adv.Funct.Mater.* **13**(5), 393 (2003).

Sano, M.; Kamino, A.; Okamura, J.; Shinkai, S. Self-organization of PEO-graft-single-walled carbon nanotubes in solutions and langmuir-blodgett films. *Langmuir* **17**(17), 5125 (2001).

Satishkumar, B.C.; Govindaraj, A.; Vogl, E.M.; Basumallick, L.; Rao, C.N.R. Oxide nanotubes prepared using carbonnanotubes as templates. *J Mater Res* **12**(3), 604 (1997).

Satishkumar, B.C.; Govindaraj, A.; Nath, M.; rao, C.N.R. Synthesis of metal oxide nanorods using carbon nanotubes as templates. *J Mater Chem* **10**, 2115 (2000).

Seifert, G.; Kohler, T.; Tenne, R. Stability of metal chalcogenide nanotubes. *J Phys Chem B* **106**, 2497 (2002).

Senddon, I.N. The relation between load and penetration in the axisymetric boussinesq problem for a punch of arbitrary profile. *Int J Enging Sci* **3**, 47 (1965).

Sergent, M.; Chevrel, R. Sur de nouvelles phases séléniées ternaires du molybdène. *J Solid State Chem* **6**, 433 (1973).

Sergent, M.; Chevrel, R.; Fischer, O. On the conductivity of $PbMo_6S_8$ and the series $M_xPbMo_6S_8$ and $M_xPb_{1-x}Mo_6S_8$. *J Less Common Metals* **58**(2), 179 (1978).

Sergent, M.; Fischer, O.; Decroux, M. Stabilization of Mo_6S_8 by halogens; new superconducting compounds: $Mo_6S_6Br_2$, $Mo_6S_6I_2$. *J Solid State Chem* **22**, 87 (1977).

Serwer, P. Electrophoresis of duplex deoxyribonucleic acid in multiple-concentration agarose gels: fractionation of molecules with molecular weights between $2x10^6$ and $110x10^6$. *Biochemistry* **19**, 3001 (1980).

Sethuraman, A.; Han, M.; Kane, R.S.; Belfort, G. Effect of surface wettability on the adhesion of proteins. *Langmuir* **20**(18), 7779 (2004).

Sha, J.; Niu, J.; Ma, X.; Xu, J.; Zhang, X.; Yang, Q.; Yang, D. Silicon nanotubes. *Adv Mater* **14**(17), 1219 (2002).

Shcherbakov, D.; Piendl, W. A novel view of gel-shifts: Analysis of RNA-protein complexes using a two-color fluorescence dye procedure. *Electrophoresis* **28**(5), 749 (2007).

Shelimov, K.B.; Esenaliev, R.O.; Rinzler, A.G.; Huffman, C.B.; Smalley, R.E. Purification of single-wall carbon nanotubes by ultrasonically assisted filtration. *Chem Phys Lett* **282**, 429 (1998).

Shelton, R.N., McCallum, R.W.; Adrian, H. Superconductivity in rare earth molybdenum selenides. *Phys Lett A* **56**(22), 213 (1976).

Shimizu, T.; Teranishi, T.; Hasegawa, S.; Miyake, M. Size evolution of alkanethiol-protected gold nanoparticles by heat treatment in the solid state. *J Phys Chem B* **107**(12), 2719 (2003).

Shipway, A.N.; Katz, E.; Willner, I. Nanoparticle arrays on surfaces for electronic, optical and sensor applications. *Chem Phys Chem* **1**, 18 (2002).

Shulha, H.; Kovalev, A.; Myshkin, N.; Tsukruk, V.V. Some aspects of AFM nanomechanical probing of surface polymer films. *Eur Polym J* **40**, 949 (2004).

Sibbald, M.S.; Chumanov, G.; Cotton, T.M. Reduction of cytochrome c by halide-modified, laser-ablated silver colloids. *J Phys Chem* **100**(11), 4672 (1996).

Simard, J.; Briggs, C.; Boal, A.K.; Rotello, V.M. Formation and pH-controlled assembly of amphiphilic gold nanoparticles. *Chem Com* 1943 (2000).

Sistare, M.F.; Holmberg, R.C.; Thorp, H.H. Electrochemical studies of polynucleotide binding and oxidation by metal complexes: effects of scan rate, concentration and sequence. *J Phys Chem B* **103**(48), 10718 (1999).

Slater, G.W.; Guo, H.L. An exactly solved Ogston model of gel electrophoresis: VI. Towards a theory for macromolecules. *Electrophoresis* **22**(4), 673 (2001).

Smithies, O. Zone electrophoresis in starch gels: group variations in the serum proteins of normal human adults. *Bioch J* **61**, 629 (1995).

Smolka, A.; Kempner, D.; Rembaum, A. Electrophoretic separation of human lymphocytes by means of immunomicrospheres. *Electrophoresis* **3**(5), 300 (2005).

Smoluchowski, M.V. Versuch einer mathematishen theorie der koagulationskinetik kolloider losungen. *Z Phys Chem* **92**, 124 (1917).

Snellings, G.M.B.F.; Vansteenkiste, S.O.; Cornaillie, S.I.; Davies, M.C.; Schacht, E.H. Protein adhesion at poly(ethylene glycol) modified surfaces. *Adv Mater* **12**(24), 1959 (2000).

Sol, C.J.A.; Walig, C.; ter Schegget, J.; van der noordaa, J. Analysis of defective SV40 DNA by agarose gel electrophoresis. *J Gen Virol* **28**, 285 (1975).

Song, J.H.; Wu, Y.; Messer, B.; Kind, H.; Yang, P. Metal nanowire formation using Mo_3Se_3 as reducing and sacrificing templates. *J Am Chem Soc* **123**, 10397 (2001).

Spahr, M.E.; Bitterli, P.; Nesper, R.; Muller, M.; Krumeich, F.; Nissen, H.U. Redox-active nanotubes of Vanadium oxide. *Angew Chem Int Ed* **37**(9), 1263 (1998).

Spatz, J.P.; Roescher, A.; Moller, M. Gold nanoparticles in micellar poly(styrene)-b-poly(ethylene oxide) films – size and interparticle distance control in monoparticulate films. *Adv Mater* **8**(4), 337 (1996).

Star, A.; Gabriel, J.-C.P.; Bradley, K.; Gruner, G. Electronic detection of specific protein binding using nanotube FET devices. *Nano Lett* **3**(4), 459 (2003).

Stejny, J.; Dlugosz, J.; Keller, A. Electron microscope diffraction characterization of the fibrous structure of poly (sulphur nitride) crystals *J. Materials Science* **14**(6), 1291 (1979).

Stejny, J.; Trinder, R.W.; Dlugosz, J. Preparation and structure of poly(sulphur nitride) whiskers *J. Materials Science* **16** (11), 3161 (1981).

Stephan, O.; Ajayan, P.M.; Colliex, C.; Redlich, Ph.; Lambert, J.M.; Bernier, P.; Lefin, P. Doping graphitic and carbon nanotubes structures with boron and nitrogen. *Science* **266**, 1683 (1994).

Stifter, T.; Marti, O.; Bhushan, B. Theoretical investigation of the distance dependence of capillary and van der Waals forces in scanning force microscopy. *Phys Rev B* **62**(20), 13667 (2000).

Stiles, J.Jr.; Davies, P.J. Qualitative analysis by isoelectric focusing of the protein content of Pharbtis nil apices and cotyledons during floral induction. *Plant and Cell Physiology* **17**(4), 855 (1976).

Storhoff, J.J.; Elghanian, R.; Mucic, R.C.; Mirkin, C.A.; Letsinger, R.L. One-Pot Colorimetric Differentiation of Polynucleotides with Single Base Imperfections Using Gold Nanoparticle Probes. *J Am Chem Soc* **120**(9), 1959 (1998).

Stroh, C.; Wang, H.; Bash, R.; Ashcroft, B.; nelson, J.; Gruber, H.; Lohr, D.; Lindsay, S.M.; Hinterdorfer, P. Single-molecule recognition imaging microscopy. *Proc Natl Acad Sci USA* **93**(34), 12503 (1996).

Su, K.H.; Wei, Q.H.; Zhang, X. Interparticle coupling effects on Plasmon resonances of nanogold particles. *Nano Lett* **3**(8), 1087 (2003).

Sudeep, P.K.; Ipe, B.I.; Thomas, K.G.; George, M.V.; Barazzouk, S.; Hotchandani, S.; Kamat, P.V. Fullerene-funtionalized gold nanoparticles. A self-assembled photoactive antenna-metal nanocore assembly. *Nano Lett* **2**(1), 29 (2002).

Sun, L.; Searson, P.C.; Chien, C.L. Finite-size effects in nickel nanowires arrays *Phys.Rev. B* **61**(10), R6463 (2000).

Sun, L.; Crooks, R.M.; Chechik, V. Preparation of polycyclodextrin hollow spheres by templating gold nanoparticles. *Chem Commun* 359 (2001).

Sun, Y.; Mayers, B.; Xia, Y. Transformation of silver nanospheres into nanobelts and triangular nanoplates thorough a thermal process *NanoLetters* **3**(5), 675 (2003).

Sun, Y.; Akhremitchev, B.; Walker, G.C. Using the adhesive interaction between atomic force microscopy tips and polymer surfaces to measure the elastic modulus of compliant samples. *Langmuir* **20**(14), 5837 (2004).

Sun, X.; Yu, B.; Ng, G.; Nguyen, T.D.; Meyyappan, M. III-IV compund semiconductor indium selenide (in_2Se_3) nanowires: synthesis and characterization *Appl.Phys.Lett.* **89**(23), 233121 (2006).

Symington, J.; Green, M.; Brackmann, K. Immunoautoradiographic detection of proteins after electrophoretic transfer from gels to diazo-paper: analysis of adenovirus encoded proteins. *Proc Natl Acad Sci USA* **78**, 177 (1981).

Tak, Y.; Yong, K. Controlled growth of well-aligned ZnO nanorod array using a novel solution method *J.Phys.Chem. B* **109**(41), 19263 (2005).

Tang, H.; Chen, J.; Yao, S.; Nie, L.; Deng, G.; Kuang, Y. Amperometric glucose biosensor based on adsorption of glucose oxidase at platinum nanoparticle-modifed carbon nanotube electrode. *Analyt Biochem* **331**, 89 (2004).

Tang, T.; Liu, X.; Li, C.; Lei, B.; Zhang, D.; Rouhanizadeh, M.; Hsiai, T.; Zhou, C. Complementary response of In2O3 nanowires and carbon nanotubes to low-density lipoprotein chemical gating. *Appl Phys Lett* **86**, 103903 (2005).

Tao, N.J.; Lindsay, S.M.; Lees, S. Measuring the microelastic properties of biological material. *Biophys J* **63**, 1165 (1992).

Tarascon, J. M.; DiSalvo, F. J.; Waszczak, J. V. Physical properties of several $M_2Mo_6X_6$ compunds (M= group IA metal; X= Se, Te) *Solid State Comm.* **52**(3), 227 (1984).

Tarascon, J. M.; DiSalvo, F.J.; Chen, C. H.; Carroll, P. J.; Walsh, M.; Rupp, L. First example of monodispersed $(Mo_3Se_3)_\infty$ clusters *J. Solid State chemistry* **58**(3), 290 (1985).

Taton, T.A.; Lu, G.; Mirkin, C.A. Two-color labeling of oligonucleotide arrays via size-selective scattering of nanoparticle probes. *J Am Chem Soc* **123**(21), 5164 (2001).

Teker, K.; Wickstrom, E.; Panchapakesan, B. Biomolecular tuning of electronic transport properties of carbon nanotubes via antibody functionalization. *IEEE sensors journal* **6**(6), 1422 (2006).

Templeton, A.C.; Pietron, J.J.; Murray, R.W.; Mulvaney, P. Solvent refractive index and core charge influences on the surface plasmon adsorbance of alkanethiolate monolayer protected gold clusters. *J Phys Chem B* **104**(3), 564 (2000).

Tenne, R.; Margulius, L.; genut, M.; Hodes, G. Polyhedral and cylindrical structures of tungsten disulphide. *Nature* **360**, 444 (1992).

Tessema, G.X.; Tseng, Y.T.; Skove, M.J.; Stillwell, E.P.; Brusetti, R.; Monceau, P.; Potel, M.; Gougeon, P. Stree-induced metal-to-nonmetal transition in the quasi-one-dimensional superconductor $Tl_2Mo_6Se_6$ *Phys.Rev. B* **43**(4), 3434(1991).

Thiruvengadathan, R.; Levi-Kalisman, Y.; Regev, O. Synergetic effect of ultrasound and sodium dodecyl sulphate in the formation of CdS nanostructures in aqueous solution. *Ultras Sonochem* **14**, 398 (2007).

Thiruvengadathan, R.; Regev, O. Hierarchically ordered cadmium sulfide nanowires dispersed in aqueous solution. *Chem Mater* **17**, 3281 (2005).

Thomas, K.G.; Kamat, P.V. Making gold nanoparticles glow: enhanced emission from a surface-bound fluoroprobe. *J Am Chem Soc* **122**(11), 2655 (2000).

Tobola, J.; Pecheur, P.; Scherrer, H.; Kaprzyk, S.; Ohta, Y.; Matsumura, Y. The electronic structure of $M_xMo_{6S8-\delta}$ Chevrel phases with defects. *J Phys: Condens Matter* **15**(44), L655 (2003).

Tokudome, H.; Miyauchi, M. Electrochromism of titanate-based nanotubes. *Angew Chem Int Ed* **44**(13), 1974 (2005).

Tong, L.; Lou, J.; Gattass, R.R.; He, S.; Chen, X.; Liu, L.; Mazur, E. Assembly of silica nanowires aerogels for microphotonic devices *Nano Lett.* **5**(92), 259 (2005).

Torma, V.; Schmid, G.; Simon, U. Structure-property relations in Au_{55} cluster layers studied by temperature-dependent impedance measurements. *Chem Phys Chem* **5**, 321 (2001).

Tourillon, G.; Pontonnier, L.; Levy, J.P.; Langlais, V. Electrochemically synthesized Co and Fe nanowires and nanotubes. *Electrochem Solid-State Lett* **3**(1), 20 (2000).

Tskhovrebova, L.; Trinick, J.; Sleep, J.A.; Simmons, R.M. Elasticity and unfolding of single molecules protein titin. *Nature* **387**, 308 (1997).

Tuukkanen, S.; Toppari, J.J.; Kuzyk, A.; Hirviniemi, L.; Hytonen, V.P.; Ihalainen, T.; Torma, P. Carbon nanotubes as electrodes for dielectrophoresis of DNA. *Nano Lett* **6**(7), 1339 (2006).

Tzhayik, O.; Sawant, P.; Efrima, S.; Kovalev, E.; Klug, J.T. Xanthate capping of silver, copper and gold colloids. *Langmuir* **18**(8), 3364 (2002).

Umek, P.; Mihailovic, D. Separation of SWNTs by diffusion. *Synthetic Metals* **121**(1-3), 1211 (2001).

Ung, T.; Liz-Marzan, L.M.; Mulvaney, P. Gold particles thin films. *Colloids Surf A* **202**, 119 (2002).

Uplaznik, M.; Bercic, B.; Strle, J.; Ploscaru, M.I.; Dvorsek, D.; Kusar, P.; Devetak, M.; vengust, D.; Podobnik, B.; Mihailovic, D. Conductivity of single $Mo_6S_{9-x}I_x$ molecular nanowire bundles. *Nanotechnology* **17**, 5142 (2006).

Venkataraman, L.; Lieber, C.M. Molybdenum selenide molecular wires as one-dimensional conductors *Phys. Rev. Lett.* **83**(25), 5334 (1999).

Vigolo, B.; Penicaud, A.; Coulon, C.; Sauder, C.; Pailler, R.; Journet, C.; Bernier, P.; Poulin, P. Macroscopic fibers and ribbons of oriented carbon nanotubes. *Science* **290**, 1331 (2000).

Vrbanic, D.; Remskar, M.; Jesih, A.; Mrzel, A.; Umek, P.; Ponikvar, M.; Jancar, B.; Meden, A,; Novosel, B.; Pejovnik, S.; Venturini, P.; Coleman, J.N.; Mihailovic, D. Air-stable monodispersed Mo6S3I6 nanowires. *Nanotechnology* **15**, 635 (2004).

Walter, E.C.; Faview, F.; Penner, R.M. Palladium mesowire arrays for fast hydrogen sensors and hydrogen-actuated switches. *Anal Chem* **74**(7), 1546 (2002).

Wang, C.Y.; Chan, L.H.; Xiao, D.Q.; Lin, T.C.; Shih, H.C. Mechanism of solid-liquid-solid on the silicon oxide nanowire growth *J.Vac.Sci.Tech. B* **24**(2), 613-617 (2006).

Wang, J.; Liu, G.; Jan, M.R. Ultrasensitive electrical biosensing of proteins and DNA: carbon-nanotube derived amplification of the recognition and transduction events. *J Am Chem* **126**(10), 3010 (2004).

Wang, X.B.; Huang, Y.; Wang, X.; Becker, F.F.; Gascoyne, R.C. Dielectrophoretic manipulation of cells with spiral electrodes. *Biophy J* **72**(4), 1887 (1997).

Wang, Z.; Luo, G.; Chen, J.; Xiao, S.; Wang, Y. Carbon nanotubes as separation carrier in capillary electrophoresis. *Electrophoresis* **24**(24), 4181 (2003).

Wang, L.; Wei, G.; Sun, L.; Liu, Z.; Song, Y.; Yang, T.; Sun, Y.; Guo, C.; Li, Z. Self-assembly of cinnamic acid-capped gold nanoparticles. *Nanotechnology* **17**(12), 2907 (2007).

Wang, S.G.; Zhang, Q.; Wang, R.; Yoon, S.F.; Ahn, J.; Yang, D.J.; Tian, J.Z.; Li, J.Q.; Zhou, Q. Multi-walled carbon nanotubes for the immobilization of enzyme in glucose biosensors. *Electrochem Commun* **5**, 800 (2003).

Wang, X.; Ding, Y.; Summers, C.J.; Wang, Z.L. Large-scale synthesis of six-nanometer-wide ZnO nanobelts *J.Phys.Chem. B* **108**(26), 8773 (2004).

Wang, X.; Li, Q.; Liu, Z.; Zhang, J.; Liu, Z.; Wang, R. Low-temperature growth and properties of ZnO nanowires *Appl.Phys.Lett.* **84**(24), 4941 (2004).

Wang, Y.; Tang, Z.; Tan, S.; Kotov, N.A. Biological assembly of nanocircuit prototypes from protein-modified CdTe nanowires. *Nano Lett* **5**(2), 243 (2005).

Warner, M.G.; Reed, S.M.; Hutchison, J.E. Small, Water-Soluble, Ligand-Stabilized Gold Nanoparticles Synthesized by Interfacial Ligand Exchange Reactions. *Chem Mater* **12**(11), 3316 (2000).

Warren, C.R.; Adams, M.A. Capillary electrophoresis for the determination of major amino acids and sugars in foliage: application to the nitrogen nutrition of sclerophyllous species. *J Experim Botany* **51**(347), 1147 (2000).

Weisenhornt, A.L.; Khorsandit, M.; Kasas, S.; Gotzos, V.; Butt, H.J. Deformation and height anomaly of soft surfaces studied with an AFM. *Nanotech* **4**(2), 106 (1993).

Whitby, R.L.D.; Hsu, W.K.; Boothroyd, C.B.; Kroto, H.W.; Walton, D.R.M. Tungsten disulphide coated multi-walled carbon nanotubes. *Chem Phys Lett* **359**, 121 (2002).

Wiersema, P.H.; Loeb, A.L.; Overbeek, J.Th.G. Calculation of the electrophoretic mobility of a spherical colloid particle. *J Colloid Interface Sci* **22**(1), 78 (1978).

Wise, K.E.; Park, C.; Siochi, E.J.; Harrison, J.S. Stable dispersion of single wall carbon nanotubes in polyimide: the role of noncovalent interactions. *Chem Phys Lett* **391**, 207 (2004).

Wong, E.W.; Sheehan, P.E.; Lieber, C.M. Nanobeam mechanics: elasticity, strength and toughness of nanorods and nanotubes. *Science* **277**, 1971 (1997).

Wong, S.S.; Joselevich, E.; Woolley, A.T.; Cheung, C.L.; Lieber, C.M. Covalently functionalized nanotubes as nanometresized probes in chemistry and biology. *Nature* **394**, 52 (1998).

Wu, J.J.; Liu, S.C.; Wu, C.T.; Chen, K.H.; Chen, L.C. Heterostructures of ZnO-Zn coaxial nanocables and ZnO nanotubes. *Appl Phys Lett* **81**(7), 1312 (2002).

Wu, Y.; Yang, P. Germanium/carbon core-sheath nanostructures. *Appl Phys Lett* **77**(1), 43 (2000).

Wu, Y.; Yang, P. Melting and welding semiconductor nanowires. *Adv Mater* **13**(7), 520 (2001).

Wuelfing, W.P.; Zamborini, F.P.; Templeton, A.C.; Wen, X.; Yoon, H.; Murray, R.W. Monolayer-protected clusters: molecular precursors to metal films. *Chem Mater* **13**(1), 87 (2001).

Xiao, Z.; Zhang, L.; Meng, G.; Tian, X.; Zeng, H.; Fang, M. High-density aligned SiO_2 nanowires arrays: microscopic imaging of the unique growth style and their ultraviolet light emission properties *J.Phys.Chem. B* **110**(32), 15724-28 (2006).

Xu, P.; Yanagi, H. Fluorescence patterning in dye-doped sol-gel films by generation of gold nanoparticles. *Chem Mater* **11**(10), 2626 (1999).

Yada, M.; Mihara, M.; Mouri, S.; Kuroki, M.; Kijima, T. Rare earth (Er, Tm, Yb Lu) oxide nanotubes templated by dodecylsulfate assemblies. *Adv Mater* **14**(4), 309 (2002).

Yan, X.Q.; Zhou, W.Y.; Sun, L.F.; Gao, Y.; Liu, D.F.; Wang, J.X.; Zhou, Z.P.; Yuan, H.J.; Song, L.; Liu, L.F.; Wang, G; Xie, S.S. The influence of hydrogen on the growth of gallium catalyzed silicon oxide nanowires *J.Phys.Chem.Sol.* **66** (5), 701-705 (2005).

Ye, J.-S.; Wen, Y.; Zhang, W.D.; Cui, H.F.; Gan, L.M.; Xu, G.Q.; Sheu, F.S. Application of multi-walled carbon nanotubes functionalized with hemin for oxygen detection in neutral solution. *J Electroanal*

Chem **562**, 241 (2004).

Yee, C.; Scotti, M.; Ulman, A.; White, H.; Rafailovich, M.; Sokolov, J. One phase synthesis of thiol-functionalized platinum nanoparticles. *Langmuir* **15**(13), 4314 (1999).

Yeh, M.S.; Yang, Y.S.; Lee, Y.P.; Lee, H.F.; Yeh, Y.H.; Yeh, C.S. Formation and characteristics of Cu colloids from CuO powder by laser irradiation in 2-propanol. *J Phys Chem B* **103**(33), 6851 (1999).

Ying, L.; White, S.S.; Bruckbauer, A.; Meadows, L.; Korchev, Y.E.; Klenermen, D. Frequency and voltage dependence of the dielectrophoretic trapping of short lengths DNA and dCTP in a nanopipette. *Biophy J* **86**, 1018 (2004).

Yu, D.P.; Hang, Q.L.; Ding, Y; Zhang, H.Z.; Bai, Z.G.; Wang, J.J.; Zhou, Y.H.; Qian, W.; Xiong, G.C.; Feng, S.Q. Amorphous silica nanowires: intensive blue light emitters *Appl.Phys.Lett.* **73**(21), 3076 (1998).

Zhao, Q.; Xu, X.Y.; Song, X.F.; Zhang, X.Z.; Yu, D.P.; Li, C.P.; Guo, L. Enhanced field emission from ZnO nanorods via thermal annealing in oxygen *Appl.Phys.Lett.* **88**(3), 033102 (2006).

Zamborini, F.P.; Hicks, J.F.; Murray, R.W. Quantized double layer charging of nanoparticle films assembled using carboxylate/(Cu^{2+} or Zn^{2+})/carboxylate bridges. *J Am Chem Soc* **122**, 4514 (2000).

Zhang, H.; Schmid, G.; Hartmann, U. Reduced metallic properties of ligand-stabilized small metal clusters. *Nano Lett* **3**(3), 305 (2003).

Zhang, J.; Sun, L.; Liao, C.; Yan, C. A simple route towards tubular ZnO. *Chem Commun* 262 (2002).

Zhang, L.; Zhao, G.-C.; Wei, X.W.; Yang, Z.S. A nitric oxide biosensor based on myoglobin adsorbed on multi-walled carbon nanotubes. *Electroanalysis* **17**(7), 630 (2005).

Zhang, Z.; Sun, X.; Dresselhaus, M.S.; Ying, J.Y.; Heremans, J. Electronic transport properties of single-crystal bismuth nanowires arrays. *Phys Rev B* **61**(7), 4850 (2000).

Zhang, J.; Tang, J.; Yang, G.; Qiu, Q.; Qin, L.C.; Zhou, O. Efficient fabrication of carbon nanotubes point electron sources by dielectrophoresis. *Adv Mater* **16**(14), 1219 (2004)

Zhang, Y.; Kim, H.-H.; Heller, A. Enzyme-amplified amperometric detection of 3000 copies of DNA in a 10-μL droplet at 0.5 fM concentration. *Anal Chem* **75**(13), 3267 (2003).

Zhao, B.; Hu, H.; Yu, A.; Perea, D.; Haddon, C. Synthesis and characterization of water soluble single-walled carbon nanotube graft copolymers. *J Am Chem Soc* **127**(22), 8197 (2005).

Zhao, G.-C.; Zhang, L.; Wei, X.W.; Yang, Z.S. Myoglobin on multi-walled carbon nanotubes modified electrode: direct electrochemistry and electrocatalysis. *Electrochem Commun* **5**, 825 (2003).

Zhao, G.-C.; Zhang, L.; Wei, X.W. An unmediated H_2O_2 biosensor based on the enzyme-like activity of myoglobin on multi-walled carbon nanotubes. *Analyt Biochem* **329**, 160 (2004).

Zhao, Y.-D.; Zhang, W.-D.; Chen, H.; Luo, Q.M.; Li, S.F.Y. Direct electrochemistry of horseradish peroxidase at carbon nanotube powder microelectrode. *Sens Actuat B* **87**, 168 (2002).

Zhang, B.; Hou, W.; Ye, X.; Fu, S.; Xie, Y. 1D tellurium nanostructures: photothermally assisted morphology-controlled synthesis and aplications in preparing funtional nanoscale materials *Adv. Funt.Mater.* **17**(3), 486 (2007).

Zhang, D.; Zhang, R.Q. Structural model of silica nanowire assembled from a highly stable $(SiO_2)_8$ unit *J.Phys.Chem.* **110**(3), 1338-1343 (2005).

Zhang, J.; Du, J.; Han, B.; Liu, Z.; Jiang, T.; Zhang, Z. Sonochemical formation of single-crystalline gold nanobelts *Angew.Chem.Int.Ed.* **45**(7), 1116 (2006).

Zhang, Y.; Franklin, N.W.; Chen, R.J.; Dai, H. Metal coating on suspended carbon nanotubes and its implication to metal-tube interation *Chem.Phys.Lett.* **331**, 35 (2000).

Zheng, L.; Li, S.; Brody, J.P.; Burke, P.J. Manipulating nanoparticles in solution with electrically contacted nanotubes using dielectrophoresis. *Langmuir* **20**(20), 8612 (2004).

Zheng, D.N.; Ramsbottom, H.D.; Hampshire, D.P. Reversible and irreversible magnetization Chevrel-phase superconductor $PbMo_6S_8$. *Phys Rev B* **52**(17), 12931 (1995).

Zheng, M.; Jagota, A.; Semke, E.D.; Diner, B.A.; McLean, R.S.; Lustig, S.R.; Ruchardson, R.E.; Tassi, N.G. DNA-assisted dispersion and separation of carbon nanotubes. *Nature Mater* **2**, 338 (2003).

Zhirnov, V.V.; Choi, W.B.; Cuomo, J.J.; Hren, J.J. Diamond coated Si and Mo field emitters: diamond thickness effect. *Appl Surf Scienc* **94**(95), 123 (1996).

Zhou, R.; Chang, H.-C.; Protasenko, V.; Kuno, M.; Singh, A.K.; Jena, D.; Xing, H. CdSe nanowires with

illumination-enhanced conductivity: induced dipoles, dielectrophoretic assembly and field-sensitive emission. *J Appl Phys* **101**, 073704 (2007).

Zhou, X.T.; Lai, H.L.; Peng, H.Y.; Au, F.C.K.; Liao, L.S.; Wang, N.; Bello, I.; lee, C.S.; Lee, S.T. Thin β-SiC nanorods and their field emission properties. *Chem Phys Lett* **318**, 58 (2000).

Zhu, D.; Li, Y.; Wang, S.; Shi, Z.; Du, C.; Xiao, S.; Fang, H.; Zhou, Y. Design, synthesis and properties of functional materials based on fullerene. *Synth Met* **133-134**, 679 (2003).

Zhu, Y.Q.; Hsu, W.K.; Frth, S.; Terrones, M.; Clark, R.J.H.; Kroto, H.W.; Walton, D.R.M. Nb-doped WS_2 nanotubes. *Chem Phys Lett* **342**, 15 (2001).

Zhu, Y.Q.; Hsu, W.K.; Kroto, H.W.; Walton, D.R.M. An alternative route to NbS_2 nanotubes. *J Phys Chem B* **106**, 7623 (2002).

Zimina, A.; Eisebitt, S.; Freiwald,M.; Cramm, S.; Eberhardt, W.; Mrzel, A.; Mihailovic, D. Electronic structure of subnanometer diameter MoS_2-I_x nanotubes. *Nanoletters* **4**(9), 1740 (2004).

Zumer, M.; Nemanic, V.; Zajec, B.; Remskar, M.; Ploscari, M.; Vengust, D.; Mrzel, A.; Mihailovic, D. Field emission of point-electron source $Mo_6S_3I_6$ nanowires. *Nanotech* **16**, 1619 (2005).

Books:

Chrambach, A. *The practice of quantitative gel electrophoresis* (VCH Weinheim, 1985).

Clausius, R. *Die mechanische WS.rmetheorie* (Vieweg, Braunschweig, Vol. II, 1879).

Dawn, Chescoe & Peter, J. Goodhew *The operation of Transmission and Scanning Electron Microscopes* (Royal Microscopical Society, microsopy handbooks, Oxford University Press, 1879).

Everaerts, F.M.; Beckers, J.L. & Verheggen, Th.P.E.M. *Isotachophoresis, theory, instrumentation and applications* (Elsevier Scientific Publishing Co., Amsterdam, 1976).

Handley, D.A. *Colloidal gold. Principles, methods and Applications* (Academic Press, New York vol 1, 1989).

von Hippel, A.R. *Dielectrics and Waves* (Wiley, New York., 1954).

Israelachvili, J.N. *Intermolecular and surface forces* (Academic Press, London., 1992).

Joseph, Goldstein; Dale, Newbury; David, Joy; Charles, Lyman; Patrick, Echlin; Eric, Lifshin; Linda, Sawyer & Joseph, Michael *Scanning Electron Microscopy and X-ray Microanalysis* (Third Edition, Kluwer Academic/Plenum Publisher., 2003).

Ludwig, Reimer *Transmission Electron Microscopy. Physics of image formation and microanalysis* (Fourth Edition, Springer Series in Optical Sciences: vol 36, 1997).

Mosher, R.A.; Saville, D.A. & Thormann W. *The dynamics of electrophoresis* (VCH Weinheim, 1992).

Nicolosi, V. *$Mo_6S_{9-x}I_x$ nanowires: purification, dispersion and structure studies* (Ph.D. thesis, School of Physics, Trinity College Dublin, 2005).

Pohl, H.A. *Dielectrophoresis: the behavior of neutral matter in non-uniform electric fields* (Cambridge Univ.Press., 1978).

Stratton, J.A. (1941). *Electromagnetic Theory*. McGraw-Hill, New York.

Vargas, F.F. (1994). *Cell electrophoresis*. J. Bauer, CRC Press, Boca Raton, USA: p. 241.

Zworykin, V. K.; Hiller, J. & Snyder, R. L. *Scanning electron microscope* (ASTM Bull.: 117, pg. 15, 1942).

Chapters:

R. Chevrel (1981). *Superconductor materials science: metallurgy, fabrication and applications*. Plenium press: New York, chapter 10.

Reports:

O'Brien R.W. & L.R. White (1978). *Electrophoretic mobility of a spherical colloidal particle.* J Chem Soc: Faraday Trans. vol 74, p 1607.

Turkevitch, J., P.C. Stevenson & J. Hillier (1951). *Nucleation and growth process of in the synthesis of colloidal gold*. Discuss Faraday Soc, vol. 11, p. 55

Conference or Symposium Proceedings:

Baumann G. & Chrambach A. (1976). *Gram-preparative protein fractionation by isotachophoresis: isolation of human growth hormone isohormones*. Proc Nat Acad Sci USA, vol 73, nr 3, p. 732-36. Biochemistry

Holzel R. and F.F. Bier (2003). *Dielectrophoretic manipulation of DNA*. IEE Proc. Nanobiotechnology, vol 150 p. 47-49.

Patolsky, F., G. Zheng, et al. (2004). *Electrical detection of single viruses.* Proc Natl Acad Sci USA vol. 101(39). P. 14017-14022.

Raschke G., T. Franzi, et al. (2004). *Biomolecular sensor based on optical spectroscopy of single gold nanoparticles*. Lasers and Electro-Optics. Conference vol. 2, pg. 2.

Tanaka, K., T. Yamaba, et al. (1992). *The science and technology of carbon nanotubes.* Elsevier, New York. p. 267.

Tiselius A.W.K., (1948). *Electrophoresis and absorption analysis as aids in investigations of large molecular weight substances and their breakdown products*. Nobel Prize lecture.

References sourced via the Internet:

www.veeco.com

www.mo6.com

Index of Figures

Index of Tables

Bibliography

Articles

Field emission of point-electron source $Mo_6S_3I_6$ nanowires

ŽUMER Marko, NEMANIČ Vincenc, ZAJEC Bojan, REMŠKAR Maja, **PLOSCARU Mihaela**, VENGUŠT Damjan, MRZEL Aleš, MIHAILOVIĆ Dragan. Nanotechnology (Bristol), vol. 16, pp. 1619-1622, 2005

Force spectroscopy measurements of MoSIx nanowires with functionalized molecules

PLOSCARU Mihaela, JENKO KOKALJ Saša, UPLAZNIK Marko, VENGUST Damjan, TURK Dušan, MIHAILOVIĆ Dragan, Phys. Status Solidi b, vol 243, nr 13, pg 3325, 2006

Longitudinal conductivity of $Mo_6S_{9-x}I_x$ molecular nanowires bundles

UPLAZNIK Marko, BERČIČ Boštjan, STRLE Jure, **PLOSCARU Mihaela**, DVORŠEK Damjan, KUŠAR Primož, DEVETAK Miha, VENGUST Damjan, PODOBNIK Boštjan, MIHAILOVIĆ Dragan, Nanotechnology (Bristol), vol 17, pg 5142, 2006

$Mo_6S_{9-x}I_x$ nanowire recognitive molecular-scale connectivity

PLOSCARU Mihaela, JENKO KOKALJ Saša, VENGUST Damjan, MRZEL Aleš, MIHAILOVIĆ Dragan, NanoLett., vol 7, nr 6, pg 1445, 2007

Conferences

Isolation, positioning and manipulation of $Mo_6S_3I_6$ by (di)electrophoresis

PLOSCARU Mihaela, MRZEL Aleš, VRBANIĆ Daniel, UMEK Polona, UPLAZNIK Marko, PODOBNIK Boštjan, MIHAILOVIĆ Dragan, VENGUST Damjan, NEMANIČ Vincenc, ŽUMER Marko, ZAJEC Bojan, Electronic properties of synthetic nanostructures : XVIII International Winterschool/Euroconference on Electronic Properties of Novel Materials, Kirchberg, Tirol, Austria, 6-13 March 2004, (AIP conference proceedings, v. 723). Melville: American Institute of Physics, 2004, pp. 435-438.

Field emission of point-electron source $Mo_6S_3I_6$ nanowires

ŽUMER Marko, NEMANIČ Vincenc, ZAJEC Bojan, REMŠKAR Maja, **PLOSCARU Mihaela**, VENGUST Damjan, MRZEL Aleš, MIHAILOVIĆ Dragan, V: the 1st International Conference on Nanomaterials, January 10-14, 2005, Taipei, Taiwan, Program book 2005, pp.71

The influence of annealing on transport properties of MoSIx nanowires

UPLAZNIK Marko, BERŠIŠ Boštjan, STRLE J., **PLOSCARU Mihaela**, RANGUS Mojca, MRZEL Aleš, PANJAN Peter, VENGUST Damjan, PODOBNIK Boštjan, MIHAILOVIĆ Dragan, Electronic properties of novel nanostructure: XIX International Winterschool/Euroconference on Electronic Properties of Novel Materials, Kirchberg, Tirol, Austria, 12-19 March 2005, (AIP conference proceedings, v. 786). Melville: American Institute of Physics, 2005, pp. 370-373.

Self-assembly of gold particles to $Mo_6S_3I_6$ nanowires ends

PLOSCARU Mihaela, UPLAZNIK Marko, MRZEL Ales, REMSKAR Maja, JENKO Saša, TURK Dusan, VENGUST Damjan, MIHAILOVIĆ, Dragan, Electronic properties of novel nanostructure: XIX International Winterschool/Euroconference on Electronic Properties of Novel Materials, Kirchberg, Tirol, Austria, 12-19 March 2005, (AIP conference proceedings, v. 786). Melville: American Institute of Physics, 2005, pp. 374-377.

Force spectroscopy measurements of MoSIx nanowires with functionalized molecules

PLOSCARU Mihaela, JENKO KOKALJ Saša, UPLAZNIK Marko, VENGUST Damjan, TURK Dušan, MIHAILOVIĆ Dragan, Electronic properties of novel nanostructure: XX International Winterschool/Euroconference on Electronic Properties of Novel Materials, Kirchberg, Tirol, Austria, 4-11 March 2006, (AIP conference proceedings, v. 786). Melville: American Institute of Physics

Transport Properties studies of molecular devices using MoSIx nanowires

UPLAZNIK Marko, MRZEL Aleš, **PLOSCARU Mihaela**, PODOBNIK B., BERČIČ Boštjan, PANJAN Peter, MIHAILOVIĆ Dragan, Electronic properties of novel nanostructure: XX International Winterschool/Euroconference on Electronic Properties of Novel Materials, Kirchberg, Tirol, Austria, 4-11 March 2006, (AIP conference proceedings, v. 786). Melville: American Institute of Physics

Force spectroscopy measurements of MoSIx nanowires with functionalize biological molecules

PLOSCARU Mihaela, JENKO KOKALJ Saša, UPLAZNIK Marko, VENGUST Damjan, TURK Dušan, MIHAILOVIĆ Dragan, International Conference on Science and Technology of Synthentic Metals, Dublin, Ireland, 2-7 July 2006

Nanoscale physical and chemical properties of MoSI nanowires

STRLE Jure, **PLOSCARU Mihaela**, DVORŠEK Damjan, VENGUST Damjan, MIHAILOVIĆ Dragan. V: 2nd DESYGN IT nanotube workshop : The Octagon, Queen Mary, University of London, 23rd November 2007, 2007

Invited talks

Purification and positioning of $Mo_6S_3I_6$ nanowires by (di)electrophoresis

PLOSCARU Mihaela, MRZEL Aleš, VRBANIĆ Daniel, MIHAILOVIĆ Dragan, VENGUST Damjan. V: 3rd Slovenian workshop on nanoscience and nanotechnology, Ljubljana, 21-22 October, 2004. SLONANO 2004 : programme and book of abstracts. Ljubljana: Institut Jožef Stefan, 2004, pp. 14.

Functional properties of $MoSl_X$ nanowires

MIHAILOVIĆ Dragan, UPLAZNIK Marko, **PLOSCARU Mihaela**, VENGUŠT Damjan, BERČIČ Boštjan. V: QT 2005: QTSM & QFS 2005 : program and abstracts : [International conference on] Quantum Transport in Synthetic Metals & Quantum Functional Semiconductors : Bologna, Italy, July 3-5, 2005. Bologna: CNR - Area della Ricerca, 2005, pp. 26.

Immobilization of proteins onto MoSxly nanowires

JENKO KOKALJ Saša, **PLOSCARU Mihaela**, VENGUST Damjan, MRZEL Aleš, GUNČAR Gregor, ŽEROVNIK Eva, BRIX Klaudia, MIHAILOVIĆ Dragan, TURK Dušan, V: 4th Symposium of science and technology of nanomaterials in Slovenia, October 24th -25th, 2005, Ljubljana, Slovenia. SLONANO 2005: programme and book of abstracts. Ljubljana: Jozef Stefan Institute: National Institute of Chemistry, 2005, pp. 38.

MoSIx nanowires functionalization for molecular-scale connectivity

PLOSCARU Mihaela, JENKO Saša, UPLAZNIK Marko, VENGUST Damjan, TURK Dušan, MRZEL Aleš, MIHAILOVIĆ Dragan. V: *SLONANO 2007 : 10-12 October, Jožef Stefan Institute, Ljubljana, Slovenia : programme & abstracts*. Ljubljana: Jožef Stefan Institute, 2007

Self-assembled $Mo_6S_{9-x}I_x$ networks

STRLE Jure, VENGUST Damjan, UPLAZNIK Marko, **PLOSCARU Mihaela**, MIHAILOVIĆ Dragan. V: *SLONANO 2007 : 10-12 October, Jožef Stefan Institute, Ljubljana, Slovenia : programme & abstracts*. Ljubljana: Jožef Stefan Institute, 2007